A satellite image of a tropical cyclone, showing a large, swirling cloud system over the ocean. The cyclone's eye is visible in the center, surrounded by dense, white clouds. The surrounding ocean is dark blue, and some landmasses are visible on the left and bottom edges.

LARGE-SCALE AND FULL-SCALE METHODS FOR EXAMINING WIND EFFECTS ON BUILDINGS

EDITED BY: Gregory A. Kopp

PUBLISHED IN: Frontiers in Built Environment



frontiers

Frontiers Copyright Statement

© Copyright 2007-2018 Frontiers Media SA. All rights reserved.

All content included on this site, such as text, graphics, logos, button icons, images, video/audio clips, downloads, data compilations and software, is the property of or is licensed to Frontiers Media SA ("Frontiers") or its licensees and/or subcontractors. The copyright in the text of individual articles is the property of their respective authors, subject to a license granted to Frontiers.

The compilation of articles constituting this e-book, wherever published, as well as the compilation of all other content on this site, is the exclusive property of Frontiers. For the conditions for downloading and copying of e-books from Frontiers' website, please see the Terms for Website Use. If purchasing Frontiers e-books from other websites or sources, the conditions of the website concerned apply.

Images and graphics not forming part of user-contributed materials may not be downloaded or copied without permission.

Individual articles may be downloaded and reproduced in accordance with the principles of the CC-BY licence subject to any copyright or other notices. They may not be re-sold as an e-book.

As author or other contributor you grant a CC-BY licence to others to reproduce your articles, including any graphics and third-party materials supplied by you, in accordance with the Conditions for Website Use and subject to any copyright notices which you include in connection with your articles and materials.

All copyright, and all rights therein, are protected by national and international copyright laws.

The above represents a summary only. For the full conditions see the Conditions for Authors and the Conditions for Website Use.

ISSN 1664-8714
ISBN 978-2-88945-510-2
DOI 10.3389/978-2-88945-510-2

About Frontiers

Frontiers is more than just an open-access publisher of scholarly articles: it is a pioneering approach to the world of academia, radically improving the way scholarly research is managed. The grand vision of Frontiers is a world where all people have an equal opportunity to seek, share and generate knowledge. Frontiers provides immediate and permanent online open access to all its publications, but this alone is not enough to realize our grand goals.

Frontiers Journal Series

The Frontiers Journal Series is a multi-tier and interdisciplinary set of open-access, online journals, promising a paradigm shift from the current review, selection and dissemination processes in academic publishing. All Frontiers journals are driven by researchers for researchers; therefore, they constitute a service to the scholarly community. At the same time, the Frontiers Journal Series operates on a revolutionary invention, the tiered publishing system, initially addressing specific communities of scholars, and gradually climbing up to broader public understanding, thus serving the interests of the lay society, too.

Dedication to quality

Each Frontiers article is a landmark of the highest quality, thanks to genuinely collaborative interactions between authors and review editors, who include some of the world's best academicians. Research must be certified by peers before entering a stream of knowledge that may eventually reach the public - and shape society; therefore, Frontiers only applies the most rigorous and unbiased reviews.

Frontiers revolutionizes research publishing by freely delivering the most outstanding research, evaluated with no bias from both the academic and social point of view. By applying the most advanced information technologies, Frontiers is catapulting scholarly publishing into a new generation.

What are Frontiers Research Topics?

Frontiers Research Topics are very popular trademarks of the Frontiers Journals Series: they are collections of at least ten articles, all centered on a particular subject. With their unique mix of varied contributions from Original Research to Review Articles, Frontiers Research Topics unify the most influential researchers, the latest key findings and historical advances in a hot research area! Find out more on how to host your own Frontiers Research Topic or contribute to one as an author by contacting the Frontiers Editorial Office: researchtopics@frontiersin.org

LARGE-SCALE AND FULL-SCALE METHODS FOR EXAMINING WIND EFFECTS ON BUILDINGS

Topic Editor:

Gregory A. Kopp, Western University, Canada



Hurricane Maria makes landfall in Puerto Rico in September 2017 - elements of this image furnished by NASA.
Image: lavizzara/Shutterstock.com

Global economic losses due to severe weather events have grown dramatically over the past two decades. A large proportion of these losses are due to severe wind storms such as tropical cyclones and tornadoes, which can cause destruction to buildings, houses, and other infrastructure over large areas. To address the growing losses, many new large-scale and full-scale laboratories have been developed. These tools are used to examine the issues that could not be solved with the traditional tools of wind engineering including model-scale boundary layer wind tunnels, simplified standardized product tests, and other methods of analysis. This book presents state-of-the-art results from the development of the many novel approaches being used to mitigate natural disasters around the world.

Citation: Kopp, G. A., ed. (2018). Large-Scale and Full-Scale Methods for Examining Wind Effects on Buildings. Lausanne: Frontiers Media. doi: 10.3389/978-2-88945-510-2

Table of Contents

05 Editorial: Large-Scale and Full-Scale Laboratory Test Methods for Examining Wind Effects on Buildings

Gregory A. Kopp

CHAPTER 1

FULL-SCALE WIND TUNNELS

07 Reducing Losses from Wind-Related Natural Perils: Research at the IBHS Research Center

Christine D. Standohar-Alfano, Heather Estes, Tim Johnston, Murray J. Morrison and Tanya M. Brown-Giammanco

26 Experimental Assessment of Wind Loads on Vinyl Wall Siding

Mohammadtaghi Moravej, Ioannis Zisis, Arindam Gan Chowdhury, Peter Irwin and Bodhisatta Hajra

35 From Load Estimation to Performance Estimation—From Model-Scale Test to Full-Scale Test: With Special Interest in Asian Region

Yukio Tamura, Kazuyoshi Nishijima, Masahiro Matsui, Pham Van Phuc and Qingshan Yang

CHAPTER 2

LARGE-SCALE WIND TUNNELS

47 An Examination of Static Pressure and Duration Effects on Tornado-Induced Peak Pressures on a Low-Rise Building

Fred L. Haan Jr.

58 Full Aeroelastic Model Testing for Examining Wind-Induced Vibration of a 5,000 m Spanned Suspension Bridge

Yaojun Ge, Jinlin Xia, Lin Zhao and Shiyu Zhao

CHAPTER 3

FULL-SCALE METHODS

70 Simulation of Time-Varying Spatially Uniform Pressure and Near-Surface Wind Flows on Building Components and Cladding

Seraphy Y. Shen, Forrest J. Masters, Henry. L. Upjohn II and Jon Sinnreich

84 A Multichamber, Pressure-Based Test Method to Determine Wind Loads on Air-Permeable, Multilayer Cladding Systems

Connell Shamus Miller, Gregory A. Kopp, Murray J. Morrison, Gary Kemp and Nick Drought

96 Development of a Full-Scale Structural Testing Program to Evaluate the Resistance of Australian Houses to Wind Loads

Geoffrey Neville Boughton, Korah Parackal, Navaratnam Satheeskumar and David James Henderson

CHAPTER 4

COMPUTATIONAL METHODS

110 *A Cyber-Based Data-Enabled Virtual Organization for Wind Load Effects on Civil Infrastructures: VORTEX-Winds*

Ahsan Kareem and Dae Kun Kwon



Editorial: Large-Scale and Full-Scale Laboratory Test Methods for Examining Wind Effects on Buildings

Gregory A. Kopp*

Boundary Layer Wind Tunnel Laboratory, Faculty of Engineering, University of Western Ontario, London, ON, Canada

Keywords: natural disaster mitigation, wind loads, large-scale testing, components and cladding, wind tunnels

Editorial on the Research Topic

Large-Scale and Full-Scale Laboratory Test Methods for Examining Wind Effects on Buildings

The idea for this Topic originated at a special session of the 3rd United Nations Conference on Disaster Risk Reduction entitled “Necessity and Efficiency of Large-Scale Facilities for Wind-Related Disaster Risk Reduction,” in Sendai, Japan in 2015. There has been significant growth in losses caused by disasters around the world (see Figure 14 in Tamura et al.), which this conference series is attempting to address. Losses caused by severe storms dominate the overall losses, with houses, the places where we live, where we shelter during storms, being disproportionately damaged or destroyed. In contrast, engineered buildings tend to perform better, although cladding systems remain vulnerable.

Engineered buildings tend not to have major structural failures, even in the most severe tornadoes. When structural failures do occur, they are (i) often preceded by a cladding/component failure such as a large window or door, which causes internal pressurization and subsequent overloading, or (ii) a fastener failure, caused by inappropriate consideration of the load path in design. This contrasts with earthquakes where the ground shaking tends to first cause failures of major structural components. So, in earthquakes, one tends to see collapsed buildings while in severe wind storms one sees an exposed structural system with the cladding missing. Once cladding fails during a storm, two things happen: (i) debris enters the wind field which can significantly increase damage downstream (Kaye, 2018), and (ii) rain and wind can enter the building, destroying the contents (Sparks et al., 1994). Wind-borne debris is also a significant life-safety issue, particularly in tornadoes, as discussed by Simmons and Sutter (2011).

As Prof. Yukio Tamura stated so eloquently and succinctly in his presentation in Sendai: “wind resistant design = cladding/component design.” To improve the design process for structures in severe storm conditions, many new, large-scale, and novel methods have been developed. Many of these are represented by this collection of papers. These include large-scale or full-scale wind tunnels (Moravej et al.; Haan; Standohar-Alfano et al.; Tamura et al.; Ge et al.), full-scale pressure testing systems (Miller et al.; Shen et al.), other full-scale methods (Boughton et al.), and computational approaches (Kareem and Kwon; Shen et al.).

Wind loads for use in design are typically obtained from scale model tests in boundary layer wind tunnels. Requirements in building codes are based on data from such facilities. However, wind tunnels were historically built to determine loads on high-rise buildings at model scales of 1/300 to 1/500. For low-rise residential structures (Tieleman, 2003), or for multi-layer, air-permeable cladding on high-rise buildings, such scales cannot resolve critical geometric details (Kopp and Banks, 2013). In many cases, it may only be possible to determine loads on full-scale structures. This implies a need for larger wind tunnels, four of which are described in this collection, that can test full-scale cladding and fastener systems placed on relatively small, but complete, buildings.

OPEN ACCESS

Edited by:

Forrest Masters,
University of Florida, United States

Reviewed by:

Ioannis Zisis,
Florida International University,
United States

*Correspondence:

Gregory A. Kopp
gakk@blwtl.uwo.ca

Specialty section:

This article was submitted to
Wind Engineering and Science,
a section of the journal
Frontiers in Built Environment

Received: 23 March 2018

Accepted: 16 April 2018

Published: 03 May 2018

Citation:

Kopp GA (2018) Editorial: Large-Scale
and Full-Scale Laboratory Test
Methods for Examining Wind Effects
on Buildings.
Front. Built Environ. 4:25.
doi: 10.3389/fbuil.2018.00025

In the controlled laboratory environment, wind loads can be measured along with actual responses or failures, providing a missing link in understanding performance that cannot be obtained from post-event field surveys alone. While there are no papers using full-scale field studies in this collection of papers, such methods are also of critical importance for validation of all test methods and improved fundamental understanding of the physical process including details about the wind field and the wind loads (Leviton and Mehta, 1992; Liu et al., 2009).

Cladding systems are manufactured products, so they are designed according to various product test standards. For wind resistance, many of these standards are based on simple, inexpensive load tests. The advantage of these test methods is their simplicity and low cost, while their disadvantage is that they often eliminate the correct physics such that passing a test does not guarantee good performance in practice (Kopp et al., 2012). One such example is (ASTM D5206, 2013), which eliminates the mechanism of pressure equalization for air-permeable, cladding system, and (ASTM Standard D3679, 2013), which interprets the loads incorrectly. This leads to loads that can be low by a factor of two (Moravej et al.; Miller et al.). Developing simplified and cost-effective pressure-based test methods is one of the goals of these new labs so that the product test standards are, ultimately, a better indicator of real performance (Miller et al.; Shen et al.). Rain-water intrusion is a significant challenge and cause of losses. While water can be introduced in pressure-based systems, realistic simulations can be developed in full-scale (and large-scale) wind tunnels as demonstrated by Standohar-Alfano et al.

A topic of emerging importance is the design of buildings, communities, and critical infrastructure for tornadoes. In light of recently devastating events, several communities are requiring tornadoes be considered in design (e.g., City of Moore, 2014; ICLR, 2018). As a result, several new tornado simulators (Mishra et al., 2008; Haan et al., 2010; Sabaheesh et al., 2012; Refan and Hangan, 2016) have been built to provide wind loads and improved understanding of the wind fields associated with these events. The paper by Haan provides some significant new information about tornadic wind loads. Resilient communities and societies rely on the performance of civil infrastructure during severe events. The survival of transportation and power systems are critical. The paper by Ge et al. describes tests of a super-long bridge at the bounds of what is physically possible to build.

While improved test methods will improve our understanding of failure mechanisms and performance, design wind loads, and product test standards, designers and engineers need to be able to compute these things. The paper by Kareem and Kwon describes one such approach. It is hoped that by developing these new large-scale and full-scale research facilities, disseminating the subsequent research to various stakeholders, and engaging leaders in our communities, that losses caused by severe wind storms can be significantly reduced. There is a lot of work that remains to be done.

AUTHOR CONTRIBUTIONS

The author confirms being the sole contributor of this work and approved it for publication.

REFERENCES

- ASTM D5206 (2013). *Standard Test Method for Windload Resistance of Rigid Plastic Siding*. West Conshohocken, PA: ASTM International.
- ASTM Standard D3679 (2013). *Standard Specification for Rigid Poly Vinyl Chloride (PVC) Siding*. West Conshohocken, PA: ASTM International.
- City of Moore (2014). Available online at: www.cityofmoore.com/sites/default/files/main-site/high-winds-codes-passed.pdf
- Haan, F. L., Balaramudu, V. K., and Sarkar, P. P. (2010). Tornado-induced wind loads on a low-rise building. *J. Struct. Eng.*, 136, 106–116. doi: 10.1061/(ASCE)ST.1943-541X.0000093
- ICLR (2018). *Durham Region Climate Resilience Standard for New Houses*. Toronto, ON: Institute for Catastrophic Loss Reduction.
- Kaye, N. B. (2018). *Wind-Borne Debris Hazards*. Reston, VA: American Society of Civil Engineers.
- Kopp, G. A., and Banks, D. (2013). Use of the wind tunnel test method for obtaining design wind loads of roof-mounted solar arrays. *J. Struct. Eng.* 139, 284–287. doi: 10.1061/(ASCE)ST.1943-541X.0000654
- Kopp, G. A., Morrison, M. J., and Henderson, D. J. (2012). Full-Scale Testing of Low-Rise, Residential Buildings with Realistic Wind Loads. *J. Wind Eng. Ind. Aerodyn.* 104–106, 25–39. doi: 10.1016/j.jweia.2012.01.004
- Leviton, M. L., and Mehta, K. C. (1992). Texas Tech field experiments for wind loads part I: Building and pressure measuring system. *J. Wind Eng. Ind. Aerodyn.* 43:1565.
- Liu, Z., Prevatt, D. O., Aponte-Bermudez, L. D., Gurley, K. R., Reinhold, T. A., and Akins, R. E. (2009). Field measurement and wind tunnel simulation of hurricane wind loads on a single-family dwelling. *Eng. Struct.* 31, 2265–2274. doi: 10.1016/j.engstruct.2009.04.009
- Mishra, A. R., James, D. L., and Letchford, C. W. (2008). Physical simulation of a single-celled tornado-like vortex, Part A: Flow field characterization. *J. Wind Eng. Ind. Aerodyn.* 96, 1243–1257. doi: 10.1016/j.jweia.2008.02.063
- Refan, M., and Hangan, H. (2016). Characterization of tornado-like flow fields in a new model scale wind testing chamber. *J. Wind Eng. Ind. Aerodyn.* 151, 107–121. doi: 10.1016/j.jweia.2016.02.002
- Sabaheesh, G. R., Matsui, M., and Tamura, Y. (2012). Dependence of surface pressures on a cubic building in tornado like flow on building location and ground roughness. *J. Wind. Eng. Ind. Aerodyn.* 103, 50–59. doi: 10.1016/j.jweia.2012.02.011
- Simmons, K. M., and Sutter, D. (2011). *Economic and Societal Impacts of Tornadoes*. Boston, MA: American Meteorological Society.
- Sparks, P. R., Schiff, S. D., and Reinhold, T. A. (1994). Wind damage to envelopes of houses and consequent insurance losses. *J. Wind Eng. Ind. Aerodyn.* 53, 145–155. doi: 10.1016/0167-6105(94)90023-x
- Tieleman, H. W. (2003). Wind tunnel simulation of wind loading on low-rise structures: a review. *J. Wind Eng. Ind. Aerodyn.* 91:1627. doi: 10.1016/j.jweia.2003.09.021

Conflict of Interest Statement: The author declares that the research was conducted in the absence of any commercial or financial relationships that could be construed as a potential conflict of interest.

Copyright © 2018 Kopp. This is an open-access article distributed under the terms of the Creative Commons Attribution License (CC BY). The use, distribution or reproduction in other forums is permitted, provided the original author(s) and the copyright owner are credited and that the original publication in this journal is cited, in accordance with accepted academic practice. No use, distribution or reproduction is permitted which does not comply with these terms.



Reducing Losses from Wind-Related Natural Perils: Research at the IBHS Research Center

Christine D. Standohar-Alfano, Heather Estes, Tim Johnston, Murray J. Morrison* and Tanya M. Brown-Giammanco

Insurance Institute for Business & Home Safety, Richburg, SC, USA

OPEN ACCESS

Edited by:

Gregory Alan Kopp,
University of Western Ontario,
Canada

Reviewed by:

Arindam Gan Chowdhury,
Florida International University, USA
Nigel Berkeley Kaye,
Clemson University, USA

*Correspondence:

Murray J. Morrison
mmorrison@ibhs.org

Specialty section:

This article was submitted to
Wind Engineering and Science,
a section of the journal
Frontiers in Built Environment

Received: 01 October 2016

Accepted: 19 January 2017

Published: 24 February 2017

Citation:

Standohar-Alfano CD, Estes H,
Johnston T, Morrison MJ and
Brown-Giammanco TM (2017)
Reducing Losses from Wind-Related
Natural Perils: Research at the IBHS
Research Center.
Front. Built Environ. 3:9.
doi: 10.3389/fbuil.2017.00009

The capabilities of the Insurance Institute for Business & Home Safety (IBHS) Research Center full-scale test chamber are described in detail. This research facility allows complete full-scale structures to be tested. Testing at full-scale allows vulnerabilities of structures to be evaluated with fewer assumptions than was previously possible. Testing buildings under realistic elevated wind speeds has the potential to isolate important factors that influence the performance of components, potentially allowing for modifications to standard testing procedures that are commonly used to evaluate product performance. IBHS' wind-related research is discussed, along with research examining natural perils that are highly affected by wind flows around a structure, such as wind-driven rain during high-wind events and firebrand exposures during wildfires. In addition, IBHS' hail testing capabilities are described.

Keywords: damage, full-scale, hail, water ingress, wildfires, wind

INTRODUCTION

In 2010, the Insurance Institute for Business & Home Safety (IBHS) opened its Research Center in Richburg, South Carolina. The purpose of the facility was to conduct realistic, objective, state-of-the-art research to reduce losses to infrastructure resulting from exposures to wind-related natural perils. Rather than conducting research on all potential perils that threaten the built environment, IBHS focused on filling research gaps where there was a lack of realistic scientific research and, therefore, where the new facility could have the largest impact. Based on this objective, the IBHS Research Center was designed to focus on four perils: high wind, hail, wind-driven rain, and wildfire. The central part of the IBHS Research Center is a large test chamber which allows for one- or two-story residential and small commercial buildings to be subjected to the four previously mentioned perils. The Research Center also has small-scale laboratory capabilities to further investigate the perils. The objective of the research is to identify ways to reduce losses for homeowners, business owners, insurance companies, and society at large. Research results can provide valuable information and visuals that can be used in public outreach and educational programs, providing information, which allows individuals to make informed decisions regarding effective mitigation strategies to protect their property, and providing guidance on how to implement these mitigation strategies. The following sections will describe the facility capabilities and core research being conducted in each of the four addressed perils.

High Wind

Wind loads on low-rise structures have been studied extensively over the past 35 years using model-scale wind tunnels. While these facilities have provided valuable information on wind loads that act

on buildings, they are not as well suited for predicting performance of building components or evaluating how buildings fail when subjected to high winds. Moreover, determining the wind loads for extremely complex geometries or cavity flows, which are present for many types of building assemblies, is difficult to measure, if not impossible in many cases due to the small physical model sizes used in these facilities.

Due to increasing wealth and associated infrastructure in regions vulnerable to high winds, infrastructure losses have been increasing (Pielke et al., 2008). Understanding how structures are damaged and fail is critical in improving their performance and ultimately reducing losses. Post-event damage investigations have provided good information on building component failures, but it is often difficult to determine which component initiated failure. Component testing provides valuable information on the capacities of individual elements; however, there is a need for a better method to evaluate the overall performance of the complete structure under more realistic wind loading.

Identification of the vulnerable components, i.e., the weakest link(s), allows for targeted improvement of building codes and/or standards that will have the largest impact in improving the high-wind performance of both residential and commercial buildings. In addition, having specific knowledge of which components are the most likely to fail can allow for targeted, cost-effective mitigation or retrofit strategies to improve the performance of existing buildings subjected to high-wind events. The IBHS test chamber consists of an array of fans which are capable of creating a realistic simulation of the lowest portion of the atmospheric boundary layer (ABL). This capability allows IBHS to subject full-scale buildings to high-wind loads in a controlled, repeatable laboratory setting so that the actual performance of the building and its components can be evaluated.

Hail

There are approximately 3,000 hailstorms in the US every year, which typically cause \$1–2 billion in damages annually (Changnon et al., 2009), with an increasing trend attributed to changing dollar values, growing wealth, and exposure of properties at risk from severe hail (Changnon et al., 2009; Roeder, 2012). Despite the high financial costs of hail events, injury and fatality rates are low, especially when compared to other natural hazards. Because of this, insurers are the primary party concerned with the increasing loss trends attributed to hail and in determining ways to reduce losses. Some impact-resistant (IR) roofing materials are available in the marketplace that can potentially reduce hail-related losses, but there are concerns regarding how those products are tested, and their long-term performance. As a result, there are several hail research thrusts running concurrently at IBHS to address the specific concerns of the insurance industry. These projects also have implications for roofing product manufacturers, as well as modeling and forecasting applications. The three primary research avenues undertaken at IBHS are: field investigations, small-laboratory testing, including standardized testing, and full-scale testing in the test chamber.

IBHS has conducted annual field experiments during active severe weather months in the Central Plains since 2012, to collect

ground-truth hail data [e.g., Giammanco and Brown (2014) and Giammanco et al. (2015)]. The knowledge gained from field studies is used to improve testing using IBHS' unique laboratory capabilities, which allows for investigations of realistic building damages caused by hail (Brown and Giammanco, 2013). Small-laboratory investigations examine the performance of products using several standard impact test methods. In addition, IBHS has developed capabilities to manufacture ice spheres (simulated hail) that replicate properties of real hailstones obtained from field investigations. Impacts from realistic ice spheres can be contrasted against impacts using projectiles prescribed in standardized test methods. Full-scale testing in the IBHS test chamber allows the field and small-laboratory testing to be applied to recreate realistic events, which allows researchers to evaluate full building systems in a controlled environment.

Wind-Driven Rain

Water entry through the building envelope can lead to damaged interiors, including the development of mold and structural degradation of building materials. Sparks et al. (1994) reported that a wind-driven rain incident on a residential building caused damage nearing the insured value of the building. High levels of interior damage often lead to prolonged periods in which a building is not usable, leaving occupants displaced and further contributing to high loss costs.

Prior to the development of IBHS's wind-driven rain system, water entry research primarily existed in the form of field-based studies or laboratory and assembly scale studies utilizing models of individual roof and wall sections [e.g., Bitsuamlak et al. (2009) and Masters et al. (2010)]. The wind-driven rain capabilities at IBHS enable controlled experiments on complete full-scale structures. Studies have primarily focused on research to assess building vulnerabilities to water entry as a means to understand the potential for losses associated with high-wind rainstorms and determine effective mitigation strategies to reduce these losses by preventing or reducing water entry into a building. Thus, one of the key, foundational pieces of IBHS's code-plus construction program, FORTIFIED Home™, includes the use of a sealed roof deck to prevent or reduce water entry if the primary roof cover is lost during high winds. IBHS is able to collect water that enters through the roof deck, attic vents, and penetrations on the exterior wall (e.g., doors and windows) of a test building. These capabilities allow for evaluation and comparison of specific components and mitigation strategies.

Wildfires

On average, the US experiences over 73,000 wildfires annually (United States Forest Service, 2016), burning millions of acres, destroying homes, and in some cases, causing injuries or fatalities of residents and/or firefighting personnel. Wildfire occurrence and intensity is increasing worldwide, with major wildfires occurring outside of the normal fire season (Short, 2015) stretching firefighting resources. There is continual interest in understanding wildfire hazards and mitigation strategies as communities continue to expand into the wildland–urban interface (WUI).

Ignition of a structure can be caused by direct flame contact from the primary fire front or flames from a spot fire, elevated levels of radiant heat, or by wind-blown firebrands (also referred to as embers) that ignite vegetation and/or other combustible fuels closer to the primary building (Potter and Leonard, 2010; Quarles et al., 2010). Post-fire investigations have demonstrated the importance of building ignitions resulting from wind-blown firebrands and not from flames from the wildfire itself. This mode was reported to account for two of every three structural ignitions during the 2007 Witch Creek fire in Southern California (Maranghides and Mell, 2009).

Researchers at IBHS are able to mimic a firebrand attack in a controlled, laboratory setting in order to assess structural vulnerability to this exposure. The risk of ignition from firebrand attacks depends on several factors, including the size and number of firebrands, the amount of combustible debris or other combustible materials in the vicinity of the building, duration of the firebrand attack, and environmental conditions. Experiments to evaluate (1) the vulnerability of buildings to firebrand exposure and (2) potential associated mitigation strategies, accounts for the majority of research at IBHS, since there is limited information available on the vulnerability of buildings to firebrand exposures. Likewise, there is limited coupling between current building codes and standards to firebrand exposure from wildfires (Maranghides and Mell, 2012). One cause of this knowledge gap is the lack of quantification of the firebrand exposure, resulting in an uncertain relationship between exposure and building ignition. The full-scale facilities at IBHS allow for realistic wildfire experiments that address the critical information needed to help mitigate wildfire hazards in WUI communities.

LARGE TEST CHAMBER FACILITY OVERVIEW

The IBHS Research Center is located on a 99-acre campus in Richburg, SC, USA. The focus of the facility is the large test chamber which is capable of subjecting full-scale residential and small commercial structures to Category 3 hurricane winds, hail storms, wind-driven rain, and firebrand exposures. The flow through the test chamber is produced using 105, 1.68 m (5.5 ft) diameter vane-axial fans, each driven by a 261-kW (350 hp) motor. The goal of the test chamber was to develop a space where one- and two-story residential and small commercial structures could be tested at full scale. In conventional model-scale boundary layer wind tunnels, the cross section of test specimens is typically kept to less than 8% of the wind tunnel cross section to limit blockage effects (ASCE 49-12, 2012). To use this approach in the IBHS facility would require a test section so large that it would be economically unfeasible to achieve flow velocities sufficiently high to bring building components to failure. Instead, the IBHS test chamber uses an open-jet wind tunnel design where the test section is larger than the inlet jet, which reduces blockage effects compared to closed jet wind tunnel designs

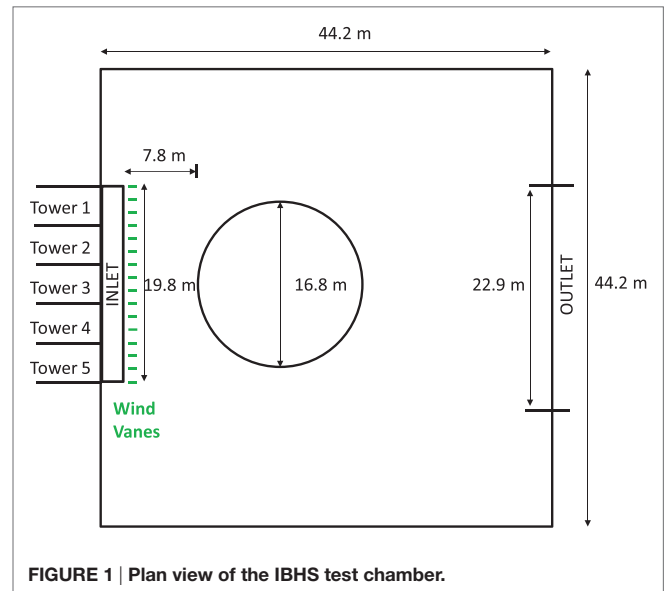


FIGURE 1 | Plan view of the IBHS test chamber.

(Barlow et al., 1999). Buildings tested in the IBHS facility typically have blockage areas between 20 and 30% based on the inlet jet area, and the effects of blockage will be discussed in Section “Surface Pressure Measurements.”

Figure 1 presents a plan view of the IBHS test chamber. The test section has dimensions 44.2 m (145 ft) wide by 44.2 m (145 ft) long, with a clear interior height of 18.3 m (60 ft), while the inlet jet has dimensions of 19.8 m (65 ft) wide by 9.1 m (30 ft) tall. The inlet jet dimensions result in an overall contraction ratio of approximately 2:1. The outlet of the test chamber is about 10% larger than the inlet with a short diffuser section at the outlet. Test specimens are placed on a 16.8-m (55 ft) diameter turntable, which can rotate over a full 360°. The leading edge of the turntable is located 7.8 m (25.6 ft) downstream of the inlet jet. The inlet jet is divided into 15 independent cells, 5 cells spanning horizontally and 3 cells spanning vertically. The 5 lowest cells contain 9 fans each, with the remaining 10 cells having 6 fans each. The fan speed in each cell is controlled independently from the others using 15 variable frequency drives, allowing for shear flows across horizontal and vertical cells to be achieved. The speed of the fans can be updated as fast as 10 times a second with a maximum acceleration rate of 2.6 m/s². At full power, code-equivalent 3-s gust wind speeds at 10 m (33 ft) up to approximately 58 m/s (130 mph) can be simulated, requiring about 30 MW of power.

HIGH WIND RESEARCH CAPABILITIES

Turbulent wind flows around structures give rise to complex flow patterns in close proximity to low-rise structures. The interaction between building-generated vortices and free stream turbulence results in wind loads that have large spatial and temporal gradients. Model-scale wind tunnels have been shown to provide reasonably accurate wind loads on structures, but do have limitations with complex geometries or where small

gaps or local flow fields significantly affect loads. The IBHS test chamber provides a unique opportunity to examine wind loads on components that are difficult to accurately reproduce in model scale.

In addition, the IBHS test chamber allows for the performance of building components, installed in the same way they would be in practice, to be evaluated under realistic wind loading. The true performance of different building components can then be compared to the expected performance from standard test methods. Based on these comparisons, improvements can be made in product evaluations. Since becoming operational in 2010, IBHS has conducted numerous studies to determine the wind loads on building components that cannot be well modeled in model-scale wind tunnels, such as asphalt shingles, multi-layer wall and roofing systems (Morrison and Cope, 2015), roof-mounted equipment (Morrison et al., 2013), and commercial standing seam metal roofing (Morrison and Reinhold, 2015).

As discussed in Section “Large Test Chamber Facility Overview,” the IBHS test chamber has a large test cross section; however, the test section is relatively short in the streamwise direction. As a result, the facility cannot naturally produce the mean flow and turbulence characteristics of the ABL. In fact, the correct replication of the ABL is one of the largest challenges of full-scale wind tunnels. In order to achieve an accurate simulation of the ABL, active and passive control elements are used. The three control elements used are active control of the fan speed to generate large-scale gusts, passive spires located in the lower and middle fan cells to inject small-scale turbulence, and active wind vanes that move horizontally, which injects lateral turbulence into the flow. Both the spires and the wind vanes are indicated in **Figure 2**.

The ability of the IBHS test chamber to simulate realistic wind pressures was also evaluated as part of the facilities commissioning. A replica of the Texas Tech University Wind Engineering Field Research Laboratory (WERFL) experimental building was constructed and tested at the IBHS Research Center. Details of the WERFL experiments and building details can be found in Levitan and Mehta (1992a,b) and Lombardo (2009). Results from the IBHS test chamber were compared to both those from the WERFL building (Smith, 2010) and those from model-scale wind tunnel experiments on the WERFL building conducted at the boundary layer wind tunnel at the University of Western Ontario’s (UWO) boundary layer wind tunnel.

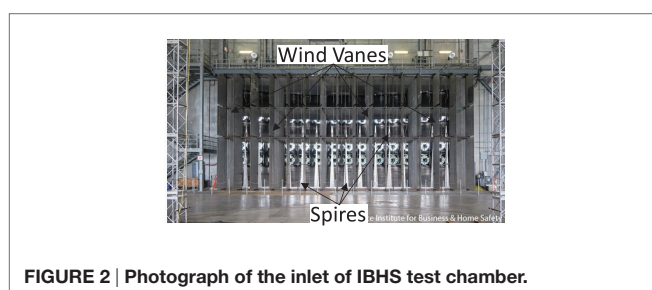


FIGURE 2 | Photograph of the inlet of IBHS test chamber.

Boundary Layer Flow Characteristics

The flow characteristics in the IBHS test chamber were quantified using two multi-hole pressure probes manufactured by Turbulent Flow Instruments. The probes are capable of measuring the flow velocity in 3-components and were mounted on a gantry and traversed across the cross section of the wind tunnel 10.2 m (33.5 ft) downstream of the inlet to the test chamber. The work of Gartshore (1973) suggests that the flow and turbulence characteristics along the stagnation streamline significantly affect the separated shear layers on bluff bodies and their point of reattachment onto the body. Therefore, achieving realistic flow characteristics along the center line of the IBHS test chamber, between the leading edge of the turntable and the front of the building [downstream distances between 5.8 and 8.65 m (19 and 28.4 ft)], where the stagnation point is likely located, is critical in recreating realistic wind loads on test specimens. **Figure 3** presents the mean and streamwise turbulence intensity (I_u) profiles at the centerline of the test chamber at 7.9 m (25.9 ft) downstream of the inlet. The mean velocity profile follows a target theoretical logarithmic boundary layer profile with roughness length $z_0 = 0.01$ m and matches TTU field data with a similar roughness length from Smith (2010), also shown in **Figure 3**. A slight deficit in the mean profile exists at the interface between the lower and middle cells of the fan array. At heights lower than 5 m (16.4 ft) there is good agreement between measured I_u in the IBHS test chamber and the theoretical profiles from Engineering Data Science Unit (1983). However, above 5 m (16.4 ft), I_u decreases much more rapidly than would be predicted from the theoretical profiles, with I_u being approximately 3% lower than the theoretical profile at 6 m (19.7 ft). The reduction of I_u at these heights corresponds to the location where the spires in the middle cells terminate.

In addition, the vertical velocity profiles measurements were conducted across the span of the IBHS test chamber to ensure mean uniformity of the incoming flow. Since the fan speed of each cell can be independently controlled, adjustments were made to the RPM of each cell to achieve horizontal uniformity cell-to-cell without the spires in place. In addition, measurements were conducted across the lower cells with the spires in place to examine the uniformity across the cell itself. Mean flow uniformity across the cells were found to be approximately $\pm 3\%$.

Figure 4 presents the longitudinal power spectra at a vertical height of approximately 2.4 m (7.9 ft) above the ground at both the field site at TTU and in the IBHS test chamber. The active control elements within the IBHS test chamber are able to change the variance of the velocity over a specific frequency range. Since energy is being artificially added over a specific frequency range, normalization by the variance can skew the comparison between the IBHS theoretical and field measurements, particularly at higher frequencies. Therefore, the power spectra presented herein are normalized by the mean velocity squared, similar to Davenport (1961), rather than the variance of the velocity which is more common. Also included in **Figure 4** are the generalized spectral models from Engineering Data Science Unit (1983). The match of the longitudinal spectra between the TTU field case and ESDU is quite good up to a wave

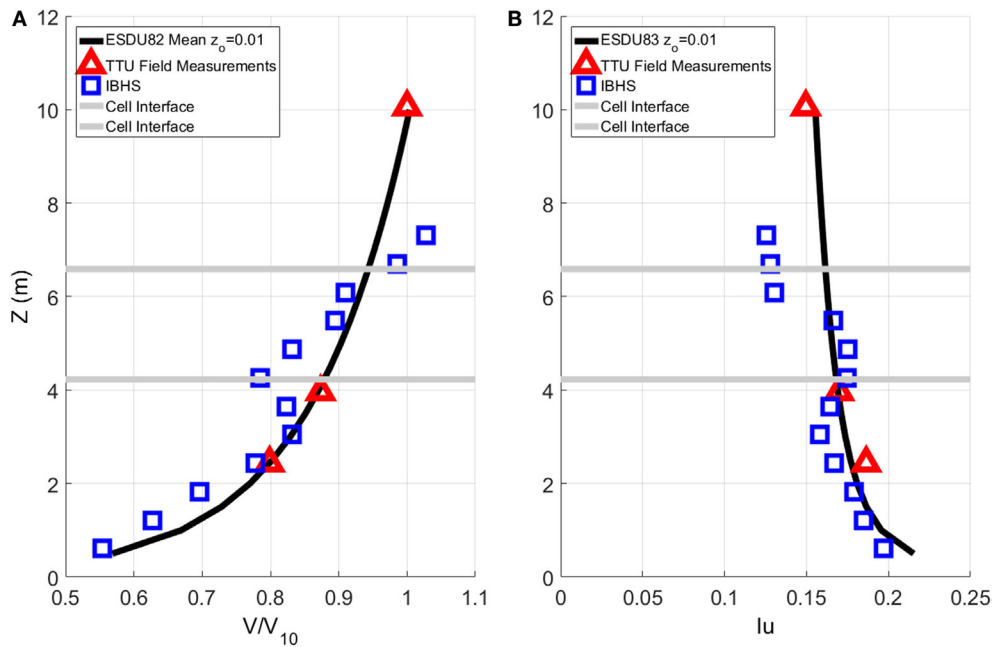


FIGURE 3 | Streamwise development of the mean velocity profiles (A) and the streamwise turbulence intensity, I_u (B). ESDU 82 refers to Engineering Data Science Unit (1982), while ESDU 83 refers to Engineering Data Science Unit (1983).

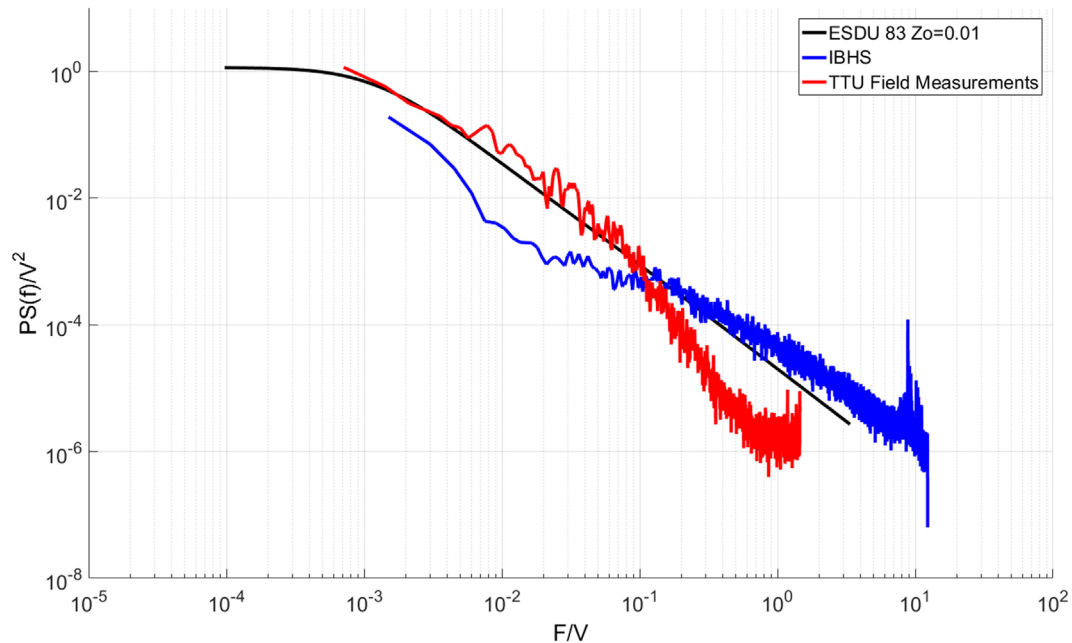


FIGURE 4 | Streamwise velocity spectra, P_u , normalized by the streamwise velocity squared. ESDU 83 refers to Engineering Data Science Unit (1983).

number (F/V) of 0.1. The drop off of the field spectra is a result of the frequency response of the field instrumentation. Between wave numbers of 0.01 and 0.1, the IBHS data show a spectral gap where there is too little energy at these frequencies. At

wave numbers greater than 0.1, the match is good, although the presence of the spires increases the amount of energy at smaller scales (as would be expected), creating too much fine-scale turbulence compared to the ESDU spectrum. The problem of

too much fine-scale turbulence is quite common in model-scale wind tunnel experiments of low-rise buildings [see Tieleman (2003), for a discussion]. The amount of additional energy relative to the target power spectrum at higher frequencies in the IBHS test chamber is relatively small compared to the mismatch present in model-scale wind tunnel investigations [e.g., Kopp et al. (2005)]. However, unlike model-scale wind tunnel facilities, the IBHS test chamber is able to match the large turbulent scale through the active modulation of the fan speeds in time and movement of the wind vanes.

Surface Pressure Measurements

Pressures measured in the IBHS test chamber were normalized using

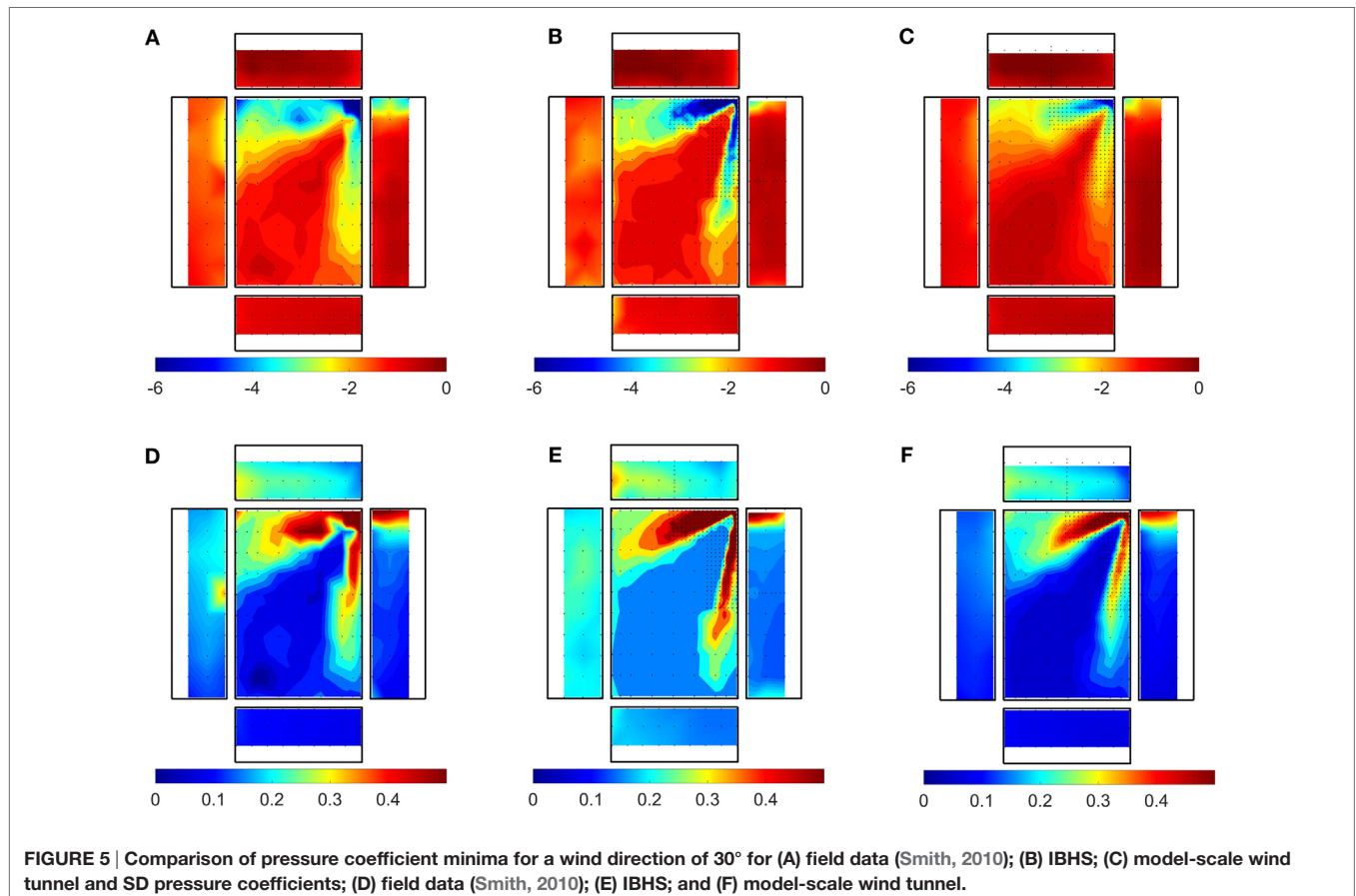
$$C_p = \frac{P - P_\infty}{0.5\rho V^2} \quad (1)$$

where P is the surface pressure, P_∞ is the static pressure within the test chamber and V is the 15 min mean velocity at roof height. **Figures 5A–C** presents a comparison of minimum surface pressures between IBHS, field data from TTU (Smith, 2010), and model-scale wind tunnel data from UWO. Overall, the match between minimum surface pressures from the IBHS test chamber to the field observations shows generally good agreement. The magnitude of the peak point pressures from IBHS lie in between

those from field observations and model-scale wind tunnel results. Previous studies [e.g., Cohran and Cermak (1992), Lin et al. (1995), and Xu and Reardon (1996)] have shown that peak point pressures under separation bubbles on the roof are typically under-estimated in model-scale wind tunnels, when compared to full-scale field observations.

A comparison of the standard deviation (SD) between IBHS, TTU field data, and model-scale wind tunnel data is shown in **Figures 5D–F**. Similar to the minimum pressures, the three studies match reasonably well along the edges of the roof (in the separation regions of the roof). However, the IBHS data have much higher fluctuations in the field of the roof after the reattachment points than both the field and model-scale wind tunnel studies. These higher SDs in the field of the roof may be a consequence of the spectral gap between wave numbers of 0.01 and 0.1; however, the exact cause has not been definitively identified.

For the wind angle shown in **Figure 5**, the blockage ratio relative to the inlet jet is approximately 32%. The mean windward wall pressures (not shown) are higher than would be expected from both field and model-scale wind tunnel experiments. These higher mean windward wall pressures are likely the result of blockage or the proximity of the building to the inlet of jet. While there are likely some blockage affects, the building surface pressures in the IBHS facility provide a good match to field observations particularly in the highest loaded regions of the building



which are of primary interest when evaluating the performance of building components.

Figure 6 presents a comparison of mean pressure coefficients along the centerline of the building including the windward wall, roof, and leeward wall at a wind angle of 0° . Similar to the contour plots presented in **Figure 5** there is generally good agreement between all three studies with the IBHS data typically between the model-scale wind tunnel data and the field data from Smith (2010) within the separated region on the roof. Beyond the reattachment point on the roof and the leeward wall, the mean pressure coefficients of the model-scale wind tunnel and IBHS data are similar, with the field data having larger suctions. The pressures of the model-scale wind tunnel data and field data have very good agreement along the windward wall, while the higher windward wall pressures in the IBHS are observed similar to the trends shown in **Figure 5** discussed above.

The uncertainty of mean pressure coefficients can be as high as 10% in model-scale wind tunnel studies, as discussed by Quiroga (2006). To the author's knowledge, the uncertainty of field pressure coefficients has not been quantified. However, it is likely that they are larger than those in model scale. Overall, the minimum pressures are within approximately 10% of the field measurements at most locations on the roof. As such, it is reasonable to state that the IBHS test chamber is able to replicate realistic wind loads on structures within the uncertainty of the measurements, notwithstanding the effects of turbulence scale mismatches and blockage effects.

Installing additional passive flow control elements to improve the turbulence intensities above 6 m (19.7 ft) and reduce the spectral gap observed in the streamwise power spectrum was considered. However, the added blockage these elements would introduce would reduce the maximum wind velocity and reduce the ability of the test chamber to look at failures of elements at higher wind speeds. Given the good agreement in surface pressures, the benefit of any improvements in the flow

field and resulting surface pressures would be small compared to the drawbacks of reducing the wind speeds. As a result, additional flow control elements have not been pursued further at this point.

HAIL RESEARCH CAPABILITIES

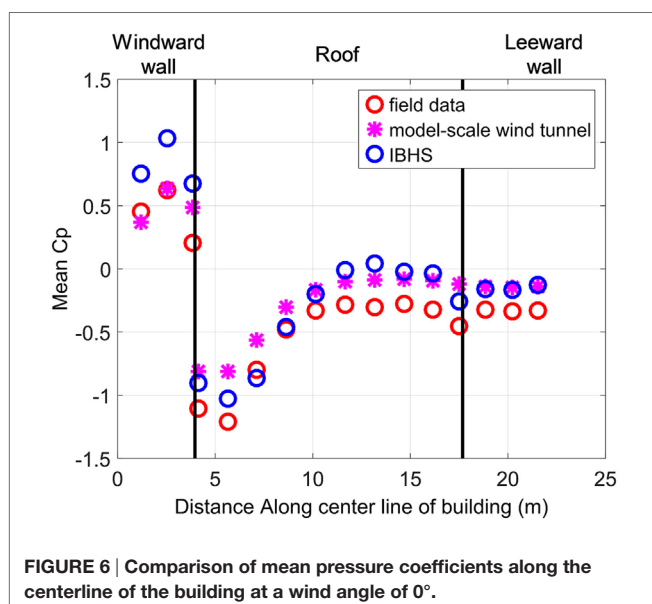
While improvements in severe weather warning times have provided increased safety for individuals, property losses attributed to hail have been rising in recent years (Changnon et al., 2009; Roeder, 2012). Existing test methods for rating the impact resistance of roofing products were based on studies conducted by Bilhelm and Relf (1937) and Laurie (1960). However, these methods did not always produce results consistent with field observations of damage from insurance claims adjusters, and results do not necessarily serve as predictors of real-world performance. The capabilities of the IBHS test chamber allow the performance of building components, installed in the same way they would be in practice, to be evaluated for realistic impacts, filling an existing knowledge gap. The true performance of different building components can then be compared to the expected performance from standard test methods.

The objective of the hail research program at IBHS is to properly understand natural hail characteristics and to replicate those in the small- and full-scale testing facilities, so building damage from hail impacts can be better understood and mitigated. Small-laboratory capabilities to assess building material performance include standardized impact test methods and replication of the properties of real hailstones. Hailstone properties can be further replicated for use in full-scale testing in the IBHS test chamber, where researchers can test full-scale residential and commercial structures to determine how building systems respond to hail impacts. Field research is conducted to collect data on the physical properties of hailstones and the environmental conditions that create them. This information is then incorporated into laboratory testing, to ensure realistic impact modes and energies are being simulated. These data can further be used to validate modeling and forecast applications, as well as for improving dual-polarimetric hail detection algorithm capabilities.

Field Research Program

Field research experiments are conducted during active severe weather months in the Central Plains to collect ground-truth hail data, which are used in modeling, forecasting, and hail detection applications, and are applied to improve small- and full-scale laboratory impact tests (Brown and Giammanco, 2013). The project is fully mobile and strives to collect measurements within 10–30 min after the time of hailfall. A database of more than 2,500 measured hailstones has been created through this work (Giammanco and Brown, 2014; Giammanco et al., 2015). Hail impact disdrometers (**Figure 7A**) (Giammanco and Brown, 2014), handheld compressive strength devices (**Figure 8A**) (Giammanco et al., 2015), and a 3D laser scanner (Giammanco et al., 2016) are used for data collection.

Impact disdrometers are rapidly deployable hail impact probes that capture a time history of hail size distributions



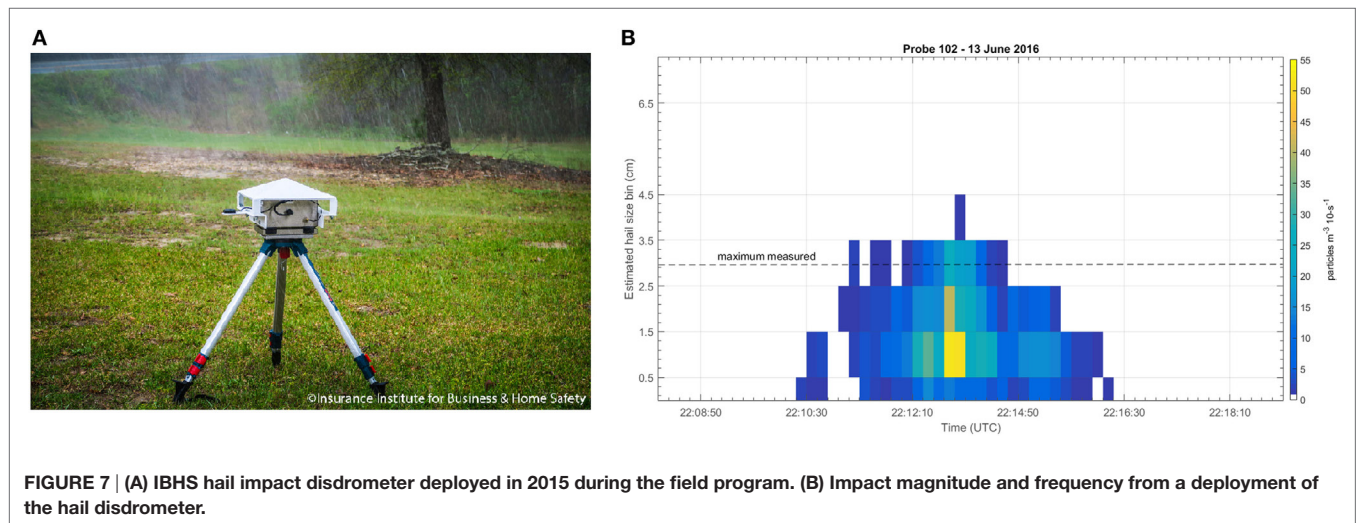


FIGURE 7 | (A) IBHS hail impact disdrometer deployed in 2015 during the field program. **(B)** Impact magnitude and frequency from a deployment of the hail disdrometer.

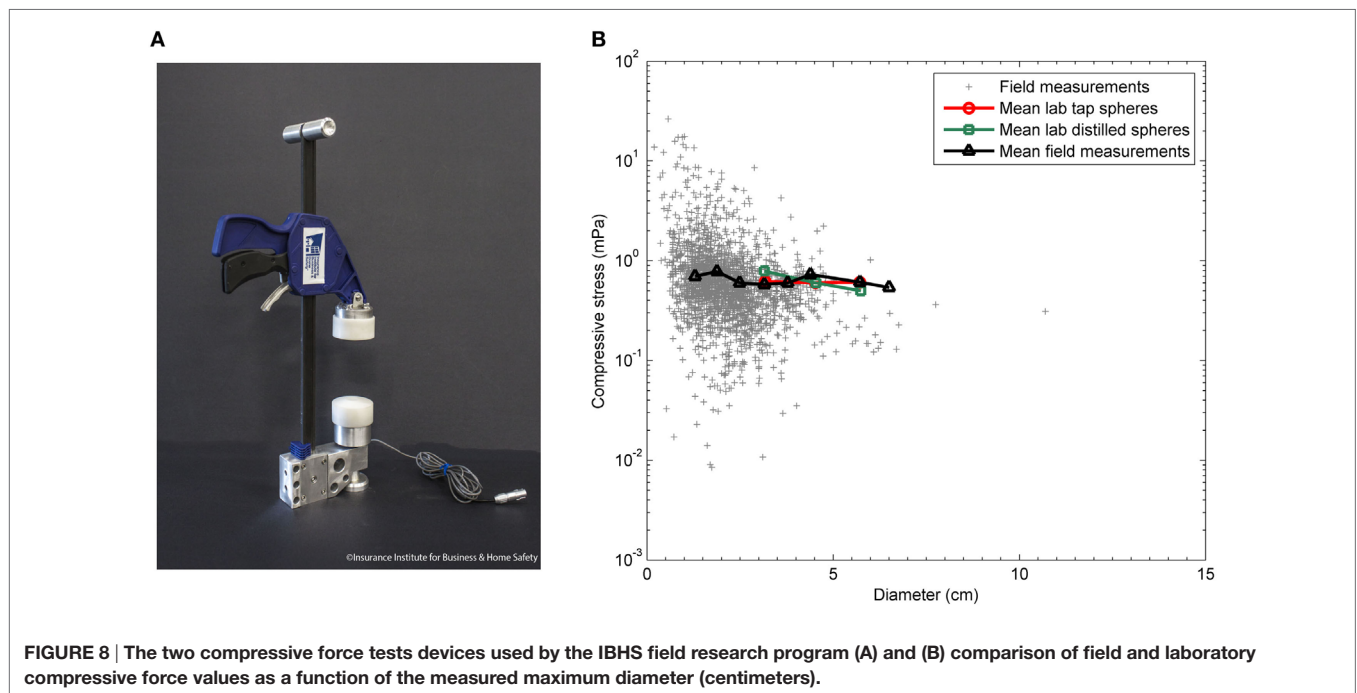


FIGURE 8 | The two compressive force tests devices used by the IBHS field research program (A) and (B) comparison of field and laboratory compressive force values as a function of the measured maximum diameter (centimeters).

and kinetic energies. They use a single piezoelectric disk to detect falling hail and/or rain (Mikhaylovskaya, 1964; Joss and Waldvogel, 1969; Kinnell, 1972). Laboratory calibrations of the probes are conducted prior to field deployments; however, if impact energies are similar between large raindrops and small hailstones, they cannot be differentiated within the data. **Figure 7B** provides an example of the type of data collected by the hail impact disdrometers. As shown in **Figure 7B**, the size of the rain or hail is plotted versus time with the colors showing the number of impacts of each size. The increased number of impacts per minute appears in the warmer colors, while the cooler colors represent fewer impacts during a specific bin of time. **Figure 7B** shows that as the swath passed over the disdrometer, the frequency of hail impacts increased, but the size

of hail or rain remained consistent during the core of the swath, and settled out as the swath passed by. These data are used directly to influence kinetic energies used for impact testing of building materials (discussed in Section “Small-Laboratory Testing Capabilities”), and concentration data can be used for radar-based hail detection applications. In the future, impact concentrations and size distributions could be used to improve full-scale hailstorm simulations, as discussed further in Section “Full-Scale Testing Capabilities.”

To better assess the physical properties of hail, a handheld device, shown in **Figure 8A**, is used to measure the compressive strength of hailstones, which is expected to relate to the energy transferred to a building component which may cause damage (Giammanco et al., 2015). These data can be applied

to improve testing capabilities in small-laboratory and full-scale production of hailstones to better match the strength characteristics of real hailstones. Improved characteristics of the test projectiles, coupled with improved kinetic energy estimates from the disdrometers and Heymsfield et al. (2014), will result in better testing and a better understanding of impact resistance and damage modes for building materials, when compared to the standard test methods discussed in Section “Small-Laboratory Testing Capabilities.” **Figure 8B** shows a comparison of field and laboratory compressive force values as a function of the measured diameter of the hailstone. The mean laboratory compressive strength measurements (red and green) are consistent with the mean field measurements (black). The gray points also show that field measurements can vary, and researchers are evaluating options to consistently recreate certain sizes, shapes, compressive strengths, and densities of projectiles to improve the standard impact test methods described in the next section.

Hailstones come in many different shapes and sizes and are often irregularly shaped. However, the size of a hailstone is typically reported as the largest dimension, which inherently implies a spherical shape. This assumption can lead to significant errors when calculating the density of hailstones. Furthermore, impact test standards, which are discussed in the next section, prescribe the use of spherical projectiles and, therefore, do not account for the aerodynamic effects that would result from tumbling of irregularly shaped objects, which ultimately affects impact kinetic energy. In addition to impact energy effects, it is unclear as to whether the shape of a hailstone affects the impact mechanics as a result of “spiky” features making contact with a building material instead of the smooth surface of a sphere. In September 2015, IBHS first used a handheld 3D laser scanner to accurately measure the shape, size, and volume of hailstones. When the volume of hailstones is calculated using the maximum diameter of a sphere, the calculated volume may be higher than field values (Giammanco et al., 2016). This difference is shown in **Figure 9A** where the volume of a scanned stone was 54% less than would have been predicted from the assumption of a sphere based on the maximum measured diameter. The collection of 3D models of hailstones can be used to create molds and artificial stones (**Figure 9B**). Coupled with disdrometer and hailstone strength

data, the 3D model data can be used to improve product test standards to account for differences in shape, strength, density, and kinetic energy to better understand damage modes and real-world performance for different building materials.

Small-Laboratory Testing Capabilities

IBHS hail research capabilities include small-laboratory standard test methods such as UL 2218 steel ball (Underwriters Laboratory, 2012) and FM 4473 (FM Approvals, 2005) pure ice ball impact tests, which assess the impact performance of new roofing materials available in the market. Both tests utilize four classes of spherical impact projectiles that range from Class 1 [3.18 cm (1.25 in.) diameter] to Class 4 [5.08 cm (2.00 in.) diameter]. The tests are intended to match the impact kinetic energy that a similarly sized spherical, high-density hailstone would have when falling at theoretical terminal velocity. Kinetic energies for projectiles range from 4.78 to 32.2 J depending on the size and type.

Current test programs are focused on asphalt shingles because of their large market share in residential steep-slope construction (approximately 80%). One drawback of the UL 2218 test method is the steel ball impacts create crushed granules which is an atypical damage mode for asphalt shingles, and which are not observed in post-event damage investigations. Crushed granules are rarely observed in the FM 4473 test method, which uses ice spheres as projectiles. **Figure 10** provides a comparison of impact test results on new products, using (A) UL 2218, (B) FM 4473, and on an aged product using (C) ice spheres with dissolved carbon dioxide (CO_2). Dissolving CO_2 into the water prior to freezing introduces gas bubbles into the ice sphere, which reduces the density, thus creating ice spheres that more closely mimic natural hailstones, and better replicate field damage observations.

While the FM 4473 test method produces more realistic damage modes compared to UL 2218, the pure ice spheres are created in silicone molds as part of the test method, which can result in inconsistent densities, shapes, bubble distributions, and micro fractures. Inconsistent impact modes have also been observed (hard and soft), which can cause different material responses. Ongoing research programs use knowledge gained from field measurements to guide laboratory ice ball production, with a goal of better simulating real-world impact damage modes.

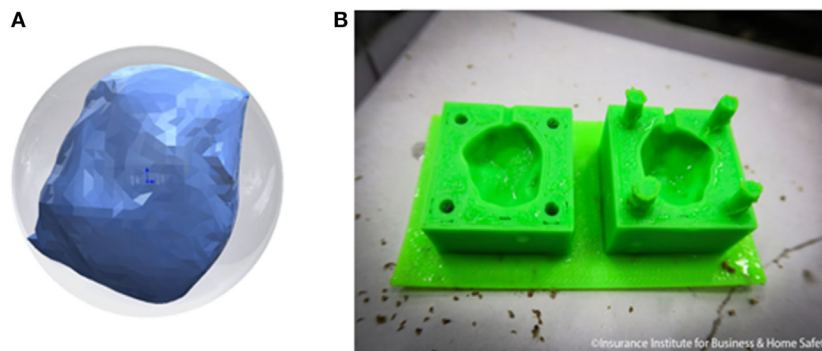


FIGURE 9 | 3D model data (A) of a hailstone scanned using the handheld scanner system. A 3D printed cavity mold of this hailstone is also shown (B).

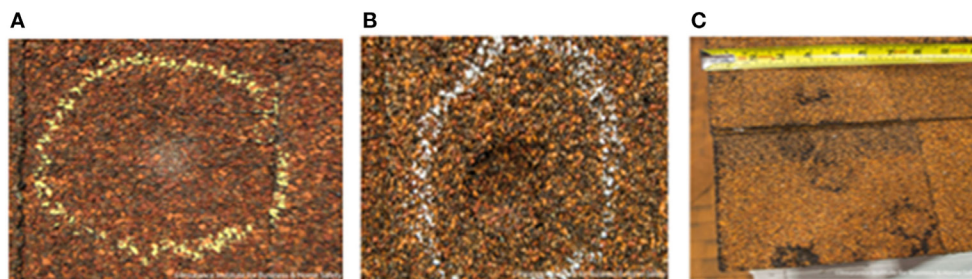


FIGURE 10 | (A) Crushed granules on an asphalt shingle impacted with UL 2218 Class 4 steel ball. (B) Indented surface of an asphalt shingle impacted with FM 4473 Class 4 ice sphere. (C) Damage on a naturally aged two-year-old asphalt shingle impacted with multiple dissolved CO₂ ice spheres. Reproduced from Giammanco et al. (2015).

Improvements in simulating realistic damages will allow for improved small-laboratory and full-scale investigations, resulting in more representative tests that allow for better prediction of real-world performance.

In 2015, IBHS added a new Hail Machine (**Figure 11**) as a result of collaboration with Accudyne Systems Inc., which produces repeatable and controllable laboratory ice spheres. With this new capability, hailstone characteristics obtained from field data can be more easily replicated for use in small- and full-scale laboratory impact testing. Testing is ongoing to replicate the spread of data that is observed in the field (**Figure 7**), and to better understand the relationship between compressive strength and damage to materials. The IBHS Hail Machine also allows for rapid automated bulk production of ice spheres, which will improve efficiency and repeatability for full-scale testing programs.

As part of the commissioning of the Hail Machine, comparisons between compressive strength and density of natural hailstones and those produced with the machine have been made. Results have shown that the machine-produced stones better match the values found for real hailstones, and that they are more consistent and repeatable than ice spheres created using silicone molds following FM 4473. Although the hailstones produced from the Hail Machine are frozen from the outside in, rather than the natural formation which starts from the center and grows outward, the rapid freezing of the ice slug in the machine allows for the dissolved gas to remain within the ice. When compared to FM 4473 ice spheres frozen in molds, the density is more consistent from the machine since the 1-h freeze time is significantly less than the 48-h freeze time. **Figure 12** compares compressive strength results for stones at various storage times at -12°C (10°F) to the mean and median compressive strength of natural hail. Machine settings and storage times and temperatures can be adjusted to create stones which are lower or higher in density, or lower or higher in compressive strength, and work is ongoing to better match field and lab data. Different control parameters on the Hail Machine and different storage times and conditions can also be used to drive different ice sphere impact modes (bounce, shatter, liquefy), which affect the coefficient of restitution. These controls will help researchers better understand how density and compressive strength relate to impact damages caused by hail.



FIGURE 11 | IBHS Hail Machine that was developed with Accudyne Systems Inc., to mass produce laboratory hailstones, which mimic material properties of natural hail.

Full-Scale Testing Capabilities

IBHS full-scale hail research capabilities include an impact test system in the test chamber, where various sizes of ice spheres can be propelled to create a realistic hailstorm. The IBHS test chamber is equipped with 72 impact barrels, grouped in sets of six, to create the hailstone propulsion cannons shown in **Figure 13A**. These cannons propel various sizes of lab-created ice spheres at full-scale test buildings (B) from 18.3 m (60 ft) above ground. Laboratory ice spheres ranging from 2.54 cm (1.00 in.) to 5.08 cm (2.00 in.) in diameter can be manually fed into the automated cannon firing system, which pneumatically projects the stones into the wind stream. Ice spheres are propelled at speeds such that impact kinetic energies are similar to the energies outlined in the UL 2218 and FM 4473 test methods. Therefore, the wind speeds in the test chamber can be left at idle or 6 m/s (14 mph) during full-scale hail testing. Previous studies (Morgan and Towery, 1976, 1977; Changnon et al., 2009) have indicated hailfall occurrences with wind speeds over 27 m/s (60 mph), which can lead to enhanced damage caused by higher energies in wind-blown hail. Future full-scale experiments could investigate the influence of

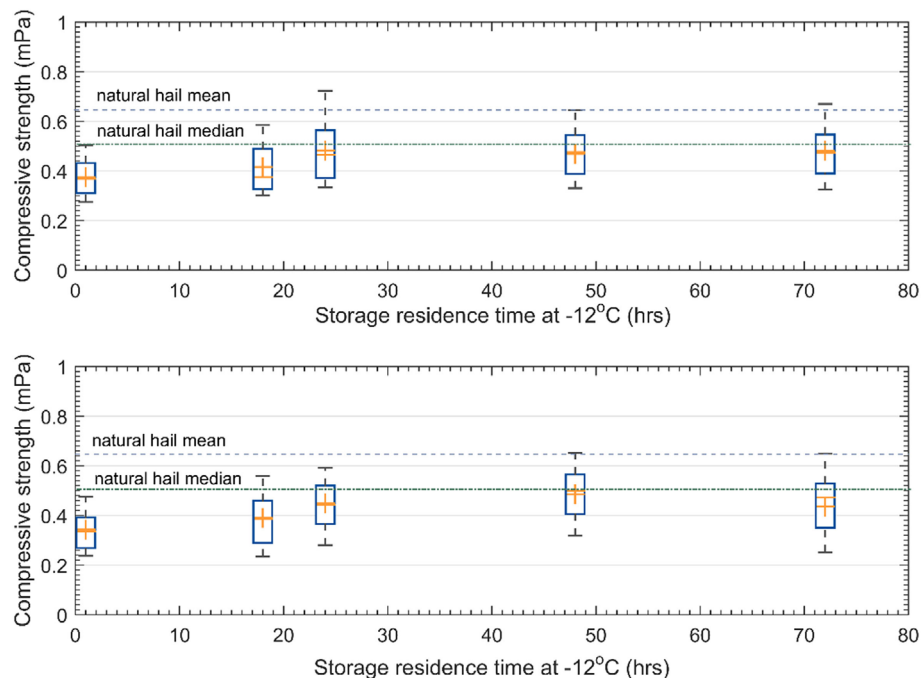


FIGURE 12 | Using particular settings on the IBHS Hail Machine, lab-created ice spheres were stored at -12°C and tested to evaluate their compressive stress. These data compare compressive strength data to storage residence time for (top) 3.81 cm and (bottom) 5.08 cm ice spheres. The mean and median of the measured distribution of natural hailstones tested by IBHS from 2012–2015 field experiments are also shown.



FIGURE 13 | (A) One of 12 cannons, featuring 6 impact barrels, located in the test chamber at the IBHS Research Center. (B) IBHS full-scale hailstorm demonstration in 2013. (C) Damage on a 3-tab shingle on the test specimen. (D) Damage on the metal roof on the test specimen.

increased wind speeds during hail impact testing, by increasing the propulsion speed and varying the angle of impact. The cannons in the chamber are modular and controllable such that impact energies and hailstone sizes can be adjusted for future testing based on field measurements of impact energies

and size distributions using the hail disdrometers, or desired experimental plans.

In 2013, a full-scale hailstorm demonstration was conducted in the IBHS test chamber, in which more than 9,000 laboratory ice spheres were made and projected at a full-scale residential building.

The test building featured different materials or configurations in different quadrants of the roof (**Figure 13B**) to demonstrate the capabilities of the cannon system and ability to create realistic damage modes which included dents in aluminum gutters, cracks and tears in asphalt shingles (**Figure 13C**), and indentations of metal roof materials on the test building (**Figure 13D**). IR asphalt shingles were observed to have less severe damage than unrated shingles, and the metal roof was observed to have only cosmetic damage.

Future full-scale testing will include performance evaluations of different materials and systems, evaluations of cosmetic and functional damage modes, and evaluations of repair and replacement techniques. Ultimately, the knowledge gained through these kinds of tests could be applied to mitigate damage by selecting products with better impact performance, or effectively repair damage that may be seen during a typical supercell thunderstorm that produces hail, to reduce the need for expensive full roof cover replacements and potential loss of use.

WIND-DRIVEN RAIN FULL-SCALE TESTING CAPABILITIES

Water entry into a building can cause damage not only to exterior and interior finishes, but also to furniture and personal belongings. If not remedied quickly, extensive water entry can result in mold growth and/or prolonged loss of use, leading to even further loss costs. Because post-event damage investigations have reported that failure of the roof cover is commonly observed in hurricanes (Liu et al., 2010), the IBHS code-plus construction program, FORTIFIED Home™, requires the use of a sealed roof deck for residential construction to minimize water entry into the structure if the primary roof cover has failed. Evaluation of these systems, as well as other components vulnerable to water entry, has been limited in the past, primarily because of the inability to fully replicate complex building geometries. Inadequate modeling of these building geometries can affect the local aerodynamics close to the building which will affect the wetting of the building surfaces. The IBHS full-scale wind-driven rain system provides a unique capability to fill this gap. The primary goal of IBHS' wind-driven rain research program is to better understand the vulnerabilities of roof systems and penetrations in exterior walls to the entry of wind-driven water. Research projects also focus on the effectiveness of mitigation strategies and help inform recommendations for incorporating effective methods into the FORTIFIED Home™ program.

The two primary design criteria for the wind-driven rain system were to create realistic rain droplet size distributions and raindrop deposition rates. Rain droplet size distribution targets were based on data collected during Hurricane Ike (Lopez, 2011), while a deposition rate of 203 mm/h (8 in/h) in 58 m/s (130 mph) winds was selected because of its use in ASTM Test Standards E331 (ASTM E331-00, 2016), E547 (ASTM E547-00, 2016), E1105 (ASTM E1105-15, 2015), and E2268 (ASTM E2268-04, 2016). Commercially available spray nozzles arranged in a 0.66 m by 0.61 m (2.2 ft × 2 ft) grid across the fan inlet were used. Grid spacing was selected to maximize water delivery uniformity.

It is important to note that deposition rate is not equivalent to the wind-driven rain intensity, R_{WDR} , which is the flux of water through a vertical plane, but is instead a function of several factors including building geometry and orientation. Straube and Burnett (2005) define the rain deposition rate as

$$r_{vb} = RDF * DRF * \cos(\theta) * V(h) * r_h \quad (2)$$

where the driving rain factor DRF accounts for the interaction of wind and rain in undisturbed wind, θ is the angle between the wind vector and the vector normal to the building wall, r_h is the rainfall rate through a horizontal plane, $V(h)$ is wind velocity at some height h , and RDF is the building-dependent rain deposition factor, as defined for various building categories.

In the commissioning of the wind-driven rain system, Lopez (2011) utilized an OTT Parsivel disdrometer and precipitation imaging probe manufactured by Droplet Measurement Technologies to demonstrate that the installed gridded nozzle system can produce a wetting rate at the building facade of 203 mm/h (8 in/h) with a raindrop size distribution that matches well with historical literature (Marshall and Palmer, 1948; Best, 1950). However, historically, these data have been difficult to acquire in field settings due to the extreme environments present in tropical cyclones and thunderstorms so there are limited datasets for which comparisons can be done. **Figure 14** provides an example of a droplet size distribution and concentration measured during a recent test series, where smaller droplets were produced in larger quantities than larger droplets for the wind speed, pump, and valve settings used. These types of data can be used to compare simulations. In addition to droplet sizes and concentrations, rainfall accumulation rates have been investigated using Parsivel disdrometers. Water flow rates of the wind-driven rain system affect the accumulated rainfall amount, as illustrated in **Figure 15**. These data were collected with varying valve settings, but a constant pump setting of approximately 60%. Both settings can be controlled based on the experimental design. As additional field data are collected in the future, or based on experimental design, droplets sizes, concentrations, and deposition rates can be altered by adjusting valve opening percentages and pump rates on the wind-driven rain system, and adjusting the wind speed records. The wind-driven rain system is explained in more detail in Lopez (2011) and summarized in Brown et al. (2015) and Quarles et al. (2012).

The wind-driven rain system injects water into the wind stream in a horizontal trajectory, which is different from actual wind-driven rain that would likely have a greater vertical component. The system can accurately capture a real raindrop's horizontal velocity component (Lopez, 2011), which is approximately equal to the wind speed, by injecting the droplets into the wind stream at fan level. However, rainfall created in the test chamber has a weaker vertical component than real rainfall as the fetch is too short for the horizontally injected rainfall to reach terminal velocity before reaching the test building, and therefore impacts the building at a more horizontal angle than would real rainfall. As a result, walls, which would be more protected from vertical rainfall by eaves or other overhangs in a

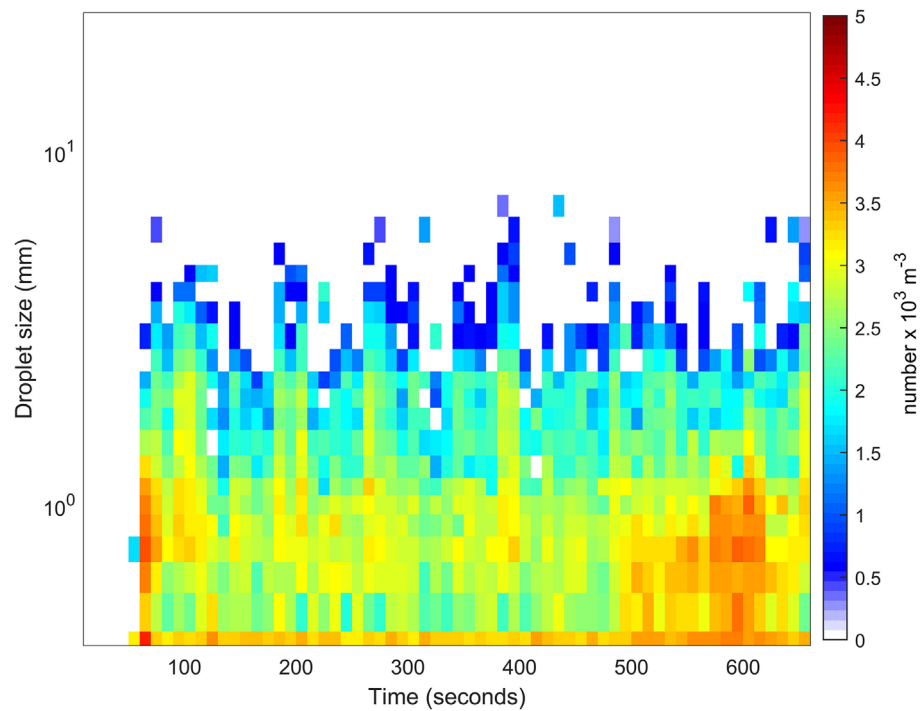


FIGURE 14 | Time history of droplet size and concentrations during a test series using a 22 m/s (49 mph) constant wind speed.

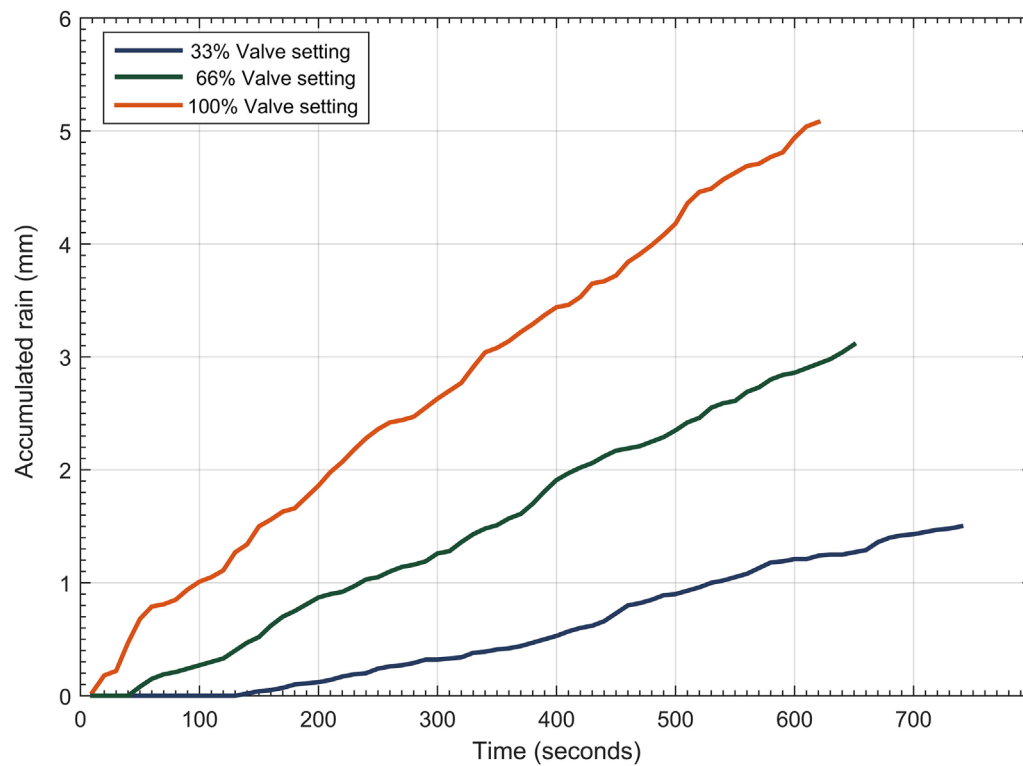


FIGURE 15 | Rainfall accumulation rates as measured by a Parsivel disdrometer, as a function of flow rate for the wind-driven rain system at IBHS. The pump rate was held constant at approximately 60%.

real wind-driven rain scenario, would receive a greater amount of rainfall during testing.

Recent experiments have evaluated the efficacy of several sealed roof deck strategies allowed in the IBHS FORTIFIED Home™ program, such as those shown in **Figure 16** (Brown et al., 2015; Johnston et al., 2016). These strategies, each evaluated individually, included double layer ASTM D226 Type II 30# felt underlayment and synthetic underlayment applied across the roof deck, modified bitumen and acrylic 10.2 cm (4 in.) tape applied at sheathing seams, and closed cell spray foam applied at panel-to-panel joints and sheathing seams on the interior of the roof. Water entry through vents has also been investigated (Quarles et al., 2012). In each of these studies, water collection systems such as those shown in **Figure 17B** were designed to capture and quantify water that entered the building (shown in **Figure 17A**) in different capture zones under the roof, or from different vents, windows, or doors on the test building. Using these systems, water weight, volume, and entry rates were determined, allowing for direct comparisons of the performance of sealing strategies and vent systems, which varied as a result of different wind speed and building orientations based on the geometry of the building.

WILDFIRE FULL-SCALE TESTING CAPABILITIES

As communities continue to expand into the WUI, the potential for property losses, injuries, and fatalities increases. In the past,

research programs have focused on mitigation guidance, specifically the concept of defensible space surrounding a structure. Identification and evaluation of structural vulnerabilities has been limited, relying on post-event damage surveys and anecdotal information from fire officials. Similar to the wind-driven rain peril discussed in Section “Wind-Driven Rain Full-Scale Testing Capabilities,” experimental testing of systems and components has been limited primarily because of the inability to replicate complex building geometries, which will affect the local flow close to the building and, therefore, firebrand exposure and accumulation. The IBHS full-scale firebrand generator system provides a unique capability to fill this gap. The capabilities for studying the effects of wildfire include both small- and large-scale testing of structural ignition potential when exposed to firebrands, direct flame contact, or radiant heat. Results from experiments conducted add to the understanding of the relationship between firebrand exposure and building ignition, which is useful for developing mitigation strategies for individual buildings and communities.

A custom-made firebrand generator system, shown in **Figure 18**, was designed and manufactured at the IBHS Research Center to simulate a firebrand exposure similar to conditions observed in wildfires. The initial design was based on the generator developed at the National Institute for Standards and Technology (Manzello et al., 2008). To automate fuel delivery during testing, an auger system was developed. The fuel is comprised of a mixture of 80% pine wood chips and 20% wooden dowels that is dried to a moisture content of less than 10% before being placed in the

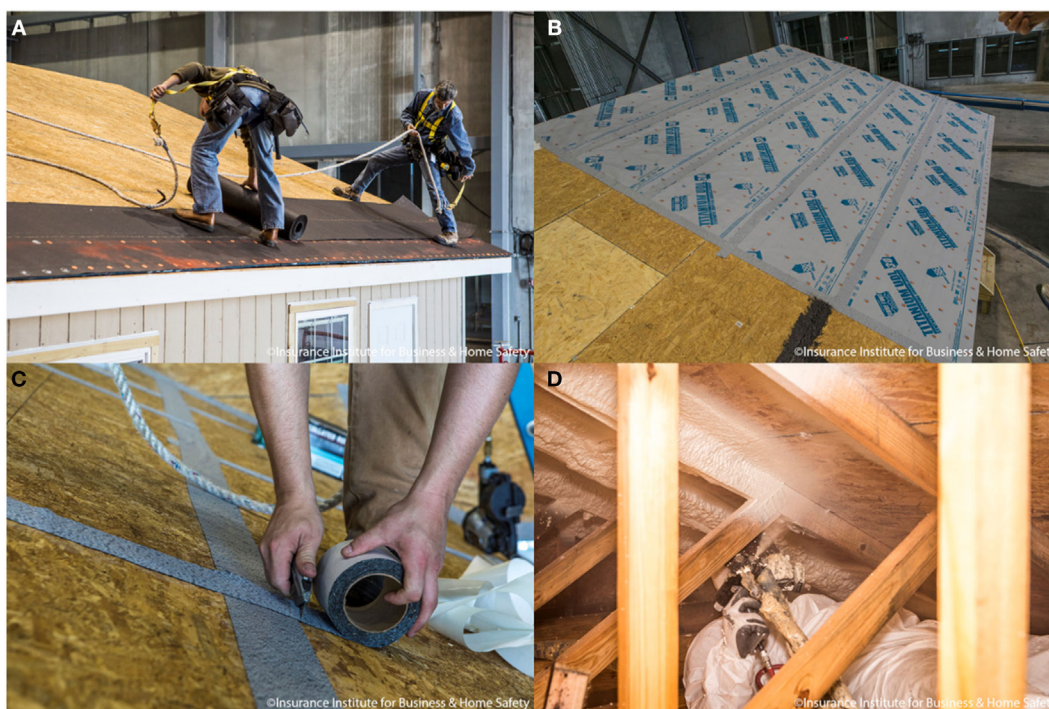


FIGURE 16 | Roof deck sealing strategies included (A) double layer felt underlayment, (B) synthetic underlayment, (C) modified bitumen tape, and (D) closed cell spray foam.

hoppers shown on the left side of **Figure 18** at point A. Beneath the hoppers, five augers (not shown) are used to feed the fuel into the auger feed lines shown at point B of **Figure 18**. The auger feed lines move the fuel to the generators at point C in **Figure 18**. Fuel is delivered intermittently to prevent the generators from overheating.

The right side of **Figures 18F–H** illustrates one of the firebrand generators. The auger feed lines previously described connect to individual generators at point F. Fuel falls onto a metal grate (not shown) located over a burner inside the generator. Below the burner, a vertically oriented fan is placed on the bottom of the generator, indicated at point G on the right side of **Figure 18**. The fan introduces a vertical component of wind which pushes firebrands up and out of the exhaust into the wind stream of the test chamber at location H.

Figure 19 shows the operation of the firebrand generator system during testing. Experiments conducted using this system are unique compared to previous studies because of the ability to test full-sized buildings rather than individual components or two-dimensional assemblies, with exposure to realistic fluctuating boundary layer wind conditions (described in Section “Boundary Layer Flow Characteristics”), rather than constant winds. In addition, the effect of wind direction on the deposition of firebrands relative to the building geometry can be evaluated, allowing researchers to investigate where firebrands accumulate. This can be especially useful for complex building geometries where localized wind patterns can impact the location of maximum firebrand accumulation. Likewise, the performance of structural features subjected to a firebrand exposure can be assessed. Recent experiments have evaluated the ignition potential of wood and

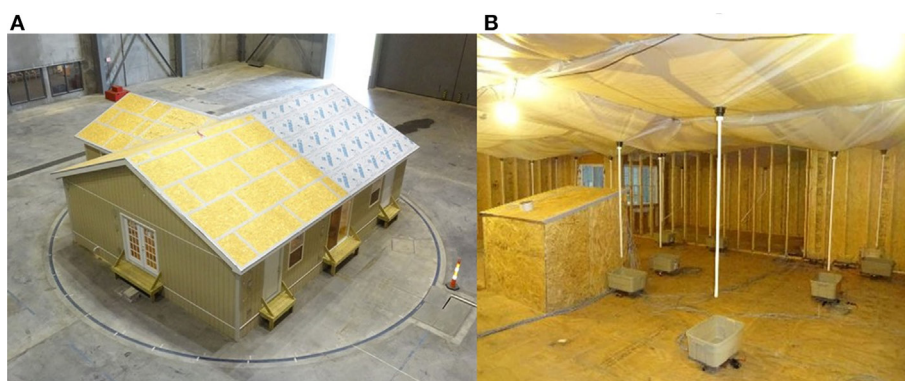


FIGURE 17 | (A) Test building featuring two different sealed roof deck methods positioned on the turntable in the test chamber. **(B)** Water collection system allows water entry rates to be monitored in real time for different roof zones and penetrations.

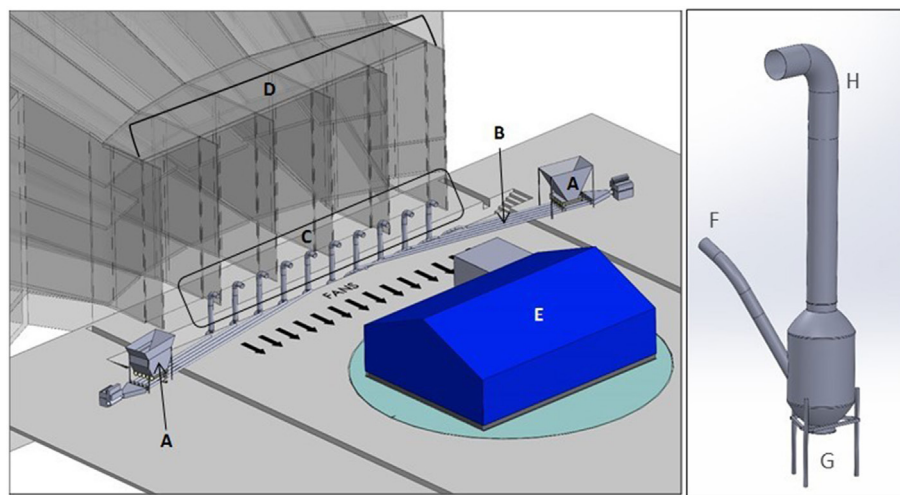


FIGURE 18 | (A–E) Auger feed and firebrand generation system installed at the IBHS Research Center. The two hoppers are shown in (A); (B) indicates the auger feed lines which deliver fuel to the 10 generators indicated in (C); (D) is the fan array behind the generators; and (E) is a representative test building. **(F–H)** Schematic of the firebrand generators used in the wildfire experiments. (F) is the auger feed line which introduced the fuel into the generator; (G) is the location of the vertically oriented fan; and (H) is the exhaust chute.

wood-plastic composite decking materials, vegetation materials, and roof and wall materials resulting from firebrand exposures. Firebrand entry through vents has also been investigated. Both quantitative and qualitative observations of entry, accumulation, and ignition are used to understand implications of firebrand exposures.

Accumulation of Firebrands

The accumulation of firebrands close to a structure is linked with ignition potential, so understanding the impact of wind speed and direction on firebrand accumulation in the vicinity of a structure is important in identifying vulnerable locations. Firebrand accumulation is typically evaluated using water-filled pans placed at select locations adjacent to a test building. The water quenches the firebrands, which are then collected, oven-dried, and weighed to determine spatial variations in accumulation. Observations during recent experiments indicated that re-entrant corners, shown in **Figure 19**, were an area with high firebrand deposition. Previous experiments at IBHS have also qualitatively investigated the location of maximum firebrand accumulation based on surface roughness immediately adjacent to a building. Firebrands on smooth surfaces were captured in the recirculation flow and able to settle further from the building. For rough surfaces, firebrands caught in the recirculation were captured in the rougher surface, resulting in areas of maximum accumulation immediately adjacent to the wall, which creates a higher risk of ignition and a subsequent flame contact and/or elevated amount of radiant heat.

Results from a recent accumulation study are shown in **Figure 20**. For each test, pans were placed at various locations along a test building. As expected, there was variability in the accumulation depending on building orientation, wind speed, and pan section [wall is immediately adjacent to the building; field is approximately 0.3 m (1 ft) from the building]. As indicated in **Figure 20**, a total of 13 different orientations were investigated in this given experiment. The orientation of the test building as shown in **Figure 19** was designated as 90°. A clockwise rotation of the turntable allowed for an assessment of angles less than

90°. Similarly, for the larger angles investigated, the turntable was rotated counter-clockwise. The difference between 0°A and 0°B was the location of the re-entrant corner on the test building. In most cases, the accumulations for the wall sections were larger than the accumulations for the field sections, thus indicating greater vulnerability at locations immediately adjacent to the building. This is problematic, especially if the building is constructed with combustible materials that can directly ignite from a firebrand exposure. Likewise, a building can indirectly ignite if combustible material (i.e., vegetation, fences, etc.) near the building ignites from the firebrand exposure. These results highlight the importance of maintaining a non-combustible region immediately adjacent to a home or business.

Firebrand Characteristics

Representative samples of firebrands generated by IBHS were collected so they could be characterized by their mass and surface area to allow for comparison in future active wildfires. An example of firebrand characterization from recent IBHS experiments is shown in **Figure 21**. The firebrands produced at the IBHS Research Center are smaller than those observed by Manzello et al. (2011). However, this is compensated by the fact that the IBHS generators produced significantly more firebrands than the firebrand generators used by Manzello et al. (2011). Overall, the characterization of IBHS produced firebrands provided an initial assessment of the mass and size distribution. The fuel used in future research initiatives can be modified to better replicate the characterization of firebrands collected from active wildfires. Additionally, several recent tests at IBHS have included high resolution video of firebrand exposure in the vicinity of test buildings that will be used to track and count individual firebrands. This can be used to count firebrands impacting a specific location of a building or to count firebrands as they are generated from different fuels. This information, in conjunction with the mass and surface area of firebrands, can be used to estimate a firebrand mass flux (grams per square meter). Quantification of this variable will aid in the development of a WUI hazard scale that could be used to consistently quantify expected fire severity based on firebrand and fire exposure (Maranghides and Mell, 2012). By understanding the firebrand flux and resulting structural ignition, fragility curves could be developed for wildfire hazards.

CONCLUSION

Over the last 50 years, important advances have been made to improve the performance of both commercial and residential infrastructures subjected to wind-driven natural hazard events. Casualties in the US are dramatically lower for high-wind events than in developing countries around the world. Despite these improvements to the built environment, economic losses due to these natural perils have continued to increase (Pielke et al., 2008). Often, damage to a structure is severe enough to make it uninhabitable until repairs are made, resulting in social consequences for both individuals and communities at large.

Research programs at IBHS have focused on creating unique and realistic testing capabilities to improve understanding of



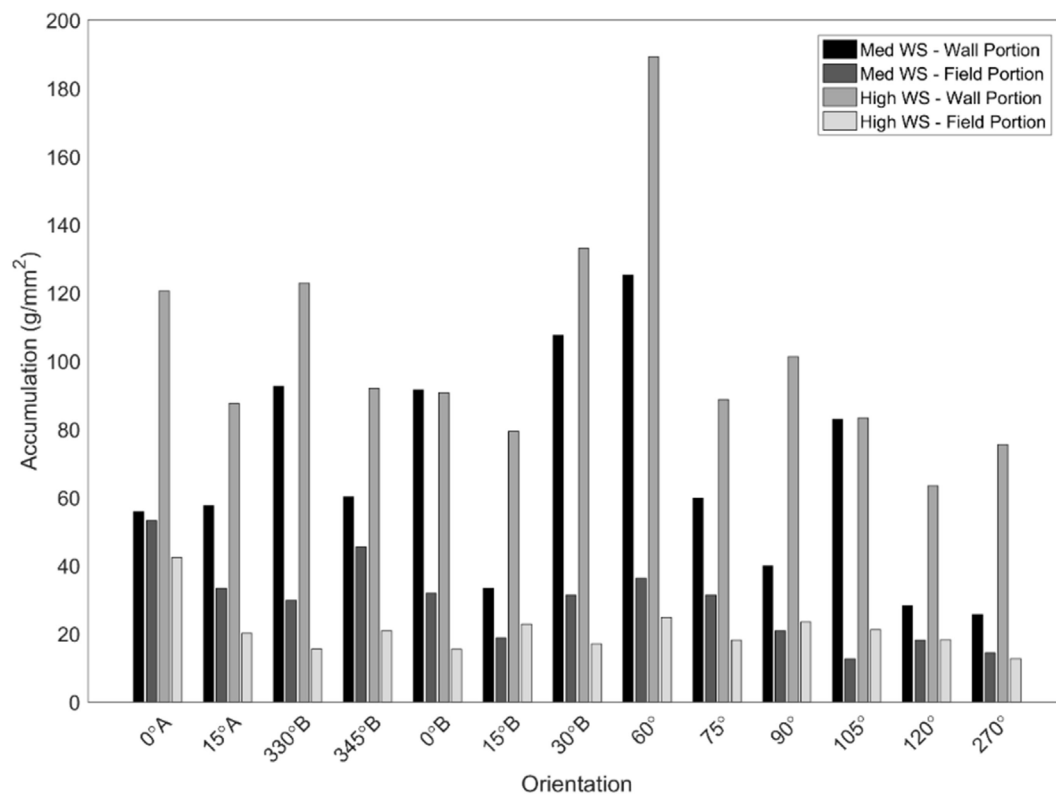


FIGURE 20 | Firebrand accumulation by orientation, pan location, and wind speed.

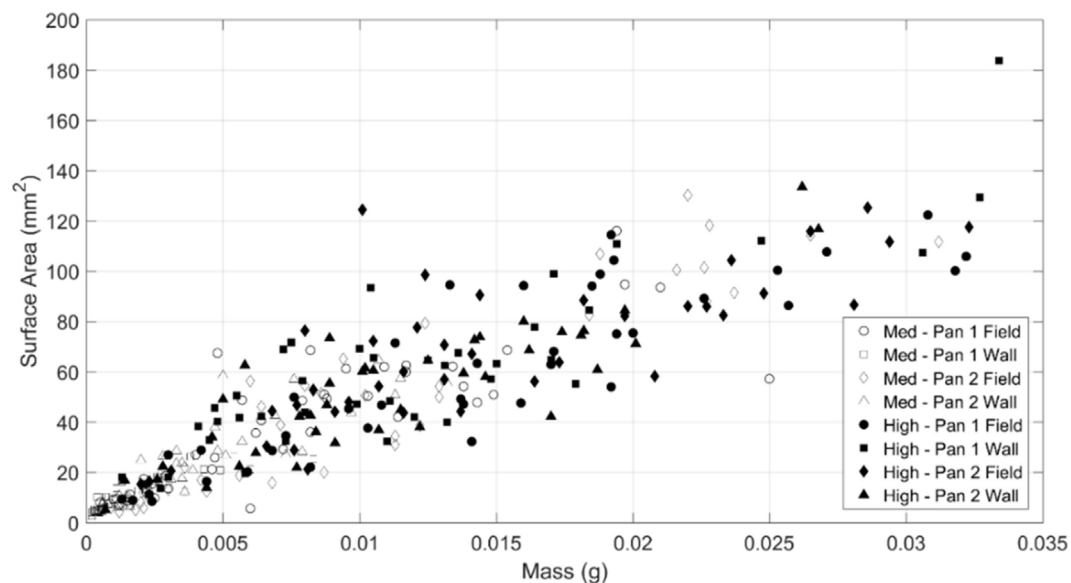


FIGURE 21 | Mass versus surface area for firebrands collected from the firebrand generators.

real-world performance. Furthermore, these programs focus on identifying ways to make structures more resilient with the goal of reducing both the economic and social impact natural

perils have both in the US and around the world. Research at the IBHS Research Center for high wind, hail, wildfire, and wind-driven rain aim to identify vulnerabilities in structures

so that cost-effective mitigation strategies can be developed or identified. In addition, the performance simulated at the IBHS Research Center is compared to results from standardized testing and real-world observations, to facilitate improvements to standardized test methods. Future testing programs will address the effects of natural weathering, defining best practices for installation and maintenance, and distinguishing between cosmetic and functional damage modes, among other topics. Research results can be used in voluntary programs, such as FORTIFIED Home™, or in public policy, building codes and standards, and modeling applications. The insurance industry members that support IBHS can use findings in their underwriting and claims business practices, and society as a whole will benefit from reduced losses attributed to improved building performance.

Full-scale testing allows for a look at building system and component performance, something that is not often possible in

model-scale testing. By using a combination of full-scale, small-scale, and field studies, research can be conducted to improve testing such that real-world performance can be better predicted and building systems improved to reduce losses.

AUTHOR CONTRIBUTIONS

CS-A contributed to both experiments analysis and writing/approval of wildfire sections of the manuscript. HE contributed to both experiments analysis and writing/approval of hail sections of the manuscript. TJ contributed to analysis and writing/approval of wind-driven rain sections of the manuscript. MM contributed to experiments, analysis, and writing/approval of wind flow and wind pressures sections of the manuscript; in addition, wrote/approval introduction conclusions and facility overview sections. TB-G contributed to experiments and writing/approval of hail and wind-driven rain sections.

REFERENCES

- FM Approvals. (2005). *Specification Test Standard for Impact Resistance Testing of Rigid Roofing Materials by Impacting with Freezer Ice Balls (FM 4473)*. West Gloucester, RI: FM Approvals.
- ASCE 49-12. (2012). *Wind Tunnel Testing for Buildings and Other Structures*. Reston, VA: American Society of Civil Engineers.
- ASTM E1105-15. (2015). *Standard Test Method for Field Determination of Water Penetration of Installed Exterior Windows, Skylights, Doors, and Curtain Walls, by Uniform or Cyclic Static Air Pressure Difference*. West Conshohocken.
- ASTM E2268-04. (2016). *Standard Test Method for Water Penetration of Exterior Windows, Skylights, and Doors by Rapid Pulsed Air Pressure Difference*. West Conshohocken, PA.
- ASTM E331-00. (2016). *Standard Test Method for Water Penetration of Exterior Windows, Skylights, Doors, and Curtain Walls by Uniform Static Air Pressure Difference*. West Conshohocken, PA: ASTM International.
- ASTM E547-00. (2016). *Standard Test Method for Water Penetration of Exterior Windows, Skylights, Doors, and Curtain Walls by Cyclic Static Air Pressure Difference*. West Conshohocken, PA.
- Barlow, J. B., Rae, W. H., and Pope, A. (1999). *Low-Speed Wind Tunnel Testing*. New York, NY.
- Best, A. C. (1950). The size distribution of raindrops. *Q. J. Roy. Meteorol. Soc.* 76, 16–36. doi:10.1002/qj.49707632704
- Bilhelm, E. G., and Relf, E. F. (1937). The dynamics of large hailstones. *Q. J. Roy. Meteorol. Soc.* 63, 149–162. doi:10.1002/qj.49706326904
- Bitsumalak, G., Gan Chowdhury, A., and Sambare, D. (2009). Application of a full-scale testing facility for assessing wind-driven-rain intrusion. *Build. Environ.* 44, 2430–2441. doi:10.1016/j.buildenv.2009.04.009
- Brown, T. M., and Giammanco, I. M. (2013). Multifaceted hail research initiative by IBHS. *Interface* 31, 5–8.
- Brown, T. M., Quarles, S. L., Giammanco, I. M., and Brown, R. (2015). “Building vulnerability to wind-driven rain entry and effectiveness of mitigation techniques,” in *Proceedings for 14th International Conference on Wind Engineering*, Porto Alegre.
- Changnon, S. A., Changnon, D., and Hilberg, S. D. (2009). *Hailstorms across the nation: an atlas about hail and its damages*. Champaign, IL: Illinois State Water Survey.
- Cohcran, L. S., and Cermak, J. E. (1992). Full and model-scale cladding pressures on the Texas Tech University experimental building. *J. Wind Eng. Ind. Aerod.* 43, 1589–1600. doi:10.1016/0167-6105(92)90374-J
- Davenport, A. G. (1961). The spectrum of horizontal gustiness near the ground in high winds. *Q. J. Roy. Meteorol. Soc.* 87, 194–211. doi:10.1002/qj.49708737208
- Engineering Data Science Unit. (1982). *Strong Winds in the Atmosphere Boundary Layer. Part 1: Mean-Hourly Wind Speeds, Data Item 82026*. London, UK.
- Engineering Data Science Unit. (1983). *Strong Winds in the Atmosphere Boundary Layer. Part 2: Discrete Gust Speeds, Data Item 83045*. London, UK.
- Gartshore, I. S. (1973). *The Effects of Free Stream Turbulence on the Drag of Rectangular Two-Dimensional Prisms*. London, Canada: Boundary Layer Wind Tunnel Laboratory, 25.
- Giammanco, I. M., and Brown, T. M. (2014). “Observation of hailstone characteristics in supercell and multicell thunderstorms,” in *94th Annual Meeting of the American Meteorological Society, Special Symposium on Severe Local Storms* (Atlanta, GA). p. 1–12.
- Giammanco, I. M., Brown, T. M., Grant, R. G., Dewey, D. L., Hodel, J. D., and Stumpf, R. A. (2015). Evaluating the hardness characteristics of hail through compressive strength measurements. *J. Atmos. Ocean. Tech.* 32, 2100–2113. doi:10.1175/JTECH-D-15-0081.1
- Giammanco, I. M., Maiden, B. R., Estes, H. E., and Brown-Giammanco, T. M. (2016). Using 3-D laser scanning technology to create digital models of hailstones. *Bull. Amer. Meteor. Soc.* doi:10.1175/BAMS-D-15-00314.1
- Heymsfield, A. J., Giammanco, I. M., and Wright, R. L. (2014). Terminal velocities and kinetic energies of natural hailstones. *Geo. Phys. Res. Lett.* 41, 8666–8672.
- Johnston, T., Quarles, S. L., and Brown-Giammanco, T. M. (2016). “The effectiveness of roof-level selected secondary sealing strategies in minimizing water entry during high-wind and rain events,” in *Proceedings for 4th American Association for Wind Engineering Workshop*, Miami, FL.
- Joss, J., and Waldvogel, A. (1969). Raindrop size distributions and sampling errors. *J. Atmos. Sci.* 26, 566–569. doi:10.1175/1520-0469(1969)026<0566:RSDASS>2.0.CO;2
- Kinnell, P. I. A. (1972). The acoustic measurement of water drop impacts. *J. Appl. Meteor.* 11, 691–694. doi:10.1175/1520-0450(1972)011<0691:TAMOWD>2.0.CO;2
- Kopp, G. A., Mans, C., and Surry, D. (2005). Wind effects of parapets on low buildings part I. Basic aerodynamics and local loads. *J. Wind Eng. Ind. Aerod.* 93, 817–841. doi:10.1016/j.jweia.2005.08.006
- Laurie, J. A. P. (1960). *Hail and Its Effects on Buildings*. Pretoria: Council for Scientific and Industrial Research.
- Leviton, M. L., and Mehta, K. C. (1992a). Texas Tech field experiments for wind loads part I: meteorological instrumentation and terrain parameters. *J. Wind Eng. Ind. Aerod.* 43, 1565–1576. doi:10.1016/0167-6105(92)90372-H
- Leviton, M. L., and Mehta, K. C. (1992b). Texas Tech field experiments for wind loads part II: building and pressure measuring system. *J. Wind Eng. Ind. Aerod.* 43, 1565–1576. doi:10.1016/0167-6105(92)90372-H
- Lin, J. X., Surry, D., and Tieleman, H. W. (1995). The distribution of pressure near roof corners of flat roof low buildings. *J. Wind Eng. Ind. Aerod.* 56, 235–265. doi:10.1016/0167-6105(94)00089-V
- Liu, Z., Pogorzelski, H., Masters, F., Tezak, S., and Reinhold, T. (2010). Surviving nature’s fury: performance of asphalt shingle roofs in the real world. *Interface* 28, 29–44.

- Lombardo, F. T. (2009). *Analysis and Interpretation of Thunderstorm Wind Flow and its Effects on a Bluff Body [PhD Dissertation]*. Lubbock, TX: Texas Tech University.
- Lopez, C. R. (2011). *Measurement, Analysis, and Simulation of Wind Driven Rain*. Gainesville, FL: The Graduate School of the University of Florida.
- Manzello, S. L., Shields, J. R., Cleary, T. G., Maranghides, A., Mell, W. E., Yang, J. C., et al. (2008). On the development and characterization of a firebrand generator. *Fire Saf. J.* 43, 258–268. doi:10.1016/j.firesaf.2007.10.001
- Manzello, S. L., Suzuki, S., and Hayashi, Y. (2011). *Summary of Full-Scale Experiments to Determine Vulnerabilities of Building Components to Ignition by Firebrand Shower*. NIST Special Publication 1126. Gaithersburg, MD: National Institute of Standards and Technology.
- Maranghides, A., and Mell, W. (2009). *A Case Study of a Community Affected by the Witch and Guejito Fires*. NIST Technical Note 1635. Gaithersburg, MD: National Institute of Standards and Technology.
- Maranghides, A., and Mell, W. (2012). *Framework for Addressing the National Wildland Urban Interface Fire Problem – Determining Fire and Firebrand Exposure Zones using a WUI Hazard Scale*. NIST Technical Note 1748. Gaithersburg, MD: National Institute of Standards and Technology.
- Marshall, J. S., and Palmer, W. M. (1948). The distribution of raindrops with size. *J. Meteorol.* 5, 165–166. doi:10.1175/1520-0469(1948)005<0165:TDORWS>2.0.CO;2
- Masters, F., Prevatt, D., and Gurley, K. (2010). *Reduction of Wind-Driven Rain Intrusion through the Building Envelope*. Tallahassee, FL: Florida Catastrophic Storm Risk Management Center.
- Mikhaylovskaya, V. V. (1964). Theory of measuring the size of raindrops by acoustic method. *Sov. Hydrol. Sel. Paper* 1, 85–90.
- Morgan, G. M., and Towery, N. G. (1976). On the role of strong winds in damage to crops and its estimation with a simple instrument. *J. Appl. Meteorol.* 8, 891–898. doi:10.1175/1520-0450(1976)015<0891:OTROSW>2.0.CO;2
- Morgan, G. M., and Towery, N. G. (1977). Hailstripes. *Bull. Am. Meteorol. Soc.* 58, 588–591.
- Morrison, M. J., and Cope, A. D. (2015). “Wind Performance and evaluation methods of multi-layered wall assemblies,” in *Proceeding of ASCE Structures Congress* (Portland, OR), 2735–2748.
- Morrison, M. J., Miccolis, C., and Reinhold, T. A. (2013). “Wind loads on small roof mounted air-conditioning units,” in *Proceeding of the 12th Americas Conference on Wind Engineering* (Seattle, WA).
- Morrison, M. J., and Reinhold, T. A. (2015). “Performance of metal roofing to realistic wind loads and evaluation of current test standards,” in *Proceeding of the 14th International Conference on Wind Engineering* (Porto Alegre, Brazil).
- Pielke, R. A. Jr., Gratz, J., Landsea, C. W., Collins, D., Saunders, M. A., and Musulin, R. (2008). Normalized hurricane damage in the United States: 1900–2005. *Nat. Hazards Rev.* 9, 29–42. doi:10.1061/(ASCE)1527-6988(2008)9:1(29)
- Potter, M., and Leonard, J. (2010). “Spray system design for ember attack – research findings and discussion paper,” in *CSIRO – Sustainable Ecosystems, Report No. EP103159*, 1–27. Available from: http://www.bushfirecrc.com/sites/default/files/managed/resource/ember_attack_spray_research_report_final_0.pdf
- Quarles, S. L., Brown, T. M., Cope, A. D., Lopez, C., and Fasters, F. J. (2012). “Water entry through roof sheathing joints and attic vents: a preliminary study,” in *ATC-SEI Advances in Hurricane Engineering Conference* (Miami, FL), 283–294.
- Quarles, S. L., Valachovic, Y., Nakamura, G. M., Nader, G. A., and De Lasaux, M. J. (2010). *Home Survival in Wildfire-Prone Areas: Building Materials and Design Considerations*. Richmond, CA: University of California Agriculture and Natural Resources. ANR Publication 8393.
- Quiroga, P. S. (2006). *Uncertainty Analysis of Surface Pressure Measurements on Low-Rise Buildings [Masters Thesis]*. London, ON: The University of Western Ontario.
- Roeder, P. (2012). *Severe Weather in North America: Perils Risks, and Insurance*. Munich, Germany: Munich RE.
- Short, J. R. (2015). *The West Is on fire – and the US Taxpayer Is Subsidizing It*. The Conversation. Available at: <https://theconversation.com/the-west-is-on-fire-and-the-us-taxpayer-is-subsidizing-it-47900>.
- Smith, D. (2010). *Validation of Wind and Wind-Induced Pressure Data Collected at The Institute for Building and Home Safety's State-of-the-Art Multi-Peril Applied Research and Training Facility*. Lubbock, TX: Wind Science and Engineering Research Center.
- Sparks, P. R., Schiff, S. D., and Reinhold, T. A. (1994). Wind damage to envelopes of houses and consequent insurance losses. *J. Wind Eng. Ind. Aerod.* 53, 145–155. doi:10.1016/0167-6105(94)90023-X
- Straube, J. F., and Burnett, E. F. P. (2005). *Building Science for Building Enclosures*. Westford, MA: Building Science Press Inc.
- Tieleman, H. W. (2003). Wind tunnel simulation of wind loading on low-rise structures: a review. *J. Wind Eng. Ind. Aerod.* 91, 1627–1649. doi:10.1016/j.jweia.2003.09.021
- Underwriters Laboratory. (2012). *UL 2218: Standard for Impact Resistance of Prepared Roof Covering Materials*. Northbrook, IL: UL.
- United States Forest Service. (2016). *Managing Land – Fire*. Available at: <http://www.fs.fed.us/managing-land/fire>
- Xu, Y. L., and Reardon, G. F. (1996). *Full-Scale and Model-Scale Wind Pressure and Fatigue Loading on the Texas Tech University Building*. Townsville: Cyclone Testing Station JCU.

Conflict of Interest Statement: The authors declare that the research was conducted in the absence of any commercial or financial relationships that could be construed as a potential conflict of interest.

Copyright © 2017 Standohar-Alfano, Estes, Johnston, Morrison and Brown-Giammanco. This is an open-access article distributed under the terms of the Creative Commons Attribution License (CC BY). The use, distribution or reproduction in other forums is permitted, provided the original author(s) or licensor are credited and that the original publication in this journal is cited, in accordance with accepted academic practice. No use, distribution or reproduction is permitted which does not comply with these terms.



Experimental Assessment of Wind Loads on Vinyl Wall Siding

Mohammadtaghi Moravej¹, Ioannis Zisis^{1*}, Arindam Gan Chowdhury¹, Peter Irwin¹ and Bodhisatta Hajra²

¹ Department of Civil and Environmental Engineering, Florida International University, Miami, FL, USA, ² International Hurricane Research Center, Florida International University, Miami, FL, USA

OPEN ACCESS

Edited by:

Gregory Alan Kopp,
University of Western Ontario,
Canada

Reviewed by:

Bochao Cao,
Fudan University, China
Dorothy Reed,
University of Washington, USA
Chris Geurts,
Netherlands Organisation for
Applied Scientific Research,
Netherlands

*Correspondence:

Ioannis Zisis
izisis@fiu.edu

Specialty section:

This article was submitted to Wind
Engineering and Science,
a section of the journal
Frontiers in Built Environment

Received: 01 October 2016

Accepted: 12 December 2016

Published: 27 December 2016

Citation:

Moravej M, Zisis I, Chowdhury AG,
Irwin P and Hajra B (2016)
Experimental Assessment of Wind
Loads on Vinyl Wall Siding.
Front. Built Environ. 2:35.
doi: 10.3389/fbuil.2016.00035

Wind-induced damage to multi-layer building wall systems, such as systems with vinyl siding, is common, especially in hurricane-prone areas. Wind load distribution through these multi layered walls and the amount of load reduction due to pressure equalization is expressed through pressure equalization factors (PEFs). The ASTM D3679 standard suggests a PEF of 0.36, which means a 64% reduction in the net pressure on the siding. This paper presents results from an experimental study conducted on a low-rise building subjected to realistic wind loading conditions at the wall of wind (WOW) experimental facility at Florida International University. Results from area-averaged mean and peak pressure coefficients indicated that a very small portion of the total wind load is carried by the vinyl siding. However, PEFs were found to be much higher when individual taps were considered. For instance, PEFs ranged from 71 to 106% for the case of pressure coefficients with negative sign (suction) and from 39 to 110% for the case of pressure coefficients with positive sign (pressure). When a combined set of taps was considered, PEFs ranged approximately from 50 to 80% for the case of “suction” and from 15 to 75% for “pressure.” Based on the 1 m² of tributary area used in ASCE 7-10 Standard, results show that the net load on vinyl wall siding can be obtained by reducing the net design load for the entire wall assembly by 25 and 60% for suction and pressures, respectively. However, a smaller tributary area (<1 m²) can experience a local peak load that can induce damage to connections, especially in the case of relatively flexible wall coverings, with no or very little load sharing between connection points. Results indicate that for smaller areas (~0.2 m²) the allowable percentage reductions should not be more than 15 and 25% for suction and pressures, respectively. This study shows that the suggested ASTM PEF of 0.36 may lead to the underestimation of loads for the design of details affected by local loads. However, further research is needed to consider more cases when developing adequate design load guidelines for vinyl wall sidings.

Keywords: pressure equalization factor, vinyl siding, PVC siding, multi-layer wall, wall of wind, low-rise building

INTRODUCTION

Multi-layer wall systems such as vinyl siding walls can provide continuous insulation for buildings. Furthermore, their satisfactory performance in preventing water intrusion and their esthetic quality are among the factors that account for their popularity. However, the performance of these walls during extreme wind events raises concerns. In a detailed study of wood framed buildings damaged by

hurricane Katrina, vinyl siding failures were reported in several cases to be the initiation source of more extensive damages, such as gable end wall losses, through a progressive failure mechanism (van de Lindt et al., 2007). In June 2014, more than 25% of homes experienced damage to vinyl siding due to a tornado strike at Angus, ON, Canada (Miller et al., 2015).

The distribution of wind loads across multi-layer systems is complex and is affected by several contributing factors, such as the temporal and spatial gradient of the wind load, the magnitude of the load, spacing between layers, and the flexibility of the siding material. These factors have not yet been investigated extensively but have been the subject of several studies by Kramer et al. (1979), Amano et al. (1988), Cheung and Melbourne (1988) on wind pressure distribution through permeable roofs, and Oh and Kopp (2014), who developed a mathematical model for double-layer roof systems to study the pressure distribution in the cavity of air-permeable layers for given pressures on the external surfaces. In addition, there have been several studies focusing on the wind load distribution across multi-layered walls [e.g., Suresh Kumar (2000), Kopp and Gavanski (2011), Miller et al. (2015), Van Benthum and Geurts (2015)]. Assessing wind loads on the fasteners used in multilayer systems is also an important topic that has been studied by Cope et al. (2014).

Basically, the air permeation into the cavity between layers leads to a pressure equalization on opposite sides of a layer, which can reduce the net loads acting on that layer and thus result in a reduced design load. This equalization mechanism, which develops in small volume cavities, has been observed in other cases of wind studies, e.g., by Moravej et al. (2016), in which hurricane shutters were found to carry just a small amount of the wind load, causing the unprotected window surface to be the main carrier of the induced load.

To design the multi-layer wall systems, the commentary to chapter 30 of the ASCE 7-10 Standard (2010) addresses the load reduction due to the partial air pressure equalization between exterior and interior surfaces. In the absence of detailed information on the load distribution across individual layers, it is conservatively suggested to apply the entire pressure difference of the wall system in the design of individual load carrying layers, or to look for an alternative solution in the recognized literature. However, very few published studies are available on this topic.

Except for a field measurement by TenWolde et al. (1999), the research done on multi-layer wall systems has been conducted primarily in pressure chambers and under uniform static loading. In 2002, a study by Architectural Testing Inc. reported that the pressure equalization factor (PEF) for vinyl siding ranged from 0.03 to 0.18 (Architectural Testing Inc., 2002). The PEF value of 0.03 means a 97% reduction in net pressure on the siding, which implies almost full pressure equalization. Annex A1 of ASTM Standard D3679 (2009, 2013) applies a 0.36 PEF to evaluate the pressures on vinyl siding, which translates into a load obtained by applying a 64% reduction to the net pressure across the entire wall system. It has been observed that when there is a uniformly distributed static pressure applied, the pressure on the back of the siding equalizes the external pressure completely, whereas when there is a pressure gradient across the wall, the net load increases substantially (Miller et al., 2015).

To overcome the limitations of uniform static pressure testing, there have been some efforts to simulate a more realistic testing condition by using dynamic pressure chambers. These studies showed that the PEF value is sensitive to the magnitude of the applied load: a higher magnitude of negative load leads to a lower equalization factor (Kopp and Gavanski, 2011; Kochkin et al., 2012). The PEFs they evaluated for the vinyl siding were close to zero, which was in agreement with the earlier research conducted in uniform static tests (Architectural Testing Inc., 2002). However, the critical point is that the effect of a spatial pressure gradient on the wall's outer surface was not assessed. Without the spatial pressure gradient, unrealistically low PEF values are quite possible. A recent study by the Insurance Institute for Business & Home Safety (IBHS) research center, which included the spatial pressure gradient effects through tests in a full-scale wind tunnel facility (Cope et al., 2012) and a multi-chamber pressure testing apparatus (Miller et al., 2015), showed high PEF values of about 0.8 for the case of pressure coefficients with negative sign (suction), that is, only a 20% reduction in net pressure. Therefore, according to these studies, carried out in more realistic test conditions, the PEF value of 0.36 (i.e., 64% reduction) suggested by ASTM D3679 should be considered as unconservative. These uncertainties in design load calculations call for further study into the wind effects on vinyl siding walls.

In the current study, wind-induced pressures on a vinyl siding wall were investigated at full scale for various wind directions to determine pressure equalization effects as a function of tap locations and combinations. The objective was to study localized wind effects on smaller tributary areas. The research was conducted at Florida International University (FIU) wall of wind (WOW) experimental facility, which can generate design level wind speeds in a boundary-layer flow. Sections "Experimental Setup" and "Data Analysis Methods" of the paper describe the experiments carried out at the WOW and the analysis method and are followed by Section "Results and Discussion." Conclusions are presented in Section "Conclusion."

EXPERIMENTAL SETUP

WOW Experimental Facility

The WOW is a state-of-the-art large scale wind engineering experimental facility consisting of 12 fans (Figure 1A), each powered by a 700-hp motor. The 12-fan system is capable of generating

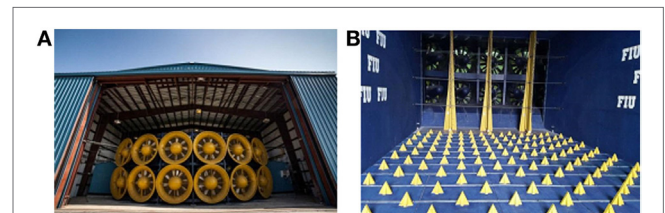


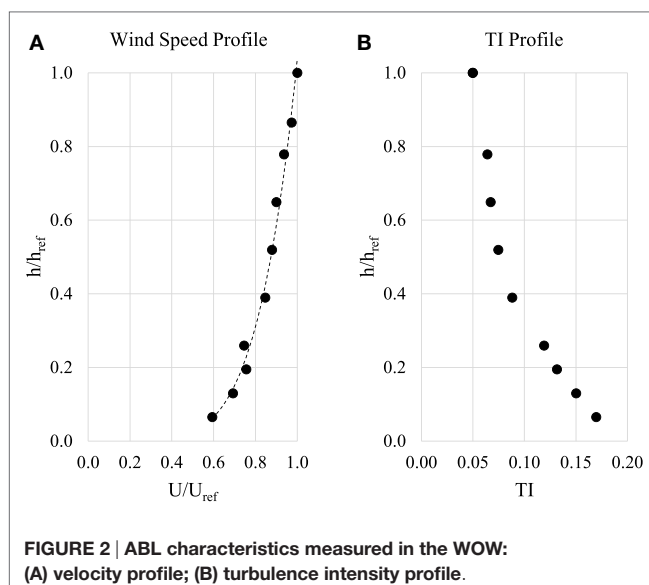
FIGURE 1 | Wall of Wind (WOW) at Florida International University: (A) 12 fans; (B) spires and roughness elements.

wind speeds exceeding 70 m/s (157 mph), which is equivalent to Category 5 hurricane wind speeds as per Saffir–Simpson scale. Spires and roughness elements in a flow management box help generate an atmospheric boundary layer over a length of 9.75 m downstream of the contraction zone (Figure 1B). The open jet test section is 4.3 m high by 6.1 m wide.

The velocity and turbulence intensity profiles corresponding to an open terrain ABL simulation used for this experiment are shown in Figure 2. Wind velocities were measured by Cobra probes (Turbulent Flow Instrumentation, 2008). The velocity profile plot is normalized with the mean wind speed of 28.4 m/s at the reference height, which is taken as the test building model eave height (2.34 m).

Building Model Used for the Study

The wood frame building model used for the study had plan dimensions of 2.43 m × 2.74 m and eave height of 2.34 m. The wood frame building was sheathed by a layer of plywood over which a moisture barrier layer was applied and was then covered by the vinyl siding. Figure 3 shows a view of the finished building placed on the turntable. The vinyl siding consisted of several individual panels that were connected to the building wall sheathing using nails (using spacing of 23 cm or 9"). In order to collect the pressure data on the vinyl siding, one side of the building was instrumented with 49 pressure taps on both the exterior surface of the siding and on the plywood layer. The schematic of Figure 4A shows the locations of the exterior, cavity, and internal taps, that is, (i) exterior taps on the vinyl siding to measure external pressures, (ii) cavity taps on the inner layer (plywood with moisture barrier) to measure pressures in the cavity between the vinyl siding and the inner layer, and (iii) internal taps inside the building model to measure building internal pressures. The model had a total of 102 taps. Sample taps on the building model are shown in Figure 4B, while Figure 4C shows the location of the taps on the building wall and the cavity.



The model was placed on a turntable, which was rotated to test for wind directions ranging from 0° to 180°, where 0° is wind normal to the wall with siding (shown using bold line in Figure 5A). A section of the wall showing the various parts of the vinyl wall siding is shown in Figure 5B. The pressure data collected on the test model wall system were sampled at a rate of 512 s⁻¹ using a “Scanivalve ZOC 33” miniature pressure system (Scanivalve Corporation, 2013). A tubing transfer function was used to correct for the distortion effects introduced by the tubing (Irwin et al., 1979). The partial turbulence simulation (PTS) technique was used to determine the peak pressure coefficients, as described in Asghari Mooneghi et al. (2016). The PTS technique focuses on obtaining a good match of the high frequency part of the turbulence spectrum, while the effect of the missing low frequency part of the spectrum for large scale models is compensated in the post-test analysis process through a quasi-steady approach. This peak analysis method was used to study the area-averaged net loads on the entire wall. To study the PEF for individual taps or combination of them, observed peaks of instantaneous load summations were calculated, which will be discussed in the following sections.

DATA ANALYSIS METHODS

The collected pressures at each of the taps were initially area averaged over the whole wall area to obtain the mean and peak area-averaged pressure coefficients using Eqs 1 and 2.



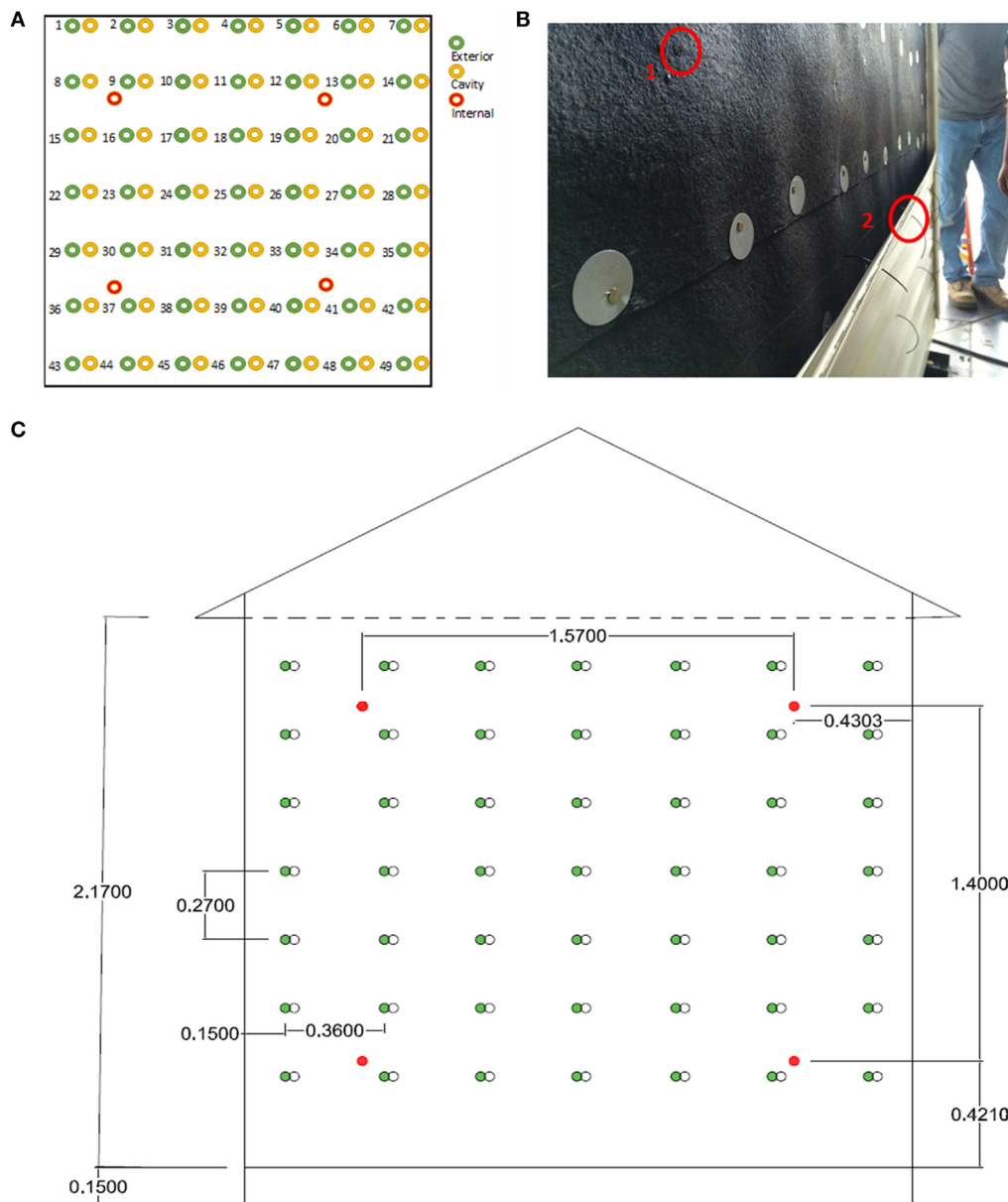


FIGURE 4 | (A) Schematic showing the locations of taps, **(B)** circles marked as 1 and 2 show sample cavity and exterior surface tap locations, **(C)** location of taps on the vinyl wall siding (locations marked in green are exterior taps, those marked in red are interior taps, while the remaining taps are located within the cavity).

$$C_{p_{\text{mean}}} = \frac{P_{\text{mean}}}{\frac{1}{2} \rho U_{\text{mean}}^2} \quad (1)$$

$$C_{p_{\text{peak}}} = \frac{P_{\text{peak}}}{\frac{1}{2} \rho U_{3s}^2} \quad (2)$$

where P_{mean} and P_{peak} are the mean and peak area-averaged pressures, respectively, and U_{mean} and U_{3s} are the mean and peak (i.e., 3 s) wind speed at the eave height, respectively.

To study the extent of wind load reduction on the siding, peak pressure coefficients on the exterior side of the wall and in the cavity are reported herein, followed by the net peak C_p coefficients on the vinyl siding. The area-averaged peak net pressures were calculated based on the instantaneous pressure differences across each layer to provide an understanding of the pressure equalization phenomenon. In this paper, the terms “pressure” and “suction” have been used to indicate positive and negative pressure differences (relative to an ambient reference pressure), respectively.

However, to further examine the degree of load reduction and the effect of including various areas in the calculation of the

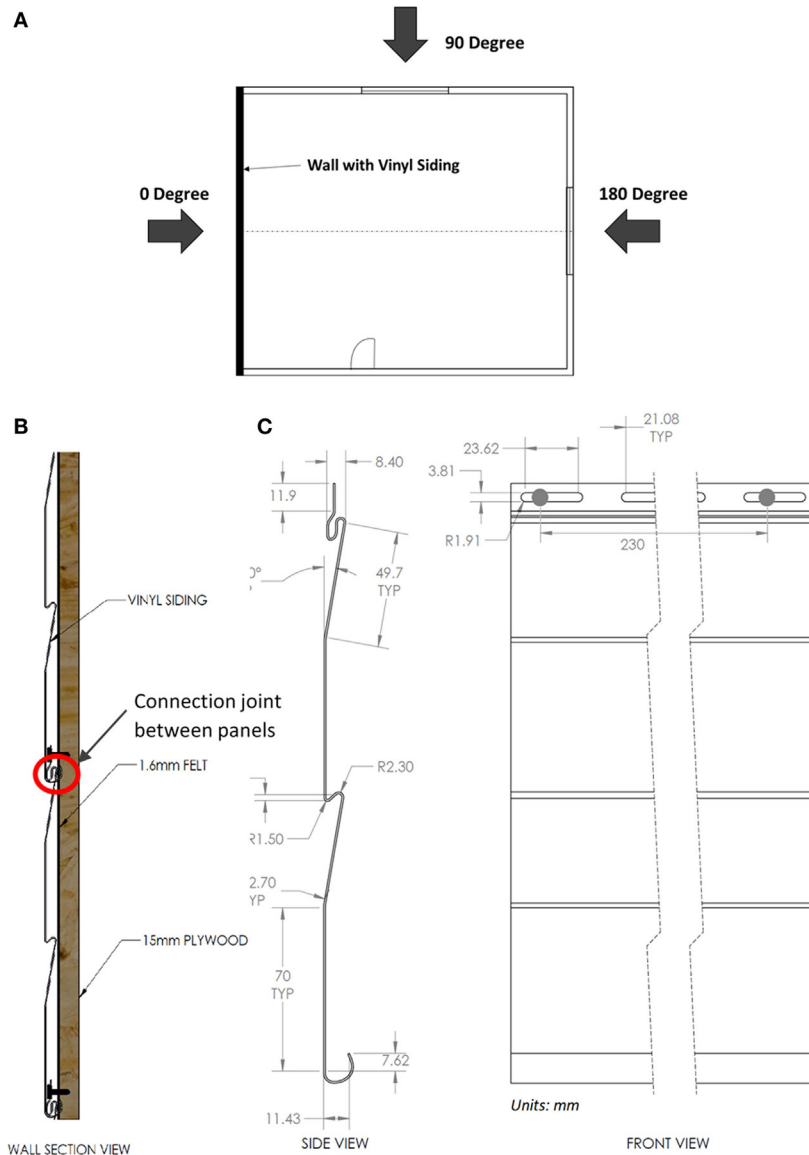


FIGURE 5 | Building model used for the study: (A) plan view and the convention for wind direction; (B) vertical section showing the various parts of the vinyl siding; (C) side and front views of one siding panel (showing nail connections).

PEF, individual taps as well as various combinations of multiple taps were considered. Two methods for calculating the PEF are reported in the literature. One method is based on the peak values over all the directions, which is similar to the approach used in the ASCE 7 for components and cladding (Cope et al., 2012). Following this concept, the PEF of peak values is defined in this paper by Eqs 3–7.

$$\Delta P_i(t, \theta) = P_{\text{ext}}(t, \theta) - P_{\text{cav}}(t, \theta) \quad [\text{net load on the vinyl siding}] \quad (3)$$

$$\Delta P_{\text{total}}(t, \theta) = P_{\text{ext}}(t, \theta) - P_{\text{int}}(t, \theta) \quad [\text{net load on wall assembly}] \quad (4)$$

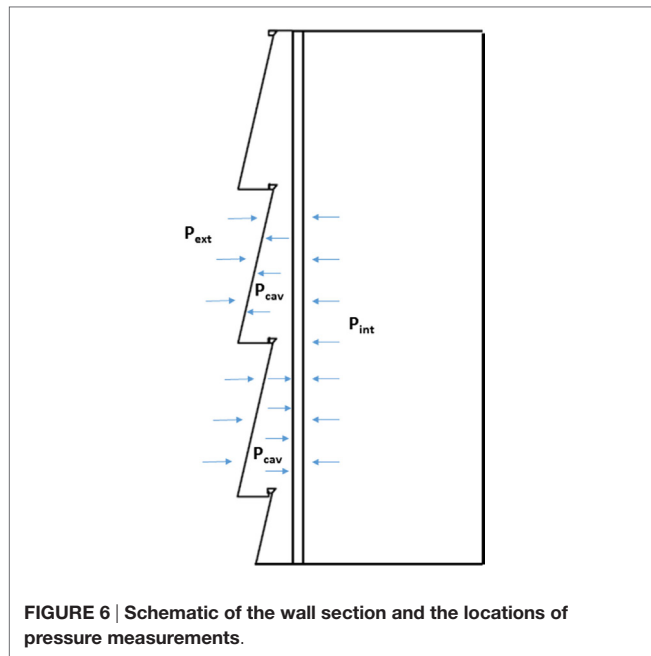
$$\Delta P_{1, \text{max}} = \max[\Delta P_1(t, \theta)] \quad (5)$$

$$\Delta P_{\text{total}, \text{max}} = \max[\Delta P_{\text{total}}(t, \theta)] \quad (6)$$

$$\text{PEF}_i = \frac{\Delta P_{1, \text{max}}}{\Delta P_{\text{total}, \text{max}}}, \quad i = 1, 2, \dots, 49 \quad (\text{tap number}) \quad (7)$$

where P_{ext} is the pressure on vinyl siding, P_{cav} is the pressure on the exterior side of the plywood, which is assumed to be same as the pressure in the cavity between vinyl siding and plywood, and P_{int} is the internal pressure in the building, as illustrated in **Figure 6**.

Then $\Delta P_{1, \text{max}}$ and $\Delta P_{\text{total}, \text{max}}$ are defined, respectively, as the peak values of the ΔP_1 and ΔP_{total} over all wind directions. The parameter θ denotes the direction as defined in **Figure 5**. Having $\Delta P_{1, \text{max}}$ and $\Delta P_{\text{total}, \text{max}}$, the PEF_i is calculated for each tap location.



Also to calculate the PEF for a group of taps, $\Delta P_i(t, \theta)$ and $\Delta P_{total}(t, \theta)$ should be constructed by summation of instantaneous load vectors formed on the tributary areas of each included tap.

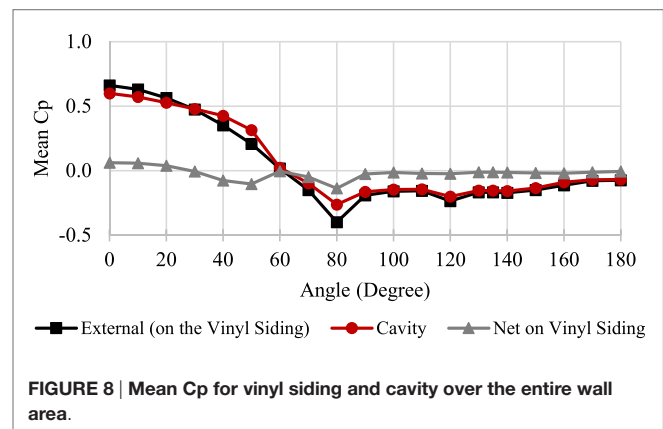
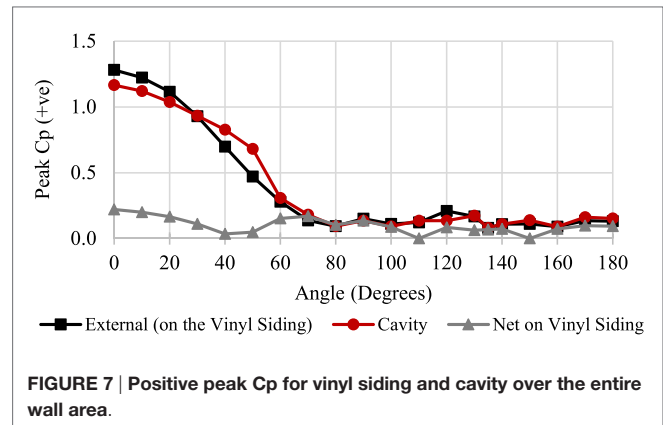
The other method used is to calculate instantaneous PEFs for individual taps or a combination of adjacent taps and generate a time history of PEFs (Cope et al., 2012; NAHBRC, 2012). The PEF time history is calculated for all wind directions and is plotted against the time history of the external pressure exerted on the tributary area of each tap, which eventually produces a plot with a wide dispersion, especially at the lower magnitudes of external pressures. As a result, higher PEFs are obtained at lower external pressures. When used with the worst case exterior pressure, these PEFs could lead to highly conservative results. Therefore, the method of maximum PEFs (Eq. 7) is deemed more appropriate for practical design applications.

Since code provisions provide the worst case combination of exterior and internal pressures, the PEF can be applied to obtain the critical net load on the siding as expressed by Eq. 8.

$$P = q_h [(GCp) - (GCpi)] \times PEF \quad (8)$$

where q_h is velocity pressure, and GCp and $GCpi$ are external and internal pressures, respectively, as described by ASCE7-10 Eq. 30.4-1.

The pressure equalization across a component of the wall is dependent on the instantaneous pressures on both sides on that component as conceptualized using the schematic shown in **Figure 6**. As explained earlier, the net pressure on the vinyl siding is represented as $\Delta P_1 = (P_{ext} - P_{cav})$, where P_{ext} is the external pressure on vinyl siding and P_{cav} is the pressure inside the cavity between the vinyl siding and the plywood sheathing. Pressure equalization across the vinyl siding will be significant when the external pressure and the cavity pressure act in opposite directions and have comparable magnitudes. As noted in **Figure 3**, the



corners of the building model were fitted with vertical L-shaped edge trim fittings, which ensure that there is not an opening at the extremities. In addition, the vinyl siding panels were connected to each other using a sliding interlocking mechanism to minimize airflow and water intrusion through the overlaps. These design details are expected to minimize air leakage; however, this also reduces the effect of pressure equalization. The results presented in the study corroborate this phenomenon as they indicate a limited reduction of the net loading on vinyl siding due to pressure equalization.

RESULTS AND DISCUSSION

Figures 7–9 illustrate the results for area-averaged mean and peak pressure coefficients over the entire wall, including (i) external pressures (measured on the vinyl siding), (ii) cavity pressures (measured on the plywood), and (iii) net pressures (based on instantaneous differences between the external and cavity pressures). **Figure 7** shows that due to pressure equalization the peak C_p values obtained in the cavity and on the exterior of the wall are very comparable for all wind directions. As a result, for all tested wind directions the net peak C_p is considerably low. **Figure 8** shows that the mean C_p values for the exterior and cavity had similar trends, as observed in the positive peak C_p plots. In a similar manner, the net mean C_p values are minimal for all wind

directions. Finally, **Figure 9** shows that peak C_p values (suction) for the exterior and cavity were also comparable for most of wind directions, except between 70° and 90° . For these directions, the net mean C_p values were higher. This observation is generally in agreement with past studies, in which a lower load reduction was observed for higher magnitudes of negative load (Kopp and Gavanski, 2011; Cope et al., 2012). Overall, the results show that for a non-sealed system (as the current vinyl wall siding), when pressures are averaged over a large area of the vinyl siding, significant pressure equalization is observed and net wind pressure is minimal. This effect has been captured in the current testing also. Results presented later (in **Table 2**) show that, in general, pressure equalization effects increase when pressures are averaged over larger areas, which reduce the net wind pressures.

However, damage reconnaissance after high wind events indicated that the failure of siding is initiated by localized damage. Therefore, the analysis of the experimental data needs to take into consideration smaller tributary areas. Such areas can experience high localized wind loads that may cause local damage leading to progressive failures of large portions of the wall siding. The following section focuses on studying PEFs for smaller tributary areas comprising various combinations of taps.

Pressure Equalization Factors

The PEFs (as discussed earlier) were obtained for individual taps and combination of taps based on Eqs 3–7. **Table 1** presents peak PEF values for individual tap locations (see **Figure 4A** for tap locations) for pressure coefficients with negative sign (suction) and positive sign (pressure). The PEF values shown in **Table 1** are the highest (in magnitude) values obtained from all wind directions tested. The results indicate that when local pressure differences are considered, higher values of PEF are possible. Essentially, PEF values are expected to fall between 0 and 1, but the results of individual tap locations showed a few cases with PEFs greater than 1 or less than 0. A value greater than 1 indicates that the pressure on one side of a wall layer is of opposite sign to that on the other. In summary, the PEF values range from 71 to 106% for suctions and from 39 to 110% for pressures.

As discussed previously, aside from looking at individual taps it is important to consider various combinations of multiple taps. The tap combinations considered in this study are shown in

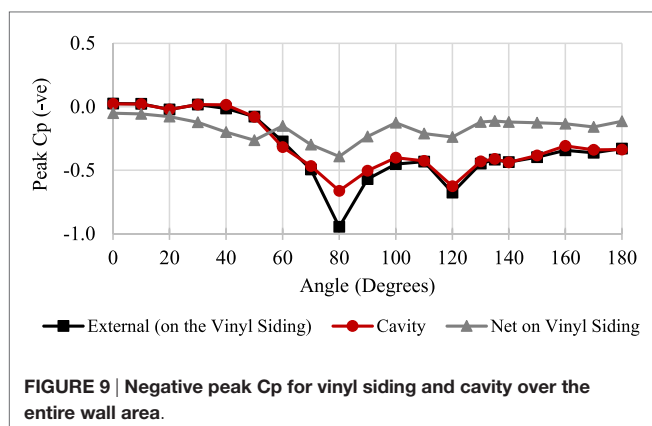


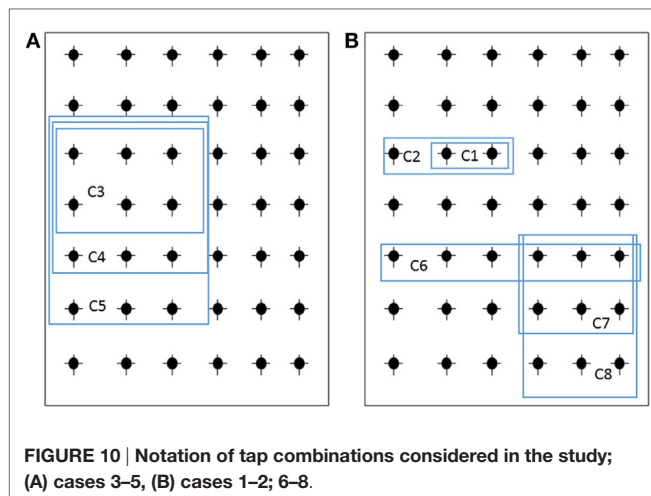
Figure 10. The tap combinations were mainly chosen to capture wind effects on tributary areas for one or more connections (i.e., nails connecting the vinyl siding panels to the wall sheathing). This was considered to be important as damages often occur when a single connection fails or a group of connections fail. When considering smaller numbers of taps, such as in combinations C1, C2, C3, C6, and C7, the taps were chosen in one or two row(s) [instead of in column(s)] as that would engage one or more nails attaching the siding panels, which were oriented horizontally as shown in **Figure 3**. **Table 2** presents peak PEF values for a combination of taps as well as the corresponding area covered by those taps. The findings show some considerable differences compared to the individual tap approach. For instance, by considering taps 16 and 17 in case 1 (shown as “C1” in **Figure 10B**), a peak suction PEF of 0.83 was obtained, which means that the load reduction due to pressure equalization is about 17%—note that the load reduction when taps 16 and 17 were considered individually was 9 and 16% respectively. According to **Table 2**, PEFs range from 52 to 83% for the case of “suctions” and between 13 and 74% for the case of “pressures.”

TABLE 1 | Peak pressure equalization factor (PEF) values for individual tap locations.

Tap number	Peak PEF (suction)	Peak PEF (pressure)
1	0.90	0.74
3	0.87	0.91
5	0.90	1.08
7	0.91	1.04
9	0.89	1.06
11	0.86	1.10
13	0.88	0.89
15	1.00	0.97
16	0.91	1.05
17	0.84	1.01
19	0.90	1.06
21	0.94	0.88
24	0.86	1.08
26	0.97	0.92
28	1.06	0.77
30	0.91	0.85
32	0.91	0.94
34	1.03	0.77
37	1.02	0.95
40	0.92	0.83
43	0.88	0.80
47	0.78	0.39

TABLE 2 | Peak PEF values for combinations of adjacent taps.

Case no.	Included taps	Peak suction	Peak pressure	Tributary area (m ²)
1	16:17	0.83	0.74	0.214
2	15:17	0.77	0.64	0.315
3	15:17,22:24	0.69	0.55	0.641
4	15:17,22:24,29:31	0.71	0.47	0.956
5	15:17,22:24,29:31, 36:38	0.73	0.43	1.272
6	29:35	0.69	0.19	0.743
7	33:35,40:42	0.81	0.36	0.641
8	33:35,40:42, 47:49	0.82	0.35	0.956
9	1:49	0.52	0.13	5.205



These results are considerably different from those of pressure chamber tests addressed earlier. However, they are in close agreement with the full-scale study conducted at IBHS (Cope et al., 2012), the result of which indicated that the vinyl siding was subjected to 75–80% of the “suction” design pressures. ASCE 7 wind load provisions use a smallest tributary area of about 1 m² to estimate localized design pressures for component and cladding elements of buildings. **Table 2** shows in bold italic the WOW test-based PEF values for similar tributary areas. The average of these values indicate that for tributary areas of about 1 m² the design wind loads can be estimated by using PEF values of 0.75 and 0.4 for “suctions” and “pressure” loading, respectively. This suggests that based on Eq. 8, the net load on vinyl wall siding can be obtained by reducing the net design load for the entire wall assembly by 25 and 60% for “suction” and “pressure” loading, respectively. However, it might be more relevant to relate the results to a smaller tributary area (<1 m²) experiencing a local peak load that can induce damage to connections, especially in the case of relatively flexible wall coverings, with no or very little load sharing between connection points. This aspect of smaller tributary areas is relevant to higher maximum loads on the connections (fixings) leading to the initiation of damage to vinyl siding. Depending on the installation method and considering the tributary area of the connections, the effective area may be much smaller than 1 m², as is the case for C1 and C2 in **Figure 10** (which represent the tributary areas for three and five nail connections, respectively). Based on this study, for smaller areas (~0.2 m²) the allowable percentage reductions should not be more than 15 and 25% for suction and pressures, respectively. It should be emphasized that connection failures will be generally due to suction.

As discussed earlier and also indicated in **Table 2** (and **Figures 7–9**), when considering the entire wall, there is an increased effect of pressure equalization. This could be attributed to the lack of correlation of external pressures on the vinyl siding over a larger area. The cavity pressure is expected to be more uniform as compared to the external pressure. As a result, the net pressure on the vinyl siding, represented as $\Delta P_1 = (P_{\text{ext}} - P_{\text{cav}})$,

is expected to be smaller in magnitude when averaged over a larger area, which implies higher pressure equalization. As the tributary area reduces (such as for smaller areas as C1), the correlation of external pressures increases, which leads to limited load reduction. Further study is recommended to delve into the aspect of spatial and temporal correlations of external and cavity pressures to improve our understanding of effects of tributary areas on pressure equalizations. Further testing is also needed to consider more types of vinyl siding systems (with different design configurations, panel flexibility, corner details, etc.) when developing adequate design load guidelines for vinyl wall sidings and their connections.

CONCLUSION

This paper presented results from an experimental study conducted at the WOW experimental facility at FIU to study wind effects on vinyl siding on low-rise buildings. One of the walls of a full-scale test building was cladded with vinyl siding and instrumented to estimate net pressures across the siding and across the entire wall system as a function of different wind directions. The findings from this study indicated that when the area being considered is the whole wall, area-averaged mean and peak pressure coefficients, indicate very low net loads on the wall siding. However, designing vinyl wall siding for these low net loads may not be adequate, as was indicated by the poor performance of vinyl wall systems during past high wind events where most of the failures were initiated by local damages. Thus, it deemed necessary to study localized wind pressures that may lead to local damages and cascading failures.

To study local wind pressures on the wall siding, PEFs were calculated for various tributary areas. Results indicated that for individual points PEFs are not less than about 70% for cases of negative pressure coefficients and about 40% for cases of pressure coefficients with positive sign (pressure). When tap combinations covering larger areas were considered, PEFs ranged from approximately 50 to 80% for cases of pressure coefficients with negative sign (suction) and from 15 to 75% for cases of “pressure.” According to various cases considered, the average wind pressure carried by the vinyl siding is about 75% of the design suction pressure for the whole wall assembly and about 40% of the “pressure.” These results indicate that the suggested ASTM PEF of 0.36 is somewhat unconservative for the design of details and local supports. The current results suggest that the net load on vinyl wall siding for 1 m² of tributary area can be obtained by applying PEFs of 0.75 and 0.40 to the net design “suction” and “pressure” loading, across the whole wall assembly, respectively. However, for smaller tributary areas (~0.2 m²), the PEF should be about 0.85 to help prevent local failure of connection(s) that could lead to cascading failure. Further research on pressure equalization on vinyl siding cladded wall systems is needed to explore the effects of different size internal cavities and different types of siding materials and wall details. Future studies on this topic should also consider other factors such as different ratio of plan dimensions, change in building height, etc. This will help to establish appropriate wind design provisions to lessen the risk of damage to vinyl wall sidings under high winds.

AUTHOR CONTRIBUTIONS

MM is a Ph.D. student supervised by AC (associate professor in CEE, FIU) and PI (professor of practice in CEE, FIU). MM has carried out most of the data analysis along with PI and AC as part of a research project funded by “The State of Florida Division of Emergency Management” and has written sections of this paper in collaboration with co-authors. BH is a research scientist at the WOW at FIU and has carried out data analysis, in addition to writing parts of this paper. IZ is an assistant professor at the CEE at FIU and has reviewed the results presented and developed the structure of the paper, in addition to checking all the data collected during the experiments and revising the manuscript.

REFERENCES

- Amano, T., Fujii, K., and Tazaki, S. (1988). Wind loads on permeable roof-blocks in roof insulation systems. *J. Wind Eng. Ind. Aerodyn.* 29, 39–48. doi:10.1016/0167-6105(88)90143-2
- Architectural Testing Inc. (2002). *Wind Pressure Equalization Research Project Report. No. 01-40776.01*. Washington, DC: Vinyl Siding Institute. Available at: <https://www.vinylsiding.org/>
- ASCE 7-10 Standard. (2010). *Minimum Design Loads for Buildings and Other Structures*. Reston, VA: American Society of Civil Engineers.
- Asghari Mooneghi, M., Irwin, P., and Gan Chowdhury, A. (2016). Partial turbulence simulation method for predicting peak wind loads on small structures and building appurtenances. *J. Wind Eng. Ind. Aerodyn.* 157, 47–62. doi:10.1016/j.jweia.2016.08.003
- ASTM Standard D3679. (2009). *Standard Specification for Rigid Poly Vinyl Chloride (PVC) Siding*. West Conshohocken, PA: ASTM International.
- ASTM Standard D3679. (2013). *Standard Specification for Rigid Poly Vinyl Chloride (PVC) Siding*. West Conshohocken, PA: ASTM International.
- Cheung, J. C. K., and Melbourne, W. H. (1988). Wind loading on a porous roof. *J. Wind Eng. Ind. Aerodyn.* 29, 19–28. doi:10.1016/0167-6105(88)90141-9
- Cope, A., Crandell, J., Liu, Z., and Stevig, L. (2014). Wind loads on fasteners used to attach flexible porous siding on multi-layer wall systems. *J. Wind Eng. Ind. Aerodyn.* 133, 150–159. doi:10.1016/j.jweia.2014.06.007
- Cope, A. D., Crandell, J. H., Johnston, D., Kochkin, V., Liu, Z., Stevig, L., et al. (2012). “Wind loads on components of multi-layer wall systems with air-permeable exterior cladding”, in *Advances in Hurricane Engineering : Learning from Our Past* (American Society of Civil Engineers), 238–257. doi:10.1061/9780784412626.022
- Irwin, H. P. A. H., Cooper, K. R., and Girard, R. (1979). Correction of distortion effects caused by tubing systems in measurements of fluctuating pressures. *J. Wind Eng. Ind. Aerodyn.* 5, 93–107. doi:10.1016/0167-6105(79)90026-6
- Kochkin, V., Davies, R., and DeRenzis, A. (2012). “Evaluation of the wind pressure performance of walls with exterior rigid foam sheathing”, in *Advances in Hurricane Engineering : Learning from Our Past* (American Society of Civil Engineers), 258–269. doi:10.1061/9780784412626.023
- Kopp, G., and Gavanski, E. (2011). Effects of pressure equalization on the performance of residential wall systems under extreme wind loads. *J. Struct. Eng.* 138, 526–538. doi:10.1061/(ASCE)ST.1943-541X.0000476
- Kramer, C., Gerhardt, H. J., and Kuster, H. W. (1979). On the wind-loading mechanism of roofing elements. *J. Wind Eng. Ind. Aerodyn.* 4, 415–427. doi:10.1016/0167-6105(79)90016-3

ACKNOWLEDGMENTS

The authors greatly acknowledge the help offered by Walter Conklin and Roy Liu-Marques to conduct the experiments at FIU Wall of Wind. Also, The authors acknowledge Jorge Damas for his valuable help with the technical drawings presented in this paper.

FUNDING

The authors would like to acknowledge the financial contributions of the State of Florida Division of Emergency Management, USA, and also support from the National Science Foundation (NSF Award No. CMMI-1151003).

- Miller, C., Kopp, G., and Morrison, M. (2015). “Pressure equalization in residential wall cladding systems,” in *Presented at the 14th International Conference on Wind Engineering*, Porto Alegre, Brazil.
- Moravej, M., Gan Chowdhury, A., Zisis, I., Irwin, P., and Hajra, B. (2016). “The effect of a shutter on the wind induced loads on a window and wind driven rain intrusion into the building through experiments at the Wall of Wind Experimental Facility,” in *8th International Colloquium on Bluff Body Aerodynamics and Applications* (Boston: Northeastern University).
- National Association of Home Builders Research Center (NAHBRC). (2012). *Evaluation of the Wind Pressure Performance of Walls with Exterior Rigid Foam Sheathing*. Upper Marlboro, MD: NAHB Research Center, Inc.
- Oh, J. H., and Kopp, G. A. (2014). Modelling of spatially and temporally-varying cavity pressures in air-permeable, double-layer roof systems. *Build. Environ.* 82, 135–150. doi:10.1016/j.buildenv.2014.08.008
- Scanivalve Corporation. (2013). *ZOC 33/64Px Electronic Pressure Scanning Module, Instruction and Service Module*. Liberty Lake, WA: Scanivalve Corporation. Available at: www.scanivalve.com
- Suresh Kumar, K. (2000). Pressure equalization of rainscreen walls: a critical review. *Build. Environ.* 35, 161–179. doi:10.1016/S0360-1323(99)00015-3
- TenWolde, A., Carll, C. G., and Malinauskas, V. (1999). “Air pressures in wood frame walls,” in *Proceedings Thermal VII* (Atlanta: ASHRAE Publications).
- Turbulent Flow Instrumentation. (2008). *Series 100 Cobra Probe Manual, Turbulent Flow Instrumentation*. 1–13. Available at: <http://www.turbulentflow.com.au/>
- Van Bentum, C., and Geurts, C. (2015). “Full scale measurements of pressure equalization on air permeable façade elements,” in *Presented at the ICWE14* (Porto Alegre, Brazil).
- van de Lindt, J. W., Graettinger, A., Gupta, R., Skaggs, T., Pryor, S., and Fridley, K. (2007). Performance of wood-frame structures during Hurricane Katrina. *J. Perform. Constr. Facil.* 21, 108–116. doi:10.1061/(ASCE)0887-3828(2007)21:2(108)

Conflict of Interest Statement: The authors declare that the research was conducted in the absence of any commercial or financial relationships that could be construed as a potential conflict of interest.

Copyright © 2016 Moravej, Zisis, Chowdhury, Irwin and Hajra. This is an open-access article distributed under the terms of the Creative Commons Attribution License (CC BY). The use, distribution or reproduction in other forums is permitted, provided the original author(s) or licensor are credited and that the original publication in this journal is cited, in accordance with accepted academic practice. No use, distribution or reproduction is permitted which does not comply with these terms.



From Load Estimation to Performance Estimation—From Model-Scale Test to Full-Scale Test: With Special Interest in Asian Region

Yukio Tamura^{1,2*}, Kazuyoshi Nishijima³, Masahiro Matsui², Pham Van Phuc⁴ and Qingshan Yang¹

¹School of Civil Engineering, Beijing Jiaotong University, Beijing, China, ²Wind Engineering Research Center, Joint Usage/Research Center Program, Tokyo Polytechnic University, Tokyo, Japan, ³Disaster Prevention Research Institute, Kyoto University, Kyoto, Japan, ⁴Research Institute, Shimizu Corporation, Tokyo, Japan

OPEN ACCESS

Edited by:

Gregory Alan Kopp,
University of Western Ontario,
Canada

Reviewed by:

Suren Chen,
Colorado State University, USA
Arindam Gan Chowdhury,
Florida International University, USA

*Correspondence:

Yukio Tamura
yukio@arch.t-kougei.ac.jp

Specialty section:

This article was submitted to
Wind Engineering and Science,
a section of the journal
Frontiers in Built Environment

Received: 01 November 2016

Accepted: 19 January 2017

Published: 14 February 2017

Citation:

Tamura Y, Nishijima K, Matsui M,
Phuc PV and Yang Q (2017) From
Load Estimation to Performance
Estimation—From Model-Scale Test
to Full-Scale Test: With Special
Interest in Asian Region.
Front. Built Environ. 3:8.
doi: 10.3389/fbuil.2017.00008

This paper first discusses the current status of natural hazard-induced disasters, with special focus on devastating wind-related disasters in the Asian region. The importance of the combined effects of wind and water hazards, the importance of performance of cladding and components in wind-resistant design of buildings, and deterioration of metal roofing systems of long-span structures mainly caused by fatigue of fixing joints due to daily solar heating effects are demonstrated. Some human errors caused by lack of attention to aerodynamic and structural behaviors are also indicated. Then, psychological impacts and social impacts are discussed, and common underestimation of social impacts of wind-induced disasters on society is pointed out. The main reason for repeated wind-induced damage is lack of information on the real performance of claddings, components, and main frames under wind actions. The demand and necessity for full-scale tests are emphasized, aiming to check the performance of building and structural systems under realistic and controlled conditions of extremely strong actions of wind, rain, snow, fire, solar heating, and so on. Finally, the academic and social significance of the full-scale storm simulator is discussed.

Keywords: full-scale storm simulator, wind-related disaster, tropical cyclone, tornado, economic loss, human loss, psychological impact, social impact

INTRODUCTION

Human beings spend their daily lives within the range of the atmospheric boundary layer (ABL), in which the air flow is affected by friction due to ground surface roughness. The air flow within this range is generally called wind, and strong wind occasionally causes severe damage to infrastructures and people due to its aerodynamic effects. However, weak- or medium-level wind can cause severe vibrations of structures or members and can have serious environmental impacts on human society,

such as air pollution problems and thermal effects. There are several wind climates that cause damage to buildings and structures, including monsoons, frontal depressions, tropical cyclones, gust fronts, downbursts, tornadoes, dust devils, katabatic winds, lee waves, and so on. Tropical cyclones are intense cyclonic storms that occur over tropical oceans, mainly in summer and early autumn. They are known as typhoons in the West Pacific Ocean region, cyclones in the Oceania and the Indian Ocean regions, and hurricanes in American and Caribbean regions, with slightly different definitions. The diameters of tropical cyclones, defined by the isobar of 1,000 hPa, range from around 100 to 2,000 km, but are usually of the order of several 100 km. The thickness of the atmosphere involved is about 10–12 km, and a roughly circular “eye,” or “hot tower,” is formed in the storm’s center. It should be noted that tropical cyclones are often accompanied by severe local storms (SLSs) such as tornadoes and downbursts. Almost all devastating wind-induced disasters result from combined effects of strong wind and accompanying water hazards due to heavy rain and storm surge. The social impacts of these “wind-related” disasters have been some of the most severe in our human society (Tamura et al., 2012). At the bottom of the ABL, human activities are also seriously disturbed by other meteorological phenomena such as snow, hail, extremely hot/cold temperature, and so on, and winds always have strong impacts on those phenomena. Fire hazards also occur at the bottom of the ABL either as meteorological/natural hazards or man-made hazards, and they cannot be treated without wind effects.

The risk of future disasters continues to escalate with population shifts toward urban centers, and the impending threat of their increased intensity and frequency as hypothesized by potential climate change. Urbanization has also led to the deterioration of regional and global environmental quality with a far reaching impact on public health. Not only accidentally occurring extremely strong wind events but also serious environmental problems in weak- or medium-level wind conditions should be treated as hazards causing severe disasters in our human society. The latter are invisible and long-lasting disasters and can be more dangerous than the former. This calls for a sustainable society that emphasizes reduced energy consumption and improved environmental quality (Tamura et al., 2012).

The Science Council of Japan (SCJ) selected 207 projects as the Academic Master Plans 2014 of Large Research Facilities and Large Research Projects (Master-Plan-2014, hereafter) (SCJ, 2014). In addition, the SCJ especially selected the 27 most important and most urgent projects from among the 207 projects in the Master-Plan-2014 as Priority Policy Projects (PPPs). The SCJ belongs to the Cabinet Office, Government of Japan, and consists of 210 Council Members and 2,000 Members from 30 academic fields including civil engineering and in various areas such as liberal arts, social sciences, life sciences, physical sciences, chemical sciences, and engineering including civil engineering. The majority of the 27 selected PPPs are from areas in the life and physical sciences, and a few are from engineering. The “full-scale storm simulator (FSSS) and Meteorological Hazards Science Park (MHSP)” proposed by the first author of this paper has been selected as one of the 27 PPPs.

This paper emphasizes the importance, efficiency, and necessity for full-scale facilities for disaster risk reduction (DRR), especially in the Asian region.

DEVASTATING WIND-RELATED DISASTERS (WRDs) ESPECIALLY IN ASIAN REGION

Typhoon Vera attacked the central part of Japan in September 1959. Its maximum recorded peak gust was 55.3 m/s, and the Japan Meteorological Agency estimated 75 m/s as the maximum peak gust from the lowest pressure recorded of 895 hPa. Fatalities and missing numbered 5,098, and the majority were caused by the storm surge. We should emphasize the combined effects of wind and water hazards.

In 1970, Cyclone Bhola (see **Figure 1**) struck East Pakistan. The highest record of 10-min mean wind speeds was 57 m/s, and the lowest pressure was 966 hPa. Economic loss was estimated at 460 million USD, which is relatively high considering the GDP of this country. However, more seriously, a shocking number of fatalities and missing were reported, 300,000–500,000, of which there is no exact information. The majority of fatalities and missing were caused by the storm surge, again resulting from the combined effects of strong wind and water hazards. It is said that one of the reasons, why East Pakistan became independent from West Pakistan in 1971, was insufficient support from West Pakistan for this devastating disaster. Thus, the hot spots of human losses are in developing countries, especially in the South Asian region.

Typhoon 7513 recorded a maximum peak gust of 67.8 m/s at Hachijo Island, Tokyo, Japan, in 1975. The effects of topography and impacts of wind-borne debris were significant as seen in **Figure 2**.

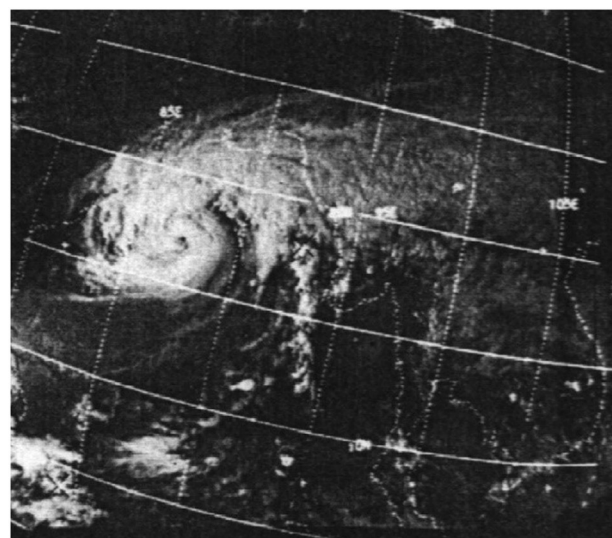


FIGURE 1 | Image of Cyclone Bhola, November 11, 1970 (NOAA, Wikipedia).



FIGURE 2 | Debris impacts, Typhoon 7513 at Hachijo Island, Tokyo, Japan.



FIGURE 3 | Tornado damage in Manikganj, Bangladesh, April 1989.¹

One of the most serious cases of damage in terms of fatalities due to tornados happened in Manikganj, Bangladesh, in April 1989 as shown in **Figure 3**. Fatalities unofficially numbered 800–1,300 (DMB, 2009). Based on the statistics of 36 years from 1961 to 1996, the total number of fatalities due to tornados and SLSs in Bangladesh were 10,766, averaging around 300 people killed every year.

Examples of typical recent damage to long-span roof structures in Japan in 2004 are shown in **Figures 4–7**. Ten typhoons made landfalls on the Japanese main islands in 2004, which was a special year, while three or fewer typhoons make landfalls annually on average.

Figure 4 shows damage to roof plates of SPring-8 in Hyogo, Japan, due to two typhoons in 2004. Bolts connecting a two-layer folded steel plate roofing system to the main frames of the building had been damaged by fatigue effects due to daily solar heating before two typhoons struck this area. The peak gusts recorded at the site during these two typhoons, Chaba and Songda, were 39 and 36 m/s, respectively. These were far below the corresponding design wind speed, which was around 60 m/s at 10 m high over open flat terrain. One side of the upper folded steel plate was engaged between the saddle and the clamp metal and crimped. The opposite side covered the end of the next upper folded steel plate on the clamp metal, and the upper folded steel plates were not fixed to prevent rain leakage and to allow the upper folded steel plates to slide along the roof span. This was expected to deal with the extension and contraction of the folded steel plate due to temperature change. This building was a special experimental facility having a 1.5-km-long perimeter and a 30-m roof span, and contained ultra-precision devices and instruments, which did not allow building deformation. The number of striations observed in the bolts closely corresponded to the number of days after building construction in 1996. This suggests the need for careful design of the building's cladding and components, as well as emergency inspections of this kind of structure and periodic inspections every 5–10 years to maintain the quality of the roof system. Structural designers are mainly concerned with structural frames and give less attention to cladding and components.



FIGURE 4 | Damage to two-layer folded steel plate roofing system of SPring-8, Riken, Hyogo, Japan, by Typhoon Chaba and Typhoon Songda, 2004 (by Kyodo: Tamura et al., 2005).

An efficient and feasible system to guarantee the performance of claddings with close collaboration between structural designers, manufacturers, and constructors should be established.

¹Rahman, M. S. (2014). *Bangladesh Disaster Preparedness Center (BDPC), Personal Communication*.

Figure 5 shows damage to a dome structure with wooden truss frames in Shimane, Japan, due to Typhoon Songda. The membrane was made of glass fibers with a Teflon coating. In order to create the beautiful V-shape waves seen in **Figure 5**, outer cables are used. However, dust had accumulated between the outer cables and membranes, and their surfaces had been continually rubbing each other due to micro-tremors by ambient excitations. As a result, the coated upper surface of the membrane had already been damaged before the typhoon event.

Figures 6 and 7 suggest a similar situation of roof cladding systems to **Figure 4** due to solar heating and resultant fatigue effects on connecting bolts and elements as well as less attention to periodic maintenance. It is especially ironical that the upstream non-engineered traditional house survived without serious damage but the steel roof sheets of the engineered downstream school gymnasium were significantly damaged, as seen in **Figure 7**. This demonstrates that the roof sheets of the gymnasium had not been sufficiently fixed to the roof frame and had no resistance to suction forces. The reason for this can be attributed to deterioration over time, including fatigue effects.

In 2005, a single-layered lattice dome coal yard in Hualien, Taiwan, collapsed during Typhoon Haitang. The open-top structure has disadvantages from both aerodynamic and structural rigidity viewpoints, and the single-layered-dome system fosters structural instability. Hurricane Katrina caused serious human and economic losses to the US due to the combined effects of wind and water hazards. It has been reported that more than 2,500 people were killed, and 108 billion USD of damage was caused (Brunkard et al., 2008; Blake et al., 2011) also in 2005. Some damage to tall buildings reported by the media strongly suggested the importance of cladding design, especially window panes and roof cover sheets. Damage to the Louisiana Super Dome also suggested poor performance checking and maintenance of a roofing system similar to those shown

in **Figures 4, 6 and 7**. More importantly, many people evacuated to this dome and were forced to spend a very uncomfortable time inside it. This devastating disaster by Hurricane Katrina also suggested the serious combined effects of wind and water hazards.

Damage to cladding and components of a building is not limited to them. The situation inside the building can become terrible, as seen in **Figure 8**, which shows damage to window panes of a tall building in Houston, TX, USA, due to Hurricane Ike in 2008. Wind and rain got into rooms and destroyed almost everything, because design of materials and systems used inside rooms of buildings basically do not consider the effects of external forces (Brewick et al., 2009). Damage to furniture, equipment, and other articles contained inside this building stopped its required functions and caused significant economic losses.

In the same year, 2008, Cyclone Nargis made landfall in Myanmar and had significant impacts on the society, as seen in **Figure 9**. Fatalities and missing numbered more than 138,000, and economic losses were estimated at 10 billion USD (Zaw, 2009). There was a shocking number of human losses and a high ratio of economic losses to Myanmar's GDP. This devastating disaster was also due to the combined effects of wind and water hazards.

Figure 10 shows collapsed roof frames of a convention center in Leyte, the Philippines, due to Typhoon Haiyan in 2013. The Severe Weather Bulletin for Typhoon Haiyan by the National Disaster Risk Reduction and Management Council estimated the maximum peak gust at 76 m/s from the lowest observed pressure. The highest maximum peak gust actually observed by PAGASA stations was 57 m/s in the City of Roxas, Capiz. Although the meteorological records at Tacloban Airport Weather Station were lost in the 7-m-high storm surge, one of the officers gave evidence that the maximum 3 s peak gust he saw was 65–69 m/s, which coincided with the wind speed estimated from bent rebars at 65–70 m/s (Sanada et al., 2015). The mechanism of collapse of the steel trussed roof beams is estimated as follows. There are many ventilating openings on the windward wall as seen in **Figure 10**. So, the internal pressure became positive due to the air flow coming into the room, and the uplift force acting on the roof increased, especially near the roof's leading edge. Combined with the high negative pressure on the roof's external surface, the lift force acting on the upstream end significantly increased. It is not clear if the designer considered this exaggerating effect on the lift force of the roof frame, but the uplift could have been more than the design estimation. Then, the roof beams at the upstream end were lifted up and dropped from the beam supports. Many evacuated people were killed in this building, which had been designated as one of the evacuation places in case of disasters, as was the Louisiana Super Dome. The fatalities and missing were reported at 7,986 (NDRRMC, 2014).

As is easily understood, some of those failures were caused by more or less human error, and provided by poor knowledge and less attention to the performance of cladding and roofing systems. The necessity for FSSSs should be realized and emphasized.

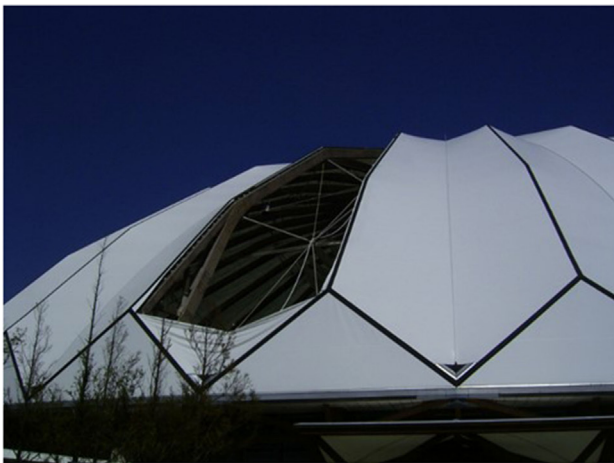


FIGURE 5 | Damage to membrane dome structure in Shimane, Japan, caused by Typhoon Songda, 2004 (Nishimura et al., 2005).



FIGURE 6 | Damage to steel roof sheets on a gymnasium in Kagawa, Japan, caused by Typhoons Dianmu, Namtheun, and Tokage, 2004 [courtesy of F. Nagao and H. Nishimura (Nishimura et al., 2005)].

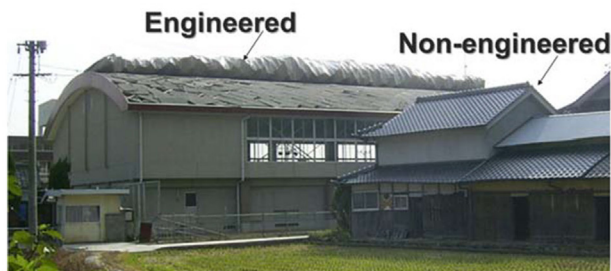


FIGURE 7 | Damage to a school gymnasium in Hiroshima, Japan, caused by Typhoon Tokage on October 20, 2004.



FIGURE 9 | Damage due to Cyclone Nargis in 2008, Ayeyarwaddy Division, Myanmar (Zaw, 2009).



FIGURE 8 | Damage to a tall building in Houston, TX, USA, due to Hurricane Ike in 2008 (Brewick et al., 2009, courtesy of A. Kareem).

PSYCHOLOGICAL IMPACT AND SOCIAL IMPACT

As already discussed, Cyclone Nargis struck Myanmar on May 2, 2008, and left more than 138,000 dead or missing. However, this devastating disaster is only remembered by a few people. On the other hand, many people remember the M_w 7.9 (USGS) Wenchuan Earthquake, which happened on May 12, 2008

in China, just 10 days after Cyclone Nargis. The Wenchuan Earthquake was also a devastating disaster and fatalities and missing numbered more than 87,000, but the disaster caused by Cyclone Nargis is as serious as or more so than that caused by the Wenchuan Earthquake.

Similar phenomena have often been observed in Japan when comparing typhoon disasters and earthquake disasters. For example, the Niigata Prefecture Chuetsu Earthquake occurred on October 23, 2004, in Japan, and fatalities and missing numbered 68, and the majority of Japanese people remember this disaster. However, almost nobody remembers a disaster that occurred 3 days prior to the Niigata Prefecture Chuetsu Earthquake. Typhoon Tokage struck the central part of Japan on October 20, 2004, and left 98 fatalities and missing. The media widely disseminated and reported the disaster scenes for 3 days after October 20, 2004. However, when the Niigata Prefecture Chuetsu Earthquake occurred, the media's interest, people's concern, and rescue by governments were all shifted and directed to the people and the area affected by the Earthquake, and people almost forgot about the disaster caused by Typhoon Tokage. In this case, the fatalities and missing resulting from Typhoon Tokage were also much larger than those resulting from the Niigata Prefecture Chuetsu Earthquake.

Why are people's reactions to tropical cyclone events and earthquake events different? One of the reasons may be attributed to the difference between the psychological impacts



FIGURE 10 | Failure of a convention center in Leyte, The Philippines, due to Typhoon Haiyan in 2013.

of these two natural hazards. Earthquakes strike suddenly without warning, thus having intense psychological impacts on us. However, tropical cyclones and their tracks can be predicted with a sufficient lead time of 5 days or so, and we know the time of a tropical cyclone strike beforehand based on more or less established early warning systems. So, we know and can understand a tropical-cyclone-induced disaster's happening, and its psychological impact is not significant. However, earthquakes come randomly and occur unexpectedly. An earthquake-induced disaster is always surprising and is too abrupt to accept. This confusion magnifies its psychological impacts. Although it is obvious that the psychological impact is not proportional to the social impact, people tend to equate psychological impact and social impact. Biased coverage by media stimulates people and governments' reactions, and this kind of misunderstanding is widely made even in local and the central governments. Thus, people tend to consider that earthquake disasters are more significant than tropical-cyclone disasters and show less consideration for their actual social impacts. This can also result in a difference between research funds for the two academic fields.

There are similar misunderstanding between tornados and tropical cyclones. As for earthquakes, tornado occurrences are rarely predicted and strike suddenly. Thus, the psychological impacts of tornado disasters are much higher than those of tropical cyclone disasters. This of course differs from country to country, but damaged areas due to tornados are very limited compared to those due to tropical cyclones. The damaged area caused by a tornado is around 0.16 km² on average in Japan (Niino et al., 1997). The average damaged area caused by a landfall typhoon in Japan is not clear, but a very rough and general estimation would be in the order of 100 km × 200 km. The annual number of tornados occurring in Japan is estimated at 26, excluding waterspouts and other SLSs (JMA Tornado Database, 2016), and 3 typhoons strikes every year. Thus, damaged areas caused by typhoons are around 15,000 times larger than those caused by tornados. The social and economic losses caused by typhoons are much higher than those caused by tornados, but the media prefer to show images and videos of funnel-shaped clouds of tornados taken by commonly used cell phones, which maximize the impressions of

viewers. Thus, people misunderstand the importance or social impacts of typhoon and tornado disasters.

REPEATED DAMAGE DUE TO NATURAL HAZARDS

It is estimated that 70–80% of natural hazard economic losses have been caused by strong wind hazards and related water hazards (Cermak, 1993; Kareem et al., 2008; Tamura, 2009; Tamura and Cao, 2011; Munich, 2015). Almost 80% of insured losses have been caused by wind storms only, and more than 90% have been caused by wind and water hazards (Munich, 2014). The majority of strong wind storms are accompanied by heavy rain and storm surges, e.g., Hurricane Katrina, 2005, in the US and Cyclone Nargis, 2008, in Myanmar, and to cope with the combined effects of such multi-hazards of wind and water is a pressing issue. Fire, snow, hail, and so on can also be strongly affected by winds, and the combined effects of those events should also be considered.

The majority of buildings damaged by strong winds are non-engineered wooden houses and low-rise steel-frame buildings. As mentioned before, the annual number of tornados in Japan is 26, while the total number of SLSs reported every year including waterspouts, downbursts and others is 64. The number of US tornados is estimated at around 1,000–1,200. However, considering the more than 20 times difference between the land areas of the two countries, the probability of tornado events in Japan is comparable with that in the US. Even so, the probability of a particular individual building encountering a tornado is very low: 40,000-year-recurrence level on average in Japan and 230,000-year-recurrence level for strong tornados such as F2 or more in the US (Tamura et al., 2008). This low probability has resulted in the fact that tornado actions are largely ignored even in design of high-risk facilities such as nuclear power plants, LNG tanks, and industrial waste disposal facilities, and also for highly important facilities such as data centers. There are piles of emerging issues to be solved related to SLSs.

In the concluding remarks in post-wind-disaster investigation reports, the following are commonly said:

- The majority of damage is to roofs and windows;
- Cladding and component damage initiate overall building damage;
- Topographic effects and debris effects are significant.

Thus, by only reading the concluding remarks, you would not be able to identify when the report was written, 1975, 1991, or 2014. The same things are repeated without any essential improvement.

These difficulties in coping with natural hazards including wind hazards result from the fact that the performance validation of buildings and structures against devastating rare events of several decades-, hundred-, or thousand-year-recurrence level have been made only by ambiguous estimation from incidentally occurring damage marks, and is like groping in the dark. The main problem is that performance evaluations done to date are inadequate.

DEMAND AND NECESSITY FOR FULL-SCALE TESTS

In order to solve those difficult problems by improving the performance of infrastructures, we need to construct a large FSSS that can contain full-scale buildings and simultaneously generate meteorological events including strong wind, fire, rain, snow, hail, and solar heating, and we need to examine the performance of cladding/components and main frames of buildings. It is not possible to make an ordinary boundary layer wind tunnel large, and new devices are required for simulating nature and typical characteristics of typhoon winds and/or tornados by using actively controlled multiple fans and/or spires such as the Insurance Institute for Business and Home Safety (IBHS) Research Center (2010) in the US and the WindEEE Dome (2013) of the Western University in Canada. We could then conduct efficient full-scale investigations under controlled conditions for saving lives and maintaining the integrity of buildings, structures, and other infrastructures from devastating meteorological hazards with recurrence periods of several decades, or hundreds, or thousands of years.

It is interesting that the University of Florida (UF) established the Storm Protection Laboratory in 1952. Since then, they have consistently been concentrating their interest on performance evaluation of houses and buildings during strong wind events. The UF was recently equipped with a Spatiotemporal Pressure Loading Actuator and a Multi-Axis Wind Load Simulator, so they can now do full-scale tests applying realistic fluctuating wind loads on mainly parts of buildings.

Pioneer works using a large-scale wind tunnel facility to investigate the performance of building parts, low-rise houses, automobiles, and so on have been made by the Jules Verne Climate Wind Tunnel at Centre Scientifique et Technique du Bâtiment in France, since 1998 (Flamand, 2015). The maximum wind speed is 80 m/s, and 200 mm/h precipitation and 200 mm/h equivalent snow fall can be supplied. Combined effects of wind, snow, rain, and solar heating can be examined in full-scale conditions.

The International Hurricane Research Center was established in 1996 in Florida International University, and they constructed

a 2-fan Wall of Wind (WOW) in 2005 and developed a 12-fan WOW in 2011, which can simulate the combined effects of wind and rain. The aim of this facility was mainly focused on full-scale tests to determine the performance of buildings.

Similar to UF, full-scale tests using PLA and reaction frames have been conducted in the “Three Little Pigs” Project by the University of Western Ontario (UWO) (Kopp et al., 2008). Realistic fluctuating external pressures obtained from scaled wind tunnel tests can be applied to full-scale buildings using multi-chamber pressure test methods.

As mentioned already, the IBHS Research Center in the US constructed a Storm Generator with 105 actively controlled fans in 2010. The test chamber is 44.2 m × 44.2 m in plan and 18.3 m high. The IBHS Storm Generator can simulate the combined effects of wind, rain, hail, and fire. The maximum wind speed is 53 m/s, corresponding to Category 3 hurricanes. Full-scale two-story wooden houses can be blown off. The proposal of FSSS and MHSP to SCJ (SCJ, 2014) owes a lot to the idea of this IBHS Storm Generator. The WindEEE Dome was established in 2013 in the UWO in Canada (Hangan, 2015). This is a very unique facility that can generate various types of flow fields including uniform straight winds, ABL winds, shear flows, downbursts, tornados, and so on, using 106 individually controlled fans. Storm systems 5 m in diameter can be generated with 2 m/s translational speed.

OUTLINE OF FSSS AND MHSP

Full-scale storm simulator proposed to SCJ (SCJ, 2014) should contain two- or three-story full-scale houses in its test chamber, because the majority of economic losses in Japan due to wind-induced damage to buildings are to such low-rise wooden houses. Combined effects of multiple meteorological hazards such as wind, rain, snow, hails, solar heating, and fire should be tested to check the integrity and performance of claddings/components and structural frames. The test chamber part is 50 m × 50 m in plan and 25 m high, and an inlet passage part and an outlet passage part are smoothly connected to the test chamber, without sudden changes in sectional shape. The maximum wind speed should be higher than 80 m/s, and the rain and snow intensity should be more than 200 mm/h. FSSS should generate different types of extreme winds such as straight typhoon winds and tornadic winds by combining active type and passive type flow generators. The most important target is ABL flows with vertical shear reproducing extreme typhoon winds. The stronger semi-circular parts of tornadic flows with translational velocity, which cause the majority of damage areas due to tornados, should also be generated. Unsteady aerodynamic effects on buildings due to a sudden increase in wind speed should also be simulated, because these effects commonly appear in SLSs. This facility is mainly designed for performance tests on buildings/structures and their parts; load evaluation is not the main focus. The wind speeds should be very high for all types of extreme winds, and the treatment and control of debris due to failure of building/structures are important. Therefore, fans or machines for generating flows should not be located downstream of models, so a push-on-type wind tunnel system should be adopted. For these

purposes, 160 actively controlled fans might be necessary, and the required electric power is estimated at 90 MW. **Figure 11** shows a schematic image of FSSS and MHSP (Tamura, 2015), and **Figure 12** shows an example of the results of a study on a passive type flow generator simulating a part of translational tornadic winds (Phuc et al., 2016).

It should also be useful for education and enlightenment activities for DRR, because those quite rare events cannot be experienced in the life-time of individuals, and it is almost impossible to make good use of the experience gained in emergencies. Therefore, FSSS is also used as the MHSP, which should be open to the public. The MHSP has functions of a hands-on-type Science Museum, Research Institute, and a Training and Education Center related to DRR activities.

ACADEMIC AND SOCIAL SIGNIFICANCE

Studies on wind-resistant design of buildings and structures have mainly focused on improving the performance of main frames, and building standards and codes contain plenty of pages of

provisions related to this, and they of course have contributed significantly to society in realizing safer and habitable tall- or super-tall buildings and long-span structures. However, wind-induced damage has been done to non-engineered buildings, for which appropriate structural design cannot be made, and human losses have been caused by damage to these kinds of buildings. In particular, the majority of wind-induced building damage has been triggered by failures of claddings and components, and it is difficult to check their performance or resistance against wind actions in wind-resistant design.

It is commonly true anywhere in the world that what we can do about extremely strong typhoons, devastating tornados, heavy snow, heavy rain and so on with a recurrence periods of several decades/hundred/thousand years is limited to observing various marks of incidentally and randomly occurring damage due to an unexpected event at any moment at any unpredicted place, under different and limited external conditions, resulting in many fatalities and huge economic and social losses. Therefore, it is almost impossible to accurately determine the physical relation of external actions and the resultant behaviors of buildings and

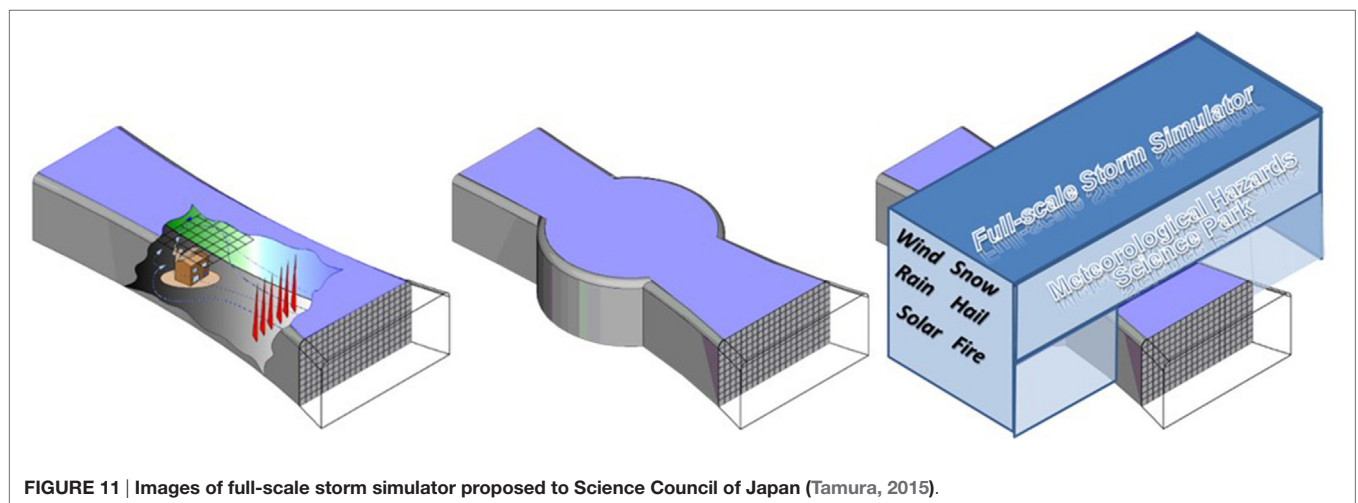


FIGURE 11 | Images of full-scale storm simulator proposed to Science Council of Japan (Tamura, 2015).

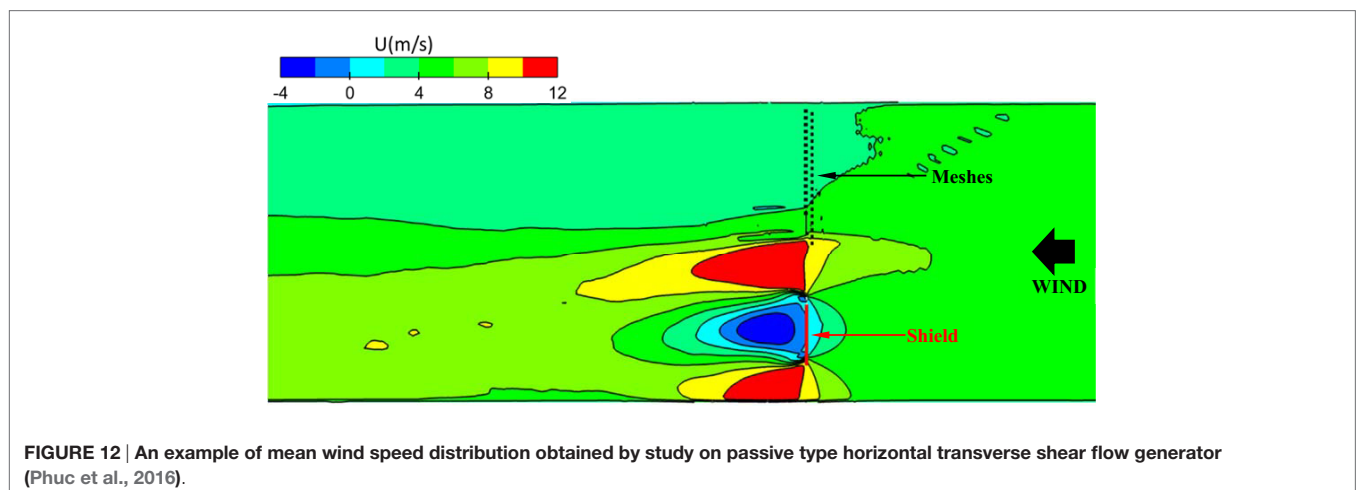


FIGURE 12 | An example of mean wind speed distribution obtained by study on passive type horizontal transverse shear flow generator (Phuc et al., 2016).

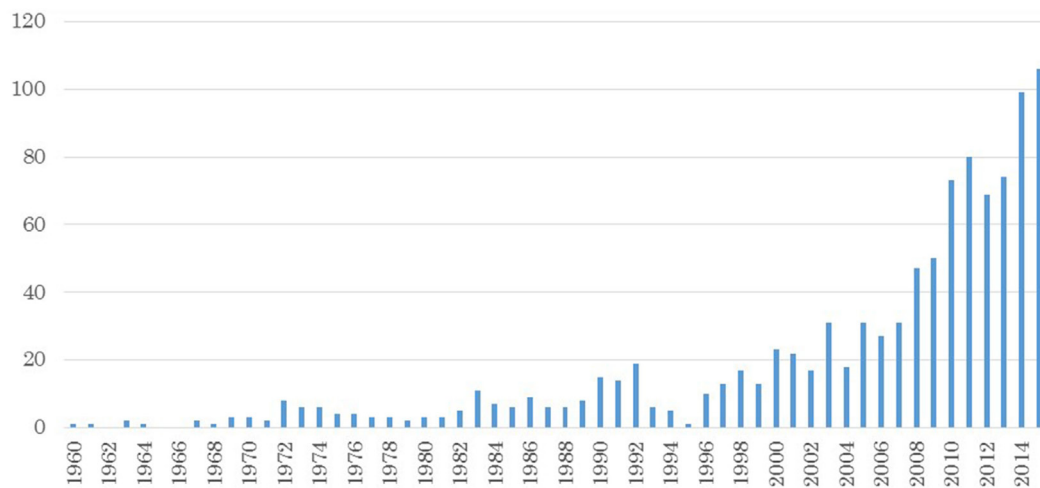


FIGURE 13 | Yearly variation of buildings 200 m or taller completed each year from 1960 to 2015 around the world (based on CTBUH, 2015).

structures. There has been little clarification of external actions of such extreme events on buildings and structures, and the failure mechanisms of building systems and similar disasters have been repeated.

For example, the recent development of wind engineering methods and technologies has significantly contributed to realization of tall and super-tall buildings or long- and super-long-span roof structures and bridges, as shown in **Figure 13** (CTBUH, 2015). However, they do not seem to have contributed to reduction in WRD risk around the world, as indicated in **Figure 14** (Munich, 2014), which clearly demonstrates the recent significant increase in the number of wind storms and floods. As is well known, strong typhoons, cyclones, and hurricanes have almost always been accompanied by heavy rain and storm surges, and wind hazards and water hazards can occur simultaneously, and the majority of devastating disasters caused by strong wind events are due to the combined effects of wind hazards and water hazards, which are expediently called “wind-related disaster” in this paper.

There are many methods for evaluating the performance of building materials and systems including pressure chambers giving repeating and fluctuating pressures on claddings and components. However, they are limited to providing specified pressures given beforehand and cannot realize the entire flow field creating the fluctuating pressure field, which essentially varies spatiotemporally and changes with the progress of the deformation of or damage to claddings, components, and partial or whole building systems. In order to check the performance of a building partially or entirely, we should follow the fracture process of the complex system of the building consisting of various materials and members including claddings, components, sub-frames, main frames, and foundations. The fracture process cannot be tested by a scaled model or numerical calculations.

The similarity laws for aerodynamic phenomena due to winds have been more or less established, and wind loading

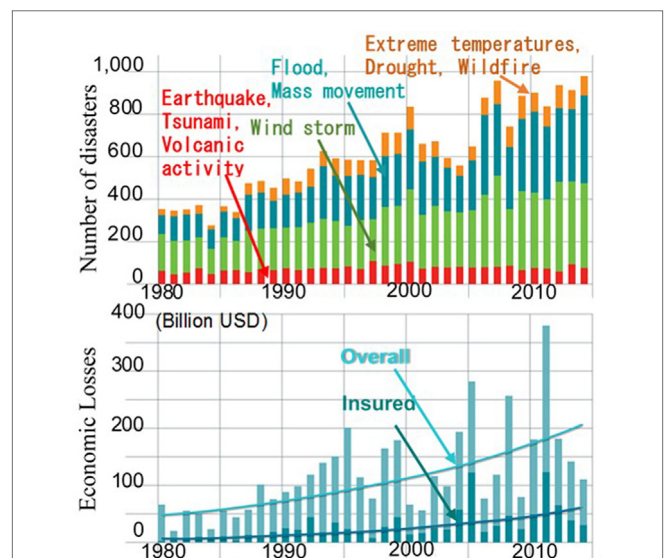


FIGURE 14 | Yearly variations of number of disasters and economic losses during 1980–2014 (Munich, 2014).

effects can be evaluated using scale models. Reynolds number effects cannot be perfectly solved, especially for structures with curved surfaces and for local peak pressures acting on roof corners. However, the majority of buildings have edged corners, and the Reynolds number effects are not so serious. However, the similarity laws are very difficult to satisfy using scale models when we consider the combined effects of two different kinds of meteorological phenomena such as wind and snow, or wind and fire, and so on. The similarity law can be satisfied for an individual phenomenon using a scale model, but it is quite difficult for two different phenomena combined, and almost impossible in many cases. Therefore, full-scale tests are required for such combined effects.

In order to overcome these difficulties, there is no other way than to conduct full-scale tests using a full-scale model. That's why a FSSS should be constructed. An FSSS can resolve the following problems that traditional wind tunnel tests using scaled models cannot achieve the following:

- Performance of entire buildings/structures and parts including fracture progress
- Combined effects of wind, snow, rain, hail, solar heating, and fire
- Reynolds number effects.

An FSSS can efficiently provide appropriate solutions for systematically controlled cladding, components, structural and building systems, construction methods, and so on, and will perform well in modeling several decades-, hundred-, or thousand-year-recurrence rare events, in a timely manner.

Consequently, we can make following paradigm shifts:

- From indirect understanding of phenomena to direct understanding;
- From a single external action to multiple external actions; and
- From load estimation to performance estimation.

Thus, a lot of break-through researches can be made over a wide range of academic fields and significant developments in relevant industries can be promised, as well as significant impacts on the DRR. Significantly improved performance of buildings and structures, power generation systems, transmission facilities, agricultural facilities, fishery facilities, and so on will have widespread effects on society, and contribute to construction of a sustainable and resilient civilian world.

Almost 45 billion USD, 27 billion USD, and 24 billion USD are lost every year in the US, China, and Japan, respectively, due to natural hazards, as shown in **Figure 15**. These losses have been accumulated year by year and have been deep

body blows to society. We should note that the hot spot of economic losses is in developed countries. If we could make a 2% reduction in economic losses by FSSS construction and efficient operation, 900 million USD, 540 million USD, and 480 million USD would be saved every year, and one or two decades accumulations would result in 9–18 billion USD, 5–11 billion USD, and 5–10 billion USD benefits to the US, China, and Japan, respectively.

This kind of facility will also have some strategic advantages by taking leadership in the following:

- Development of building materials, and structural and construction methods suitable for each country;
- Development of building materials, and suitable structural and construction methods for developing countries such as in the Asian region;
- Aid to developing countries in providing integrated network infrastructures;
- Foreign market penetration for DRR business; and
- Highest level of DRR research and education.

CONCLUDING REMARKS

Based on past discussions and the current status of natural hazards and hazard-induced disasters, difficulties in using scale models to evaluate the performance of buildings and structural systems including fracture processes of members, claddings, and components; difficulties in satisfying similarity laws for scale models in case of combined effects of multiple hazards such as wind and snow and so on; and the fact that enormous economic losses have accumulated in Japan and other countries; and so on have been recognized. Human and economic losses due to meteorological hazards have been significant. The hot spots of human losses are in developing countries such as South Asia, but the hot spots of economic losses are in developed countries such as the US, Japan, and China. Recently, the number of devastating

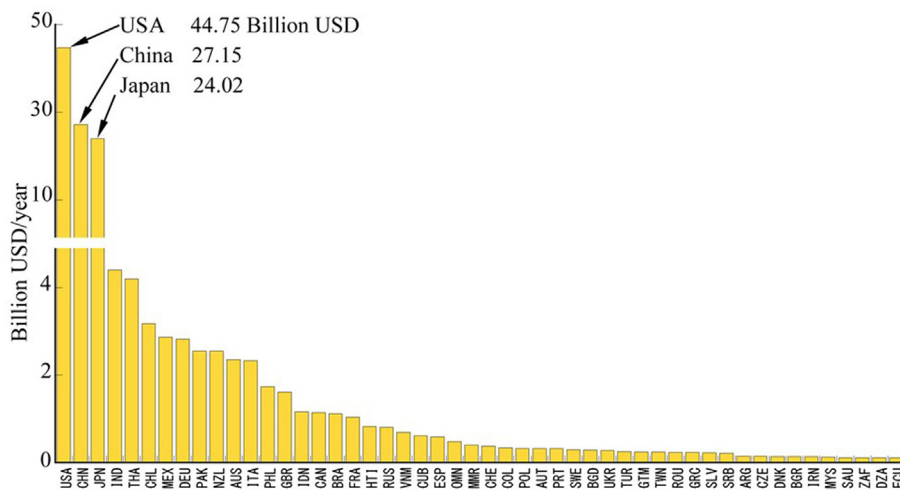


FIGURE 15 | Annual economic losses in each country due to all natural hazards from 2005 to 2014 (CRED, 2015).

disasters due to meteorological hazards has been increasing because of rapid urbanization or other reasons.

It has been demonstrated that full-scale test facilities such as FSSS and MHSP to check the performance of buildings and structures are required to minimize the effects of disasters due to natural hazards.

Incidentally, the fire insurance premium rate (FIPR) in Japan has increased by 2–4% since October 2015. The main reason for this increase is the recent significant increase in insurance payments due to increase in the effects of disasters induced by wind storms including explosive low-pressure systems, strong typhoons, tornados, and so on. The increase in FIPR may solve the economic concerns of insurance companies, but it cannot solve the social problems of the huge accumulating economic losses and strongly hypothesized future amplification of this increasing trend due to climate change effects.

Thus, there is a strong need for full-scale facilities, and they should have the highest priority from the viewpoint of national resilience policies of governments in the Asian region.

REFERENCES

- Blake, E. S., Landsea, C. W., and Gibney, E. J. (2011). *The Deadliest, Costliest, and Most Intensive United States Tropical Cyclones from 1851 to 2010 (and Other Frequently Requested Hurricane Facts)*. NOAA Technical Memorandum NWS NHC-6.
- Brewick, P., Divil, L., Butler, K., Bashor, R., and Kareem, A. (2009). "Consequences of urban aerodynamics and debris impact in extreme wind events," in *Proceedings of the 11th Americas Conference on Wind Engineering, San Juan, Puerto Rico, June 22–26, 2009*. p. 17.
- Brunkard, J., Namulanda, G., and Ratard, R. (2008). Hurricane Katrina deaths, Louisiana, 2005. *Disaster Med. Public Health Prep.* 2, 215–223. doi:10.1097/DMP.0b013e31818aaf55
- Cermak, J. E. (1993). *Wind Engineering – Engineering for Wind Damage Mitigation, ASCE Structures Congress '93*. Irvine, CA: Structural Engineering in Natural Hazards Mitigation, 37–58.
- CRED. (2015). *Centre for Research on the Epidemiology of Disasters*. Available at: <http://www.cred.be/>
- CTBUH. (2015). *CTBUH Year in Review: Tall Trends of 2015, and Forecasts for 2016*. The Council on Tall Buildings and Urban Habitat.
- DMB. (2009). *Governance and Policy Making in the Context of Disaster Management, Disaster Management Bureau, Ministry of Food and Disaster Management, Government of the People's Republic of Bangladesh, Bangladesh Disaster Preparedness Center, Proceedings of the International Forum on Tornado Risk Reduction for Bangladesh – To Cope with Neglected Severe Disasters – December*. Dhaka, Bangladesh: 13–14.
- Flamand, O. (2015). *Simulating Climate in Wind Tunnel: Why Do It at Full Scale? IAWE Public Forum "Necessity and Efficiency of Large-Scale Facilities for Wind-Related Disaster Risk Reduction", The 3rd UN World Conference on Disaster Risk Reduction*. Sendai, Japan.
- Hangan, H. (2015). *Reducing Vulnerability to Non-Synoptic Winds. The WindEEE Dome, IAWE Public Forum "Necessity and Efficiency of Large-Scale Facilities for Wind-Related Disaster Risk Reduction", The 3rd UN World Conference on Disaster Risk Reduction*. Sendai, Japan.
- JMA Tornado Database. (2016). *Japan Meteorological Agency*. Available at: <http://www.data.jma.go.jp/obd/stats/data/bosai/tornado/>
- Kareem, A., Kijewski-Correa, T., Tamura, Y., and Modeling, N. (2008). *Next Frontiers of Innovation, Discovery and Learning in Wind Engineering: A Cyberinfrastructure Perspective, The 3rd International Symposium on Wind Effects on Buildings and Urban Environment (ISWE3)*. Tokyo, Japan: The 21st Century COE Program, 1–17.
- Kopp, G. A., Morrison, M. J., Gavanski, E., Henderson, D. J., and Hong, H. P. (2008). *The "Three Little Pigs" Project: Integration of Wind Tunnel Model Scale*

AUTHOR CONTRIBUTIONS

YT: principal author, review, data collection, and discussions (70%). KN and MM: data collection and discussions (8%). PP: flow simulation and discussions (8%). QY: discussions (6%).

ACKNOWLEDGMENTS

Useful discussions were made by Prof. Yuji Hasemi from Waseda University, Profs. Yasushi Uematsu and Akashi Mochida from Tohoku University, Dr. Naoki Sakai from National Research Institute for Earth Science and Disaster resilience, and members of AIJ and JAWC Joint WG on Full-scale Storm Simulator. They are gratefully acknowledged.

FUNDING

This study is supported in part by the 1000 Talent Plan Program for Foreign Experts, China.

Tests and Full-Scale Laboratory Tests, The 3rd International Symposium on Wind Effects on Buildings and Urban Environment (ISWE3) – New Frontiers in Wind Engineering. Tokyo, Japan.

Munich, R. (2014). *Munich Re Group, Topics Geo 2014*. Munich, Germany: Munich Re Group.

Munich, R. (2015). *Munich Re Group, Topics, Annual Review*. Munich, Germany: Natural Catastrophes.

NDRRMC. (2014). *National Disaster Risk Reduction and Management Council. SitRep No. 92 Effects of Typhoon Yolanda, Haiyan*.

Niino, H., Fujitani, T., and Watanabe, N. (1997). A statistical study of tornadoes and waterspouts in Japan from 1961 to 1993. *J. Clim.* 10, 1730–1752. doi:10.1175/1520-0442(1997)010<1730:ASSOTA>2.0.CO;2

Nishimura, H., Okuda, Y., and Tamura, Y. (2005). *High Wind Damage to Buildings in Japan by Typhoons in 2004, Proceedings of the 6th Asia-Pacific Conference on Wind Engineering*. Seoul, Korea: 2935–2944.

Phuc, P. V., Kikuchi, H., Maruyama, T., Matsui, M., and Tamura, Y. (2016). *A Numerical Study on a Generation System of Tornado Flow Field Using a Boundary Layer Wind Tunnel, Summaries of Technical Papers of Annual Meeting, Architectural Institute of Japan, Structures I, 20070*. 139–140.

SCJ. (2014). *Recommendations: The Academic Master Plans 2014 of Large Research Facilities and Large Research Projects, Subcommittee on Evaluation of Academic Large Research Projects, Scientists Committee*. Japan: Science Council of Japan.

Sanada, Y., Tamura, Y., Narafu, T., Shimizu, T., and Mita, N. (2015). Damage to building structures in Philippines due to Typhoon Haiyan. *J. Wind Eng.* 40, 30–39. doi:10.5359/jwe.40.30

Tamura, Y. (2009). *Wind-Induced Damage to Buildings and Disaster Risk Reduction, Proceedings of the 7th Asia-Pacific Conference on Wind Engineering*. Taipei, Taiwan.

Tamura, Y. (2015). *IAWE Public Forum "Necessity and Efficiency of Large-Scale Facilities for Wind-Related Disaster Risk Reduction", The 3rd UN World Conference on Disaster Risk Reduction*. Sendai, Japan.

Tamura, Y., and Cao, S. Y. (2011). *International Group for Wind-Related Disaster Risk Reduction (IG-WRRR), Proceedings of the 13th International Conference on Wind Engineering*. Amsterdam, Netherlands: 8.

Tamura, Y., Niino, H., Suzuki, O., Maki, M., Maeda, J., Matsumoto, M., et al. (2008). *Research Report: Characteristics and Prediction of Tornadoes and Countermeasures (PI: Tamura, Y.), Promotion of Swift Administrative Response for Important Policy Issues, 2007FY Special Coordination Funds for the Promotion of Science and Technology*. Japan Science and Technology Agency, 486.

Tamura, Y., Kobayashi, F., Suzuki, O., Uematsu, Y., and Okuda, Y. (2012). "Air chapter 3: typhoon and tornado risk management," in *Environmental Disaster*

- Linkages, Community, Environment and Disaster Risk Management*, Vol. 9, eds R.Shaw and P.Tran (Emerald Group), 35–60.
- Tamura, Y., Ohkuma, K., Sakamoto, I., Yagi, K., Okuda, Y., Ohno, H., et al. (2005). *Lessons from Wind-Induced Damage to a Long-Span Steel Roof Due to Two Typhoons in 2004, Proceedings of the 6th Asia-Pacific Conference on Wind Engineering*. Seoul, Korea: 2907–2916.
- Zaw, W. (2009). *Cyclone Nargis in Myanmar, May 2, 2008, Proceedings of the Cooperative Actions for Disaster Risk Reduction (CADRR), The 4th International Symposium on Wind Effects on Buildings and Urban Environment (ISWE4)*. Tokyo: UN University.

Conflict of Interest Statement: The authors declare that the research was conducted in the absence of any commercial or financial relationships that could be construed as a potential conflict of interest.

Copyright © 2017 Tamura, Nishijima, Matsui, Phuc and Yang. This is an open-access article distributed under the terms of the Creative Commons Attribution License (CC BY). The use, distribution or reproduction in other forums is permitted, provided the original author(s) or licensor are credited and that the original publication in this journal is cited, in accordance with accepted academic practice. No use, distribution or reproduction is permitted which does not comply with these terms.



An Examination of Static Pressure and Duration Effects on Tornado-Induced Peak Pressures on a Low-Rise Building

Fred L. Haan Jr.*

Engineering Department, Calvin College, Grand Rapids, MI, USA

OPEN ACCESS

Edited by:

Gregory Alan Kopp,
University of Western
Ontario, Canada

Reviewed by:

Ilaria Venanzi,
University of Perugia, Italy
Aly Mousaad Aly,
Louisiana State University, USA

*Correspondence:

Fred L. Haan Jr.
fhaan@calvin.edu

Specialty section:

This article was submitted to Wind
Engineering and Science,
a section of the journal
Frontiers in Built Environment

Received: 17 October 2016

Accepted: 17 March 2017

Published: 05 April 2017

Citation:

Haan FL Jr. (2017) An Examination of
Static Pressure and Duration Effects
on Tornado-Induced Peak Pressures
on a Low-Rise Building.
Front. Built Environ. 3:20.
doi: 10.3389/fbuil.2017.00020

This study investigated the role of duration and tornado-induced static pressure on peak pressures on a low-rise building. A tornado simulator was used to generate both translating and stationary vortices to measure pressure time series on a building model. Time-resolved velocity measurements were also made on the vortex to aid in the analysis. Past studies have suggested that peak pressures on buildings in tornadoes were up to 50% higher than straight-line atmospheric boundary layer values as provided by ASCE 7–10. This study showed that much but not all of this increase can be explained by the static pressure of the vortex. While subtracting the static pressure from pressure time series and normalizing by a local horizontal velocity brought peak pressures closer to what one would expect from straight-line flows, and these data showed that some peaks could still be significantly larger than ASCE 7–10 provisions. To consider duration effects, translating and stationary vortex data were used with varying exposure times. Results showed that peak pressure magnitudes could increase by factors of 1.1–1.4 depending on duration. Work like this could lead to factors to adjust tornado pressure coefficients for the effect of event duration. The largest pressure peaks were observed to occur in or near the vortex core, and profiles of vertical velocity and static pressure suggest that strong unsteady vertical gusting and strong static pressure fluctuations could play a role in creating these large peaks.

Keywords: tornado, low-rise building, non-synoptic winds, tornado simulator, experimental aerodynamics

INTRODUCTION

This study constitutes a continuation of the work reported in Haan et al. (2010) where the Iowa State University (ISU) tornado simulator was used to measure tornado-induced pressures on a low-rise building model. The specific goal of this work was to examine how peak pressures induced by a tornado vortex depend on the static pressure induced by the vortex and on the amount of time it takes for a vortex to pass over a building (duration effect). Tornado-induced pressures on low-rise buildings have been studied by several researchers over the years. Chang (1971) and Jischke and Light (1983) were among the first to employ laboratory tornado simulators with building models to assess loading on buildings. Mishra et al. (2008) found significant differences in the character of the loading between straight-line boundary layer tests and tornado simulator tests. Haan et al. (2010) reported tornado-induced roof pressure coefficients that were 50–60% larger than ASCE 7

provisions. Integrated uplift loads were also reported and had values that were two to three times that predicted with ASCE 7 provisions. The large difference between those vertical loads and ASCE 7 are part of the motivation for the present work.

Kikitsu et al. (2011) examined the role of internal pressure along with external pressure. They reported that the total uplift loading on a building can be reduced significantly depending on the size and orientation of holes in the building envelope. More recently, Sabareesh et al. (2013a,b) has used a tornado simulator to examine pressures on low-rise buildings with respect to ground roughness. Ground roughness was found to increase both internal and external pressures. Although internal pressure plays an important role in tornado-induced loading, this study's focus was on identifying the behavior of external pressures induced by tornado vortices.

While the ISU simulator was the largest of its kind when built, the future of research on tornado-induced loading includes even larger facilities and the promise of investigations at larger Reynolds numbers. The VorTECH facility at Texas Tech and the WinDEEE Dome at the University of Western Ontario (Refan and Hangan, 2016) can simulate higher speed flows with larger diameters than the ISU simulator.

Recent field research has also aided the study of tornado-induced loading. Kosiba and Wurman (2013) reported tornado boundary layer profiles that showed the highest velocity near the ground. Velocities at 4 m above ground level were 10–30% greater than those at 10 m. Data from a vehicle-mounted anemometer (Wurman et al., 2013) also showed velocities at 3.5 m above the ground to be greater than those aloft. These general trends are

consistent with velocity measurements in the ISU simulator (Fleming et al., 2013) and lend credibility to simulator testing. Unfortunately, field data acquisition has not yet captured the turbulent flow quantities necessary to make precise estimates of aerodynamic loading. Tornado simulator velocity measurements and pressure measurement are still the only means for doing so.

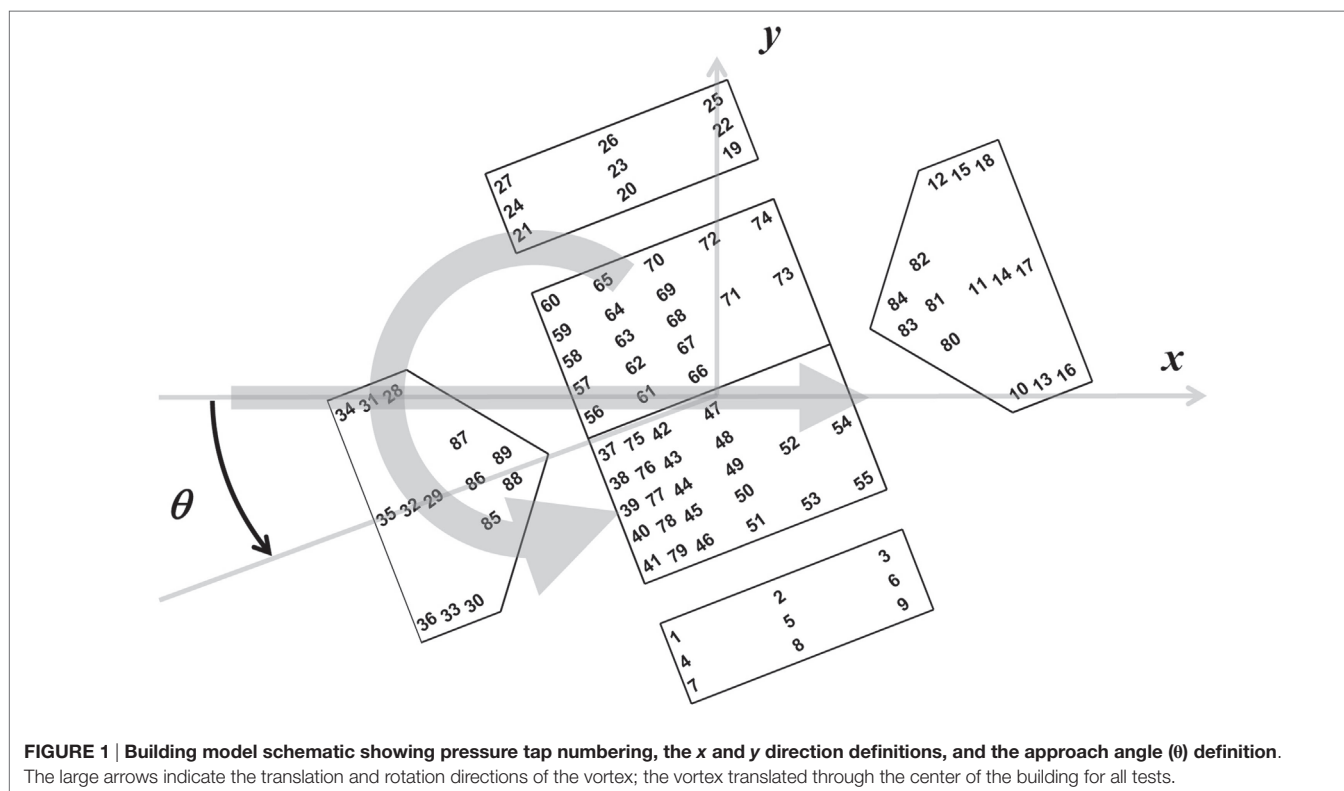
As stated above, this project is a continuation of previous work. Since that previous work, time-resolved velocity measurements have been made with the translating vortex and a data set for building pressures in the presence of a stationary tornado have been acquired. This paper uses both of these data sets to unpack the effects of static pressure and of duration.

EXPERIMENTAL AND ANALYTICAL APPROACH

The experimental approach involved use of the tornado/microburst simulator at ISU. This section will describe the wind facility, the gable roof model used in these tests, the test conditions included in this analysis, and the analytical approach for identifying peak pressure coefficients. It should be noted that the focus of this study was on external pressures. While internal pressures play an important role in tornado-induced loading, external pressures were the topic of this study.

Tornado Simulator Facility

Iowa State University houses a tornado simulator that was conceived and built for testing model structures in tornado-like



vortex flows. The facility consists of a 1.8 m diameter fan surrounded by a 5.5 m diameter annular duct. The fan is fixed in the middle of the facility and draws air upward. This upward flow is redirected back downward through the annular duct. The downward flow is given rotation with adjustable guide vanes. The rotating inflow forms a vortex beneath the fan near the updraft. This vortex-generation mechanism is qualitatively similar to that of full-scale tornadoes. The fan and duct system is mounted on an overhead crane to allow the vortex to translate past models that are mounted on a ground plane beneath the system. Further details of the facility development are described in Haan et al. (2008).

Gable Roof Building Model

The building model used in these tests was fabricated of acrylic and had plan dimensions (W) of 91 mm \times 91 mm. The eave height was 36 mm with a maximum roof height (H) of 66 mm. The gable roof angle was 35°. The model is the same as that used by Haan et al. (2010) and was fitted with 89 pressure taps. These taps were connected by plastic tubing to an electronic pressure scanner and a PC. All signals were corrected for the dynamic effects of the tubing.

Figure 1 shows the numbering system for the pressure taps on the building as well as the coordinate system. All vortices rotate counter-clockwise and travel from the negative to positive x -direction approaching the building model at an angle, θ , as indicated.

Test Conditions

A single, low-swirl vortex was used for these tests (referred to as a Vane1 vortex in Haan et al., 2010). Pressures were acquired on the building with the vortex translating and stationary. **Table 1** summarizes the test parameters, and the schematic diagram in **Figure 2** defines notation and shows the arrangement of the measurement position relative to the tornado vortex.

Velocity measurements on this vortex were performed using a TFI Cobra probe located at the same measurement position as the model but with the model absent. The velocity measurements were conducted when the vortex was translating and when it was stationary. For the translating cases, five time series were acquired for each direction of the probe (because the probe can only

acquire data within a 45° cone of acceptance, tests were run with the probe facing one way and then repeated with the probe turned around 180°). These time series were broken into 0.1-s segments. Within each segment, an average value and a peak value were computed. The nomenclature chosen for these two values was $V_{H_{avg}}^t$ and $V_{H_{peak}}^t$, respectively. The superscript t was used to denote the “translating” case, and the subscript H denotes horizontal velocity (the vector sum of the tangential and radial components of the vortex—denoted as V_θ and V_r , respectively, in **Figure 2**). The velocity data for both stationary and translating vortices are presented in **Figure 3** as a function of position (x) with respect to the center of the vortex core. The x positions are normalized by the radius of the vortex core, R_c (see **Table 1**). The stationary data in **Figure 3** (denoted by the superscript s) were found from 48 s of data at each x/R_c location. Each 48-s data set was divided into 1-s segments in which peak velocities were found. The data in **Figure 3** represent the median of the resulting 48 peak values. More details on these velocity measurements can be found in Fleming et al.’s study (Fleming et al., 2013).

Values of $V_{H_{avg}}^t$ ranged from 4 to 10 m/s and were used (along with the building height) to estimate the Reynolds numbers of the building model tests. In this project, the Re values ranged from 1.8×10^4 away from the core to 4.4×10^4 at the core radius. It has conventionally been assumed that sharp-edged bluff body flows are relatively independent of Re effects for Re greater than $\sim 3 \times 10^4$.

The pressure and velocity tests considered in this paper involved vortex translation speeds from 0.15 to 0.61 m/s, and the pressure tests considered a single building orientation of 0° with respect to the vortex translation direction (see **Figure 1** for angle definition). For translating cases, 10 passes of the vortex past the building were used to acquire pressure data. For stationary cases, 48 s of pressure data were acquired for a range of vortex distances from the building center ($x = 0.4R_c - 2.4R_c$). The analytical approach for obtaining peak pressure coefficients is described in the next section. It should also be noted that velocity measurements using the Cobra probe were conducted separately from the pressure measurements on the building. The measurements were not simultaneous.

TABLE 1 | Summary of parameters of the tornado-like vortex used in this study.

Parameter	Value
Vortex type	Low-swirl, single cell
$[V_{H_{avg}}^t]_{max}$	9.6 m/s
Swirl ratio	0.1
R_c	0.22 m
Re	$1.8\text{--}4.4 \times 10^4$
$2R_c/W$	4.8
Vortex translation speeds	0.15–0.61 m/s
Turbulence intensity at building height	28%

R_c is the radius of the vortex at the location of maximum tangential wind speed, Re is the Reynolds number based on building height, and $2R_c/W$ is the ratio of the vortex diameter to the building plan dimension.

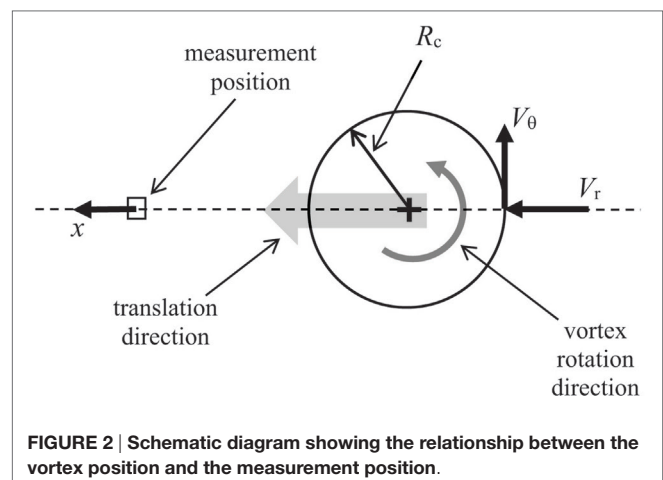


FIGURE 2 | Schematic diagram showing the relationship between the vortex position and the measurement position.

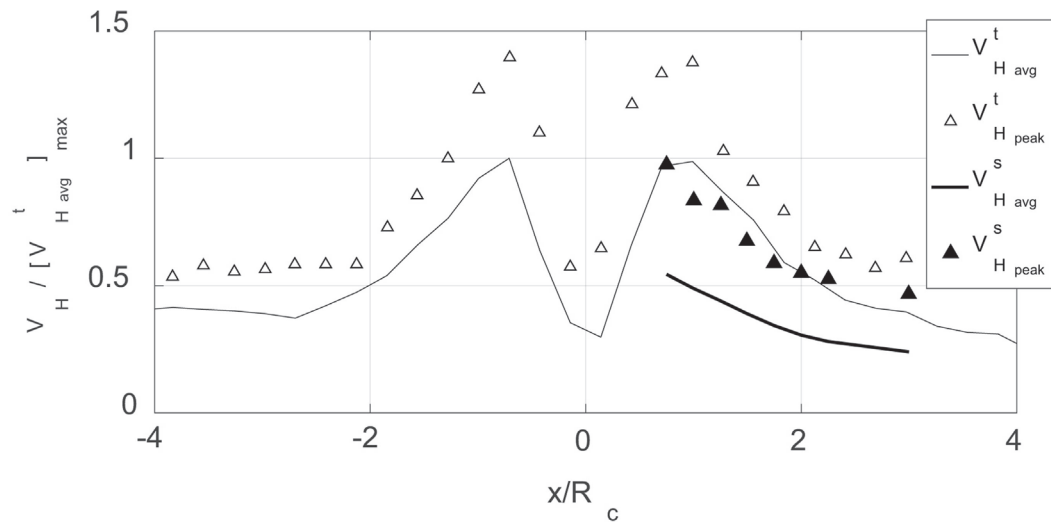


FIGURE 3 | Horizontal velocity measurements for a translating and a stationary vortex. The lines represent local average velocities while the symbols are local peak velocities.

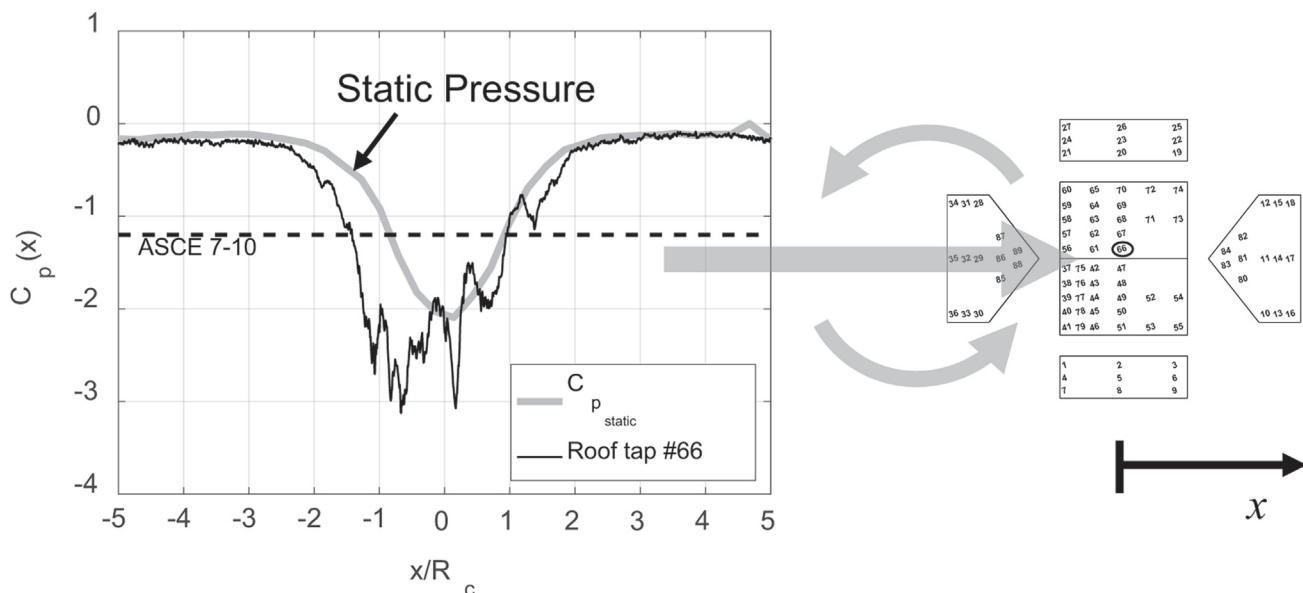


FIGURE 4 | Example time series from a roof pressure tap (#66) as the vortex passes the building as well as the static pressure generated by the vortex. Pressure tap #66 is circled on the building model. The large arrows indicate the direction of translation and rotation of the vortex. Note that both pressure coefficients were computed using a dynamic pressure based on $[V_{H_{avg}}^t]_{max}$.

Analytical Details on Peak Pressure Estimation

Figure 4 shows a single, illustrative pressure time series from roof tap #66 on the building model. This plot is a time series even though the horizontal axis has been transformed to show position of the vortex with respect to the center of the building. The figure also shows the vortex-induced static pressure ($C_{p_{static}}(x)$), the building orientation, and the rotation direction of the vortex. One method of finding peak pressure coefficients is to find the peak negative pressures from 10 of these time series,

find the median of those peak negative pressures, and report the peak C_p using a dynamic pressure based on the maximum average horizontal velocity, $[V_{H_{avg}}^t]_{max}$, as shown in Eq. 1 below:

$$C_{p_{peak}} = \frac{(p - p_{ref})_{peak}}{\frac{1}{2} \rho [V_{H_{avg}}^t]_{max}^2} \quad (1)$$

where ρ is air density, p is pressure measured at the pressure tap on the building, and p_{ref} is the laboratory pressure far outside the vortex (the reference pressure). Using this method, tap #66

experiences $C_{p_{\text{peak}}}$ values of around -3.1 . This is significantly higher than the ASCE 7–10 pressure coefficient of -1.2 for this location on the roof (ASCE, 2010). This approach to finding the peak is similar to that of Haan et al.'s study (Haan et al., 2010).

In the present study, a new approach was employed to determine the degree to which this large peak value comes from the vortex-induced static pressure in the core or from transient effects of the vortex passing. The intent was to strip away the static pressure and normalize the pressure to account for the transient velocity and see whether what remains could be considered equivalent to straight-line flow.

To implement this approach, the static pressure (as shown in **Figure 4**) was subtracted from the pressure signal to eliminate its role in generating large peaks. Also, the pressure peaks were normalized by a local velocity (following the velocity profile of **Figure 3** rather than the maximum average velocity used in Eq. 1) to determine whether the vortex flow field itself plays a role in the large peaks. This approach can be formulated as shown in Eq. 2 below if one normalizes using the peak velocity:

$$C_{p_{\text{peak}}}(x) = \frac{(p(x) - p_{\text{ref}})_{\text{peak}}}{\frac{1}{2}\rho[V_{H_{\text{peak}}}^t(x)]^2} - \frac{p_{\text{static}}(x) - p_{\text{ref}}}{\frac{1}{2}\rho[V_{H_{\text{peak}}}^t(x)]^2} \quad (2)$$

$$= \frac{(p(x) - p_{\text{ref}})_{\text{peak}}}{\frac{1}{2}\rho[V_{H_{\text{peak}}}^t(x)]^2} - C_{p_{\text{static}}}(x)$$

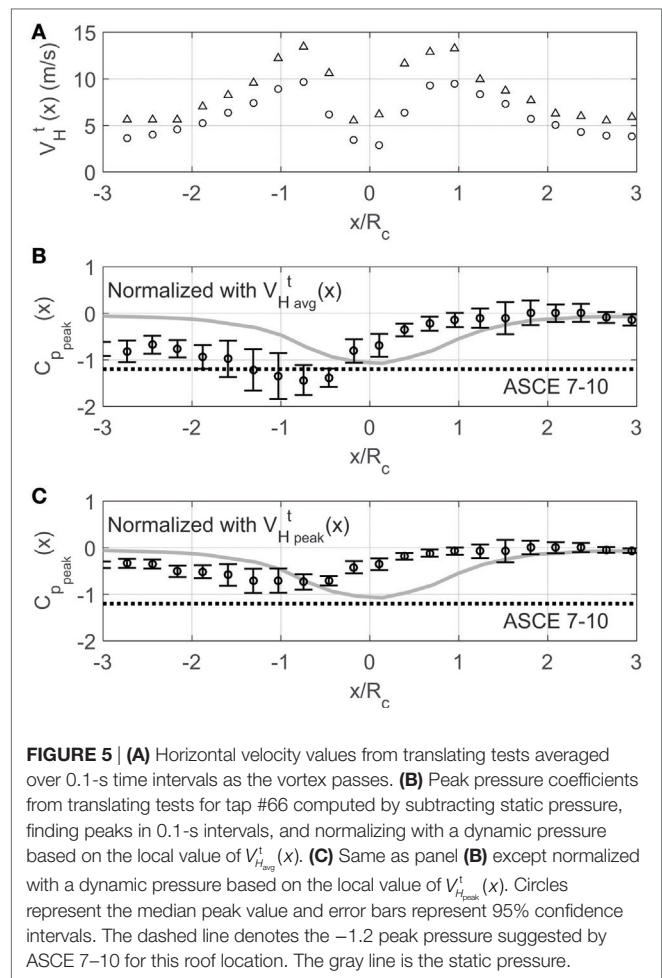
where $(p(x) - p_{\text{ref}})_{\text{peak}}$ is the peak pressure as a function of x computed over each of the 0.1-s time segments described in Section "Test Conditions." $p_{\text{static}}(x) - p_{\text{ref}}$ is the static pressure induced by the vortex and measured by averaging together all 89 building pressure taps for each time step. This vortex-induced static pressure was also measured using floor taps with the building absent and using the Cobra probe with the building absent. All three methods produced the same static pressure curve.

RESULTS AND DISCUSSION

Peak Pressures from Adjusted Pressure Signals

Adjusting the pressure signals as represented by Eq. 2 produces the $C_{p_{\text{peak}}}(x)$ profiles presented in **Figure 5**. This figure shows peak pressure profiles made using both $V_{H_{\text{avg}}}^t(x)$ and $V_{H_{\text{peak}}}^t(x)$ values and a line indicating the peak pressure provision of ASCE 7–10 for this roof location. Given the transient nature of the tornado, it is not clear which velocity would make for a more appropriate comparison with ASCE 7–10. Normalizing with local peak pressures brought the $C_{p_{\text{peak}}}(x)$ profile within the standard provisions. Further results in this study were all normalized with local peak velocity.

At the edge of the core and just outside it, peak pressures are greatest as are the confidence intervals for those peak pressures. A flat trend here would suggest that the aerodynamics outside the core might be fundamentally similar to straight-line flow if we simply account for the horizontal velocity being a function of



distance from the core. Since the $C_{p_{\text{peak}}}(x)$ values do not follow a flat trend, the idea that we have basically straight-line flow along with a static pressure adjustment appears too simplistic.

It should be noted that within the core, $C_{p_{\text{peak}}}(x)$ values produced by Eq. 2 would grow very large because the horizontal velocity decreases greatly there. Rather than artificially inflating pressure coefficients there, $C_{p_{\text{peak}}}(x)$ values for $-1 < x/R_c < 1$ were normalized using the maximum value of $V_{H_{\text{peak}}}^t(x)$.

Duration Effects

Two different approaches were used to study duration effects. Comparing pressure peaks from stationary vortex events and from translating vortex events were the first method used to study the role of event duration in pressure peak generation. A set of data was acquired for a stationary vortex at various positions relative to the building. Since the translation speed of the tests included in this study were the fastest possible with the ISU simulator, the translating and stationary data sets presented here represent the shortest and longest durations that could be studied.

Figure 6 shows $C_{p_{\text{peak}}}(x)$ profiles for tap 66 from these translating and stationary vortex tests. The stationary test coefficients were all computed by subtracting static pressure, finding peaks in 1.0-s intervals, and normalizing with a dynamic pressure based on the same local value of $V_{H_{\text{peak}}}^t(x)$ used to normalize the translating

data (using the maximum value of $V_{H_{peak}}^i(x)$ for locations inside the core as described in Section “Peak Pressures from Adjusted Pressure Signals”).

The stationary vortex peaks were significantly larger than the translating vortex peaks suggesting that a vortex that spends more time on a given building would generate larger peak pressures. The largest stationary vortex peaks have magnitudes 45% larger than the translating vortex peaks. Test results like this using stationary vortices might represent an envelope for the peak pressures one can expect on a building, that is, in the worst case, when the vortex sits on a building without moving at all. To obtain a true envelope for such pressures; however, more parameters would need to be considered. For example, the diameter of the vortex in this case is about five times the building plan dimension. Testing how this ratio affects peak pressures would also need to be done.

The second method of studying event duration was to observe changes in peak pressures as a function of vortex translation speed. This was done somewhat in Haan et al.’s study (Haan et al., 2010), but here it is done in a different form. In this study, a comparison was made between peaks found from stationary vortex pressure time series divided into segments of various lengths (to simulate various durations) and peaks from translating vortex pressure time series where the durations occur naturally given the transient nature of the tests.

For the translating vortex cases, the duration of the vortex event was estimated as the time that a point on the building is exposed to the vortex core, that is, the time it takes the vortex to translate past a single point. The duration, τ , then was estimated as follows in Eq. 3:

$$\tau = \frac{2R_c}{V_t} \quad (3)$$

where V_t is the vortex translation speed. With this study’s translation speeds of 0.15–0.61 m/s, this resulted in duration values from 0.7 to 2.9 s. Each translation speed was tested 10 times, peak C_p values were found for each of these 10 trials. A median peak value was found for the 10 trials for each translation speed.

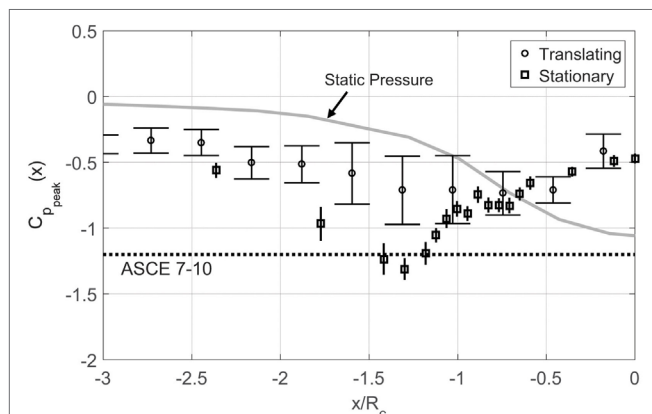


FIGURE 6 | Peak pressure coefficients for tap #66 from translating test (as in Figure 7) and also from stationary vortex tests. Error bars are 95% confidence intervals. The dashed line denotes the -1.2 peak pressure suggested by ASCE 7–10 for this roof location.

For the stationary vortex cases, data were divided in a manner similar to that employed by Kopp and Morrison (2011). The 48 s of each stationary vortex time series was divided into segments as long as 10 s and as short as 0.1 s. Given the nature of turbulent flow pressure fluctuations, the longer time segments should result in larger peak pressures. The peak C_p was obtained for each segment and the median C_p was found for the entire 48 s time series.

All the peak values from various segment lengths (for both stationary and translating cases) were then normalized with the median C_p of the entire 48 s. stationary vortex time series. The resulting peak to median ratio for tap 66 is plotted as a function of duration in Figure 7. The data show that as duration increases, the peak to median ratio increases as well. In the next section, peak/median ratios are presented for all the pressure taps, and overall trends with respect to duration are discussed.

All Pressure Taps

The analyses already presented for tap 66 were also conducted for all 89 taps on the building model. To present these results in a concise manner, the pressure taps were organized according

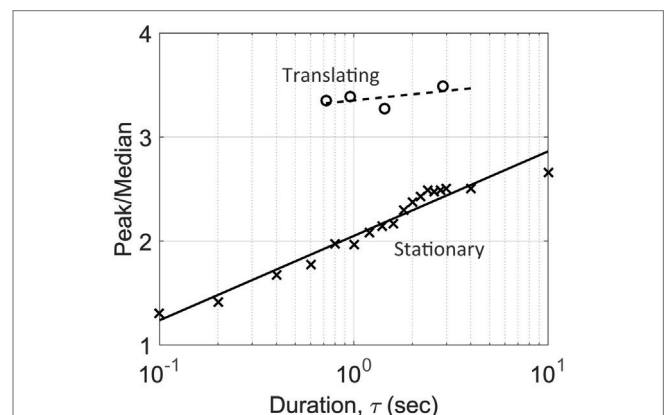


FIGURE 7 | Ratio of peak C_p to median C_p as a function of event duration, τ , for translating and stationary vortex tests on pressure tap #66.

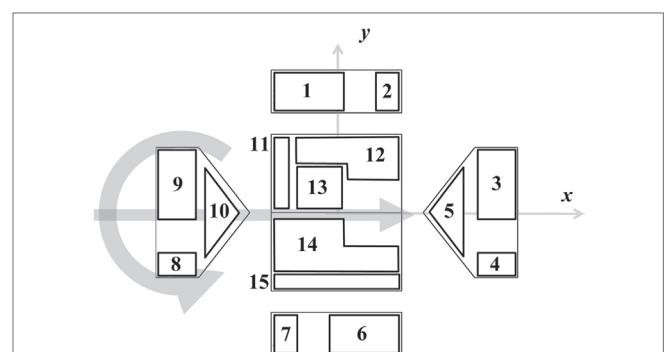


FIGURE 8 | Pressure tap zone definitions for organizing the pressure taps shown in Figure 3. These zones are used for presenting the results of peak C_p and duration analysis in Figures 9 and 10.

to zones as shown in **Figure 8**. These zones were chosen based on similarity of pressure peak behavior. **Figure 9** shows envelope curves for $C_{p_{peak}}(x)$ values for all the building's pressure taps. To generate these envelope curves, the plots shown in **Figure 6** were made for all the pressure taps in a given zone. The envelope

curves represent the upper and lower bounds of all the 95% confidence intervals of those pressure taps. As was the case with tap 66, the stationary vortex peak values have larger magnitudes than the translating vortex values. An important thing to note is that the stationary data were not acquired for the entire positive

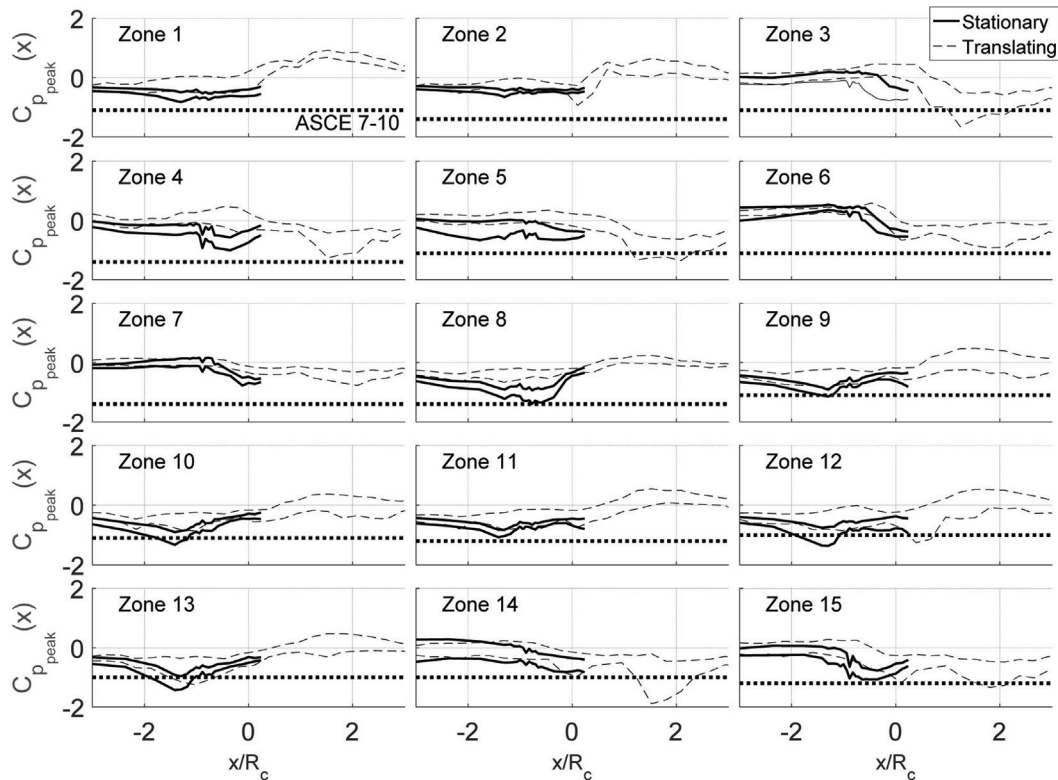


FIGURE 9 | Envelope curves for $C_{p_{peak}}(x)$ values for all pressure taps for both stationary and translating vortex tests. Zones correspond to the definitions in **Figure 8**. ASCE 7–10 provisions are provided for each zone. Note: these zones do not coincide with ASCE 7–10 zones. The lines shown here represent the smallest magnitude ASCE 7 value for any tap in the zone.

TABLE 2 | Summary table of $C_{p_{peak}}(x)$ values for all pressure tap zones.

Pressure tap zone	ASCE 7–10 C_p value	Stationary vortex		Translating vortex	
		$C_{p_{peak}}(x)$ without static	Relative difference with ASCE 7 (%)	$C_{p_{peak}}(x)$ without static	Relative difference with ASCE 7 (%)
1	–1.1	–0.83	–25	–0.55	–50
2	–1.4	–0.66	–53	–0.94	–33
3	–1.1			–1.66	51
4	–1.4			–1.26	–10
5	–1.1			–1.35	23
6	–1.1			–0.92	–16
7	–1.4			–0.77	–45
8	–1.4	–1.39	–44	–0.66	–53
9	–1.1	–1.14	4	–0.87	–21
10	–1.1	–1.33	21	–0.86	–21
11	–1.2	–1.08	–10	–1.14	–5
12	–1.0	–1.36	36	–1.26	26
13	–1.0	–1.43	43	–1.25	25
14	–1.0			–1.89	89
15	–1.2			–1.34	11

All $C_{p_{peak}}(x)$ values have static pressure removed. Shaded entries exceed ASCE 7 provisions.

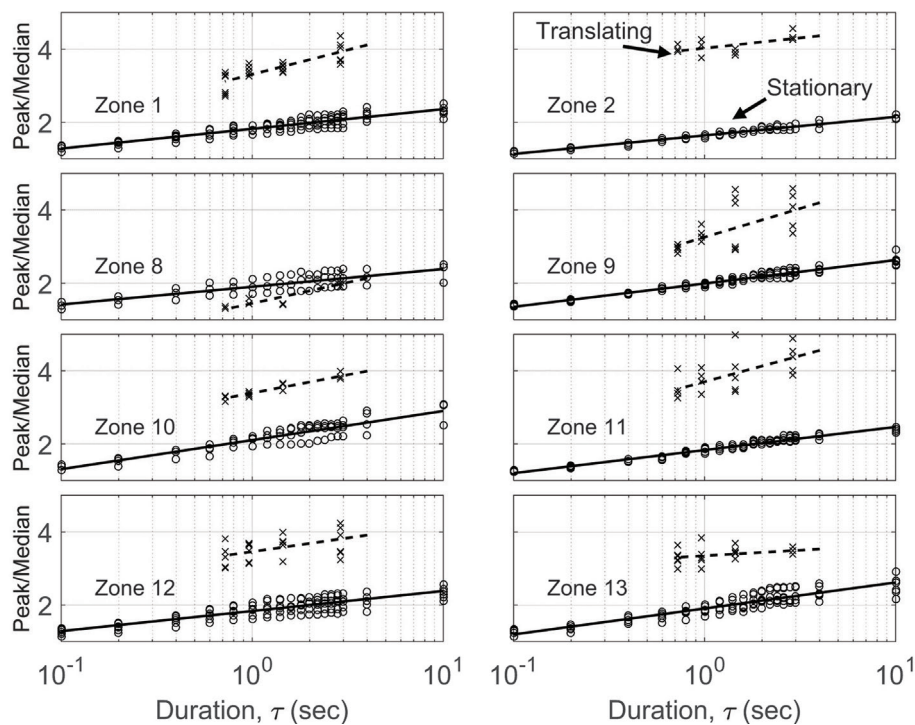


FIGURE 10 | Peak C_p to median C_p ratios as a function of event duration, τ , for every pressure tap as organized into the zones defined in Figure 8. Translating and stationary vortex test results are included.

TABLE 3 | Fit parameters and 100–10 s.

Zone	Stationary vortex			Translating vortex		
	m	b	$\frac{PM_{100s}}{PM_{10s}}$	m	b	$\frac{PM_{100s}}{PM_{10s}}$
1	0.23	1.8	1.2	0.58	3.3	1.3
2	0.22	1.6	1.2	0.24	4.0	1.1
3	0.21	1.9	1.2	0.50	1.4	1.4
4	0.28	2.0	1.2	0.68	3.3	1.3
5	0.35	2.1	1.3	0.43	3.4	1.2
6	0.27	1.8	1.3	0.62	3.7	1.3
7	0.24	1.8	1.2	0.32	3.5	1.2
8	0.31	1.9	1.3	0.13	3.3	1.1

PM ratios for all pressure tap zones to summarize effects of event duration.

and negative x/R_c range. This means that for some tap zones, the worst case vortex positions were not sampled. This is true for zones 3–7 and 14–15.

The ASCE 7–10 values are represented in Figure 9 as well; however, the zones defined in Figure 8 do not coincide with ASCE 7–10 zones. The lines in Figure 9 then represent the smallest magnitude ASCE 7 value for any tap in the zone. To summarize the trends of the figure, ratios between the $C_{p_{peak}}(x)$ values and the ASCE 7–10 provisions are presented in Table 2. All the shaded entries in the table are those which exceed the ASCE 7 provisions. In the case of zone 14, the peak values exceed ASCE 7 by 89%. Two things are worthy of mentioning in Table 2. The first is that, as expected, the stationary values have typically larger magnitudes than the translating values. The second is that

these values in Table 2 should not be used as conversion factors from ASCE 7 to tornado values because the actual pressure coefficients acting on the building model must still include a static pressure component. As discussed later in Section “Comparing Time Series of Stationary and Translating Data,” the static pressure cannot simply be added to the values in Table 2 to recover original peak pressure coefficients.

The duration analysis of Section “Duration Effects” was also applied to all the pressure taps. The results are shown in Figure 10 arranged according to zones. Those zones where the worst case vortex positions were not sampled with stationary data (3–7, 14–15) were omitted from this figure. The translating results are often too scattered to make conclusive statements, but the rough trends with duration are clear. Increasing duration increases peak pressure magnitudes. To quantify these trends, the following expression was used to fit these data:

$$PM = m \ln(\tau) + b \quad (4)$$

where PM is the peak/median ratio presented in Figures 7 and 10 and m and b are fit constants.

The fit constants, m and b , are presented in Table 3 for each zone. To tabulate how much peak C_p values would change with duration, the PM expression of Eq. 4 was used to compute a ratio of the peak/median values for τ values of 100 and 10 s. Depending on the zone, the factors between peak values at 100 s and those at 10 s are 1.1–1.4. These ratios are similar to what Kopp and Morrison (2011) found using pressures from a building in an atmospheric boundary layer (ABL).

Analysis like this could result in a factor that could be used to adjust tornado pressure coefficients for events of different duration.

Velocity and Static Pressure Profiles

The previous two sections presented data showing that peak pressures generated by tornado vortices can be larger than those from straight-line turbulent boundary layer flow. The cause for some of the differences probably lies with the unsteady effects observed in the vertical velocity and the vortex-induced static pressure. **Figure 11A** shows the vertical velocity profile normalized with the maximum horizontal velocity. When the vortex was translating, the instantaneous velocity peaks were observed to be three times as large as the average values and up to 75% of the horizontal velocity. For the stationary vortex, the peaks were four times as large as the means and equal to the horizontal velocity. Unsteadiness like this near the core was also observed for the static pressure as presented in **Figure 11B**. Although the analysis in this paper removed the average static pressure (the solid lines in **Figure 11B** and gray lines in **Figures 4–6**) from the building pressure tap signal, the static pressure fluctuates

about that average. These fluctuations would affect the building envelope. **Figure 11B** shows peaks in the static pressure 25% higher than the average.

Comparing Time Series of Stationary and Translating Data

Another way to illustrate the unique contribution of the static pressure on tornado-induced loading is shown in **Figure 12** where time series of pressure coefficients are shown for several translating vortex tests and a stationary vortex test. One interesting observation is the significant difference static pressure makes in the two types of signals. For these stationary data, removing the static pressure is simply an offset to the whole signal. In the translating cases, the peaks in the signals are drastically reduced. If the two signals are compared while including static pressure, the translating data show peaks of larger magnitude. If the static pressure is removed, the stationary data have the larger magnitude peaks. How the static pressure and the peak pressure events do or do not correlate with each other is worthy of more study.

The large stationary-vortex peak events of **Figure 12** might suggest that the vortex is oscillating in space somewhat and

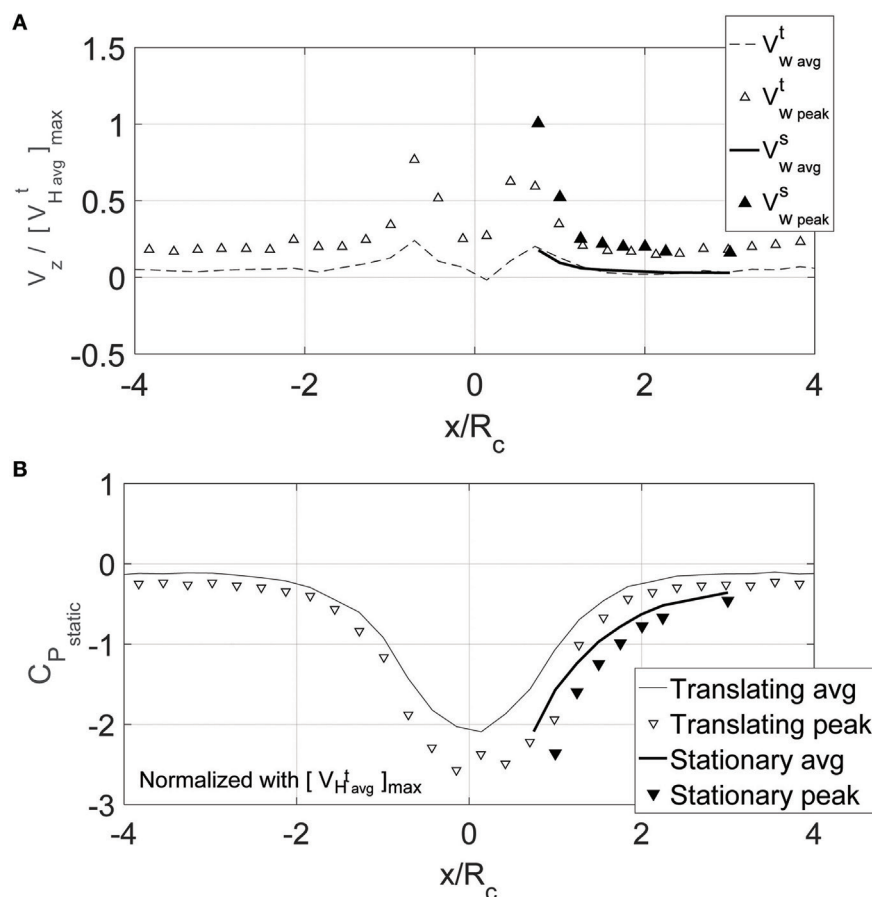


FIGURE 11 | (A) Vertical velocity measurements for the vortex when translating and stationary. Superscripts “t” and “s” denote translating and stationary tests, respectively. All velocities are normalized by the maximum horizontal velocity observed for the translating vortex, $[V_{H_{avg}}^t]_{max}$. **(B)** Vortex-induced static pressure for the vortex when translating and stationary. All pressures were normalized using a dynamic pressure based on the maximum horizontal velocity observed for the translating vortex, $[V_{H_{avg}}^t]_{max}$.

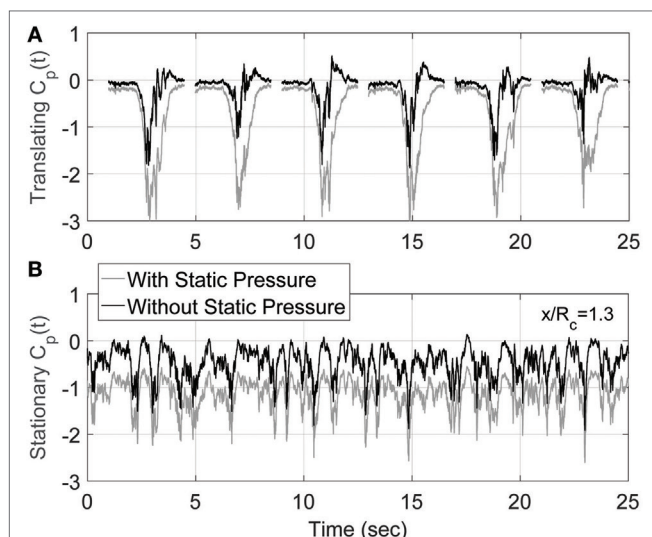


FIGURE 12 | Time series of the pressure coefficient at tap #66 for (A) translating vortex—six vortex events have been plotted together here to illustrate the variability of the signal, (B) stationary vortex at $x/R_c = 1.3$. Each time series is presented with and without static pressure.

impinging on the structure over and over. The nature of the time series should be investigated further. This might require capturing a time-resolved vortex velocity field (such as with a high-speed PIV system) simultaneous to building pressure measurements. While the results of this project show some of the distinctive attributes of tornado-induced pressures, a very interesting future study would involve simultaneous measurements of velocity and pressure such that the spatiotemporal relationships among vertical gusts, static pressure fluctuations, and the pressure peaks on the building surface could be illuminated further.

CONCLUSION

This study investigated the role of tornado-induced static pressure and duration on peak pressures on a low-rise building. Past studies have suggested that peak pressures on buildings in tornadoes were up to 50% (or more) higher than straight-line ABL values (Haan et al., 2010). This study showed that much, but not all, of this increase can be explained by the static pressure of the vortex. While subtracting the static pressure from pressure time series and normalizing by a local horizontal peak velocity brought peak pressures closer to what one would expect from straight-line ABL flows, the data showed that peaks in some portions of the building could still be as much as 90% larger the ASCE 7–10 provisions.

REFERENCES

- ASCE. (2010). *Minimum Design Loads for Buildings and Other Structures*. Reston, VA: American Society for Civil Engineers.
- Chang, C. C. (1971). "Tornado wind effects on buildings and structures with laboratory simulation," in *Proceedings of the 3rd International Conference on Wind Effects on Buildings and Structures*, Tokyo, 231–240.
- Fleming, M. R., Haan, F. L. Jr., and Sarkar, P. P. (2013). *Turbulent Structure of Tornado Boundary Layers with Translation and Surface Roughness*. 12th America's Conference on Wind Engineering. Seattle, WA.
- Haan, F. L. Jr., Balamurdu, V. K., and Sarkar, P. P. (2010). Tornado-induced wind loads on a low-rise building. *J. Struct. Eng.* 136, 106–116. doi:10.1061/(ASCE)ST.1943-541X.0000093
- Haan, F. L. Jr., Sarkar, P. P., and Gallus, W. A. (2008). Design, construction and performance of a large tornado simulator for wind engineering applications. *Eng. Struct.* 30, 1146–1159. doi:10.1016/j.engstruct.2007.07.010
- Jischke, M. C., and Light, B. D. (1983). Laboratory simulation of tornadic wind loads on a rectangular model structure. *J. Wind Eng. Ind. Aerodyn.* 13, 371–382. doi:10.1016/0167-6105(83)90157-5
- To consider duration effects, pressure peak results from both translating vortex and stationary vortex tests were considered. Increases in duration were found to increase peak pressure coefficient magnitudes. Depending on the zone of the building, changing duration from 10 to 100 s was found to increase peak magnitudes by factors of 1.1–1.4. Work such as this might lead to factors that could adjust tornado pressure coefficients for the effect of event duration.
- Both the stationary and the translating vortex pressure peaks were observed to occur in or near the vortex core, and profiles of vertical velocity and static pressure suggest that strong unsteady vertical gusting and strong static pressure fluctuations could play a role in creating these larger stationary-vortex peaks. The pressure time series resulting from these phenomena showed that removing the static pressure had a more significant effect on the translating vortex pressure signals than on the stationary vortex pressure. This indicates the significance of the correlation/timing between the static pressure and velocity-induced pressures. This is worthy of further investigation.
- While this project investigated the results from a single vortex type, future work must investigate the effects of other tornado parameters such as tornado diameter relative to building size and tornado structure as controlled by swirl ratio.

AUTHOR CONTRIBUTIONS

The corresponding author was responsible for the design of the experiments for this project, for acquiring these data, for conducting the analysis, and writing the manuscript. The corresponding author is accountable for all aspects of the work in ensuring that questions related to the accuracy or integrity of any part of the work are appropriately investigated and resolved. The author gratefully acknowledges the contributions of Partha P. Sarkar to the conception, design, and construction of the facility used for this work and the contributions of graduate assistants Vasanth Balamurdu and Mark Fleming for their work acquiring these data.

ACKNOWLEDGMENTS

The author gratefully acknowledges the work of Bill Rickard and numerous undergraduate students from the Iowa State Aerospace Engineering Department who contributed to this project.

FUNDING

This work was sponsored by the U.S. National Science Foundation under grants 0220006 and 0239070.

- Kikitsu, H., Sarkar, P. P., and Haan, F. L. (2011). "Experimental study on tornado-induced loads of low-rise buildings using a large tornado simulator," in *13th International Conference on Wind Engineering* (Amsterdam, Netherlands).
- Kopp, G. A., and Morrison, M. J. (2011). Discussion of "tornado-induced wind loads on a low-rise building" by F.L. Haan Jr., V.K. Balamuduru, and P.P. Sarkar. *J. Struct. Eng.* 137, 1620–1624. doi:10.1061/(ASCE)ST.1943-541X.0000309
- Kosiba, K., and Wurman, J. (2013). The three-dimensional structure and evolution of a tornado boundary layer. *Weather Forecasting* 28, 1552–1561. doi:10.1175/WAF-D-13-00070.1
- Mishra, A. R., James, D. L., and Letchford, C. W. (2008). Physical simulation of a single-celled tornado-like vortex, part B: wind loading on a cubic model. *J. Wind Eng. Ind. Aerodyn.* 96, 1258–1273. doi:10.1016/j.jweia.2008.02.063
- Refan, M., and Hangan, H. (2016). Characterization of tornado-like flow fields in a new model scale wind testing chamber. *J. Wind Eng. Ind. Aerodyn.* 151, 107–121. doi:10.1016/j.jweia.2016.02.002
- Sabareesh, G. R., Matsui, M., and Tamura, Y. (2013a). Characteristics of internal pressure and resulting roof wind force in tornado-like flow. *J. Wind Eng. Ind. Aerodyn.* 112, 52–57. doi:10.1016/j.jweia.2012.11.005
- Sabareesh, G. R., Matsui, M., and Tamura, Y. (2013b). Ground roughness effects on internal pressure characteristics for buildings exposed to tornado-like flow. *J. Wind Eng. Ind. Aerodyn.* 122, 113–117. doi:10.1016/j.jweia.2013.07.010
- Wurman, J., Kosiba, K., and Robinson, P. (2013). In situ, Doppler radar, and video observations of the interior structure of a tornado and the wind-damage relationship. *Am. Meteorol. Soc.* 94, 835–846. doi:10.1175/BAMS-D-12-00114.1

Conflict of Interest Statement: The author declares that the research was conducted in the absence of any commercial or financial relationships that could be construed as a potential conflict of interest.

Copyright © 2017 Haan. This is an open-access article distributed under the terms of the Creative Commons Attribution License (CC BY). The use, distribution or reproduction in other forums is permitted, provided the original author(s) or licensor are credited and that the original publication in this journal is cited, in accordance with accepted academic practice. No use, distribution or reproduction is permitted which does not comply with these terms.



Full Aeroelastic Model Testing for Examining Wind-Induced Vibration of a 5,000 m Spanned Suspension Bridge

Yaojun Ge^{1*}, Jinlin Xia^{1,2}, Lin Zhao¹ and Shiyu Zhao¹

¹ State Key Laboratory of Disaster Reduction in Civil Engineering, Tongji University, Shanghai, China, ² Boundary Layer Wind Tunnel Laboratory, Faculty of Engineering, University of Western Ontario, London, ON, Canada

OPEN ACCESS

Edited by:

Brian M. Phillips,
University of Maryland, College Park,
United States

Reviewed by:

Wenyong Ma,
Shijiazhuang Tiedao University, China
Swamy Selvi Rajan,
CSIR-Structural Engineering Research
Centre, India
Hao Wang,
Southeast University, China

*Correspondence:

Yaojun Ge
yaojunge@tongji.edu.cn

Specialty section:

This article was submitted to
Wind Engineering and Science,
a section of the journal
Frontiers in Built Environment

Received: 11 December 2017

Accepted: 19 March 2018

Published: 18 April 2018

Citation:

Ge Y, Xia J, Zhao L and Zhao S (2018)
Full Aeroelastic Model Testing for
Examining Wind-Induced Vibration of
a 5,000 m Spanned Suspension
Bridge. *Front. Built Environ.* 4:20.
doi: 10.3389/fbuil.2018.00020

This paper presents an experimental investigation on wind-induced vibrations of a suspension bridge with ultimate main span length, including flutter and buffeting. Since the upper limit of a suspension bridge's main span can reach more than 5,000 m based on strength and weight of steel main cables, a feasible prototype with a span arrangement of 2,000 + 5,000 + 2,000 m has been proposed. In order to improve flutter stability, a twin box girder has been designed with a 40 m slot in center and two 20 m wide decks suspended by four main cables. Its full aeroelastic model was designed and manufactured with the geometrical scale of 1:620, and the wind tunnel testing was carried out under smooth flows and turbulent flows for different angles of attack. A big difference in critical flutter speed was found between the proposed slotted girder and corresponding slot-sealed girder, which verifies the necessity of a widely-slotted (WS) twin box girder for a super-long suspension bridge. Among three angles of attack, the critical flutter speed under smooth flow has the maximum value of 80.9 m/s at -3° and the minimum value of 51.4 m/s at 3° . On-coming turbulence will not only cause buffeting responses but also influence the critical flutter speed in an unfavorable way.

Keywords: suspension bridge, full aeroelastic model, wind tunnel testing, flutter, buffeting

INTRODUCTION

Although ancient suspension bridges were built in China long before the Anno Domini, the construction of modern suspension bridges around the world has experienced a considerable development since 1883, when the first modern suspension bridge, Brooklyn Bridge, was built. It took about 48 years for the span length of suspension bridges to grow from 486 m of Brooklyn Bridge to 1,067 m of George Washington Bridge in 1931, as the first bridge with a span length over 1,000 m, and had a great increase factor of 2.2. Though the further increase in the next 50 years to Golden Gate Bridge of 1,280 m, Verrazano Bridge of 1,298 m and Humber Bridge of 1,410 m in 1981 was only 1.3, another factor around 1.4 was realized in Akashi Kaikyo Bridge with a 1,991 m span greater than that of Great Belt Bridge within 17 years in 1998. In the past two decades, there is no further increase of span length, but many long-span suspension bridges have been built over the world. **Table 1** shows ten longest span suspension bridges in service.

With the ever-growing span length, suspension bridges are becoming longer, lighter and more flexible, and accordingly results in wind-induced vibrations, in particular flutter

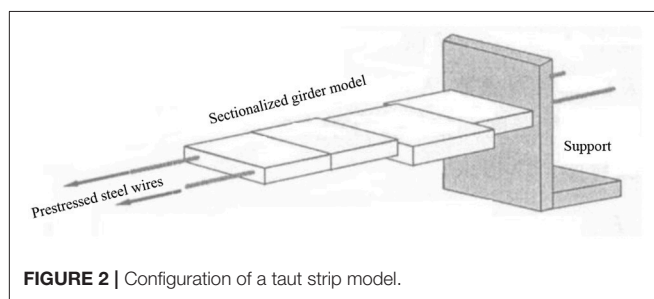
TABLE 1 | Ten longest span suspension bridges in the world.

No.	Bridge	Main span(m)	Girder	Wind-induced problems	Control method	Location	Year
1	Akashi Kaikyō Bridge	1,991	Truss	Flutter	Slotting/stabilizer	Japan	1998
2	Xihoumen Bridge	1,650	Box	Flutter	Central slot	China	2009
3	Great Belt Bridge	1,624	Box	Vortex-induced vibration	Guide vane	Denmark	1998
4	Osman Gazi Bridge	1,550	Box	–	–	Turkey	2016
5	Yi Sun-sin Bridge	1,545	Box	Flutter	Central slot	Korea	2012
6	Runyang Bridge	1,490	Box	Flutter	Central stabilizer	China	2005
7	Nanjing 4th Yangtze Bridge	1,418	Box	Vortex-induced vibration	Guide vane	China	2012
8	Humber Bridge	1,410	Box	–	–	UK	1981
9	Yavuz Sultan Selim Bridge	1,408	Box	–	–	Turkey	2016
10	Jiangyin Bridge	1,385	Box	–	–	China	1999

(four bridges in **Table 1**) and vortex-induced vibration (VIV) (two bridges in **Table 1**). Soon after the infamous incident of Tacoma Narrows Bridge in 1940, there were attempts to examine bridge's wind-induced vibration as something similar to an airfoil flutter. Depending on the participating modes during oscillation, bridge's flutter can be divided into two-degree coupled classical flutter and single-degree torsional flutter (Simiu and Scanlan, 1996). The former implies an aeroelastic phenomenon in which two degrees of freedom, torsional and vertical, couple together in a flow-driven and unstable oscillation, while the later flutter can be associated with systems undergoing strongly separated flows. With a bluff or non-streamlined girder, a suspension bridge can in various instances exhibit this torsional instability. Another ultimate state for long bridges is aerostatic torsional buckling or divergence. This phenomenon is more like a wind-induced static instability. As wind speed increases, the twisting moment increases as well, which requires additional structural resistance. Once structure cannot provide enough reactive moment as expected, it will create an unstable condition and the bridge will diverge (Simiu and Scanlan, 1996). Torsional divergence was firstly observed on cable-stayed bridges. During the full aeroelastic model testing of a suspension bridge, Hirai et al. (1996) found this instability could also occur under the action of aerostatic wind loads on suspension bridges.

In the view of reliability, wind tunnel testing is the best choice to check the aerodynamics and aeroelastics of long-span bridges. Bridge's wind tunnel testing can mainly be classified into three types according to model's dimension, namely, sectional model testing (Scanlan, 1978), taut strip model testing (Tanaka and Davenport, 1982; Scanlan et al., 1997) and full aeroelastic model testing (Sato et al., 2002).

Figure 1 shows the layout of sectional model testing. A rigid sectional model with high stiffness and a reduced scale is often built to simulate a typical girder section, and is mounted with several springs under wind flow (Scanlan, 1978). Either accelerometers or laser sensors (the red lines in **Figure 1**) can be used to record displacement signals. With strip assumption, a sectional model testing is a common technique to measure wind-induced responses of a bridge girder on account of its convenience and low-cost. However, this 2D model testing can only simulate a torsional mode and a vertical one. For a

**FIGURE 1** | Configuration of a sectional model.**FIGURE 2** | Configuration of a taut strip model.

suspension bridge with a conventional span and cable system, the result from a sectional model testing is credible since flutter is normally excited by a fundamental torsional mode and a fundamental vertical mode.

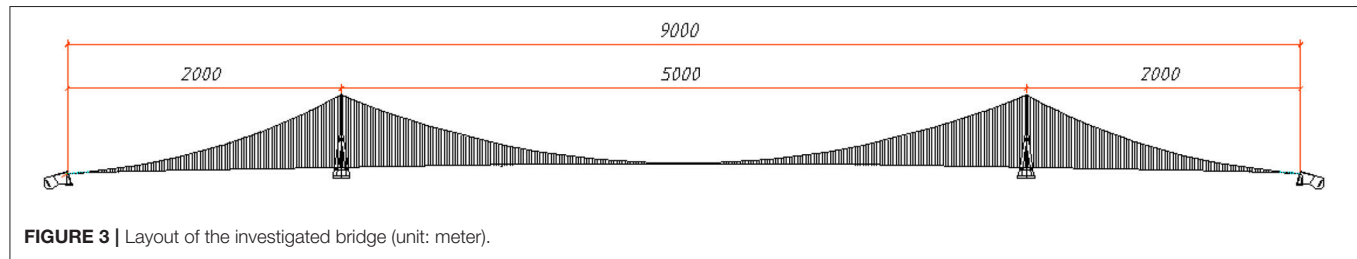


FIGURE 3 | Layout of the investigated bridge (unit: meter).

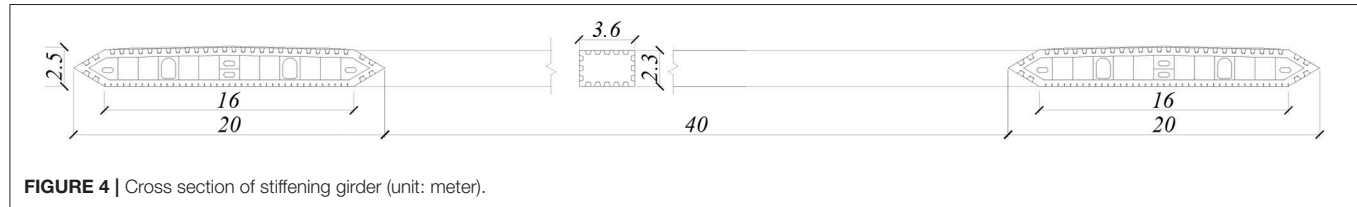


FIGURE 4 | Cross section of stiffening girder (unit: meter).

A taut strip model testing shown in Figure 2 is a transition from sectional model testing to full aeroelastic model testing. The first taut strip model was proposed in 1960s in order to consider three dimensional effect but simplify cable system's simulation. A set of sectional segments are suspended by two cables, of which the tension force can provide overall stiffness. This unique way of stiffness simulation makes the model design empiric. In contrast, a full aeroelastic model testing holds the best similarity as its ability for several natural frequencies and modal shapes. Meanwhile, it can also model the interference of pylons, cable system and piers. The disadvantages of high expenses and time cost impede its wider use.

A suspension bridge's mechanical advantage makes it possible to become the longest bridge type among girder, arch, cable-stayed and suspension bridges. Based on steel main cables, Ge and Xiang (2006, 2008) proposed the ultimate main span of suspension bridges is around 5,000–5,900 m. The sectional model testing (Shao et al., 2011) of a 5,000 m suspension bridge showed the benefit of a central-slotted girder toward flutter performance. As a more comprehensive and precise study in present research, full aeroelastic model testing has been carried out to examine wind-induced vibrations of a suspension bridge with the span arrangement of 2,000 + 5,000 + 2,000 m. The full-bridge aeroelastic model was designed and manufactured with a geometrical scale of 1:620, and wind tunnel testing was finished under smooth flow with different angles of attack and turbulent flow in TJ-3 Boundary Layer Wind Tunnel, which is 15 m wide, 2 m high, and 14 m long.

5,000 M SPANNED SUSPENSION BRIDGE

Span Arrangement

The longest suspension bridge in service is the 1,991 m Akashi-Kaikyo Bridge in Japan since 1998 (Katsuchi et al., 1998), and the longest under construction is the 3,300 m Messina Strait Bridge (Brancaleoni and Diana, 1993) although the construction has been suspended since 2010.

TABLE 2 | Reduced ratios for different properties.

Property	Unit	Reduced ratio	Principle
Length/ L	m	$\lambda_L = 1:620$	Wind tunnel width/wire size
Wind speed/ u, v, w	m/s	$\lambda_v = \lambda_L^{1/2} = 1:24.9$	Froude number
Gravity/ g	m/s ²	$\lambda_g = 1:1$	Unchangeable
Frequency/ Hz	Hz	$\lambda_f = \lambda_L^{-1/2} = 24.9:1$	Strouhal number
Time/ t	s	$\lambda_t = \lambda_L^{1/2} = 1:24.9$	Strouhal number
Mass per meter/ m	kg/m	$\lambda_m = \lambda_L^2 = 1:620^2$	Dimensional analysis
Mass inertia per meter/ J_m	kg.m ² /m	$\lambda_j = \lambda_L^4 = 1:620^4$	Dimensional analysis
Bending stiffness/ EI	N.m ²	$\lambda_{EI} = \lambda_L^5 = 1:620^5$	Dimensional analysis
Torsional stiffness/ GJ_d	N.m ²	$\lambda_{GJ} = \lambda_L^5 = 1:620^5$	Dimensional analysis
Axial stiffness/ EA	N	$\lambda_{EA} = \lambda_L^3 = 1:620^3$	Dimensional analysis
Damping ratio/ ξ	–	$\lambda_\xi = 1:1$	Unchangeable

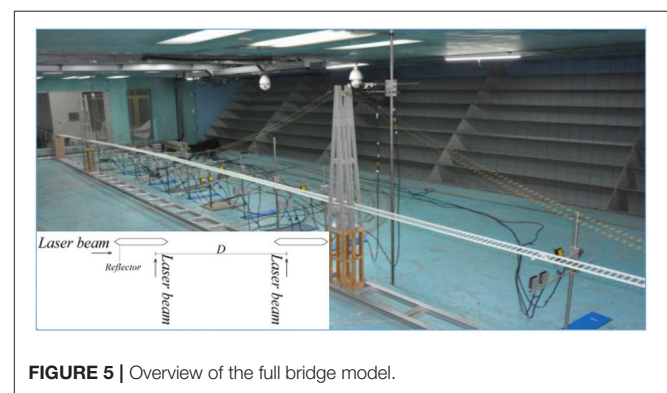


FIGURE 5 | Overview of the full bridge model.

Theoretically, the ultimate span length for a suspension bridge depends upon the strength and weight of main cables which are generally made of high-strength steel wires. By assuming the curve of steel main cables to be parabolic, the span length L can be expressed by the following inequality (Xiang and Ge, 2003),

$$L \leq \frac{8nA\sigma_a/w_c}{\sqrt{1 + 16n^2(1 + w_s/w_c)}}, \quad (1)$$

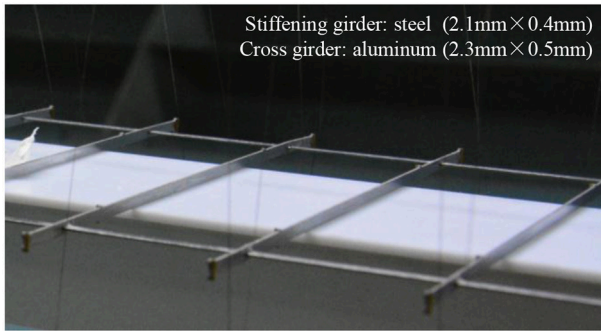


FIGURE 6 | Stiffness system of stiffening girder.

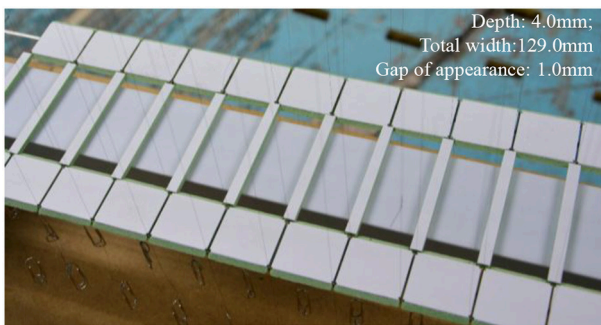


FIGURE 7 | Appearance of stiffening girder.

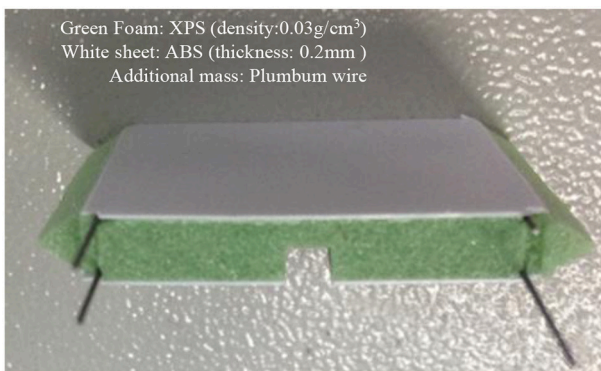


FIGURE 8 | Mass system of stiffening girder.

where n : sag-span ratio of cables; σ_a : steel cable strength; A : area of steel cables; w_c : cable's weight; w_s : total loads including dead loads and live loads. Since for a typical suspension bridge, the stiffening girder only sustains the load between two suspenders, its stiffness and mass remain constants for different spans so that the mass of main cable will be dominant for a super-long case. To make things simpler for an ultimate case, the ratio of w_s/w_c is assumed to be zero and the ultimate span L_∞ with steel main cables can be estimated as follows,

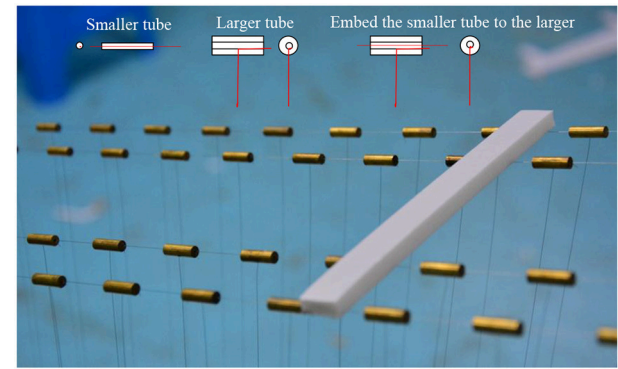


FIGURE 9 | Cable system and joints.

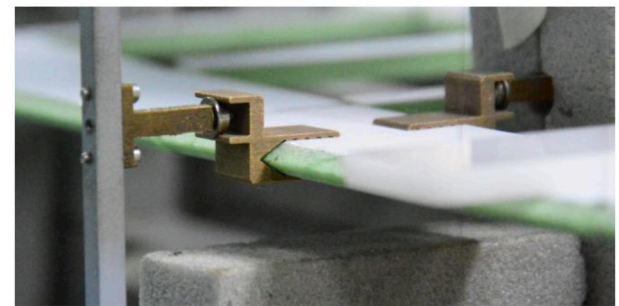


FIGURE 10 | Constraints at pylon.

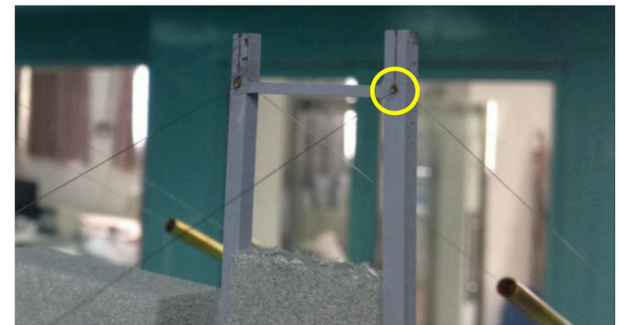


FIGURE 11 | Transition at pylon.

$$L \leq \frac{8nA\sigma_a/w_c}{\sqrt{1+16n^2}} = \frac{8000n}{\sqrt{1+16n^2}} = \begin{cases} 8100 \text{ m} (n = 1/9) \\ 7400 \text{ m} (n = 1/10) \\ 6800 \text{ m} (n = 1/11) \end{cases} \quad (2)$$

Taking as a typical sag-span ratio of 1/10 in Equation (2), if the load ratio of w_s/w_c is designed between 0.5 and 0.25, the central span can be enlarged up to 5,000 and 6,000 m respectively, considering the material properties of steel cables (Xiang and Ge, 2003). As another primary factor, the side span length is set to be 2,000 m for the matching of cable's area in central span and in side



FIGURE 12 | Anchors at end.

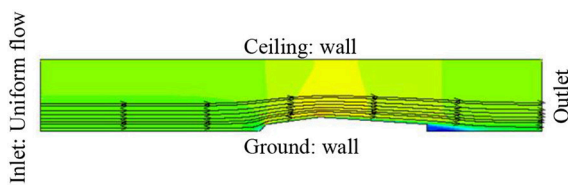


FIGURE 13 | CFD simulation of whole wind tunnel.

span. Consequently, the span arrangement of present super-long suspension bridge goes to be 2,000 + 5,000 + 2,000 m as shown in Figure 3.

Cross Section of Stiffening Girder

With the increase of span length, suspension bridges will have less stiffness and lower critical speeds for aerodynamic flutter instability and aerostatic torsional divergence. The analysis (Ogawa et al., 2002) of a 2,500 m-spanned bridge shows that, a twin-box girder can improve flutter performance by raising the critical speed from 80.9 to 98.9 m/s. Another example of Xihoumen Bridge (Lu et al., 2005) indicates the critical flutter speed can increase from 45.8 to 88.4 m/s when a central-slotted twin box girder, instead of a single box one, is employed. It is evident that a suitable slotting-ratio of a cross section will improve the flutter performance.

Based on previous investigations including numerical simulations (Ge and Xiang, 2006, 2008) and a sectional model testing (Shao et al., 2011) for two kinds of deck sections, called widely-slotted (WS) girder with four main cables and narrowly-slotted (NS) girder with vertical and horizontal stabilizers, the WS girder has greater critical flutter speeds than the NS one. Therefore, the WS box girder was chosen for present investigation, and the cross section was simplified as the

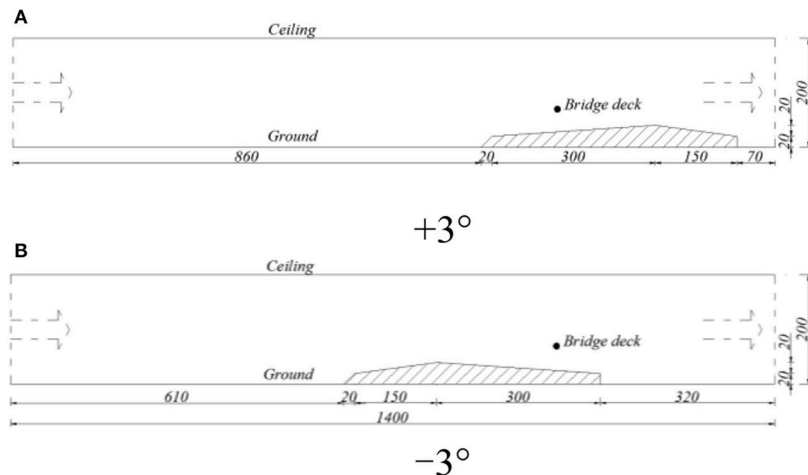


FIGURE 14 | Configuration of slope in wind tunnel (unit: cm). (A) $+3^\circ$. (B) -3° .

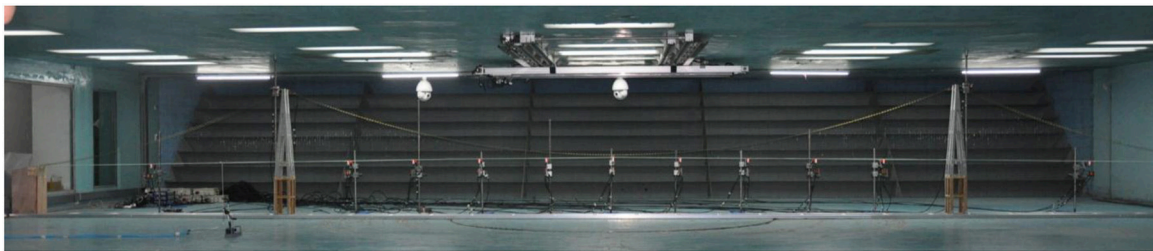
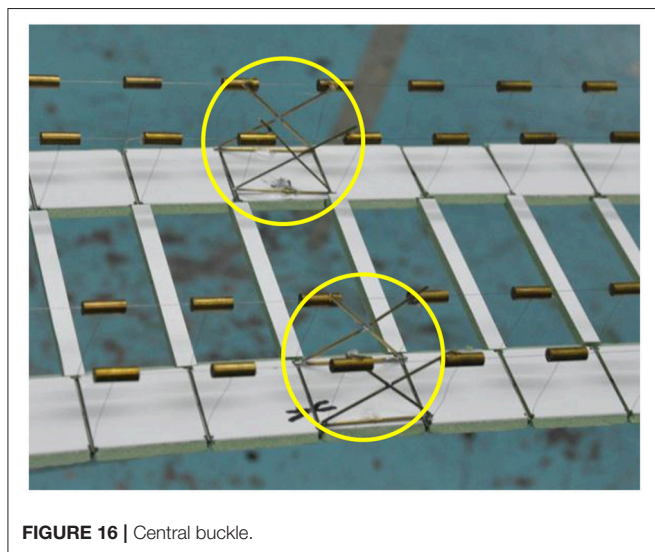


FIGURE 15 | Setting of laser sensors.

**TABLE 3 |** Case list for wind tunnel test.

No.	AOA(°)	Description	Notes
1	0	Free-vibration characteristic test	With central buckle
2	0	Flutter under uniform flow	
3	+3		
4	-3		
5	0	Flutter and buffeting under turbulence (by spires and roughness, intensity = 10%)	
6	+3		
7	-3		
8	0	Flutter under uniform flow (slot sealed)	
9	0	Free-vibration characteristic test	Without central buckle

40 m central slot and two 20 m wide boxes in both sides as is in **Figure 4** (Ge and Xiang, 2006, 2008).

Area of Main Cable

In order to select an appropriate cable area, the minimum value according to static requirement can be estimated as,

$$A = \frac{w_s}{n\gamma} \frac{L}{L_\infty - L} = \frac{3.266L}{L_\infty - L}, \quad (3)$$

where γ is the linear density of cable and L_∞ can be yielded by Equation (2) (Ge and Xiang, 2009).

With a main span of 5,000 m and a sag-span ratio of 1/10, the expected cable area is 9.066 m² after taking a safety factor of 2.0. If two cables are employed, the diameter of one cable will exceed 2.5 m, which tends to bring significant secondary stress. On the other hand, a two-main-cable design means the transverse span length is around 80 m, which complicates the lateral stress

TABLE 4 | Free-vibration characteristic with central buckle.

Mode	Mode Shapes
1st symmetric lateral (0.732 Hz)	
1st antisymmetric lateral (1.392 Hz)	
1st antisymmetric vertical (1.660 Hz)	
1st symmetric vertical (1.733 Hz)	
1st antisymmetric torsional (1.880 Hz)	
1st symmetric torsional (2.148 Hz)	

analysis. Accordingly, four main cables have been employed and the area of one cable is 1.872 m².

DESIGN AND SET-UP OF A FULL MODEL

Dynamic Similarity and Scale Ratio

Dynamic similarity means the balance of dynamic force. As for viscous force and inertial force, the wind tunnel testing must

have a same Reynolds Number with real bridges. However, the flow density and gravitational acceleration are unchangeable both in wind tunnel and in real cases, which indicates the similarity of Froude Number and Reynolds Number will contradict with each other. Unlike a circular cylinder whose flow pattern is varying, the separation points of a practical bridge section are fixed at corners so that its Reynolds Number effect is of secondary importance. Froude Number, as the ratio of the flow inertia to the external gravitational field, becomes more decisive than Reynolds Number since the overall stiffness of a suspension bridge is dominated by gravity instead of element's stiffness. Hence, more attentions will be paid toward Froude Number's similarity while Reynolds Number is not strictly modeled.

Nondimensionalization of Navier-Stokes equations shows that for a geometrically similar bodies in different fluid with different magnitude velocities and different size must yield forces of fixed ratio at a geometrically similar point. Hence, the design of an aeroelastic model should first simulate the geometry of full-scale bridge as well as the incoming flow conditions. The geometrical scale ratio is determined by the space of wind tunnel and accessibility of steel wire. For instance, the scale ratio of Xihoumen Bridge was assigned to 1:208 resulting from a 0.5 mm diameter of steel wire (Ge et al., 2003). The total length of present bridge is 9,000 m while the width of wind tunnel is 15 m, so that the geometrical scale ratio must be smaller than 1:600. The only alternative of steel wire is 0.1 mm in diameter. The geometrical scale ratio of present model was consequently determined to be 1:620 and the ratios for other properties could be yielded as **Table 2**. In particular, when Reynolds Number is not strictly modeled, the scale ratio of wind speed for a cable-stayed bridge is

adjustable while unchangeable for a suspension bridge because of Froude Number.

Design of Main Elements

Figure 5 is an overview of a suspension bridge model which consists of stiffening girder, cable system, constraints and pylons. Based on the similarity of structural dynamic characteristics and wind load, the design of each elements can be divided into a stiffness sub-system, an appearance sub-system and a mass sub-system. A suspension bridge's pylon is similar with that of a cable-stayed bridge, which wouldn't been discussed in following parts.

Stiffening Girder

Unlike a cable-stayed bridge's girder which is an axial and bending stress component, the axial stress in a suspension bridge's stiffening girder can be neglected. As a result, it's acceptable to simulate vertical, lateral and torsional stiffness but leave axial stiffness's dissimilar. The self-consistency of three independent equations requires three feature sizes, which leads U-steel or T-steel to be a practical choice for stiffness simulation. However, for a section like **Figure 4**, it is better to use two throughout steel bars located at the center of each box and join them transversely. On account of the ultra-small scale ratio, the feature sizes will be smaller than 0.2 mm for a U-steel or T-steel, and the machine precision is challenged. Further trials showed that the stiffness of girder itself is not so dominant for overall stiffness, so that the section of each steel bar was simplified to be a rectangle of 2.1×0.4 mm. Aluminum cross bars (2.3×0.5 mm) were employed to join two throughout steel bars by small holes and glues (**Figure 6**).

The appearance design requires the accurate simulation of girder's outline. To ensure the throughout steel bars are the only stiffness suppliers, other elements were gapped longitudinally (**Figure 7**). The section was covered by extreme thin acrylonitrile butadiene styrene (ABS) plates (thickness: 0.2 mm) to get a smooth surface. The filling material between steel girder and ABS cover was selected to be extruded polystyrene foam (XPS), of which the density was around 0.03 g/cm^3 . The white sheet under the central slot in **Figure 7** is an additional support which will be removed later.

The mass and the mass moment of inertia provided by stiffness sub-system and appearance sub-system turned out to be smaller than expected. A conventional way to remedy this difference is to

TABLE 5 | Comparison of frequencies (Hz).

	With central buckle (Exp.)	Without central buckle (Exp.)	Without central buckle (FEM)
1st SL	0.732	0.700	0.678
1st ASL	1.392	1.400	1.324
1st SV	1.733	1.700	1.622
1st ASV	1.660	1.300	1.390
1st ST	2.148	2.175	1.996
1st AST	1.880	1.625	1.638

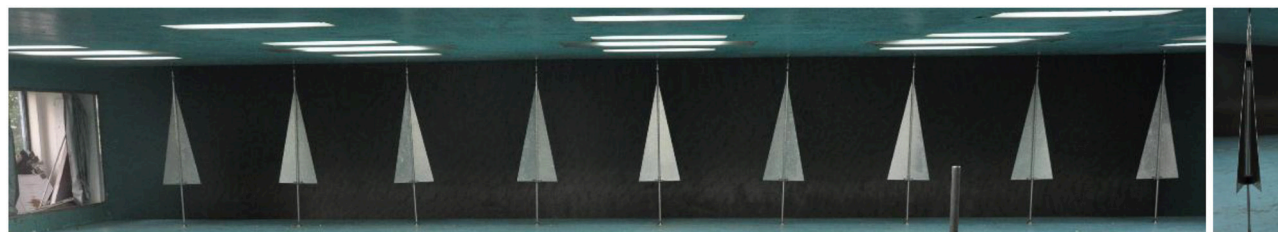
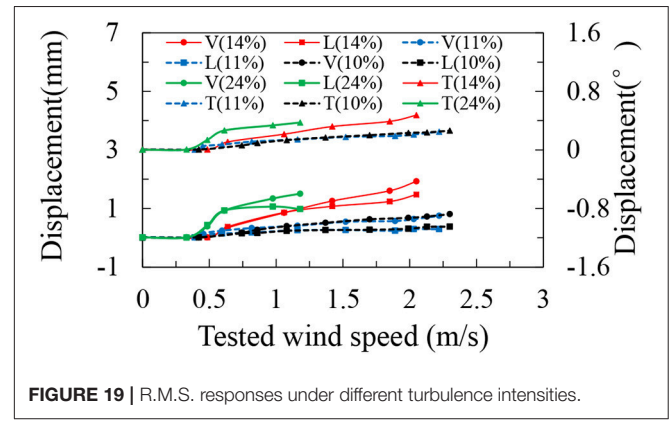
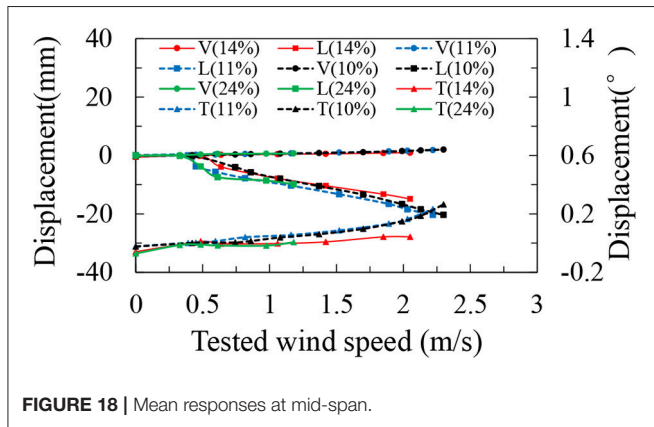


FIGURE 17 | Mobile spires for turbulence flow.



place additional mass inside. From a practical view, 4 plumbum wires were inserted into foam symmetrically (**Figure 8**). The locations and diameters of plumbum wires require a detailed calculation aiming at the simultaneous simulation of mass and mass moment.

Cable System

The modeling of cable system, viz., main cable and suspenders, was in a similar way. The diameter of main cable was 0.1 mm as a result of axial stiffness's similarity. Suspender's size was not a control factor but would be more reasonable to be smaller than that of main cable. As the inaccessibility for a smaller size, same kind of wire was used for suspenders.

Mass moment of inertia can be ignored because of its limited influence. Only drag force's similarity was considered. The insufficient mass and drag force could be modified by additional brass tubes on main cables. For a more accurate design, brass tubes should be placed both on main cables and suspenders. In present situation, all the insufficiency was remedied using the tubes on main cables. Two parameters at each node should be decided, namely brass tube's diameter and length. Assuming the drag coefficient of real cable to be 0.5 and of brass tube to be 1.0, Equations (4) aiming at drag similarity and mass similarity can determine brass tube's configuration.

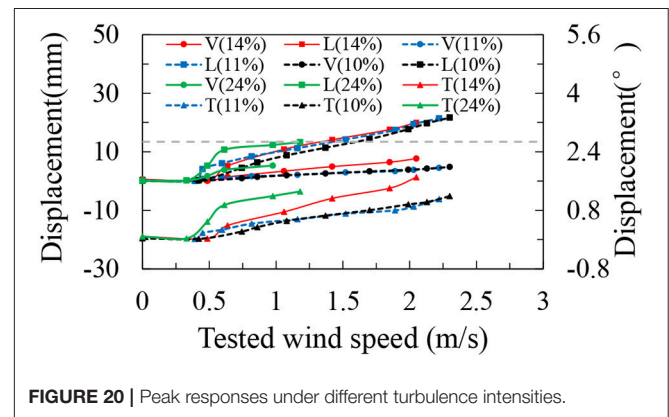
$$0.5 \times \frac{L_p D_p}{\lambda_L^2} \approx 1.0 \times L_b D_b (\text{Drag Similarity})$$

$$\frac{m_{p_cable} + m_{p_suspender}}{\lambda_L^3} = \frac{\rho \pi D_b^2 L_b}{4} + m_{m_cable} + m_{m_suspender} (\text{Mass Similarity})$$

(4)

In Equations (4), L_p and D_p are reference length and diameter of real cable segment, while L_b and D_b are those of brass tubes; m_{p_cable} and $m_{p_suspender}$ are the real mass of main cables and suspenders at each node; ρ is density of brass tube; m_{m_cable} and $m_{m_suspender}$ are model mass of main cables and suspenders.

Figure 9 shows the configuration of brass tube and white bar was used during model erection to ensure brass tube's parallelism.



The main challenge for present model was the ultra-small scale ratio and massive elements. A diameter of 0.1 mm makes the cable vulnerable to get cracked. It would be a prolonged work to replace a new wire since one wire is connected to more than 400 brass tubes and suspenders. The connection of wires with other elements was a vital topic. The top of **Figure 9** is a sketch explaining the method employed: A very small tube was first fixed to main cable by glue and then the top of a suspender was inserted into another larger tube through a hole at bottom. By embedding the smaller tube into the larger one, a joint was finished with some glues. Considering the initial deformation and bending, the steel wires were manually straightened by short time electricity.

Constraints and Joints

The girder was mainly supported by cable system. Besides, it was connected to pylons with some constraints. A sophisticated design of constraints is decisive to the simulation of dynamic characteristics. Due to model's small size, special holders and support rollers (**Figure 10**) were designed to couple the displacements of pylon and girder. The holder and support rollers were fixed on girder and pylons respectively. By embedding the roller into the groove of holder, the torsional, vertical, and lateral displacements were coupled while longitudinal degree was free.

Another important thing was the transition of main cable at the top of pylon and anchor. A bent flared tiny brass tube was mounted at the top to avoid sharp angle (**Figure 11**). A traditional

TABLE 6 | Critical flutter wind speed (with central buckle).

Case	Flutter speed in wind tunnel	Flutter speed for real bridge	Attack angle
Uniform flow (central slotting)	>3.25 m/s	>80.93 m/s	−3°
	2.78 m/s	69.22 m/s	0°
	2.07 m/s	51.54 m/s	+3°
Turbulence (Intensity = 10%, central slotting)	>3.00 m/s	>74.7 m/s	−3°
	2.80 m/s	69.72 m/s	0°
	1.85 m/s	46.06 m/s	+3°
Uniform flow (slot sealed)	1.28 m/s	31.90 m/s	0°

anchor at end for main cable is based on a clamp, which makes the steel wire suffer from shear force or extruding force. In order to make the tension force adjustable and avoid hurt to main cable, a new anchor was developed (**Figure 12**). With a repetitive twine on the anchor and additional glue, the steel wire could be fixed by friction.

Attack Angle's Adjustment

Aerodynamic stability is usually more unfavorable under a non-zero attack angle. It is easy to rotate the model in a sectional model testing. For cable-stayed bridge's full aeroelastic model, a liftable pedestal can realize the changing the attack angle. As a result of gravitational stiffness (Hayashikawa, 1997), only the upstream direction can be changed instead of model's pitch attitude. When slope plates are placed under the model to get an inclined flow, a slope of 3° may not bring an attack angle of 3° exactly. A preliminary study based on computational fluid dynamics (CFD) is advised before the wind tunnel testing.

Figure 13 is an example to determine the size and location of slope where horizontal wind velocity is presented by contour. Wind tunnel's height is 2.0 m and length is 14.0 m. By adjusting the location of slope plates, the attack angle at bridge deck could be guaranteed from ± 3.05 to $\pm 2.95^\circ$ (**Figure 14**). This result has been experimental verified in an empty wind tunnel with slope plates. Things are similar for other attack angles.

Configurations of Sensors

Both accelerometers and laser sensors can be used for displacement measurement in a sectional model testing. However, the mass of accelerometer is a non-negligible encumbrance for a full aeroelastic model. Laser sensors, as a contactless device, will be more satisfying. When the number of laser sensors is limited, it is a tough work to test the free-vibration features since the difficulty in judging movement's symmetry. The data at mid-span can only recognize symmetric modes. A correct identification of both symmetric and anti-symmetric modes requires the synchronous recording at different span-wise locations. An adequate observation points can also realize the measurement of vibration shapes excited by wind load.

Considering the specificity of present model, it would be worthwhile to record the displacements at different span-wise locations for further analysis of modal participation during

oscillation. The total number of observation points in main span was nine with an equal space interval and in each side span, one observation point was set at middle (**Figure 15**). The displacement at the top of pylon was also recorded by two orthogonal sensors.

The measurement of girder's torsional, vertical and lateral movement requires three sensors at one observation point. The setting of laser sensors at a certain location can be seen from **Figure 5**: two laser beams were installed vertically, which can realize vertical displacement's and twist angle's testing. The recording of lateral displacement needs an additional reflector while the XPS cover of girder could act this role for vertical laser beams. The HL-G112-S-J laser sensors used have a resolution of 8 μm .

WIND TUNNEL TESTING AND RESULT

Case List

Bridge's wind-induced response can be classified into stabilized oscillation and aerodynamic instability based on phenomenon. The former oscillation involves turbulence-induced buffeting and VIV. Since these kind of oscillations will bring about some fatigue problems but no overturn, it holds a secondary importance. Meanwhile, a 1:620 scale ratio for VIV investigation is not convective as VIV is a result of vortex shedding and Reynolds effect is predominant. Therefore, VIV will not be discussed in present research. Both torsional divergence and flutter can cause the collapse of overall structure. Since their analyzing methods are quite different with each other, it is helpful to figure out whether the ultimate state of a super-long suspension bridge is controlled by torsional divergence or flutter.

When all the elements, including 4 main cables, more than 1,700 suspenders and cross bars, were jointed with each other, the additional supports was be removed (**Figure 15**). The first step of a wind tunnel testing is the identification of free-vibration characteristics like natural frequencies and damping ratios. After confirming the structural dynamics, the wind-induced responses both in uniform flows and turbulence were recorded. The combination of turbulence generators and slope plates was hard to guarantee the wind profile and turbulence intensity simultaneously, so that only the intensity at deck height was simulated in present case.

Since the mechanism of Tacoma Bridge's collapse is normally regarded to be flutter of antisymmetric modes (Billah and Scanlan, 1991), it became an engineering recognition to make the anti-symmetric torsional frequency higher than a symmetric one. Some previous researches show the anti-symmetric torsional frequency tends to be lower than symmetric one when the main span exceeds 2,000 m. Located at mid-span, a central buckle (Wang et al., 2006) can provide additional constraint and raise anti-symmetric frequencies. As a comparison, a central buckle has been set as **Figure 16** and the natural frequencies with or without a central buckle have been recorded.

Table 3 is a list of cases that have been tested. In order to prove the necessity of a central-slotted section, the critical flutter wind speed when slot was sealed using tape has also been recorded.

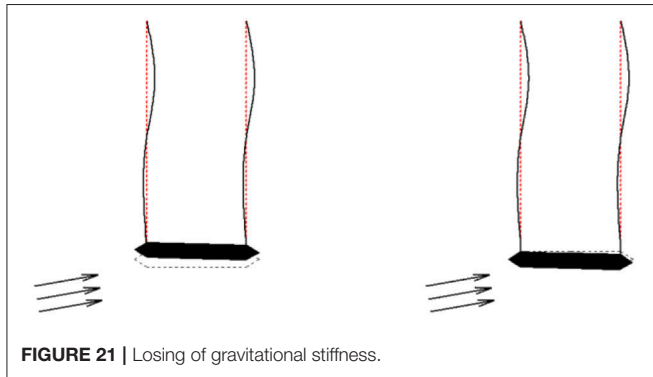


FIGURE 21 | Losing of gravitational stiffness.

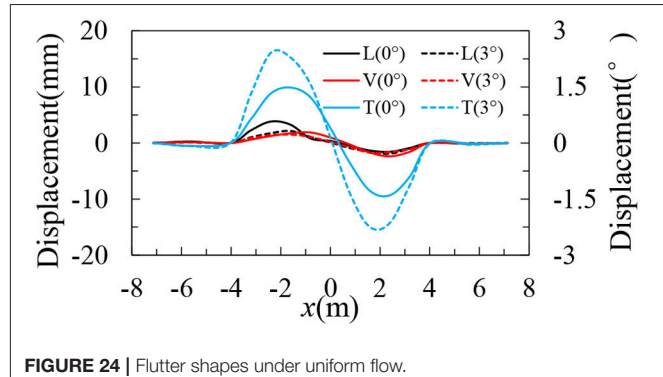


FIGURE 24 | Flutter shapes under uniform flow.

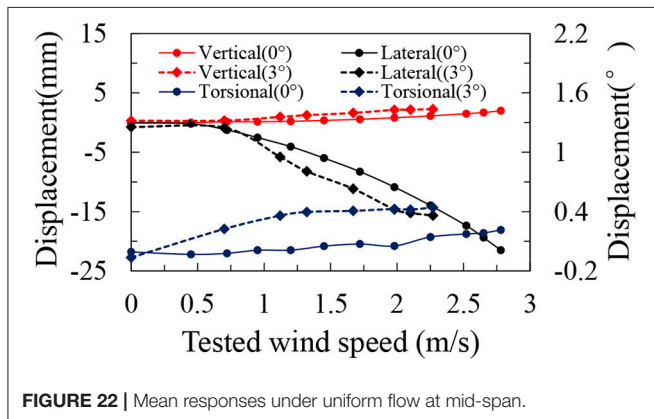


FIGURE 22 | Mean responses under uniform flow at mid-span.

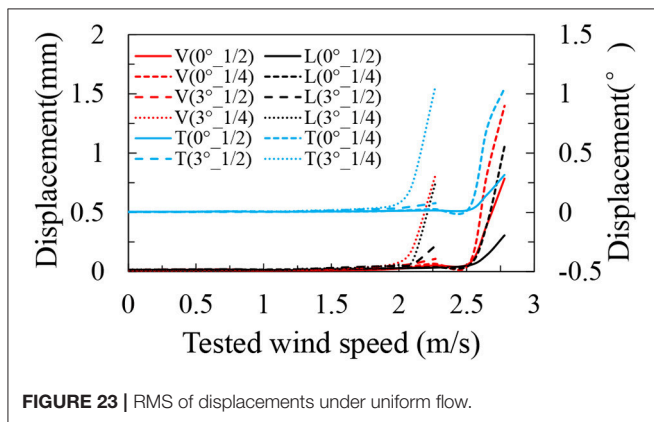


FIGURE 23 | RMS of displacements under uniform flow.

Free-Vibration Characteristics

Different types of excitation can be used for free-vibration testing, namely manual excitation, low wind excitation and environmental stochastic excitation (Natke, 1982). The small wind ratio (1:24.9) in present case means a low wind speed would add non-negligible load on the real bridge. Therefore, the model was excited manually at different span-wise points. Displacement signals after short-time impulse were recorded simultaneously at observation points. After analyzing the amplitude spectrums and phase spectrums, the modal shapes for predominant frequencies can be calculated. Table 4 is the modal shapes for the structure with a central buckle. The damping ratio remains 0.5–1.0% for

different modes and is hard to get changed for a full aeroelastic model.

In Table 5, AS or S abbreviates for anti-symmetric or symmetric modes; T, V, L means torsional, vertical, and lateral components. The comparison shows a central buckle could make the anti-symmetric frequencies higher with little influence on symmetric modes. However, for present super-long bridge, the central buckle is not strong enough to postpone the anti-symmetric torsional mode after symmetric torsional mode. The comparison with finite element model presents a deviation <8%. It is a gratifying result considering the numerous elements and details in present case.

Turbulence and Buffeting

For a passive controlled wind tunnel like TJ-3, spires and roughness are usually used to simulate wind profile and turbulence intensity (Irwin, 1981). A series of mobile spires (Figure 17) were fabricated with adjustable height and projected area. Four different turbulence intensities were generated to show the relationship between intensity and dynamic response.

According to the Davenport's theory (Davenport, 1964), the peak response \hat{r} under random excitations can be expressed as the sum of time average \bar{r} and fluctuating response \tilde{r} , as,

$$\hat{r} = \bar{r} + g\tilde{r} \quad (5)$$

where g is the peak factor. The mean responses, variances and peak values at mid-span under different turbulence intensities are going to be compared respectively. The attack angle remains zero for present part.

Mean Response by Turbulence

In Figure 18, a similar mean displacement was observed with different intensities since mean response is caused by static wind load. Lateral displacements were much larger than the vertical ones. The maximum lateral displacement almost reached 1/400 of span length when experimental wind velocity was around 2 m/s. In a suspension bridge's central span, suspenders can provide vertical constraints to stiffness girder while girder's lateral displacement can only be influenced by constraints at pylons. With the increasing of span length, the lateral mean displacement tends to be more prominent than vertical ones. It shows the benefit of a wide-slotted section in Figure 4 toward

static deformation since this section is laterally stronger than a single box girder with a same effective width.

Dynamic Buffeting Response

Standard variance is an important statistical character relating to oscillation amplitude. Unlike the previous mean displacements, the dynamic response is a directly result of turbulence intensity. As **Figure 19** shows, a higher intensity will enlarge the dynamic response while a similar fluctuation (in blue and black) leads to same structural response. For dynamic component, the difference between lateral and vertical response was not as distinct as **Figure 18**.

Peak Responses

Peak responses, as the superposition of mean and dynamic components, are employed for structural design in wind code. The distribution of maximum value (Davenport, 1964) shows the peak response of most structures to gusts lies in the range 3.5–4.5 standard deviations of the response in excess of the mean response. Taking a factor of 3.5, the peak responses for different intensities can be seen from **Figure 20**. The lateral peak responses at mid-span is around 1/600 of span length (gray dashed line) under 1 m/s wind speed which refers to 24.9 m/s in real world, while the vertical peak response is quite small. It indicates the serviceability design of a 5,000 m-spanned bridge considering wind load is not a control factor. Since the lateral peak response is mainly contributed by mean component, its variation between different turbulence intensities is minor. Turbulence intensity plays a more important role for torsional and vertical peak values.

Aerodynamic Instability

Overview of Critical Velocity

With the increasing of wind speed, the oscillation tends to be violent. Considering the case list in **Table 3**, no torsional divergence has been observed, which indicates for a 5,000 m-spanned bridge, flutter analysis is more important than aerostatic divergence. **Table 6** shows the critical flutter wind velocities for different attack angles and flow conditions. When upstream was zero degree, the critical flutter velocity was 69.2 m/s with a central-slotted girder but dropped to 31.9 m/s if the slot was sealed. An increase of critical flutter velocity more than 100% proves the benefit of a central slot toward dynamic stability. A 10%-intensity turbulence seems to be harmful to aerodynamic stability, which is different with Lin's standpoint (Bucher and Lin, 1990).

Gravitational Stiffness and Attack Angle Effect

Since the bridge section in **Figure 4** is symmetric, the critical wind speed for 3° ought to be the same with that of -3° if the stiffness system is also symmetric vs. attack angle. However, the result in **Table 6** presents a deviation around 30 m/s. A reasonable explanation is the losing of gravitational stiffness. **Figure 21** is an exaggerated schematic for a case of positive attack angle. The losing of strain in cable system caused by mean wind load will offset gravitational stiffness and then weaken flutter resistance. As a result, the model presented a better stability under negative

attack angle but a deteriorated flutter performance under a positive attack flow.

A comparison of mean displacement under smooth flow can verify the above assumption from a side view since the losing of gravitational stiffness tends to enlarge mean response. In **Figure 22**, the mean responses at mid-span are plotted which are similar with those at quarter-span. Their increasing is more rapid for a 3° than 0° . In particular, when testing wind velocity was 2 m/s, the twist angle under 3° was almost 25% larger than that for 0° . Therefore, the schematic in **Figure 21** seems to be the reason of critical wind speed's deviation: an inclined upstream flow enlarges model's static deformation, loosen the tension force in cable system and finally bring forward aerodynamic instability. As this phenomenon is likely to happen in real bridge but hardly to get reappeared through sectional model testing, a 2D sectional model testing without cable system's simulation is risky for long-span bridges.

Discussion of Flutter Shape

Figure 23 shows the increasing of displacement's RMS values vs. uniform wind speed, where 1/2 means mid-span and 1/4 accounts for quarter-span. At the build-up of flutter, the displacements at quarter-span increase more rapidly than those at mid-span. Since an anti-symmetric model presents a minor contribution at mid-span, the flutter of a 5,000 m-spanned bridge is excited by anti-symmetric modes rather than symmetric ones. In part 4.2, although a central buckle can raise anti-symmetric frequency to some extent, 1st anti-symmetric torsional mode occurs earlier than symmetric one. To improve the flutter resistance of a 5,000 m-spanned bridge, more effort is expected to provide additional stiffness for anti-symmetric modes.

A presentation of modal shapes during flutter as **Figure 24** is more visualized to understand the participation of structural modes. Almost no displacement along three directions can be observed at mid-span which accords with the data in **Figure 23** and demonstrates anti-symmetric mode's contribution toward flutter. Since anti-symmetric lateral and vertical modes also participated during flutter, the aerodynamic instability of a 5,000 m-spanned bridge is classical flutter excited by modal coupling effect. **Figure 24** refers to the build-up of flutter when system's total damping was naught and vibrations were of constant amplitudes. A comparison of vibration amplitude shows the flutter under 3° was more violent, which may also be related to gravitational stiffness losing for a positive attack angle.

CONCLUSIONS

In present paper, the full aeroelastic model of a 5,000 m-spanned suspension bridge has been designed, followed by the wind tunnel testing focusing on aerodynamic instability and turbulence-induced buffeting. The main experimental results can be concluded as follows:

- (1) Aerostatic torsional divergence hasn't been observed during all tested cases. The ultimate state of a 5,000 m-spanned bridge is determined by flutter with the participation of anti-symmetric modes. Compared with a sealed section,

the central-slotted girder can raise the critical flutter speed from 31.9 to 69.2 m/s under uniform flow when attack angle is zero. The section with a 40 m slot presents better flutter performance compared with a single-box girder.

- (2) The critical flutter speed for a positive attack angle is much lower than that of a negative angle. It is deduced to be the result of gravitational stiffness' losing. A positive attack angle tends to enlarge the mean response under smooth flows, loosen the tension force and reduce the overall stiffness. Full aeroelastic model testing is recommended especially for super-long suspension bridges since this stiffness losing can't be modeled by a sectional model testing.
- (3) For a 5,000 m-spanned bridge, the lateral buffeting response is much larger than vertical response since girder's lateral displacement can only be constrained at pylons or piers while suspenders can provide vertical constraints to stiffening girder. A central-slotted girder section with more lateral stiffness, is not only beneficial for aerodynamic stability but also for serviceability design.

REFERENCES

- Billah, K. Y., and Scanlan, R. H. (1991). Resonance, Tacoma Narrows Bridge failure, and undergraduate physics textbooks. *Am. J. Phys.* 59, 118–124. doi: 10.1119/1.16590
- Brancaleoni, F., and Diana, G. (1993). The aerodynamic design of the Messina Straits Bridge. *J. Wind Eng. Industr. Aerod.* 48, 395–409. doi: 10.1016/0167-6105(93)90148-H
- Bucher, C. G., and Lin, Y. K. (1990). Effects of wind turbulence on motion stability of long-span bridges. *J. Wind Eng. Industr. Aerod.* 36, 1355–1364. doi: 10.1016/0167-6105(90)90131-U
- Davenport, A. G. (1964). Note on the distribution of the largest value of a random function with application to gust loading. *Proc. Inst. Civil Eng.* 28, 187–196. doi: 10.1680/jicpe.1964.10112
- Ge, Y. J., and Xiang, H. F. (2006). Tomorrow's challenge in bridge span length. *IABSE Symposium Report*, 42–49.
- Ge, Y. J., and Xiang, H. F. (2008). "Bluff body aerodynamics application in challenging bridge span length," in *Proceedings of 6th International Colloquium on Bluff Bodies Aerodynamics and Applications* (Milano), 20–24.
- Ge, Y. J., and Xiang, H. F. (2009). "Aerodynamic stabilization for box-girder suspension bridges with super-long span," in *Proceedings of the 5th European and African Conference Wind Engineering* (Florence).
- Ge, Y. J., Yang, Y. X., Cao, F. C., and Zhao, L. (2003). *Study of Aerodynamic Performance and Vibration Control of Xihoumen Bridge*. Technical Report. WT200320.
- Hayashikawa, T. (1997). Torsional vibration analysis of suspension bridges with gravitational stiffness. *J. Sound Vibrat.* 204, 117–129. doi: 10.1006/jsvi.1997.0948
- Hirai, A., Okauchi, I., Ito, M., and Miyata, T. (1996). "Studies on the critical wind velocity for suspension bridges," in *Proceedings of International Research Seminar on Wind Effects on Building and Structures* (Toronto, ON: University of Toronto Press), 81–103.
- Irwin, H. P. A. H. (1981). The design of spires for wind simulation. *J. Wind Eng. Industr. Aerod.* 7, 361–366. doi: 10.1016/0167-6105(81)90058-1
- Katsuchi, H., Jones, N. P., Scanlan, R. H., and Akiyama, H. (1998). Multi-mode flutter and buffeting analysis of the Akashi-Kaikyo Bridge. *J. Wind Eng. Industr. Aerod.* 77–78, 431–441. doi: 10.1016/S0167-6105(98)00162-7
- Lu, G. C., Zhang, H. F., Yang, Y. X., and Ge, Y. J. (2005). Cross section aerodynamic optimization of steel box girder in Xihoumen Suspension Bridge Preliminary Design. *J. Southwest Jiaotong Univ.* 40, 473–477. doi: 10.3969/j.issn.0258-2724.2005.04.009
- Natke, H. G. (ed.). (1982). "Identification of vibrating structures: an introduction," in *Identification of Vibrating Structures* (Vienna: Springer), 1–14.
- Ogawa, K., Shimodoi, H., and Oryu, T. (2002). Aerodynamic characteristics of a 2-box girder section adaptable for a super-long span suspension bridge. *J. Wind Eng. Industr. Aerod.* 90, 2033–2043. doi: 10.1016/S0167-6105(02)00319-7
- Sato, H., Hirahara, N., Fumoto, K., Hirano, S., and Kusuhara, S. (2002). Full aeroelastic model test of a super long-span bridge with slotted box girder. *J. Wind Eng. Industr. Aerod.* 90, 2023–2032. doi: 10.1016/S0167-6105(02)00318-5
- Scanlan, R. H. (1978). The action of flexible bridges under wind, I: flutter theory. *J. Sound Vib.* 60, 187–199. doi: 10.1016/S0022-460X(78)80028-5
- Scanlan, R. H., Jones, N. P., and Lorendeaux, O. (1997). Comparison of taut-strip and section-model-based approaches in long-span bridge aerodynamics. *J. Wind Eng. Industr. Aerod.* 72, 275–287. doi: 10.1016/S0167-6105(97)00250-X
- Shao, Y. H., Ge, Y. J., Ke, S. T., and Yang, Y. X. (2011). Wind tunnel test on the aerodynamic stability of super-long span suspension bridge with a main span of 5000. *J. Exp. Fluid Mech.* 25, 38–44. doi: 10.3969/j.issn.1672-9897.2011.06.008
- Simiu, E., and Scanlan, R. H. (1996). *Wind Effects on Structures: Fundamentals and Application to Design*. New York, NY: John Wiley and Sons Inc, 243.
- Tanaka, H., and Davenport, A. G. (1982). Response of taut strip models to turbulent wind. *J. Eng. Mech. Divis.* 108, 33–49.
- Wang, H., Li, A. Q., Yang, Y. D., and Li, J. H. (2006). Influence of central buckle on dynamic behavior of long-span suspension bridge. *Zhongguo Gonglu Xuebao* 19, 49–53. doi: 10.3321/j.issn:1001-7372.2006.06.010
- Xiang, H. F., and Ge, Y. J. (2003). "On aerodynamic limit to suspension bridges," in *Proceedings the 11th International Conference on Wind Engineering*. Shanghai.

- (4) The flutter performance under a 10%-intensity turbulence is deteriorated compared with smooth flows, which is different with previous researches based on a relative short-span bridge. Rather than considering turbulence as a favorable factor, more attentions should be paid toward the interaction of turbulence and aerodynamic instability.

AUTHOR CONTRIBUTIONS

The wind tunnel test in the paper was finished by JX and LZ under the supervision of YG and SZ. The data analysis was mainly finished by YG and JX. Four authors all participated in the writing of manuscript and review.

ACKNOWLEDGMENTS

The authors gratefully acknowledge the support for the research work jointly provided by the National Key Basic Research Program of China (973 Program) (No. 2013CB036300), the National Science Foundations of China (No. 51078276 and 91215302).

Conflict of Interest Statement: The authors declare that the research was conducted in the absence of any commercial or financial relationships that could be construed as a potential conflict of interest.

Copyright © 2018 Ge, Xia, Zhao and Zhao. This is an open-access article distributed under the terms of the Creative Commons Attribution License (CC BY). The use, distribution or reproduction in other forums is permitted, provided the original author(s) and the copyright owner are credited and that the original publication in this journal is cited, in accordance with accepted academic practice. No use, distribution or reproduction is permitted which does not comply with these terms.



Simulation of Time-Varying Spatially Uniform Pressure and Near-Surface Wind Flows on Building Components and Cladding

Seraphy Y. Shen¹, Forrest J. Masters^{2*}, Henry. L. Upjohn II³ and Jon Sinnreich²

¹EIT, Stantec Consulting Services, Baton Rouge, LA, USA, ²Department of Civil and Coastal Engineering, University of Florida, Gainesville, FL, USA, ³Special-Lite Inc., Decatur, MI, USA

OPEN ACCESS

Edited by:

Gregory Alan Kopp,
University of Western
Ontario, Canada

Reviewed by:

David James Henderson,
James Cook University
Townsville, Australia
E. N. Farsangi,
Qazvin Islamic Azad University, Iran

*Correspondence:

Forrest J. Masters
masters@ce.ufl.edu

Specialty section:

This article was submitted to
Wind Engineering and Science,
a section of the journal
Frontiers in Built Environment

Received: 14 October 2016

Accepted: 30 March 2017

Published: 04 May 2017

Citation:

Shen SY, Masters FJ, Upjohn HL II
and Sinnreich J (2017) Simulation of
Time-Varying Spatially Uniform
Pressure and Near-Surface Wind
Flows on Building Components
and Cladding.
Front. Built Environ. 3:24.
doi: 10.3389/fbuil.2017.00024

This paper describes a new full-scale (FS) testing apparatus for conducting performance evaluations of FS building envelope systems. The simulator can generate spatially uniform, time-varying pressure conditions associated with Saffir–Simpson Hurricane Wind Scale Category 5 winds while compensating for large air leakage through the specimen and also operate a high-speed wind tunnel, both with dynamic control. This paper presents system details, operating characteristics, and an early case study on the performance of large sectional door systems under wind pressure loading. Failure mechanisms are discussed, and finite element modeling is validated for two specimens. It demonstrates successful dynamic load control for large component and cladding systems, as well as simulation of flows near the building surface. These capabilities serve to complement other FS wind tunnel facilities by offering tools to generate ultimate load conditions on portions of the building. Further, the paper successfully demonstrates the utility of combining physical testing and computational analysis as a matter of routine, which underscores the potential of evolving FS testing to encompass cyber–physical approaches.

Keywords: hurricane, wind, full-scale, destructive testing, garage door

INTRODUCTION

Damage to building envelope components (e.g., windows, roofs, and doors) can lead to adverse internal pressurization and water ingress (Minor, 2005; Gurley and Masters, 2011). Ensuring adequate performance of these components is critical to maintaining the integrity of a building and ultimately reducing cascading failures modes. In the past, building envelope components were treated as architectural components (Rosowsky and Schiff, 2003). Today, structural performance requirements are enforced in most high wind areas. Products are assessed by rational engineering analysis to ensure that structural behavior does not exceed specified limit states. In most cases, products are evaluated experimentally using standardized testing procedures, e.g., ASTM E1233 (ASTM, 2006), ASTM E330 (ASTM, 2009), ASTM E1996 (ASTM, 2012), ASTM E1886 (ASTM, 2013), AS/NZS 1170.2:2011 (AS/NZS 1170.2:2011, 2011), and BS EN 12211:2016 (BS EN 12211:2016, 2016), which apply simplified loading conditions for a few representative cases of wind–structure interaction.

This approach ensures that products are consistently evaluated from one laboratory to the next with the trade-off that “real” dynamic loading is simplified. For example, the cyclic wind

pressure loading sequence specified in IBC (2012) is derived from rainflow-counting analysis of boundary layer wind tunnel pressure coefficient data. Rainflow-counting, which applies the Palmgren–Miner rule (Miner, 1945; Golos and Ellyin, 1987), does not consider low cycle fatigue and the effects of loading sequence (Li et al., 2001; Mahendran, 2003). In addition to the simplification of actual wind loading, the installation of test specimens for the standard tests deviates from the actual boundary conditions in the field, which may influence structural behavior and further separate test results from actual field conditions (Kopp et al., 2010).

Despite the widespread use of standardized testing methods, numerous post-storm damage assessments have found recurring patterns of damage across a wide spectrum of product types (FEMA, 2005; Ginger et al., 2007; Gurley and Masters, 2011; Kopp et al., 2012). These observations underscore the need for new diagnostic tools to validate the performance of component and cladding in high wind regions. A promising approach is FS testing of building systems, which evaluates the performance of complete buildings systems that do not require alteration of boundary conditions or interfaces with other systems.

This paper presents technical details of a new large-scale wind load simulator that recreates dynamic wind and wind pressure records. A case study demonstrating its utility in investigating the performance of building components and cladding under extreme loads is presented, which includes complementary finite element analysis (FEA).

BACKGROUND

The wind load simulator was inspired by the BRERWULF system developed at the British Research Establishment (Cook et al., 1988) and its successor, the pressure loading actuator (PLA) system developed by Kopp et al. (2010) at the University of Western Ontario (now Western University). A PLA can simulate realistic wind pressure records for a wide range of loading conditions expected to occur on nominally sealed low-rise buildings. It monitors pressure in the test chamber and uses a PID control to proportion a mix of fan exhaust and return to the test chamber in order to “follow” a target pressure time history. Air leakage in/out through the specimen is compensated for through valve ports to the open atmosphere. Under optimal conditions and tuning, waveforms with frequency content up to 8 Hz can be recreated in a nominally sealed chamber. Further, individual units can be synchronized to apply spatially varying loads over a larger specimen (Morrison, 2010).

Pressure loading actuators have become standard tools for wind engineering research. In one of the first studies, Cook (1992) tested single-ply roofing systems under dynamic wind pressure loads using BREWULF and observed that the dynamic responses were non-linear and frequency-dependent. Cook also compared the test results using BREWULF to simple cyclic test results and indicated that quasi-static assumption was not appropriate for single-ply roofing systems. More recently, Morrison (2010) and Henderson et al. (2013) conducted testing on a gable roof and hip roof with toe-nailed roof-to-wall connections, respectively. Henderson and Ginger (2011) simulated cyclonic wind loads

to pierced fixed corrugated steel roofing systems. This study continues this work using a new class of PLA designed for testing of large specimens that exhibit a large degree of leakage. The next section provides technical details of its operation. A case study on the performance of rolling doors then follows.

NEW LARGE-SCALE DYNAMIC WIND PRESSURE SIMULATOR

Design Considerations

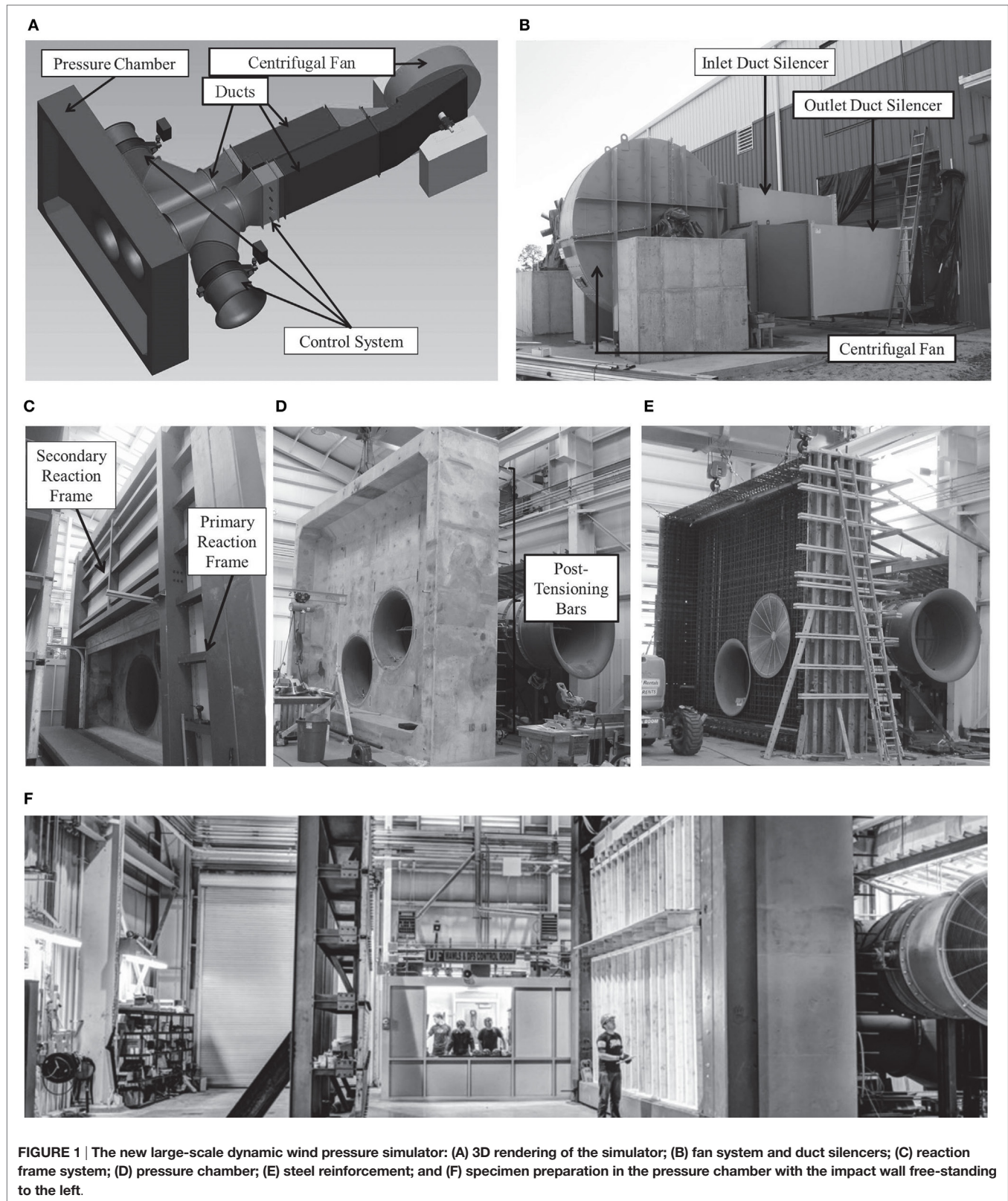
In September 2009, the University of Florida and Special-Lite, Inc. began the design of a large-scale dynamic wind load simulator to replicate intense hurricane wind loading, i.e., Category 5 hurricanes, to load large/FS building components. The simulator was designed to apply spatially uniform, time-varying pressures on the specimen surface. The simulator was specifically designed for large cladding and component systems for a large range of leakage conditions. The new system differs from the PLA in three significant ways. First, the entire system was integrated to expedite destructive testing of large cladding and component systems ($\sim 40 \text{ m}^2$) and designed to operate continuously to recreate the entire record of a tropical cyclone. Second, the system was designed to operate over a wide range of leakage conditions and changes in volume caused by specimens deflecting out-of-plane. Third, the test chamber can be bypassed to drive air through a high-speed wind tunnel that is under control of the same damper control system.

Components

Four principal components comprise the simulator (**Figure 1A**): a fan, the ducting, a control system, and the pressure chamber. The fan (**Figure 1B**) is a centrifugal blower that can generate a maximum pressure of 22.4 kPa (90" WC) at an airflow rate of 2,832 m^3/min (100,000 CFM). The pressure and flow requirements were determined from simulations of airflow movements in/out of the pressure chamber based on the Helmholtz model described in Oh (2004) and assumptions about air leakage through the test specimens. The pressure coefficient data used to estimate the requirements were obtained from generic wind tunnel models archived in the National Institute of Standard and Technology (NIST) Aerodynamics Database. Details about the wind tunnel models can be found in Ho et al. (2003) (see generic model test 2, exposure: open country).

A Caterpillar 3512 DITA diesel prime mover load rated for 1,818 HP at 1,750 RPM drives the fan. A Renold torsional vibration control coupling (model no. SAE 21 SM 60 RB 3.86) is attached to the flywheel of the prime mover to transfer power to a 0.5-m (21") Wichita Air Clutch (Model 6-12-382-313-9), which engages the fan driveshaft. The dimensions of the ducts connecting the fan and the pressure chamber are 9.5 mm (3/8") thickness and 1,524 mm (60") internal diameter. Two VAW duct silencers (**Figure 1B**) reduce the noise by 20 dBA upstream and downstream of the fan.

Flow is controlled by five dampers (valves): four butterfly dampers and a custom-built fast-acting opposed blade louver damper. The butterfly dampers change the flow configuration so that positive or negative pressure can be applied to the



specimen or alternatively bypass the chamber to drive air through a high-speed wind tunnel section. The lower damper modulates the system resistance (i.e., the operating point on the fan curve),

which changes the airflow in/out of the pressure chamber and thus causes a corresponding change in the pressure acting on the specimen.

Two Honeywell Model Z transducers measure absolute pressure inside the test chamber. A custom analog computer monitors the pressure measurements, and a bus-powered isolated data acquisition module (NI USB-6218) interfaces between the measured pressure and the computer. The computer sends commands to an analog servo that actuates the hydraulic cylinder driving the louver damper. The control/feedback process is continuous; only analog feedback/control was implemented (i.e., no A/D or D/A). The control system allows the user to select a step-and-hold input (i.e., simply setting a pressure level to be maintained indefinitely), input from a function generator (for example, a sine wave with defined mean, amplitude, and frequency), or a time-varying signal (input file containing the time history of a measured or simulated wind storm pressure signal).

The test specimen is mounted in the reaction frame (**Figure 1C**) clamped to the open side of the pressure chamber (**Figure 1D**), which is 7.3 m wide \times 5.5 m high \times 1 m deep (24 ft \times 18 ft \times 3 ft). The reaction frame attaches to the reinforced concrete pressure chamber, which has 13 t of mild steel reinforcement (**Figure 1E**) and 25 mm (1") diameter post-tensioning bars (**Figure 1D**) to minimize concrete cracking.

The reaction frame system, which mounts to the pressure chamber opening, consists of primary and secondary reaction frames (**Figure 1C**). The primary frame resists the catenary forces developed from the test specimen subjected to wind pressure loading. The primary frame is made of HSS 406 mm \times 406 mm \times 9.5 mm (16" \times 16" \times 3/8") and has a lateral force capacity of 150 kN/m (10 kip/ft). The primary frame is fixed, while the secondary reaction frame can be removed and resized to accommodate the dimensions of the specimen.

SIMULATOR VALIDATION

Dynamic Pressure Simulation

The fidelity of the pressure simulator for both positive and negative pressure modes was evaluated for sinusoidal pressure input that varied by mean, amplitudes, and frequency. The pressure box was sealed with an impact wall that typically free-stands outside the box to stop debris originating from specimens tested under positive pressure (**Figure 1F**). It allows for minor leakage at the corners of the wall. Spectral analysis was used to compare the peak power of the target frequency input and output data and generate Bode plots of the results (**Figure 2**) to evaluate the performance of the system "as-is" to establish a baseline without additional tuning or modifications to increase the fidelity, e.g., reduce the air volume in the chamber, isolating the control system to the open loop on the opposed blade damper to perform a sine sweep, adjusting the PID parameters for the specific application, or tuning the leakage to align the range of the damper movement to optimize controllability. The initial test run was conducted 1,200 RPM, i.e., the "high idle" speed of the diesel motor. A subsequent test run at 1,600 RPM, with the atmospheric butterfly dampers open 40% was also performed (**Figures 2C, D**). The figures show that the simulator can nominally produce a 1-Hz bandwidth without modifying the system, which is consistent with observations during the commissioning of the system.

Higher resolution (on the order of 2–3 Hz) should be possible applying the changes described above.

The primary purpose of the simulator is to recreate pressure time histories obtained from the boundary layer wind tunnel of field measurements on real buildings, thus the fidelity of the pressure simulator was also evaluated by recreating a pressure time history from a generic wind tunnel scale model. The pressure signal was calculated using the wind pressure coefficient (C_p) data from model m31 archived in the NIST Aerodynamics Database. The wind tunnel model is a 1:100 scale model of a 3:12 slope gable-roofed building with a 24 m \times 38 m (80 ft \times 125 ft) rectangular plan and a 9.8 m (32 ft) eave height. The exposure for this wind tunnel model is open country. The wind pressure coefficient is defined as

$$C_p = \frac{p - p_{ref}}{\frac{1}{2} \rho v_{ref}^2}, \quad (1)$$

where p is the pressure measured at a specific location on the model surface, p_{ref} is the pressure measured at a reference location (atmospheric pressure), ρ is the density of air, and v_{ref} is the velocity measured at the reference location. The pressure coefficient data at the location (expressed in terms of tap numbers) with the largest instantaneous peak C_p were extracted for use in this study. **Figure 3A** shows the location of the tap and the incident wind angle, and **Figure 3B** shows the time history of C_p data with a peak value of -7.5 .

The C_p data were scaled to FS pressures for seven intensity levels that correspond to ASCE 7 (2010) basic wind speeds of 60, 65, 70, 75, 80, 85, and 90 m/s. The sampling frequency of the NIST model data (f_M) is 500 Hz at an eave height mean wind speed (V_M) of 9 m/s (29.5 ft/s). The basic wind speed was converted to an open-exposure mean velocity using a gust factor of 1.5. The model-scale time increment was converted to its FS counterpart for each basic wind speed value from the reduced frequency relationship:

$$\left(\frac{f \cdot L}{V} \right)_{FS} = \left(\frac{f \cdot L}{V} \right)_M, \quad (2)$$

$$f_{FS} = f_M \frac{L_M V_{FS}}{L_{FS} V_M}. \quad (3)$$

The dynamic performance of the simulator was assessed by simulating wind pressure time histories that were filtered using a third-order Butterworth filter. Positive pressure sequences were simulated using the 1 and 2 Hz cutoff time histories. Negative pressure sequences were simulated using the 2 and 3 Hz cutoff time histories. In all cases, the simulator demonstrates a good ability to replicate the peak loads, which is a key consideration in designing FS experiments.

Figure 4 shows a plot of two of the pressure simulations (at 2 Hz cutoff) for seven intensity levels. A 10-s transition time was interleaved between each level, and each intensity level lasted 1 min with the exception of level 7 (46 s).

The solid black line represents target time-varying pressure derived from the NIST database, and the dash-dot gray line describes the pressure measured in the pressure chamber. **Table 1**

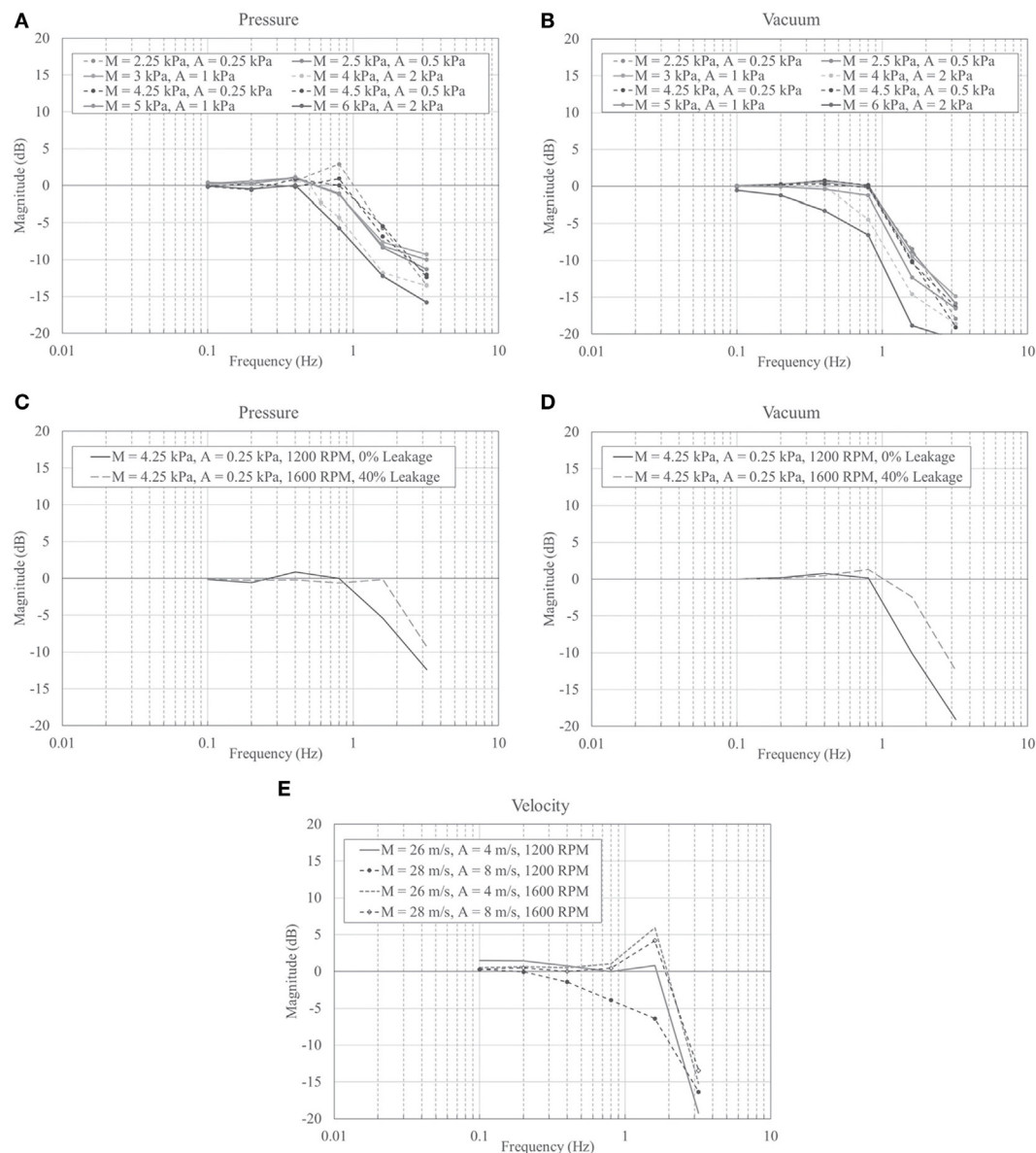


FIGURE 2 | Bode plots for no-leakage (impact wall sealing the pressure box), 1,200 RPM fan speed positive pressure (A) and negative pressure (B) sine wave function for various mean (M) and amplitude (A) settings, and no-leakage/artificial leakage comparison for positive pressure (C) and negative pressure (D) sine wave function with mean of 4.25 kPa (89 psf) and amplitude of 0.25 kPa (5 psf); simulator run at 1,200 RPM with 0% artificial leakage and 1,600 RPM with 40% artificial leakage induced by partial opening of atmospheric outlet (C) or inlet (D) butterfly valves; and for velocity (E) sine wave function for various mean (M) and amplitude (A) settings.

compares the desired and measured statistics for the simulated wind pressure time history at intensity levels 1 and 7. The statistics agree well, and the mean absolute error percentage averages are 4.5 and 1.5% for the four cases at levels 1 and 7, respectively. Overall, the simulator shows an acceptable fidelity for recreating these time histories.

Dynamic Velocity Simulation

In the velocity simulation mode, the pressure chamber is bypassed so that air moves from the exterior intake through the blower and into the high-speed wind tunnel, which

consists of a setting chamber, a contraction duct, a test section, and a diffuser. The test section cross-section area is 213 cm wide \times 38 cm tall (7 ft \times 1.25 ft). The bottom part of the test section is removable to accommodate roof samples, and it has a dimension of 243 cm long \times 182 cm wide (8 ft \times 6 ft). Wind velocity measurements were obtained from a Pitot tube upwind of the test section.

Using the same procedure as described in Section “Dynamic Pressure Simulation,” a spectral analysis was performed to compare the peak power of the target frequency input and output data and generate Bode plots of the results (Figure 2E). As with

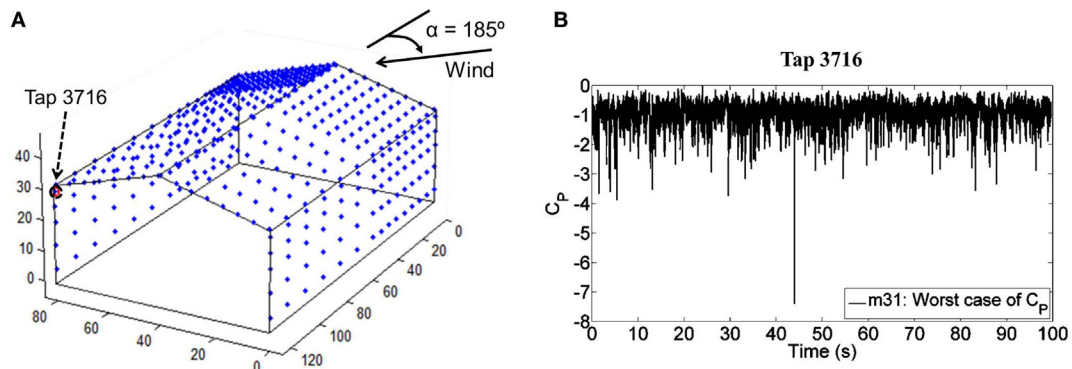


FIGURE 3 | National Institute of Standard and Technology database wind tunnel model and tap locations: (A) the location of Tap 3716 where the maximum C_p was recorded and the incident wind direction; and (B) the time history of the C_p data for Tap 3716.

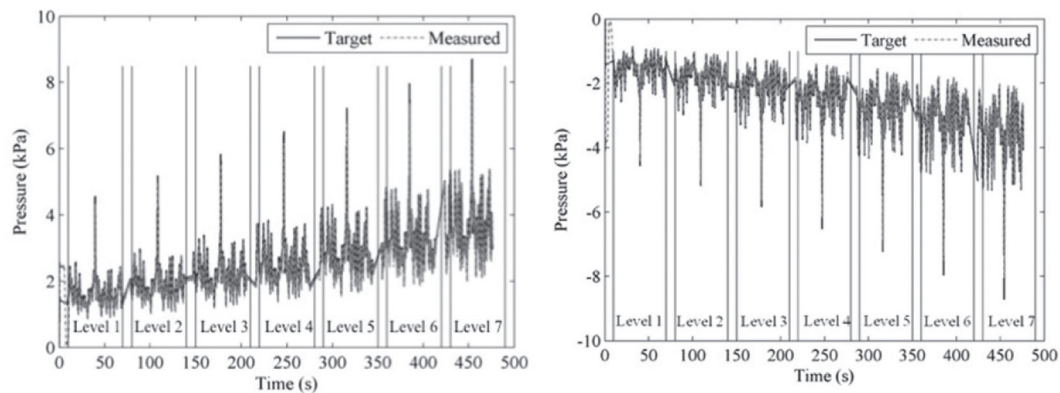


FIGURE 4 | Time histories of target and measured wind pressure at seven intensity levels for two load conditions (2 Hz positive and negative cutoff, respectively). The target pressure represents the pressure that is desired to replicate using the pressure simulator, and the measured pressure represents the actual pressure achieved in the pressure chamber.

TABLE 1 | Statistics of the target and measured wind pressure at intensity levels 1 and 7.

	1 Hz positive pressure (kPa)		2 Hz positive pressure (kPa)		2 Hz negative pressure (kPa)		3 Hz negative pressure (kPa)	
	Target	Measured	Target	Measured	Target	Measured	Target	Measured
Level 1								
Mean	1.90	1.78	1.61	1.54	-1.61	-1.55	-1.61	-1.55
CoV	0.27	0.32	0.26	0.29	0.26	0.27	0.28	0.27
Minimum	0.08	-0.01	0.08	0.36	-4.55	-4.60	-5.43	-4.58
Maximum	3.83	4.18	4.56	4.60	-0.09	-0.83	-0.09	-0.80
Level 7								
Mean	4.11	4.05	3.62	3.57	-3.65	-3.59	-3.62	-3.56
CoV	0.28	0.29	0.24	0.25	0.24	0.25	0.25	0.24
Minimum	2.41	2.02	2.07	1.56	-8.74	-8.40	-10.25	-7.78
Maximum	8.23	8.54	8.74	8.06	-2.08	-1.93	-1.95	-1.83

the pressure simulator validation, testing was conducted at 1,200 and 1,600 RPM. Additionally, wind velocity data collected from Hurricane Katrina by the Florida Coastal Monitoring Program were resampled at four intensity levels with mean wind velocity = 15, 25, 35, and 45 m/s. **Figure 5** shows these velocity simulations. Fan RPMs were varied: levels 1 and 2 correspond to a

rotational speed of 1,200 RPM, level 3 corresponds to 1,450 RPM, and level 4 corresponds to 1,700 RPM. In **Figure 5**, the solid black line represents the input (or “target”) velocity signal, and the dash-dot gray line describes the measured signal. It can be seen that the simulator follows the target signal well. **Table 2** lists the statistics of the input and measured wind velocity time histories. It is seen

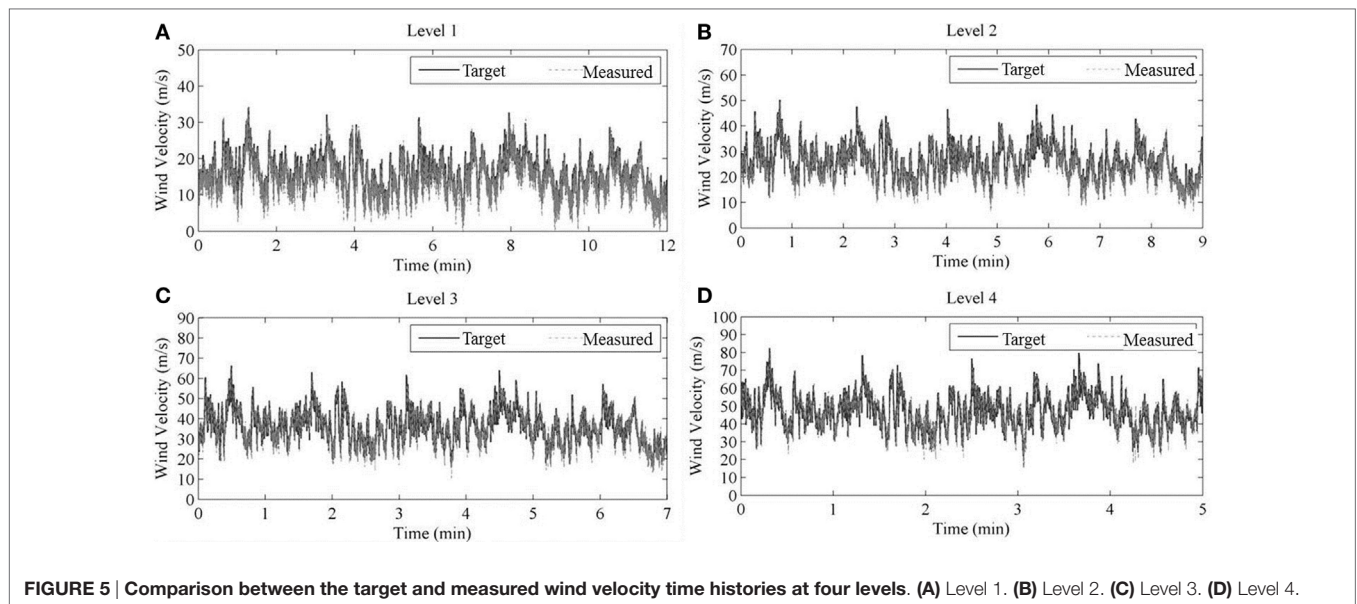


FIGURE 5 | Comparison between the target and measured wind velocity time histories at four levels. (A) Level 1. (B) Level 2. (C) Level 3. (D) Level 4.

TABLE 2 | Statistics of the input and measured wind velocity at four levels.

	Level 1 (m/s)		Level 2 (m/s)		Level 3 (m/s)		Level 4 (m/s)	
	Target	Measured	Target	Measured	Target	Measured	Target	Measured
Mean	15.8	14.6	25.7	25.3	35.7	36.3	46.6	47.7
CoV	0.30	0.33	0.25	0.28	0.22	0.24	0.21	0.21
Minimum	3.99	-3.50	10.0	6.40	16.1	10.6	22.1	15.3
Maximum	34.2	34.4	50.2	49.4	66.3	64.6	82.4	79.8

that the means, coefficients of variation, and the maximum values agree well. The mean absolute error percentages vary from 7.6% down to 1.6% for the four levels.

CASE STUDY: SECTIONAL DOOR SYSTEMS

This section describes early testing using the simulator to (a) demonstrate that the practicality of conducting FEA in conjunction with FS testing and (b) conduct data acquisition during live tests. The test subjects were sectional (garage) door systems, such as the kind that are used in fire stations and other critical facilities. As these were the first tests in the pressure chamber, the experimental design was chosen to minimize safety risks to personnel and to incrementally evaluate the capabilities of the system. Thus, step-and-hold functions patterns were applied in lieu of dynamic loads, and the loads were applied into the frame to prevent debris from flying into the testing arena. Response to dynamic loading is not addressed here but will be the subject of future studies.

FS Testing

Five commercial sectional doors from different manufacturers were evaluated. Dimensions of the doors spanned from 4.9 to 5.2 m in width and 3.7 to 4.8 m in height. Corresponding design pressures ranged from 2.0 to 2.6 kPa and 2.2 to 3.1 kPa in

positive and negative pressure, respectively. Doors were installed to manufacturers' published guidelines, with the float between the roller and track being kept to less than 5 mm.

Generally, a sectional door used in hurricane-prone regions consists of five principal structural components: door panels, stiles, reinforcing beams (U-bars), hinges, and rollers (**Figure 6**). The stiles and U-bars provide the primary resistance to out-of-plane loading. Specimens were instrumented as follows:

1. Eight Micro-Measurement C2A-06-250LW-350 strain gages were attached on eight U-bars at their mid-spans (**Figure 7A**) to measure the longitudinal strain.
2. An OptiTrack Flex-3 motion-capture camera measured displacement by recording the 3D coordinates of traceable spheres attached on U-bars at their mid-spans with sub-millimeter accuracy (**Figure 7B**).
3. Three SDI Tri-axial 70148-00B-EA00C load cells were installed between the door jamb and the reaction frame of the simulator (**Figure 7A**). The load cells were located around the rollers at bottom, middle, and top of the specimen (**Figure 7A**).

A step-and-hold pressure sequence was applied to each test specimen until failure occurred. Each specimen was assembled and mounted in the pressure chamber according to the installation manual provided by the manufacturer. The door jamb was connected to the reaction frame of the pressure chamber so that

their connection would not fail before the failure of the test specimen (i.e., the jamb was attached to a rigid assembly).

Loads were increased in 0.5 kPa (10 psf) increments for each step. Once the desired load was achieved, it was held for ~5 min and then released back to zero. After releasing the load, the operability (i.e., the ability of the door to be cycled upwards or downwards along the tracks) of the specimen was checked. This cycle repeated until a catastrophic failure occurred or was imminent or the door lost its operability. The following failure modes were observed:

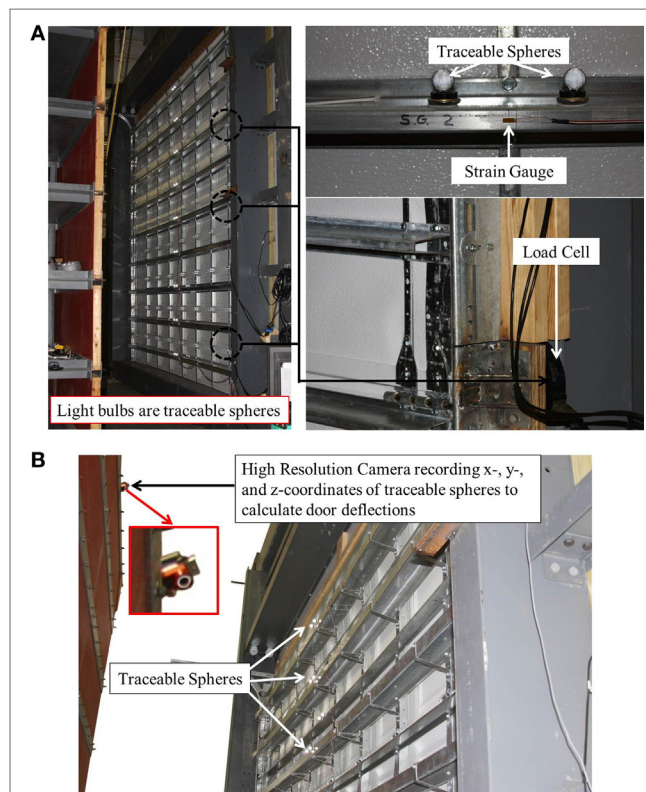
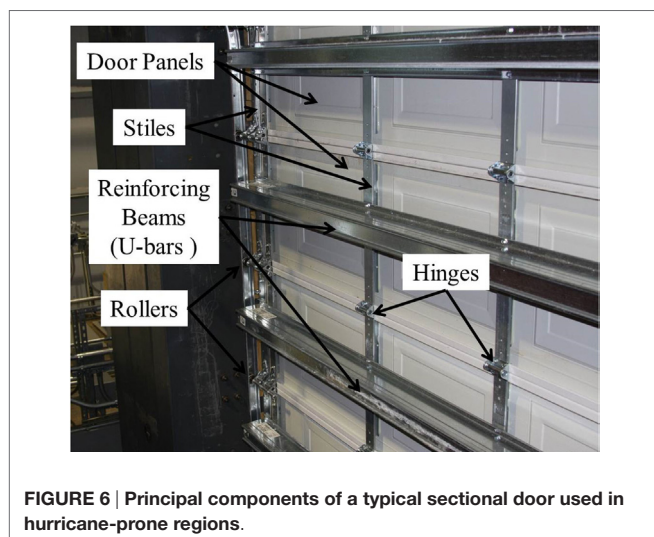
1. Local buckling of U-bars, i.e., visible plastic deformation.
2. Disengagement of door panels from the tracks, i.e., separation of the rollers attached at the back of door panels from the tracks.
3. Adhesive failure between stiles and door panels.

The adhesive failure mode appeared to largely be a cosmetic issue and did not affect the overall structural rigidity or operability, thus it was not deemed sufficient damage to stop a test. Individual performance of each door is described below. Note that strain and displacement data are plotted for the pressure intensity level leading up to failure.

- Door 1 (**Figure 8A**) exhibited a large area of adhesive failure (**Figure 8B**). After holding the load at -2.0 kPa (-42 psf) for 5 min, the load was released. No obvious plastic deformations were observed for the door panels and other components, and the door was still operable. Between -4.0 kPa (-84 psf) and -4.5 kPa (94 psf), significant local buckling of U-bars was observed, followed by disengagement failure (**Figure 8C**). **Figure 9A** presents the pressure-strain and pressure-displacement relationships of Door 1. The strain responses increased almost linearly with the applied load. Note that the strains measured at locations 2 and 5 (i.e., strains at mid-span of the U-bars at the top of door panels 1 and 4) show a sudden change in curvature when the negative pressure was increased from -1.4 kPa (-30 psf) to -1.9 kPa (-40 psf). A possible reason

for the change may be the significant adhesive failure during the fourth load step. The displacement-load relationship is almost linear. Studying **Figure 9A**, note that the adhesive failure of Door 1 affects the strains but has negligible influence on displacements.

- Door 2 (**Figure 8D**) exhibited a high resistance to static pressure. When the load was increased in Step 12 from -5.5 kPa (-115 psf) to -6.0 kPa (-125 psf), the bottom three U-bars buckled, and disengagement of the bottom four panels from the tracks followed immediately (**Figure 8E**). Strain and displacement measurements increased linearly with the applied negative pressure (**Figure 9B**). Fewer displacement measurements are plotted in **Figure 9B** than the other doors because some of the traceable spheres were not tracked successfully during FS testing on Door 2.
- Door 3 (**Figure 8F**) exhibited the first sign of damage when the load was increased from -2.0 kPa (-42 psf) to -2.5 kPa (-52 psf). A popping sound was heard, and a small separation between door panels and stiles was noted. Door 3 was able to operate after releasing the pressure from -2.5 kPa (-52 psf). During the next step from -2.5 kPa (-52 psf) to -3.0 kPa (-63 psf), a significant disengagement failure from door panels 2 through 8 was observed (**Figure 8G**). Measured strains and displacements show a linear relationship with applied negative pressure (**Figure 9C**). The bottom and top panels (panels 1



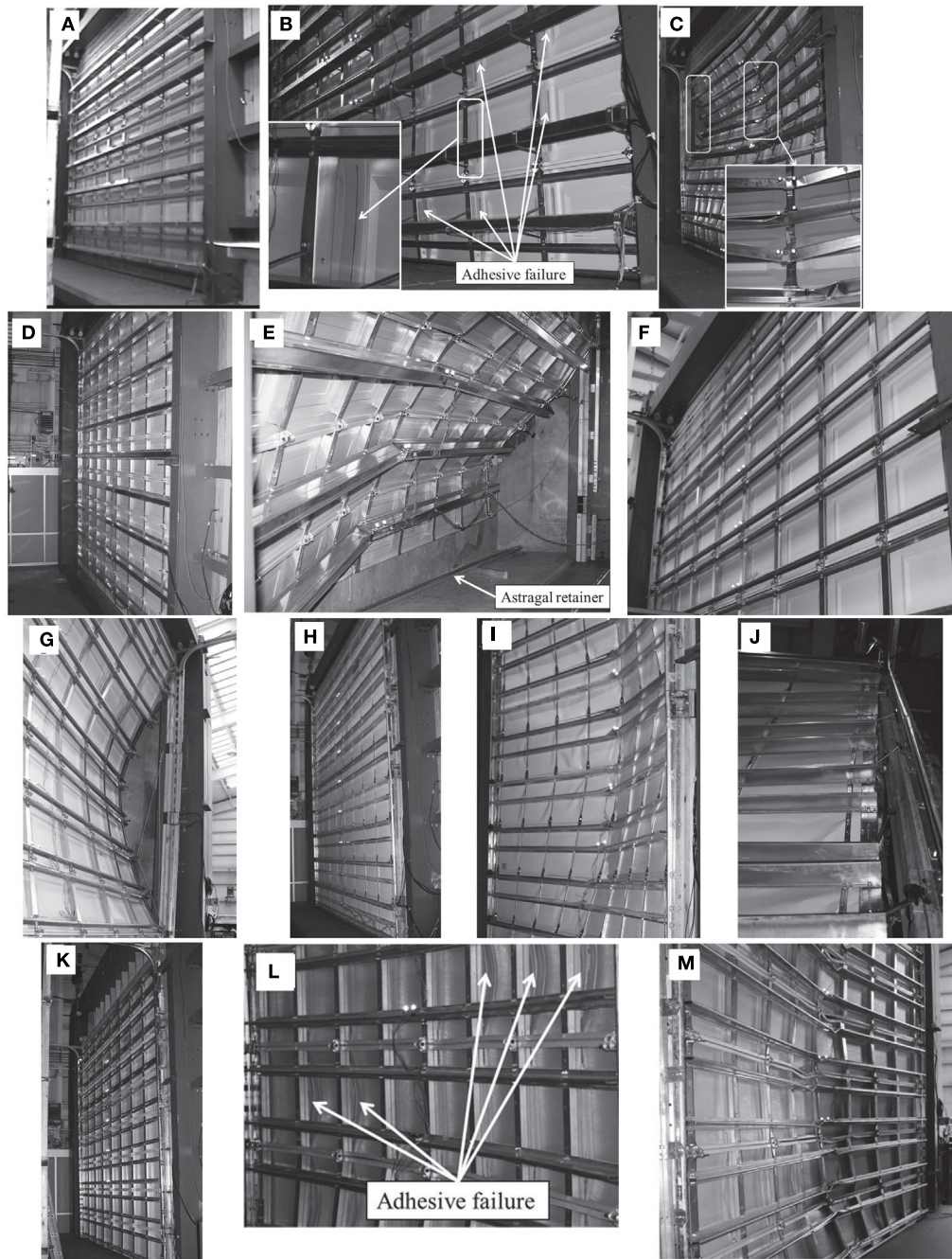


FIGURE 8 | Door 1 (A) before testing, (B) at adhesive failure, and (C) at catastrophic failure; Door 2 (D) before testing and (E) at catastrophic failure; Door 3 (F) before testing and (G) at catastrophic failure; Door 4 (H) before testing, (I) at catastrophic failure showing local buckling of U-bars, and (J) at catastrophic failure showing disengagement of rollers from the tracks; and Door 5 (K) before testing, (L) at adhesive failure, and (M) at catastrophic failure.

and 9) had smaller strain and displacement responses compared to the others, which could be a factor causing disengagement failure of panels 2 through 8.

- Door 4 (**Figure 8H**) failed in the range of -6.0 kPa (-125 psf) to -6.5 kPa (-136 psf). Significant local buckling failure was observed on the mid-span of the U-bars for door panels 2

through 8 (**Figure 8I**), and disengagement failure followed (**Figure 8J**). Strain and displacement responses exhibit an almost linear relationship with applied load (**Figure 9D**).

- Door 5 (**Figure 8K**) exhibited an adhesive from -3.5 kPa (-73 psf) to -4.0 kPa (-84 psf) (**Figure 8L**), but it did not affect the operability of the door. When the load reached -4.5 kPa

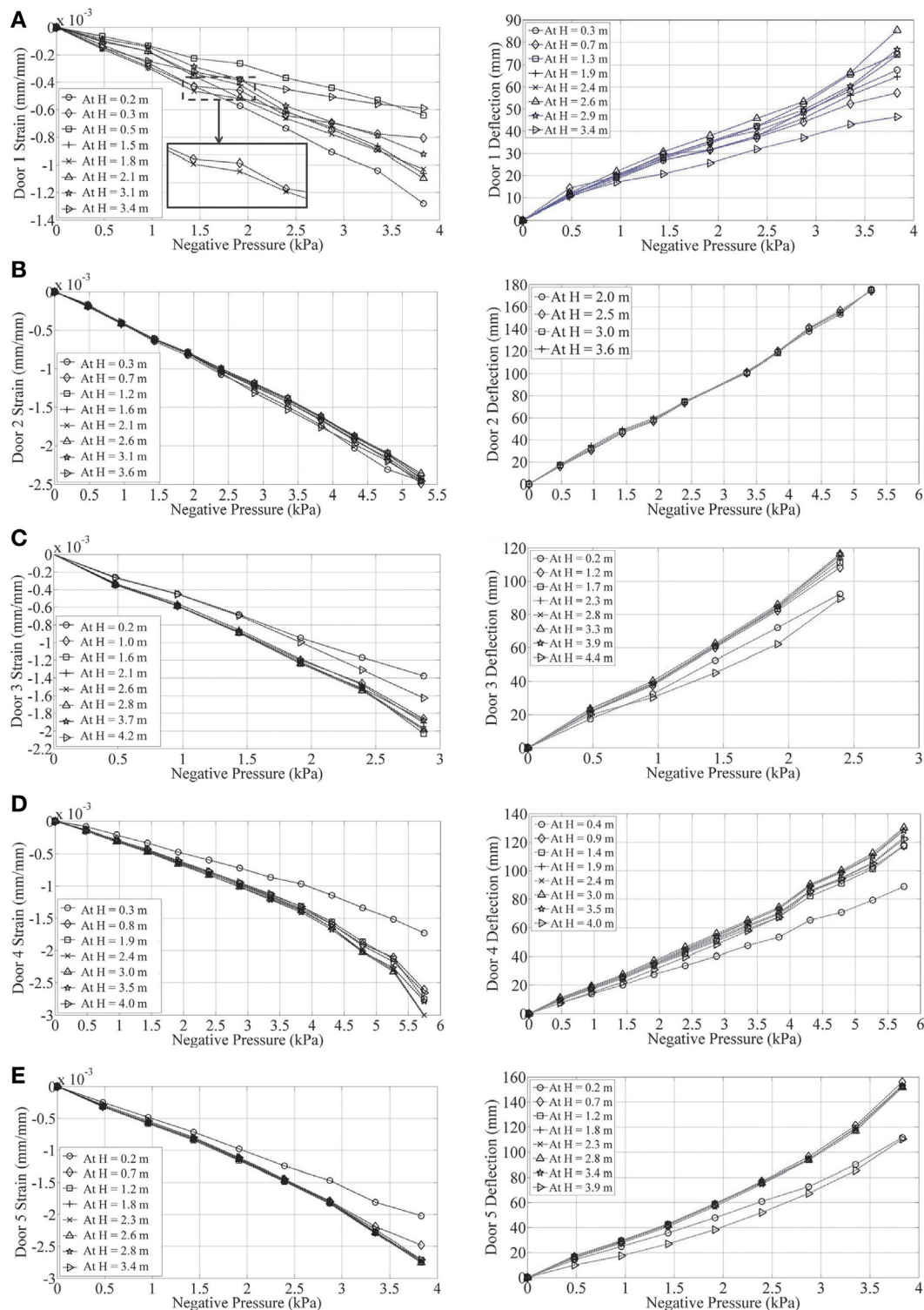


FIGURE 9 | Measured pressure–strain relationships and pressure–displacement relationships for Doors 1–5 [(A–E), respectively] at multiple locations. All strains and displacements are measured at center span (see Figure 7A) at the height indicated in the legend.

(−94 psf), local buckling occurred on all U-bars except the top one (Figure 8M). Testing on Door 5 was stopped at −4.5 kPa (−94 psf). No disengagement failure followed, since −4.5 kPa

(−94 psf) is the upper limit of the ninth step. With the load increased, the strain and displacement responses increased linearly (Figure 9E).

TABLE 3 | Summary of the pressure at failure of test specimens.

Door model	Test pressure ^a (kPa) (1.5 × design pressure)	Adhesive failure pressure (kPa)	Catastrophic failure modes	Catastrophic failure pressure (kPa)
Door 1	+3.0/−3.3	~−1.9	Local buckling of U-bars	~−4.1
Door 2	+3.1/−3.6		Local buckling of U-bars	~−5.7
Door 3	+4.0/−4.6	~−2.4	Disengagement failure	~−2.6
Door 4	+3.6/−4.1		Local buckling of U-bars	~−6.2
Door 5	+3.3/−3.7	~−3.8	Local buckling of U-bars	~−4.5

^aTest pressure is 1.5 times of design pressure (FBC, 2010).

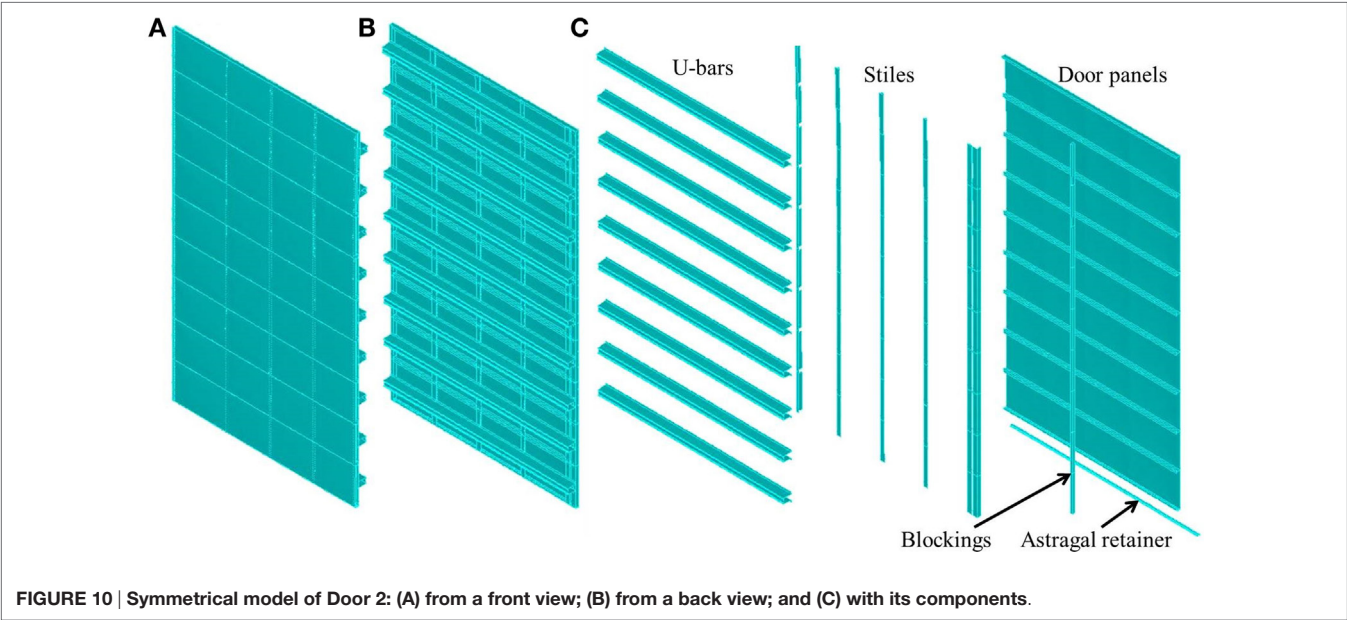


FIGURE 10 | Symmetrical model of Door 2: (A) from a front view; (B) from a back view; and (C) with its components.

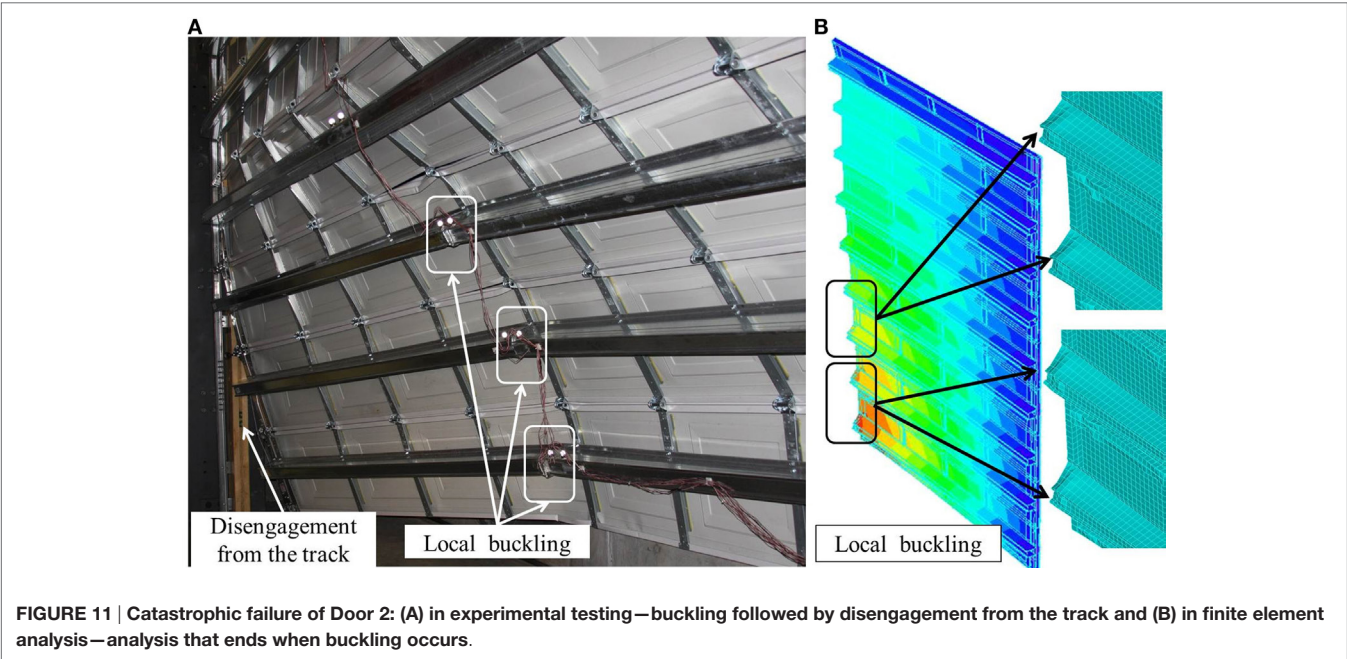


FIGURE 11 | Catastrophic failure of Door 2: (A) in experimental testing—buckling followed by disengagement from the track and (B) in finite element analysis—analysis that ends when buckling occurs.

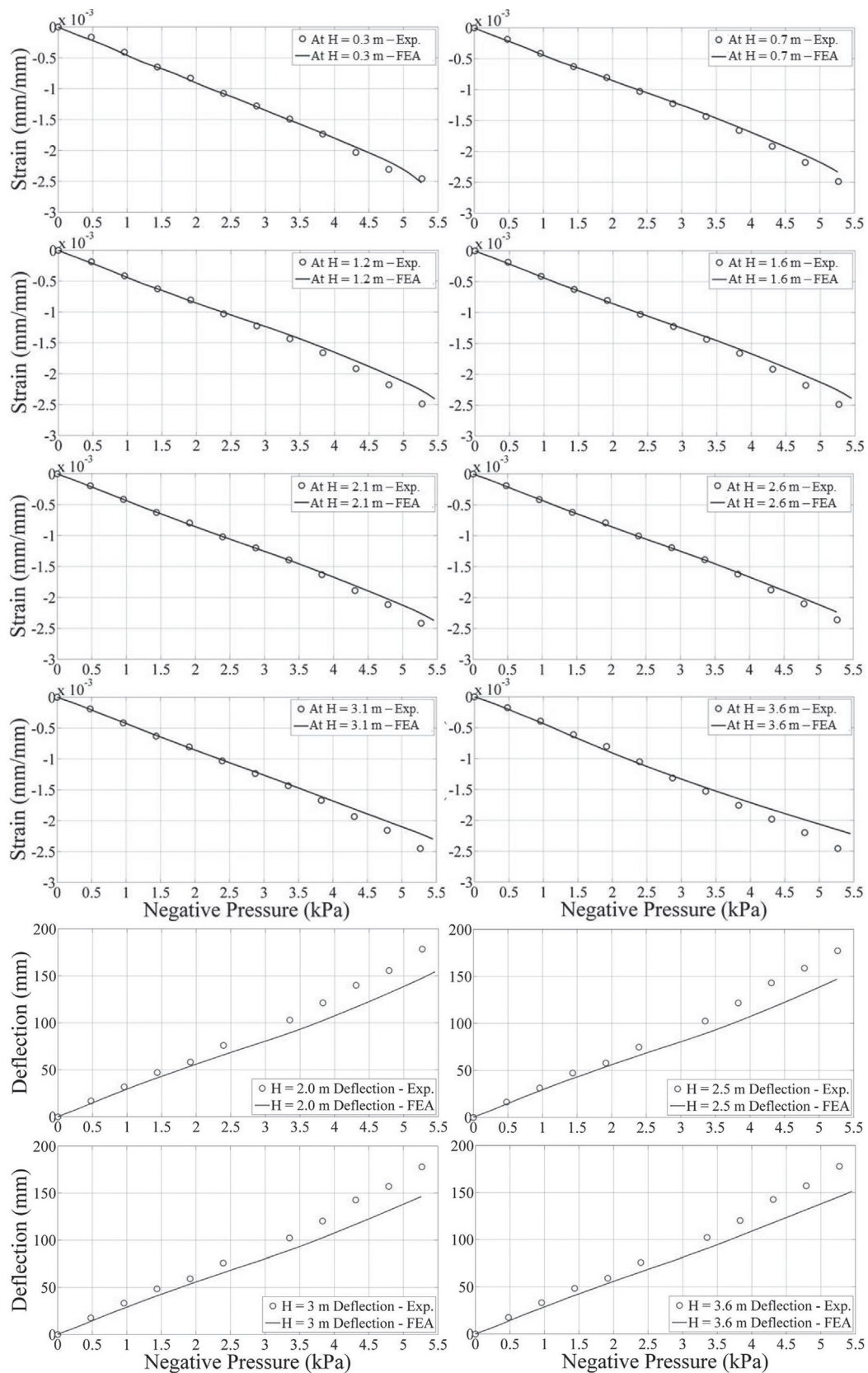


FIGURE 12 | Strain and displacement comparisons between finite element analysis (FEA) results and experimental measurements.

Local buckling of U-bars usually led to disengagement failure (Doors 1, 2, and 4); therefore, tests on Doors 1, 2, and 4 were stopped at the occurrence of disengagement failure. Examination after testing on each door specimen presented extreme bending and yielding of roller shafts occurring for Doors 1–4 that had disengagement failure. Summarizing, the failure sequence can be described as: local buckling of U-bars reduced the stiffness of the door and therefore resulted in excessive deflections of door panels, which caused large reaction forces at the rollers constrained in the tracks. The reaction forces produced large moments on the roller shafts and caused their yielding, which prompted the disengagement failure. While Door 3 did not have local buckling failure of U-bars, under that same vacuum load, it showed larger strain and displacement responses compared to the others. Its failure sequence skipped the first step of local buckling mentioned above. **Table 3** lists the negative pressure of these specimens at failure compared to their test pressure. According to Florida Building Code Testing Application Standard 202-94 (FBC, 2010), the test pressure for garage doors should be 1.5 times of their design pressure. Door 3 had catastrophic failure of disengagement at a pressure lower than its test pressure.

Finite Element Analysis

Full-scale experimental testing is an ideal method to understand the performance of a structure under a certain load condition (Sinno, 2008; Morrison, 2010; Aly et al., 2013; etc.). However, due to the inherent time and expense of testing, it is impractical to test many scenarios. Therefore, FEA was applied to complement physical testing to determine its effectiveness to capture the performance of a multi-component system under wind loading. The thought process was that if an FEA model could be quickly validated, it would open up the possibility of predicting performance of new testing configurations (e.g., the same specimen, but with a prescribed construction defect) to inductively research performance on a small set of specimens.

Door 2 was selected for modeling (**Figure 10**) because it exhibited local buckling failure of U-bars and disengagement failure of door panels as well as the highest failure pressure/test pressure ratio. The FEA model was created in ADINA 8.8 (ADINA, 2011), which accounted for contact constraints, material non-linearity, and second-order effects.

The main components of the FE model include the door panels, stiles, and U-bars (modeled as 4-node elastic-perfect plastic steel shell elements), wood blocking (modeled as an 8-node linear-elastic solid element), and the astragal retainer (modeled as a 4-node elastic-perfect plastic aluminum shell element). To simulate the constraints of the door in experimental testing, boundary conditions as described below were used for the model: symmetrical boundary conditions were applied along the vertically spanning centerline. The effects of hinges connecting adjacent door panels were modeled using corresponding constraints at the hinge locations. The connection between the astragal retainer and the bottom door panel, and fasteners used in the physical door (e.g., fasteners connecting U-bars to stiles, and fastener connecting blockings to stiles) were modeled as rigid links, constraining the linked nodes so that they move together when the model deforms. Contact boundary conditions were

used between surfaces wherever there were no constraints, but contact might occur (i.e., the bottom of one door panel and the top of the panel below it). As a preliminary model, two simplifications were made in the boundary conditions:

1. The adhesive connecting stiles to door panels was modeled as rigid links.
2. The rollers were not included in the FEA model, and instead the constraints from them were treated as boundary conditions along the sides of the model.

The material properties of door panels, stiles, and U-bars were provided by the manufacturer. For the blocking material, properties of No. 2 southern yellow pine were elastic modulus $E = 9,804$ MPa (1,422 ksi), density $\rho = 554$ kg/m³ (34.5 lb/ft³), and Poisson's ratio $\mu = 0.33$. For the aluminum, the properties were $E = 68,948$ MPa (10,000 ksi), $\rho = 2,685$ kg/m³ (167.6 lb/ft³), $\mu = 0.33$, and yielding strength $\sigma_{\text{yield}} = 276$ MPa (40 ksi), respectively. The same load measured during the experiment was applied on the model.

Figure 11 shows the catastrophic failure of Door 2 and FEA model results, which are nearly identical. The FEA captured successive failures states, i.e., local buckling of U-bars at -5.5 kPa (-115 psf) followed by a disengagement failure at -5.7 kPa (-120 psf). The comparisons between FEA and experimental results in strain and displacement responses are shown in **Figure 12**. The load limit in **Figure 12** is -5.3 kPa (-110 psf) to be consistent with the plot showing experimental measurements. From the strain and displacement comparisons, the following can be seen: (a) FEA results match well with experimental measurements in both strain and displacement responses of Door 2 and (b) the difference between FEA results and experimental measurements at larger loads is more than that at smaller loads. Differences may be attributed to the repeated step-and-hold loading pattern causing material fatigue (e.g., connecting fasteners, roller shafts, etc.) and therefore decreasing the structural stiffness; simplifications in boundary conditions might miss the deformation at the roller/track interface. These results clearly demonstrate the value of combining FEA with FS testing. This success is an important finding for the field, which today is still heavily reliant on empirical data or simplified closed-form solutions to predict behavior.

CONCLUSION

This paper presents a new large-scale dynamic wind pressure simulator developed at the University of Florida. The simulator was designed to produce wind pressures associated with a SSHWS Category 5 hurricane to test FS building components. The simulator showed an acceptable fidelity to replicate time-varying wind pressure loads up to ~ 1 Hz, without additional modification (e.g., adjustment of tuning parameters in the closed-loop control system to improve fidelity or modification of leakage conditions). The system can be widely applied to a wide range of wind engineering applications, including out-of-plane loading of components and cladding. FS experiments on whole as-installed systems provide more realism but at a much greater cost than component level

testing. Further, this paper demonstrated the practical use of FEA to quickly model the specimen. This approach, combining FS experimental testing and numerical analysis, offers a reliable and cost-efficient way to determine the fragility of building components under various hazard intensities and is ideally suited for a performance-based engineering approach (e.g., McCullough and Kareem, 2011).

AUTHOR CONTRIBUTIONS

SS assisted with the design of the testing apparatus and performed the computational analysis and FEA. FM facilitated the overall design and construction of the testing apparatus and provided

overall coordination for the experimental testing. HU led the design team. JS assisted with the performance testing.

ACKNOWLEDGMENTS

The authors wish to acknowledge Special-Lite Inc. for sponsoring research and development. Additional support was provided by Oak Ridge National Laboratory through the Southeast Region Research Initiative (SERRI), as well as the Florida Building Commission. The authors would also like to thank Jimmy Jesteadt, Alex Esposito, Ken Bowditch, Brian Rivers, and Dr. Gary Consolazio for their assistance in experimental testing and finite element analysis.

REFERENCES

- ADINA. (2011). *ADINA Theory and Modeling Guide Volume 1: ADINA Solids & Structures*. Watertown, MA: ADINA R&D Inc.
- Aly, A. M., Chowdhury, A. G., and Erwin, J. (2013). Design and fabrication of a new open jet electric-fan wall of wind facility for coastal research. *Coast. Hazards*. 29, 137–148. doi:10.1061/9780784412664.014
- AS/NZS 1170.2:2011. (2011). *Structural Design Actions – Part 2: Wind Actions*. Sydney, NSW: SAI Global Limited under licence from Standards Australia Limited.
- ASCE 7. (2010). *ASCE Standard, Minimum Design Loads for Buildings and Other Structures*. Reston, VA: ASCE Standard 7-10.
- ASTM. (2006). *Standard Test Method for Structural Performance of Exterior Windows, Doors, Skylights, and Curtain Walls by Cyclic Air Pressure Differential*. Philadelphia: ASTM E1233.
- ASTM. (2009). *Standard Test Method for Structural Performance of Exterior Windows, Doors, Skylights and Curtain Walls by Uniform Static Air Pressure Difference*. Philadelphia: ASTM E330.
- ASTM. (2012). *Specification for Performance of Exterior Windows, Curtain Walls, Doors, and Impact Protective Systems Impacted by Windborne Debris in Hurricanes*. Philadelphia: ASTM E1996.
- ASTM. (2013). *Standard Test Method for Performance of Exterior Windows, Curtain Walls, Doors, and Impact Protective Systems Impacted by Missile(s) and Exposed to Cyclic Pressure Differentials*. Philadelphia: ASTM E1886.
- BS EN 12211:2016. (2016). *Windows and Doors. Resistance to Wind Load. Test Method*. BSI.
- Cook, N. J. (1992). Dynamic response of single-ply membrane roofing systems. *J. Wind Eng. Ind. Aerod.* 42, 1525–1536. doi:10.1016/0167-6105(92)90161-3
- Cook, N. J., Keevil, A. P., and Stobart, R. K. (1988). Brerwulf – the big bad wolf: I'll huff and I'll puff and I'll blow your house down! *J. Wind Eng. Ind. Aerod.* 29, 99–107. doi:10.1016/0167-6105(88)90149-3
- FBC. (2010). *Criteria for Testing Impact & Nonimpact Resistant Building Envelope Components Using Uniform Static Air Pressure*. Washington, DC: FBC TAS 202-94, International Code Council Inc.
- FEMA. (2005). *Summary Report on Building Performance: 2004 Hurricane Season*. Washington, DC: FEMA 490.
- Ginger, J. D., Henderson, D. J., Leitch, C. J., and Boughton, G. N. (2007). Tropical Cyclone Larry: estimation of wind field and assessment of building damage. *Aust. J. Struct. Eng.* 7, 209–224.
- Golos, K., and Ellyin, F. (1987). Generalization of cumulative damage criterion to multilevel cyclic loading. *Theor. Appl. Fract. Mech.* 7, 169–176. doi:10.1016/0167-8442(87)90032-2
- Gurley, K. R., and Masters, F. J. (2011). Post-2004 hurricane field survey of residential building performance. *Nat. Hazards Rev.* 12, 177–183. doi:10.1061/(ASCE)NH.1527-6996.0000044
- Henderson, D. J., and Ginger, J. D. (2011). Response of pierced fixed corrugated steel roofing systems subjected to wind loads. *Eng. Struct.* 33, 3290–3298. doi:10.1016/j.engstruct.2011.08.020
- Henderson, D. J., Morrison, M. J., and Kopp, G. A. (2013). Response of toe-nailed, roof-to-wall connections to extreme wind loads in a full-scale, timber-framed, hip roof. *Eng. Struct.* 56, 1474–1483.
- Ho, T. C. E., Surry, D., and Morrish, D. (2003). *NIST/TTU Cooperative Agreement – Windstorm Mitigation Initiative: Wind Tunnel Experiments on Generic Low Buildings*. London, ON: The Boundary Layer Wind Tunnel Laboratory, The University of Western Ontario, 106.
- IBC. (2012). *2012 International Building Code*. Washington, DC: International Code Council Inc.
- Kopp, G., Morrison, M., Gavanski, E., Henderson, D., and Hong, H. (2010). 'Three Little Pigs' project: hurricane risk mitigation by integrated wind tunnel and full-scale laboratory tests. *Nat. Hazards Rev.* 11, 151–161. doi:10.1061/(ASCE)NH.1527-6996.0000019
- Kopp, G. A., Morrison, M. J., and Henderson, D. J. (2012). Full-scale testing of low-rise, residential buildings with realistic wind loads. *J. Wind Eng. Ind. Aerod.* 10, 25–39. doi:10.1016/j.jweia.2012.01.004
- Li, Z. X., Chan, T. H. T., and Ko, J. M. (2001). Fatigue analysis and life prediction of bridges with structural health monitoring data – part I: methodology and strategy. *Int. J. Fatigue* 23, 45–53. doi:10.1016/S0142-1123(00)00068-2
- Mahendran, M. (2003). *Simulation of Cyclonic Wind Forces on Roof Claddings by Random Block Load Testing*. Technical Report 0158-8338, No. 38. Townsville, QLD: James Cook University of North Queensland. Cyclone Testing Station.
- McCullough, M., and Kareem, A. (2011). "A framework for performance-based engineering in multi-hazard coastal environments," in *Structures Congress 2011*, eds D. Ames, T. L. Droessler, and M. Holt (Las Vegas: American Society of Civil Engineers), 1961–1972.
- Miner, M. A. (1945). Cumulative damage in fatigue. *J. Appl. Mech.* 67, A159–A164.
- Minor, J. (2005). Lessons learned from failures of the building envelope in windstorms. *J. Architect. Eng.* 11, 10–13. doi:10.1061/(ASCE)1076-0431(2005)11:1(10)
- Morrison, M. (2010). *Response of a Two-Story Residential House under Realistic Fluctuating Wind Loads*. Ph.D. thesis, The University of Western Ontario, London, ON, Canada.
- Oh, J. H. (2004). *Wind-Induced Internal Pressure in Low-Rise Building*. MS thesis, The University of Western Ontario, London, ON, Canada.
- Rosowsky, D., and Schiff, S. (2003). What are our expectations, objectives, and performance requirements for wood structures in high wind regions? *Nat. Hazards Rev.* 4, 144–148. doi:10.1061/(ASCE)1527-6988(2003)4:3(144)
- Sinno, R. R. (2008). *Response of Metal Roofs to Uniform Static and True Hurricane Wind Loads*. International Specialty Conference on Cold-Formed Steel Structures. Available at: <http://scholarsmine.mst.edu/iscss/19icfss/19icfss-session5/1>

Conflict of Interest Statement: The authors declare that the research was conducted in the absence of any commercial or financial relationships that could be construed as a potential conflict of interest.

Copyright © 2017 Shen, Masters, Upjohn and Sinnreich. This is an open-access article distributed under the terms of the Creative Commons Attribution License (CC BY). The use, distribution or reproduction in other forums is permitted, provided the original author(s) or licensor are credited and that the original publication in this journal is cited, in accordance with accepted academic practice. No use, distribution or reproduction is permitted which does not comply with these terms.



A Multichamber, Pressure-Based Test Method to Determine Wind Loads on Air-Permeable, Multilayer Cladding Systems

Connell Shamus Miller¹, Gregory A. Kopp^{1*}, Murray J. Morrison², Gary Kemp³ and Nick Drought³

¹ Boundary Layer Wind Tunnel Laboratory, Faculty of Engineering, University of Western Ontario, London, ON, Canada,

² Insurance Institute for Business and Home Safety, Richburg, SC, USA, ³ Cambridge Consultants Ltd., Cambridge, UK

OPEN ACCESS

Edited by:

Matthew Mason,
University of Queensland, Australia

Reviewed by:

Aly Mousaad Aly,
Louisiana State University, USA
Ioannis Zisis,
Florida International University, USA

*Correspondence:

Gregory A. Kopp
gak@blwtl.uwo.ca

Specialty section:

This article was submitted to Wind Engineering and Science, a section of the journal Frontiers in Built Environment

Received: 30 September 2016

Accepted: 18 January 2017

Published: 10 February 2017

Citation:

Miller CS, Kopp GA, Morrison MJ, Kemp G and Drought N (2017) A Multichamber, Pressure-Based Test Method to Determine Wind Loads on Air-Permeable, Multilayer Cladding Systems. *Front. Built Environ.* 3:7. doi: 10.3389/fbuil.2017.00007

Current standardized testing on air-permeable multilayer cladding is inaccurate since one of the primary parameters for setting the peak net wind loads across the cladding is the external pressure gradient, which is removed from all standardized testing. After implementing a latex-barrier system and examining the control strategy for the pressure loading actuators, a multichamber airbox system for testing air-permeable multilayer cladding is developed and compared to a benchmark study performed by the Insurance Research Lab for Better Homes. The results indicate that using multichamber, pressure-based testing to obtain wind loads for air-permeable, multilayer wall systems with flexible cladding is sufficiently accurate. This method also shows that eliminating temporal variations from the external pressures for easier standardized testing would provide fairly accurate results.

Keywords: wind loads, full-scale test methods, air-permeable cladding, pressure equalization, pressure loading actuators

INTRODUCTION

Background

Severe wind storms around the world continue to cause significant economic losses. While there have been significant advances and successes with building codes, design standards, and construction methods, which have reduced major structural failures (e.g., Gurley and Masters, 2011), losses caused by extreme wind storms continue to grow. These tend to be due to failures of the building envelope and connections, e.g., cladding failures caused by either net pressure loads or wind-borne debris impacts, failures of nailed connections, etc. Entry of rain water through the resulting openings is a significant source of damage (e.g., Sparks et al., 1994; Gurley and Masters, 2011). This contrasts significantly with earthquakes where a substantial portion of the losses is due to failures of major structure members. Where structural members fail in wind storms, they are often due to failure of an envelope component first, such as a window or door that allows internal pressurization. Thus, mitigation of economic losses in wind storms is strongly dependent on enhanced performance of cladding systems and their connections.

The performance of cladding and connections is usually evaluated by component tests, normally in compliance with standardized tests. Examples of standardized tests that are used to evaluate product performance under wind loads include ASTM D5206 (2013) for vinyl siding,

ASTM E1592 (2012) for metal roofing, and ASTM E1300 (2012) for glazing and glass. Most of these standardized tests make use of a sealed airbox system,¹ where the pressure required to fail the particular product is obtained. Many of these standardized tests use uniform, static pressures or slowly increasing pressures, such as those listed above. For components that have low-cycle fatigue as a failure mechanism, sinusoidally varying pressures at various frequencies and amplitudes are applied (Henderson et al., 2013a). In all cases, the pressures applied by these standard tests are uniform over the component. This, of course, provides applied loads that are significantly different than real wind loads, but which are relatively simple and inexpensive to apply (Kopp et al., 2012).

While there are standardized tests to assess the capacity of cladding systems, wind loads are much less well-defined, particularly for cladding and component systems with air-permeable, multilayer assemblies. ASCE 7-05 (American Society for Civil Engineering, 2006) acknowledges this (in section C6.5.2.2 of ASCE 7-05 or section 30.1.5 of ASCE 7-10), indicating that

The designer may elect either to use the loads derived from Section 6.5 [single-layer pressures] or to use loads derived by an approved alternative method. If the designer desires to determine the pressure differential across the air-permeable cladding element, appropriate full-scale pressure measurements should be made on the applicable cladding element, or reference be made to recognized literature for documentation pertaining to wind loads.

For such systems, net wind load coefficients are not generally known, and standard methods for determining wind loads, i.e., scale-model wind tunnel tests, cannot be used. While ASCE 7 indicates that “full-scale pressure measurements should be made,” there are limited methods that have been developed. For example, the test standard for vinyl siding, which is a type of relatively low-cost cladding used in North American residential wood-frame wall assemblies, is ASTM D5206 (2013). In this standard, pressure equalization is eliminated by placing an airtight barrier between the siding layer and internal sheathing layer or insulating layer. Uniform, static pressures are then applied *via* an airbox in order to determine the capacity of the siding. This yields the net pressure at the limit state (assuming that the failure mechanism and capacity are not substantially altered by the approach). The limit-state pressure is related to the wind loads in ASTM D3679 (2013). This standard requires that the design external pressure in ASCE 7 be multiplied by a “pressure equalization factor” (PEF), which in this case has a value of 0.36. Thus, ASTM D3679 (2013) assumes that the net pressure across the siding is 64% lower than the external pressure acting on the wall (i.e., 64% lower than the net pressure across the entire wall, assuming the building internal pressure is 0 or that there is a sealed internal layer). The PEF in ASTM D3679 (2013) was obtained from static, uniform airbox

tests conducted by Architectural Testing, Inc. (2002); with similar values found by uniform, but time-varying, pressures in Gavanski and Kopp (2011a). Recently, using full-scale wind tunnel tests from the Insurance Institute for Business and Home Safety (IBHS) Research Center, Morrison and Cope (2015) found a PEF of closer to 0.8, indicating load coefficients that are more than double those of ASTM D3679 (2013), all else being equal. As discussed in detail below, the external pressure gradient is a primary parameter in setting the net wind load on air-permeable, multilayer cladding. Clearly, there is a need to develop appropriate methodologies for assessing net pressures for air-permeable, multilayer assemblies, which is the objective of the current study.

Methods for Determining Wind Loads on Air-Permeable, Multilayer Cladding

There are at least four possible methods for determining the net pressure coefficients on air-permeable, multilayer cladding systems: (i) analytical models or computational fluid dynamics, (ii) large-scale or full-scale wind tunnel tests, (iii) full-scale field measurements, and (iv) airbox tests with applied external pressures.

Bienkiewicz and Sun (1997) have shown that the wind loads for air-permeable multilayer systems depend on the external pressure gradient, the gap between panels, the thickness of the panels, the cavity depth between the panels and the interior surface, and the loss coefficients for the flows through the various openings. Because of the prominent dependence on the external pressure gradient, compartmentalization of the cavity is extremely effective at reducing the net wind loads (Kumar, 2000) by limiting the effects of the spatial gradients, leaving only the second order dependence on the temporal gradient. Rain screen walls make extensive use of this concept (Kumar, 2000). Oh and Kopp (2014) found that, because of the external pressure gradient, there is a neutral pressure line, which causes the net, area-averaged pressure coefficients to reduce with area faster than the external pressure coefficients do. These authors’ analytical model shows that spatial and temporal variations of the cavity pressures can be modeled analytically for one-dimensional cavity pressure fields using the unsteady Bernoulli equation and appropriate loss models. Sun and Bienkiewicz (1993) used a similar, but steady-flow, model to model the mean two-dimensional cavity pressure field. However, a full spatial and temporal analytical model of cavity pressures has not yet been developed. Computational fluid dynamics-based solutions are also possible, but these have not been conducted to the authors’ knowledge.

Large-scale wind tunnel tests have been used to study pressure equalization for roof pavers. Mooneghi et al. (2014) showed that sufficient tap resolution is required to ascertain wind loads on these systems, using their 1/2-scale building model in the wall of wind facility. Considering the small gaps involved, it seems unlikely the more typical boundary layer wind tunnel model scales can be used since the full-scale gaps are often on the order of 3 mm and smaller. For roof-mounted photovoltaic arrays, larger gaps mean that standard boundary layer wind tunnels can be used at scales of 1/20 to 1/30, although there has not yet been a full-scale validation of these relatively large-model-scale

¹ We will use the terms “airbox” and “pressure chamber” synonymously to indicate the enclosed volume where pressure is applied to a specimen’s surface.

results (compared to typical model scales of 1/300 to 1/500 in most boundary layer wind tunnels). For vinyl siding, with gaps between panels that are largely undefined (because of how the panels clip together), model-scale wind tunnel methods cannot be used at all (even at 1/10). For this reason, Morrison and Cope (2015) examined such systems at full scale in the IBHS Research Center wind tunnel. The main disadvantage of this approach is that it is not cost effective for routine product testing and one can only test the products on a limited set of building sizes, limiting the generality of the findings, as discussed by Kopp et al. (2012). Full-scale field measurements are useful for validation of other test methods, but the cost, limited pressure tap resolutions, and limited numbers of building configurations mean that this approach cannot be practically used for determining design loads.

Kopp et al. (2012) have shown that full-scale multichamber airbox testing can be used to test overall building responses to wind loads. However, it has not been established whether such approaches can be used with air-permeable, multilayer systems. Given the potential advantages of a relatively low-cost and straightforward test methodology, the objective of the current study is to determine whether multichamber airbox testing is feasible for assessing wind loads on air-permeable, multilayer cladding systems. To this end, the multichamber, PLA approach of Kopp et al. (2010, 2012) is modified, as described in Section “The Multichamber, PLA Approach,” with a test case of vinyl siding examined in Section “Test Case for Air-Permeable, Multilayer Cladding.”

THE MULTICHAMBER, PLA APPROACH

Background

One of the first systems to replicate realistic fluctuating pressures on a scale suitable for representative sections of the building envelope is the Building Research Establishment's real-time wind uniform load follower (BRERWULF; Cook et al., 1988). While this test method was a significant advance, the main disadvantage of the BRERWULF system is that it could not accommodate airflow through the specimen, which is common in many standard building materials. As such, a multichamber BRERWULF system for testing air-permeable cladding would not function well because of the necessity to allow airflow between chambers.

A loading system capable of applying spatially and temporally varying loads on standing seam metal roof cladding was developed at Mississippi State University (Sinno et al., 2003; Surry et al., 2007). The test rig used large capacity electromagnets to apply an array of quickly varying uplift loads on top of a uniform positive pressure applied from an airbox underneath the cladding. Importantly, the MSU system brings the application of realistic (temporally and spatially varying) wind pressures to the test specimen. The disadvantages of this technique are that it only works with metal cladding elements and there is a significant amount of tuning to the system required before a specific loading trace could be applied to a specimen.

Kopp et al. (2010, 2012) presented a loading system based on “pressure loading actuators” (PLAs), which overcame the limitations of the BRERWULF and MSU loading systems. The

PLA system uses multiple pressure chambers to capture the spatial variations of the wind loads while each individual PLA is able to capture pressure fluctuations up to about 10 Hz with peak pressures of up to about 23 kPa in pressure and –20 kPa in suction (Kopp et al., 2010). Thus, very large loads, at the limit states of wood-frame houses, could be applied (Morrison et al., 2012; Henderson et al., 2013b) to buildings with significant leakage through the building envelope *via* a system of flexible, independent airboxes.

Pressure Chambers

All pressure-based loading systems require a chamber in which to apply the pressures. Usually, these are nominally airtight and of fixed volume, i.e., they have solid side walls. Thus, the PLAs also require pressure chambers in order to apply the load to a building surface. However, for applying loads to the surface of a house, Morrison et al. (2012) developed a system of multiple, independent, flexible airbags with rigid supporting frames. These pressure chambers consisted of a rigid modular lid, which incorporated a molded inlet duct with air filter, the surface of the building (test specimen), which forms one surface of the chamber, and a flexible vinyl skirt that encloses the space between the lid and building surface, which forms the walls of the chamber. This system was required to be at least nominally airtight so that the pressure traces could be controlled reliably with leakage coming only through the building surface (such as bricks or cracks). The lids of the pressure chambers were connected to a rigid reaction frame. The skirt or membrane was required to be flexible since the building or component could deflect (on the order of 15 cm or more). Each pressure chamber was independent of the others because they were separated by approximately 2” (5 cm) with no physical communication between them.

This pressure-chamber system was adequate for testing the structural response of buildings, but there is a significant issue that needs to be addressed for cladding tests. The surface areas outside of the chambers, but part of the test sample, are problematic for multilayer cladding tests where the intent is to determine the net pressures across layers of the cladding. The reason for this issue is that the cavity pressures depend significantly on the external pressure gradients, as discussed above. Thus, these non-pressurized areas need to be eliminated (or only located at non-porous areas of the cladding surface) because they artificially alter the pressure gradients. For vinyl siding, where there may be continuous leakage, the only solution is to eliminate the unloaded areas on the external surface of the cladding by having common “skirts” for adjacent pressure chambers. This poses a challenge for the PLA control system because there are two forms of communication between adjacent chambers: (i) net flows through the interior volume of the cavity between layers from one chamber to another and (ii) the changes in chamber volume due to the movement of the skirt because of the time-varying differences in pressure between adjacent chambers. Details of the implemented pressure-chamber solution for testing vinyl siding are provided in Section “Test Case for Air-Permeable, Multilayer Cladding.” To understand the control solution, the operation of the PLAs is described next.

Flow-Reversing Valves and the PLAs

Conceptually, the control of the pressure in an airbox can be done in two different ways. One can vary the supply pressure into the airbox by varying the fan speed and direction using a variable speed drive. Alternatively, one can use a flow-reversing valve to control the pressure inside a pressure chamber. The first option provides the simplest and cheapest solution; however, it is not technically feasible to change the fan speed fast enough to be able to meet both the pressure magnitudes and frequencies required to simulate realistic wind loads on cladding elements. As such, the conceptual design consists of a fan or blower to produce the pressures, a valve system to regulate the applied pressures, and a feedback control system in order to monitor the applied pressure and adjust the valve system accordingly.

Different valve configurations could be employed to quickly reverse airflow to and from a fan operating at constant speed. The minimum number of ports required would be four, with one into the low-pressure side of the fan, one out of the high-pressure side of the fan, one connected to atmosphere, and one to the airbox. However, for the current, as well as for the previous BRERWULF design, a five-port design was employed, with the additional port also connected to atmosphere. The advantage of a five-port design is that it avoids a closed loop between the fan inlet and outlet which would result in heat building up in the system. It should be noted that individual valves could be used on the different ports to change the flow direction but to minimize the number of components, moving parts, and control complexity, a rotating disk within the valve was chosen. This has the advantage of one moving part, which is on the axis of rotation of a servomotor.

Figure 1 shows a schematic of a five-port valve and rotating disk concept along with a flow schematic showing its operation. The valve is made in two halves (i.e., two castings), one with two ports and the other with three, with a slotted disk between them.

A schematic representation of these parts is presented in **Figure 1** while **Figure 2** depicts an assembly drawing of all the parts making up the valve. The two ports in the two-port half of the valve are connected to the fan with “i” (**Figure 1A**) representing the connection to the inlet (low-pressure side) of the fan and “o” representing the connection to the outlet (high-pressure side) of the fan. The direction of flow through these ports is also shown in **Figure 1A**. For the three-port half of the valve, there is inflow from the atmosphere into port “a” and outflow to the atmosphere from port “c.” Port “b” is connected to the pressure chamber, and flow can be either into or out of this chamber, depending on the position of the slotted disk. It is for this reason that this device is called a flow-reversing valve.

Figure 1B shows the three limiting states of the valve: (i) neutral, with no flow into or out of the pressure chamber, (ii) full flow out of the pressure chamber, and (iii) full flow into the pressure chamber. The position of the slotted disk, which is controlled by a servomotor, determines which state occurs. For example, when the disk is in the position such that port “a” is entirely blocked, there is no inflow from the atmosphere, and the flow is from the pressure chamber through port “b” into the fan inlet, through the fan, and out to atmosphere. This state leads to lower than atmospheric pressure (i.e., suction) in the pressure chamber. This is depicted in the middle schematic of **Figure 1B**, while the other two schematics in **Figure 1B** depict the other two limit states discussed above.

As noted above, the slotted disk is positioned by a servomotor, which can move the slotted disk to any angle. Depending on the disk angle, a range of positive and negative pressures can be achieved, which is determined by the fan characteristics, flow losses (i.e., pressure drops) in the ducts, valve, and other flow elements, and leakage into (or out of) the pressure chamber. **Figure 2** presents the final assembly of the different valve components, along with the symmetric slotted disk design. The final shape of the valve was determined by using computational

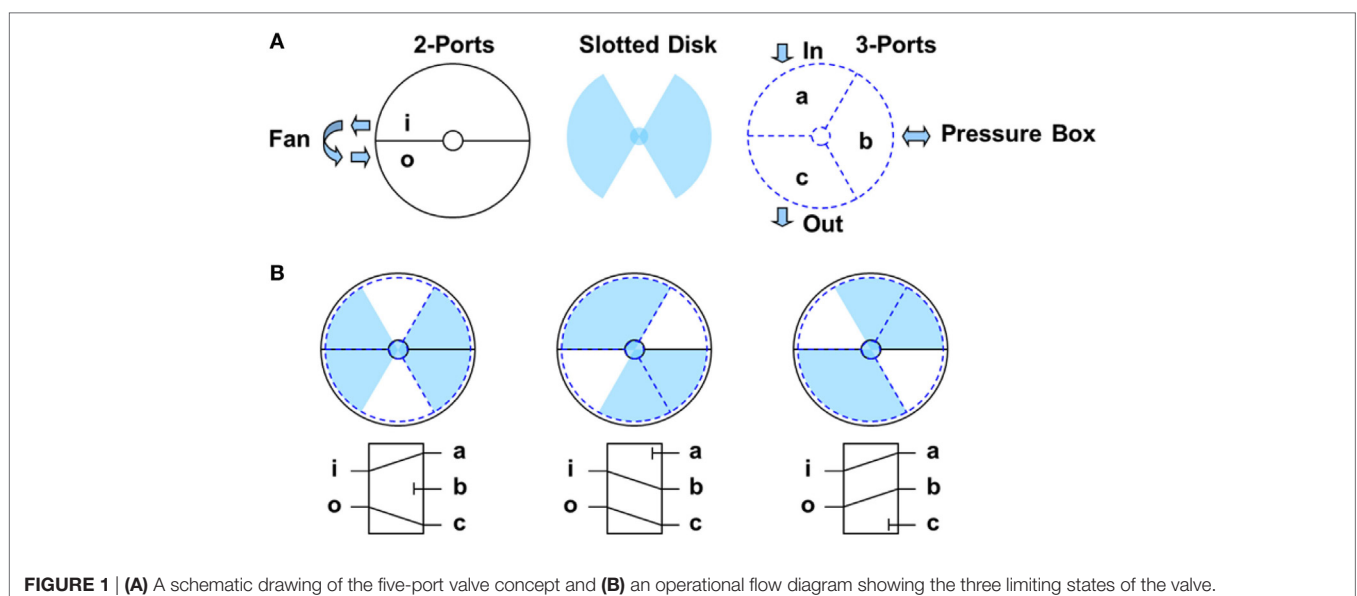


FIGURE 1 | (A) A schematic drawing of the five-port valve concept and **(B)** an operational flow diagram showing the three limiting states of the valve.

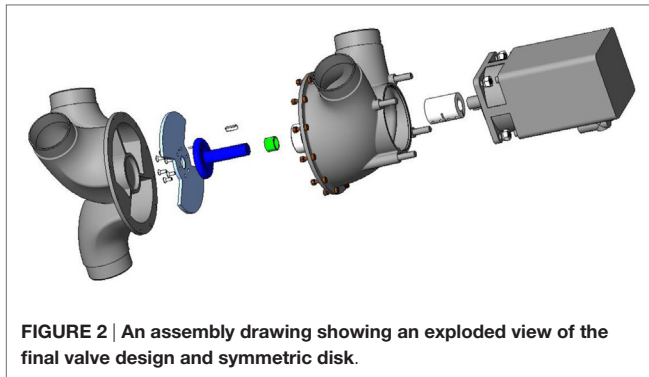


FIGURE 2 | An assembly drawing showing an exploded view of the final valve design and symmetric disk.

fluid dynamics to minimize the losses, improving the overall performance of the system (i.e., reducing power requirements to achieve particular pressures at particular leakage flow rates). The next section discusses the development of the valve in detail, and how it controls the pressure under different leakage conditions.

System Performance and Control under Variable Leakage Flows

One of the critical aspects of simplifying the computer control system was the linearization of the valve, i.e., ensuring a nearly linear relationship between airbox pressure and valve position. **Figure 3** depicts the “valve map” (the static-flow relationship between pressure and velocity) for the perfectly symmetric valve/disk arrangement (which is shown schematically in **Figure 1**) in a pressure chamber with fixed volume and very small leakage. The gradient of pressure with respect to valve position at high magnitudes of suctions and pressures is roughly 30 times the gradient in regions closer to 0 pressure (neutral position). This non-linearity would result in increased complexity of an already complex control system, significantly increasing the time critical computing resources required, particularly when operating multiple PLAs. In order to improve the linearity of the valve map with the symmetric disk, stationary tabs with a suitable profile were introduced to the valve housing. The improved linearity of the modified system can be seen in **Figure 3**. Overall performance of the PLA in fixed volumes and high peak pressures is discussed in Kopp et al. (2010). At much lower pressures, with interconnected pressure chambers, the PLAs still function with high accuracy, as discussed below. **Figure 4** shows the pressure versus valve position of the symmetric disk under different leakage conditions as indicated. While the pressures at a given valve position reduce with increasing leakage in the airbox, it decreases linearly with increasing leakage. The linearity of pressure versus leakage flow at each valve position allows the control system to automatically adjust to different initial leakage conditions or to adapt to changing leakage conditions during a test.

As can be inferred from the valve maps presented in **Figures 3** and **4**, the PLA is a single-input–single-output system with the valve position as the input and the required pressure as the output. Thus, the requested valve position and the measured pressure are an input–output pair for use in a proportional–integral–derivative

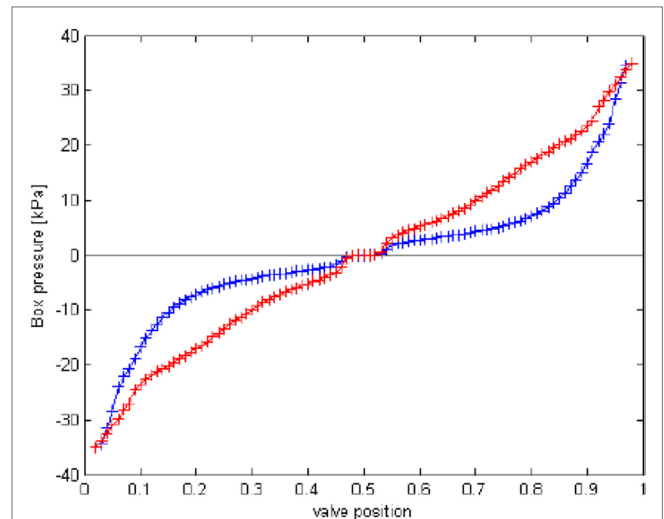


FIGURE 3 | A valve map showing the comparison between the first-generation disk (blue) and the final symmetric disk (red).

(PID) control system. The control system is effectively approximated to a linear first-order model as the required pressure trace, whether fluctuating or a simple ramp, is preloaded as a feed-forward term. The feedback PID term is based on the tracking error which is simply the difference between the required and measured pressures. The valve map is used to determine what valve position is required to meet the applied pressure under steady-state conditions resulting in a known system time constant, τ , for the PID control. In calculating τ from the requested pressure and achieved pressure in real time, the adjacent pressures from the current and previous time steps are used.

Changes in leakage and air-chamber volume cause the time constant, τ , to vary enormously. The solution for this issue was to use gain scheduling; the real-time estimation of τ is used to determine the system gain from a suite of preloaded lookup tables, which are generated for known leakage and volumes. However, the system gain (K) increases with increasing τ , which can lead to instabilities with an overestimation of τ , particularly for very small volumes relative to power or input traces that have minimal changes in time (i.e., static pressures or ramp loads). This is only an issue at start up when the control system has no information on τ , that is, the pressure chamber and test element properties. Therefore, a median value of τ and a limit on the increase in K is set for the first 10 s of program control. The system learns the chamber's characteristics within this time frame. In cases where absolute control is required in the first 10 s, a user defined value of τ can be used. However, this necessitates additional experiments to determine the correct system time constant. With the lookup tables and the linearization of the valve chamber with disk position, the PID control system then can adapt rapidly to changing chamber conditions. The control system was designed this way so that it could adapt to any pressure chamber and input trace (within certain bounds), and still run effectively without any user input into the PID.

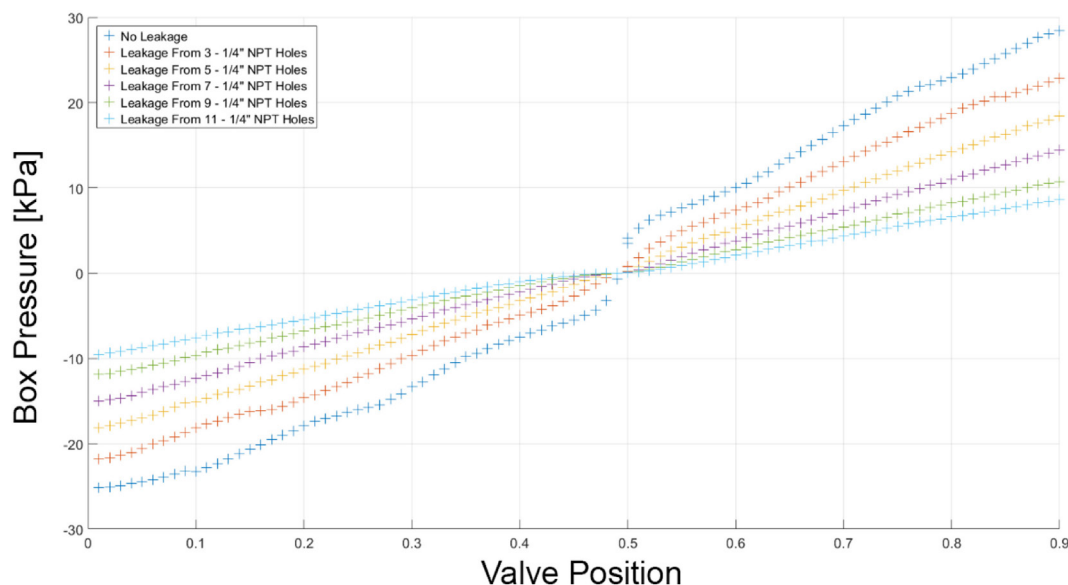


FIGURE 4 | A valve map of the final symmetric disk at different leakage conditions.

The lookup tables scale by a constant factor over the fan speed range of 30–70 Hz. (Note that the lower fan speeds are used to avoid operating in a narrow region of the valve control curve, to maintain accuracy in tests that require small excursions around neutral pressure.) The control system predicts the required position of the valve up to 1 s into the future based on the current estimations of air-chamber leakage, user requested pressures, and system gain. If the control system anticipates the valve will be unable to meet the pressure requirements of the user defined input pressure time history, referred to as valve saturation, the fan speed will be increased to meet the demands of the experiment (when possible). This avoids the need for the user to predefine the required fan speed time history in addition to the input pressure time history for the airbox.

Adaptation of the control system is also required when sudden leakage, volume change, or flow change through the cavity occurs. **Figure 5** shows results from a sinusoidal load applied to a section of metal roof cladding using a 1.8 m × 0.9 m airbox. The achieved pressure trace deviated from the requested trace at approximately 882.2 s. This occurred due to a sudden increase in the leakage and the volume of the air chamber. As can be seen, the system adapts within a tenth of a second. This fast response in adaptation of the PLA control system is important since it is able to maintain the correct pressure loading even as onset of failure of the test specimen occurs.

Airbox Leakage and Fan Performance

Airbox leakage is an extremely important system parameter and has two possible sources: the test specimen and leakages through the valve and pressure chamber. The former can be a combination of material porosity and cracks or holes in the test specimen. The latter can be a combination of the pressure-chamber fit to the test specimen, the chamber, or the pipes and fittings

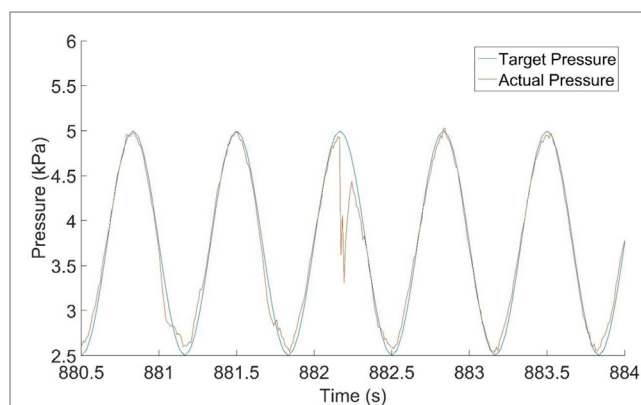


FIGURE 5 | A pressure time history showing adaptation of the proportional-integral-derivative to the change in volume and leakage after the failure of a cladding element. Data provided courtesy of Dr. David Henderson.

connected to the pressure chamber. The overall performance of the system, i.e., maximum pressure and frequency response, is highly dependent on the amount of leakage. Ultimately, the amount of allowable leakage in the system is a function of size of fan or blower used and, as such, significantly influences the power required to operate the system.

While it may be desirable to purchase the largest fan possible to provide the system with the maximum flow rate possible, there are several practical constraints of why this is not the optimal solution for the current loading system. Such a large fan would require high power consumption even for small, nominally sealed boxes; moreover, the physical size of the fan would be large and make applying spatial gradients, with many

pressure chambers in close proximity, more difficult. Finally, in order to accommodate the large flow rates, the size of the valve would also need to be increased so that the air velocity through the valve is kept to a minimum, and consequently the losses. The performance of the entire fan–valve–airbox (nominally sealed) was evaluated by using an orifice plate to measure the flow rate going into the airbox and measuring the achieved pressure. Leakage flow rates were obtained by creating controlled openings within the airbox. In addition, these tests were repeated at numerous fan frequencies ranging from 30 to 70 Hz. The results of these tests are shown in **Figure 6**. In addition to meeting other requirements such as physical size, the manufacturer's fan curve for the chosen fan is shown in **Figure 6**. The fan combined with the tuned valve is capable of providing flow rates of up to 300 CFM at ~10 kPa and 100 CFM at 20 kPa at a fan speed of 60 Hz. However, as can be seen from the figure, the system does not need to run the fan at full speed, which leads to consequent changes in maximum pressures and flow rates. This, in turn, allows the total power consumption to be reduced in aggregate for an array of PLAs that are running different pressure traces.

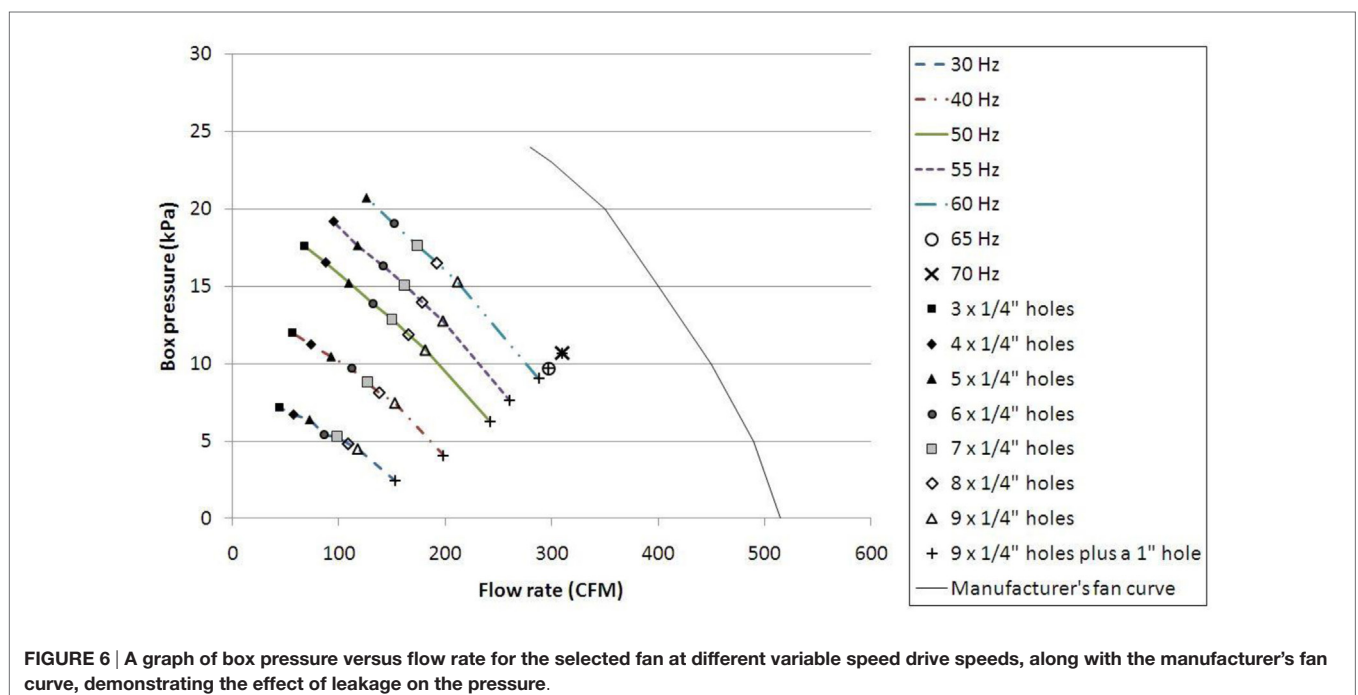
To allow greater flexibility, the PLA loading system can be run in three different configurations depending on the application. The first configuration is the simplest where a single PLA unit is connected to a single chamber. The second configuration uses a single fan/blower connected to two independent valve and servo motors. Each valve is connected to its own box, with its own feedback pressure transducer allowing two airboxes to be controlled independently of each other using only a single fan. This configuration is ideal for small airboxes with minimal leakage and has the advantage of reducing the power consumption of the system, along with reducing the per airbox capital cost of

the entire system. The third PLA configuration uses one airbox with multiple individual PLA units. Under this configuration, only the first PLA (leader unit) has a pressure transducer, and the remaining units mimic the valve movements of the leader exactly. Under this configuration, significantly higher flow rates can be realized while maintaining the performance characteristics required to simulate the real wind loads. This is the approach used for the vinyl siding tests discussed in Section “Test Case for Air-Permeable, Multilayer Cladding.”

TEST CASE FOR AIR-PERMEABLE, MULTILAYER CLADDING

Full-Scale Pressure Measurements on Vinyl Siding

Recent tests at the IBHS examined the loads on various siding systems using their full-scale wind tunnel (Cope et al., 2012, 2014; Morrison and Cope, 2015). Pressures were measured on the walls of a full-scale, single story wood-frame house with plan dimensions of 9.1 m (30 ft.) \times 12.2 m (40 ft.), a mean roof height of approximately 3.7 m (12 ft.), and a roof slope of 4-on-12. The walls of the test building were 2.4 m (8 ft.) high and clad with 11.1 mm (7/16") OSB. In the study done by Morrison and Cope (2015), a total of four siding products were tested: vinyl siding, foam backed vinyl siding, wood siding, and hardy board. In order to test all four products simultaneously the walls of the building were divided into eight sub-wall assemblies. The long walls were divided in half resulting in a test wall 6.1 m (20 ft.) long, while the shorter walls extended 3.7 m (12 ft.) from the corner leaving 6 ft. in the center of the short wall to access the interior of the building. All siding products were installed following the



manufacturers guidelines; drywall was installed on the interior of the walls so that the wall assembly matched, as accurately as possible, real construction. Along the 6.1 m (20 ft.) walls, wind-induced pressures were measured at 16 locations, while along the 3.7 m (12 ft.) walls, they were measured at 12 locations. At each measurement location, the external pressure, the net pressure across the siding, and the net pressure across the OSB were measured simultaneously. Experiments were conducted in an open exposure at four different wind speeds (Morrison et al., 2012). The orientation of the building to the wind was varied over a full 360° in 10° increments. The results of these tests indicate that pressure equalization has a significant effect on the outer layer of these systems. For example, results have shown that vinyl siding must carry a net load of up to 75–80% of the peak net load across the entire wall assembly. Given this 20–25% reduction in loads, the IBHS results are substantially different than the results obtained using a single-partitioned pressure chamber or considered through ASTM D3679 (2013). This study is used to provide benchmark data for validating the multichamber pressure-loading approach using PLAs. In particular, **Figure 7** shows segments of the measured external pressure time histories

at five locations along the wall from the IBHS experiments—it is these time histories that are applied in the multichamber tests described below.

Multichamber Pressure Test Setup

As described in Section “The Multichamber, PLA Approach,” a new pressure-chamber system is required for testing air-permeable multilayer cladding systems. The main task is to ensure that the unloaded surfaces are minimized because of the importance of the external pressure gradients on setting the cavity pressure. In addition, the chamber walls should be (i) nominally airtight, so as to minimize the direct flows between chambers, (ii) flexible, so that the barriers have limited effects on the performance or deformations of the flexible cladding, (iii) strong enough to be robust through a range of test conditions, and (iv) easily installed and repeatable. After taking the material properties into consideration, a latex-barrier system was constructed. Small-scale testing showed that latex worked well in all of its required functions and, therefore, was implemented for the full-scale testing.

Since the objective was to replicate the IBHS results, test specimen was built with the same siding. These walls were 12 ft. long by 8 ft. high, with 2-by-4s used as the studs. The sheathing was 3/4" plywood; however, a polyurethane sheet was placed in between the studs and the plywood to seal the pressure chamber, which is slightly different in setup compared to the IBHS tests, but which ensures that leakage between the pressure chamber to the atmosphere was minimized. House wrap was then placed over the plywood to replicate typical construction practice, since the focus of the study is the net loads on the outer (i.e., vinyl siding) layer. Pressure taps were then installed through the plywood and house wrap at the same locations as for the IBHS wall. Vinyl siding was installed on to the wall using appropriate nails at 16" intervals along the length of the wall. All pieces of vinyl siding were cut to be 12 ft. long in order to not have any lap splices in the test chamber. Starter strips, ending strips, and utility trim were also used to model typical construction practice. The test wall could then be placed in a rigid-sided chamber of slightly larger dimensions than the test wall, which in this case is the same chamber used by Gavanski and Kopp (2011b).

Five chambers were created within the airbox for this test by placing four latex barriers within the larger rigid box. These five chambers coincided with the pressure tap layout from the IBHS tests: four of the chambers were 2 ft. long, with one being 4 ft. long. All latex barriers ran vertically across the siding, as can be seen in **Figure 8**, which presumes that the primary external gradient was along the length of the wall. This is a reasonable approximation for the side walls when they are under suction, although further work is needed to examine the effects of these gradients. In the current case, with five pressure time histories available, five pressure chambers are used. These data were obtained from the IBHS experiments, as depicted in **Figure 7**. [Regarding the effects of pressure gradients and the use of one set of pressure time histories, as discussed in Bienkiewicz and Sun (1997) and Oh and Kopp (2014), and shown below, the pressure gradient is clearly one of the governing parameters of the

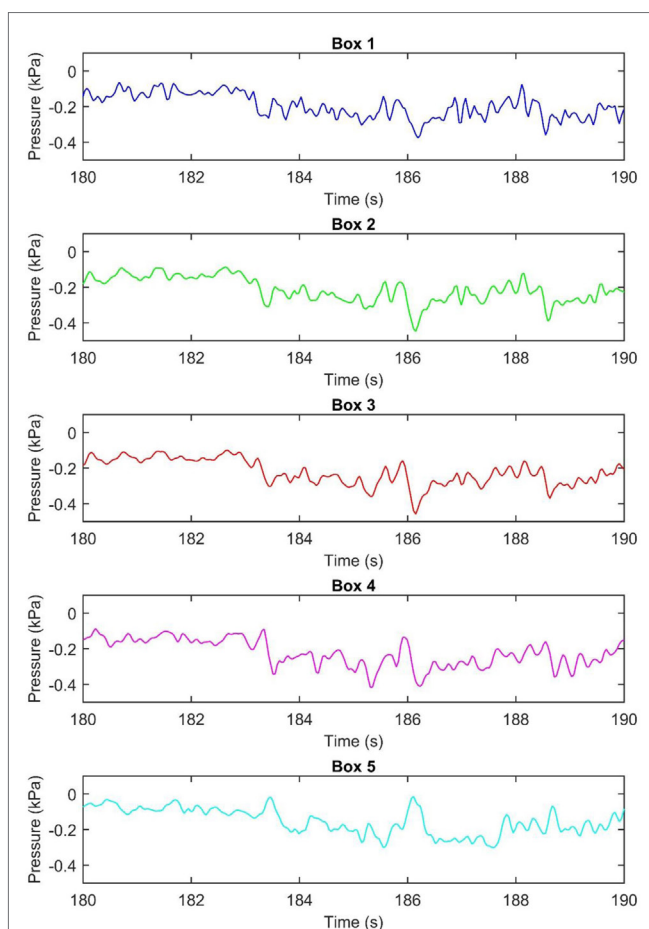


FIGURE 7 | A graph showing a portion of the external pressure time history for each individual airbox.

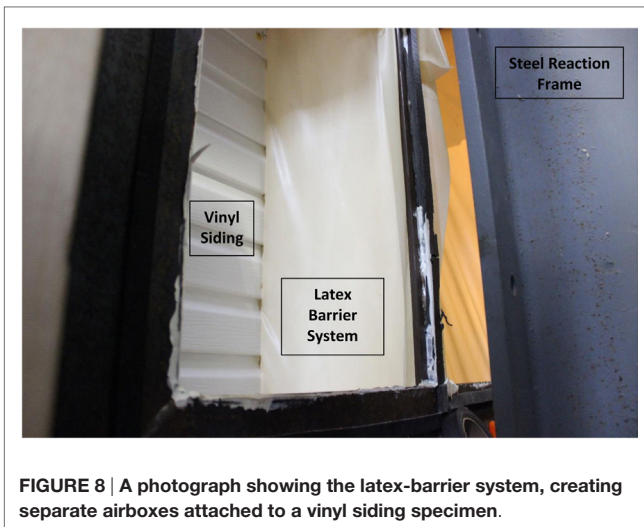


FIGURE 8 | A photograph showing the latex-barrier system, creating separate airboxes attached to a vinyl siding specimen.

net wind loads on air-permeable cladding elements, with high net loads being associated with high-pressure gradients. Due to this, further work is required to determine both appropriate design pressure gradients and the resulting number of required pressure chambers to obtain sufficient accuracy in the tests. This will involve additional wind tunnel testing to examine how the pressure gradients and pressure time histories change with overall building geometry and terrain conditions, compared to the single test case from IBHS.]

RESULTS AND DISCUSSION

The primary objective of the current tests is to determine whether multichamber pressure tests are capable of assessing net pressures on an air-permeable cladding system. This is done by applying the IBHS measurements of external pressures through the PLA system and measuring the resulting PEF. **Figure 9** shows a plot of a segment of the resulting time histories of the differential pressures across the cladding layer (i.e., the vinyl siding) for two cases: one with the external pressures from IBHS data (see **Figure 7** above) and one with spatially uniform pressures at each location. For the latter case, the pressure time history with the largest peak external pressure from the IBHS data was repeated identically in all five chambers. The different colors represent the differential pressures, p_d , in each separate airbox,

$$p_d = p_e - p_c,$$

where p_e is the external pressure coefficient and p_c is the cavity pressure coefficient. The five curves are overlaid on top of each other to determine the minimum (i.e., largest magnitude) observed differential pressure. The PEF is defined as

$$\text{PEF}(x) = \frac{P_{\text{external}}(x) - P_{\text{cavity}}(x)}{\hat{P}_{\text{external}}},$$

where $P_{\text{external}}(x)$ and $P_{\text{cavity}}(x)$ represent the external and cavity pressures, respectively, at the location on the wall and $\hat{P}_{\text{external}}$ is

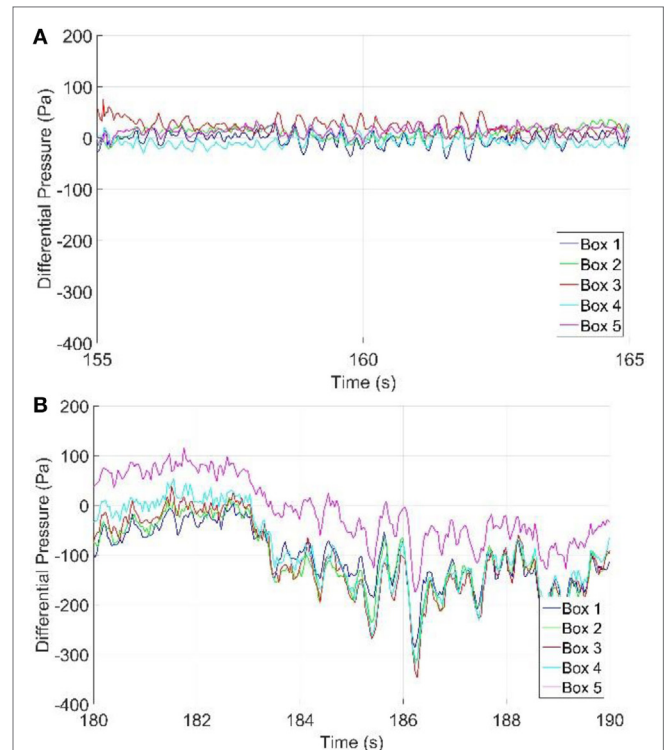


FIGURE 9 | Measured differential pressure time histories under (A) uniform and (B) gradient external pressures.

the peak external pressure across the entire wall. [Note that in these experiments there should be negligible flow or pressure transferred from the interior of the wall because the house wrap provides a sealing layer. Thus, the net pressure over the assembly from the outside (siding) layer to the sealed layer is equal to the external pressure. For this reason, we use the external pressure instead of the net wall pressure in the definition of the PEF.] The data in **Figure 9** indicate that the peak differential pressures across the siding layer are about 350 Pa, while the peak external pressures are about 400 Pa. Thus, under fluctuating, spatially varying pressures, the reduction of the largest net pressure to the largest external pressure is about 12%, leading to an approximate peak PEF of 0.88. This result is substantially different when compared with the data obtained from uniform, but time-varying, external pressures, where the largest peak differential pressure across the siding layer is about 40 Pa. Thus, under fluctuating uniform pressures, the net reduction relative to the peak external pressure is about 90%. This result is consistent with the findings of Gavanski and Kopp (2012) but leads to an even larger reduction than that used in ASTM D3679-13 [although it is reasonably consistent with the data obtained from the study performed by Architectural Testing, Inc. (2002) who obtained PEFs between 0.03 and 0.18]. These results definitively show that the spatial pressure gradient is a critical parameter for the process of pressure equalization and neglecting it leads to highly erroneous loads for these types of cladding systems.

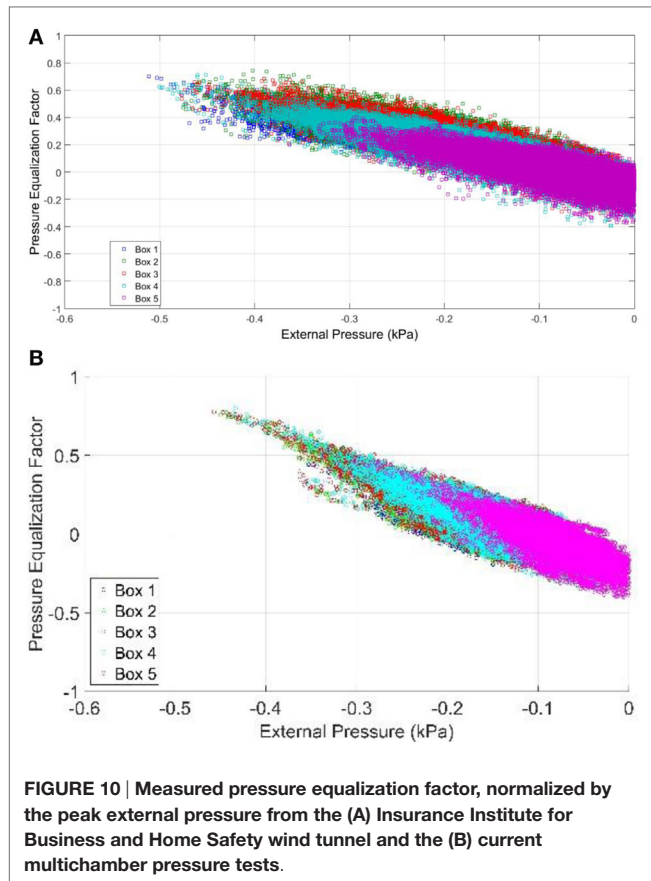
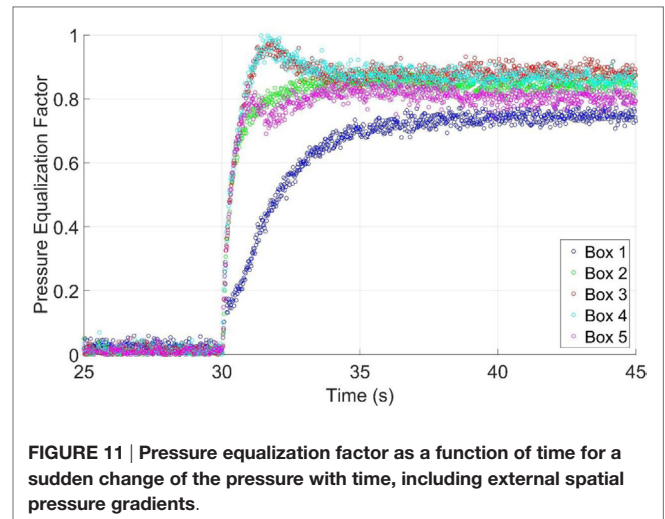


Figure 10 presents a comparison of the PEFs from the IBHS full-scale wind tunnel experiments and the current multichamber pressure-based experiments. As with the previous plots, the different colors represent the PEF in each chamber, with the colors from the two experiments matched. Between the two results, the multichamber airbox results seem to be deviating less from the mean. This is most likely because, although this new method of multichamber airbox testing is a step forward in the accuracy of the net pressure on cladding elements due to the application of spatial gradients, the spatial gradients being applied are still highly simplified. Due to limited tap resolution from IBHS, there may be subtle differences in the spatial distribution between tap locations that were not captured in original testing and which are made uniform within each airbox in the current tests.

The PLA system was able to simulate the applied external pressure time histories from IBHS results, with minor smoothing of the peak pressures. Recent model scale testing of multilayer roof systems suggests that the short duration, localized peak pressures control the cavity pressure, and the resulting net wind loads, to a significant extent (Oh and Kopp, 2014). This will have some effect on the results, but as shown in Figure 10, the distributions of the PEF values are similar, even with the minor smoothing of peak pressures. In fact, the PEF values are higher during the multichamber airbox testing, when compared to the IBHS wind tunnel experiments. In addition, further research is needed to



define the number of pressure chambers actually required, along with analysis of data to determine design pressure gradients to go with the peak pressures.

To determine whether a static, multichamber pressure test may be useful for a test standard, the external pressures at the moment that caused the peak PEF in Figure 10 were applied (i.e., all temporal variations were eliminated except for the rapid change in external pressure from 0 to the target values). Figure 11 shows the resultant PEF value, plotted against time. The results of this test show that the largest steady-state PEF is slightly larger than that obtained in the dynamic tests (Figure 9), although it is only about 5% higher. This suggests that static, but multichamber, pressure tests are feasible for a test standard so that the complexity of using the PLA system may not be required in standardized product tests. Interestingly, the temporal gradient of the rapidly changing pressure in the test caused a temporary increase of the maximum PEF in two of the five pressure chambers, which, considering that the PEF in the dynamic test is due to peak pressures that also had rapid variations, indicates there is a complexity in the temporal aspects of pressure equalization, as found by Oh and Kopp (2014). In the present case, having the pressures jump from 0 to their final values, the magnitude of the load was only altered by about 10% compared to the final steady values.

CONCLUSION

An experimental study was conducted to determine whether multichamber airbox testing is feasible for assessing wind loads on air-permeable, multilayer cladding systems. Although there is airflow between individual airboxes and uncontrolled volume changes caused by shared barriers for the pressure chambers creating complications for the PLA control system, the concept of creating a multichamber, pressure-based, testing apparatus that can accurately obtain wind loads for air-permeable, multilayer wall systems with flexible cladding has been shown to work. This was accomplished by (i) the creation of multiple flexible latex barriers to enable the

application of multiple, discreet, time-varying loads across a test specimen, (ii) the development of linearized five-port, flow-reversing valve, in conjunction with (iii) an adaptive PID control strategy. Using this multichamber pressure loading system together with external pressure data obtained at the full-scale IBHS wind tunnel, cavity pressures and PEFs were found to match the full-scale results reasonably well. The results confirm the conclusion of Cope et al., (2012) that the PEF in ASTM D3679-13 is unconservative. The good news is that static multichamber-based pressure tests are able to capture the important features of pressure equalization. Further work is required to create an improved test standard, particularly with respect to the minimum number of pressure chambers which may be required and setting the design pressure gradient or pressure pattern, neither of which were examined herein. Future work will examine these issues.

AUTHOR CONTRIBUTIONS

CM is a Ph.D. student under the supervision of GAK, and this research is a portion of what will become CM's doctoral thesis. The experiments and approach were designed collaboratively

by the authors. The manuscript was written collaboratively; CM wrote the first draft. The experiments and the direct analysis of the experimental data were conducted by CM, with direct input from GAK. MM contributed information from the full-scale testing at IBHS. GK and ND contributed information about the development of the PLA system.

ACKNOWLEDGMENTS

This work is dedicated to the memory of Mr. Geoffrey Robson, who made significant contributions to development of the PLA control system. Funding provided by the Institute for Catastrophic Loss Reduction (ICLR) and the Natural Sciences and Engineering Research Council (NSERC) of Canada under the Collaborative Research and Developed Program is gratefully acknowledged. The ongoing support and encouragement for our work provided by Mr. Paul Kovacs of ICLR is gratefully acknowledged. Some equipment was developed under funding from the Canada Foundation for Innovation. The authors also wish to acknowledge the many contributions to the development of the PLAs and PLA-based testing methodologies by Drs. Marek Myszkowski, David Henderson, and Eri Gavanski.

REFERENCES

- American Society for Civil Engineering. (2006). *ASCE 7-05: Minimum Design Loads for Buildings and Other Structures*. Reston, VA: American Society for Civil Engineering.
- Architectural Testing, Inc. (2002). *Wind Pressure Equalization Research Project Report. No. 01-40776.01 for the Vinyl Siding Institute*. Washington, DC: Architectural Testing, Inc.
- ASTM D3679. (2013). *Standard Specification for Rigid Poly (Vinyl Chloride) (PVC) Siding*. West Conshohocken, PA: ASTM International. Available at: www.astm.org
- ASTM D5206. (2013). *Standard Test Method for Windload Resistance of Rigid Plastic Siding*. West Conshohocken, PA: ASTM International. Available at: www.astm.org
- ASTM E1300. (2012). *Standard Practice for Determining Load Resistance of Glass in Buildings*. West Conshohocken, PA: ASTM International. Available at: www.astm.org
- ASTM E1592. (2012). *Standard Test Method for Structural Performance of Sheet Metal Roof and Siding Systems by Uniform Static Air Pressure Difference*. West Conshohocken, PA: ASTM International. Available at: www.astm.org
- Bienkiewicz, B., and Sun, Y. (1997). Wind loading and resistance of loose-laid roof paver systems. *J. Wind Eng. Ind. Aerodyn.* 72, 401–410. doi:10.1016/S0167-6105(97)00235-3
- Cook, N. J., Keevil, A. P., and Stobart, R. K. (1988). Brerwulf – the big bad wolf. *J. Wind Eng. Ind. Aerodyn.* 29, 99–107. doi:10.1016/0167-6105(88)90149-3
- Cope, A. D., Crandell, J. H., Johnston, D., Kochkin, V., Liu, Z., Stevig, L., et al. (2012). “Wind loads on components of multi-layer wall systems with air-permeable exterior cladding,” in *Proceedings of the ATC-SEI Advances in Hurricane Engineering Conference*, Miami, FL.
- Cope, A. D., Crandell, J. H., Liu, Z., and Stevig, L. (2014). Wind loads on fasteners used to attach flexible porous siding on multi-layer wall systems. *J. Wind Eng. Ind. Aerodyn.* 133, 150–159. doi:10.1016/j.jweia.2014.06.007
- Gavanski, E., and Kopp, G. A. (2011a). Glass breakage tests under fluctuating wind loads. *J. Arch. Eng.* 17, 34–41. doi:10.1061/(asce)ae.1943-5568.0000028
- Gavanski, E., and Kopp, G. A. (2011b). Examination of load resistance in window glass design. *J. Arch. Eng.* 17, 42–50. doi:10.1061/(asce)ae.1943-5568.0000030
- Gavanski, E., and Kopp, G. A. (2012). Effects of pressure equalization on the performance of residential wall systems under extreme wind loads. *J. Struct. Eng.* 138, 526–538. doi:10.1061/(asce)st.1943-541x.0000476
- Gurley, K. R., and Masters, F. J. (2011). Post-2004 hurricane field survey of residential building performance. *Nat. Haz. Rev.* 12, 177–183. doi:10.1061/(asce)nh.1527-6996.0000044
- Henderson, D. J., Williams, C., Gavanski, E., and Kopp, G. A. (2013a). Failure mechanisms of roof sheathing under fluctuating wind loads. *J. Wind Eng. Ind. Aerodyn.* 114, 27–37. doi:10.1016/j.jweia.2013.01.002
- Henderson, D. J., Morrison, M. J., and Kopp, G. A. (2013b). Response of toe-nailed, roof-to-wall connections to extreme wind loads in a full-scale, timber-framed, hip roof. *Eng. Struct.* 56, 1474–1483. doi:10.1016/j.engstruct.2013.07.001
- Kopp, G. A., Morrison, M. J., Gavanski, E., Henderson, D., and Hong, H. P. (2010). The ‘three little pigs’ project: hurricane risk mitigation by integrated wind tunnel and full-scale laboratory tests. *Nat. Hazards Rev.* 11, 151–161. doi:10.1061/(asce)nh.1527-6996.0000019
- Kopp, G. A., Morrison, M. J., and Henderson, D. J. (2012). Full-scale testing of low-rise, residential buildings with realistic wind loads. *J. Wind Eng. Ind. Aerodyn.* 10, 25–39. doi:10.1016/j.jweia.2012.01.004
- Kumar, K. (2000). Pressure equalization of rainscreen walls: a critical review. *Build. Environ.* 35, 161–179. doi:10.1016/S0360-1323(9)00015-3
- Mooneghi, M., Irwin, P., and Chowdhury, A. G. (2014). Large-scale testing on wind uplift of roof pavers. *J. Wind Eng. Ind. Aerodyn.* 128, 22–36. doi:10.1016/j.jweia.2014.03.001
- Morrison, M. J., and Cope, A. D. (2015). “Wind performance and evaluation methods of multi-layered wall assemblies,” in *Proceedings of ASCE Structures Congress*, Portland, OR.
- Morrison, M. J., Henderson, D. J., and Kopp, G. A. (2012). The response of a wood-frame, gable roof to fluctuating wind loads. *Eng. Struct.* 41, 498–509. doi:10.1016/j.engstruct.2012.04.002
- Oh, J. H., and Kopp, G. A. (2014). Modelling of spatially and temporally-varying cavity pressures in air permeable, double-layer roof systems. *Build. Environ.* 82, 135–150. doi:10.1016/j.buildenv.2014.08.008
- Sinno, R., Surry, D., Flower, S., and Ho, E. (2003). “Testing of metal roofing systems under simulated realistic wind loads,” in *Proceedings of the Eleventh International Conference on Wind Engineering*, Lubbock, TX.
- Sparks, P. R., Schiff, S. D., and Reinhold, T. A. (1994). Wind damage to envelopes of houses and consequent insurance losses. *J. Wind Eng. Ind. Aerodyn.* 53, 145–155. doi:10.1016/0167-6105(94)90023-x
- Sun, Y., and Bienkiewicz, B. (1993). Numerical simulation of pressure distributions underneath roofing paver systems. *J. Wind Eng. Ind. Aerodyn.* 4, 517–626. doi:10.1016/0167-6105(93)90319-j

Surry, D., Sinno, R. R., Nail, B., Ho, T. C., Farquhar, S., and Kopp, G. A. (2007). Structurally effective static wind loads for roof panels. *J. Struct. Eng.* 133, 871–885. doi:10.1061/(asce)0733-9445(2007)133:6(871)

Conflict of Interest Statement: The authors declare that the research was conducted in the absence of any commercial or financial relationships that could be construed as a potential conflict of interest.

Copyright © 2017 Miller, Kopp, Morrison, Kemp and Drought. This is an open-access article distributed under the terms of the Creative Commons Attribution License (CC BY). The use, distribution or reproduction in other forums is permitted, provided the original author(s) or licensor are credited and that the original publication in this journal is cited, in accordance with accepted academic practice. No use, distribution or reproduction is permitted which does not comply with these terms.



Development of a Full-Scale Structural Testing Program to Evaluate the Resistance of Australian Houses to Wind Loads

Geoffrey Neville Boughton, Korah Parackal, Navaratnam Satheeskumar and David James Henderson*

Cyclone Testing Station, James Cook University, Townsville, QLD, Australia

OPEN ACCESS

Edited by:

Wei Zhang,
University of Connecticut, USA

Reviewed by:

Ilaria Venanzi,
University of Perugia, Italy
Peng Huang,
Tongji University, China

*Correspondence:

David James Henderson
david.henderson@jcu.edu.au

Specialty section:

This article was submitted to
Wind Engineering and Science,
a section of the journal
Frontiers in Built Environment

Received: 06 October 2016

Accepted: 22 March 2017

Published: 07 April 2017

Citation:

Boughton GN, Parackal K,
Satheeskumar N and Henderson DJ
(2017) Development of a Full-Scale
Structural Testing Program to
Evaluate the Resistance of
Australian Houses to Wind Loads.
Front. Built Environ. 3:21.
doi: 10.3389/fbuil.2017.00021

Extensive damage to houses during severe tropical cyclones in the 1970s in Australia highlighted the need for research-based structural engineering principles to be applied in design and construction of houses. Houses have structural redundancies and complex load paths, so the analysis of even simple houses was complicated. In order to evaluate the structural performance of these parallel systems, full-scale house testing commenced at the Cyclone Testing Station (CTS) in the early 1980s with the static multipoint loading of an old house destined for demolition. Following that test program, nine full-scale houses were tested under static and cyclic loading to evaluate load paths in different types of houses with different building practices and materials. Results have been incorporated into amendments of house construction codes, standards, and manuals. Advances in computer modeling and instrumentation have led to more sophisticated full-scale studies. Data on real houses under construction have informed this work and enabled analytical models to incorporate variability in strength of connections in a way that a single test cannot. Progressive failure in the structural systems of timber-framed housing can now be studied to differentiate between houses that have significant damage and seemingly identical ones that have limited damage in the same wind event. These studies involve wind tunnel investigations to determine temporal pressure distributions; full-scale multiple tests on connections (with and without construction defects) to determine statistical distributions of strength and load/deflection relationships; and full-scale tests on houses or portions of houses to determine load sharing mechanisms between parallel structural and non-structural elements. The results of the test programs were used to calibrate the analytical models, which can be used for reliability studies. The paper presents a summary of the methodology and findings from previous CTS full-scale house tests. The results of the most recent research using full-scale tests on a portion of a house and its companion numerical models are discussed and the benefits and limitations of the process outlined.

Keywords: cyclone, full-scale, testing, wind, house, model, failure

INTRODUCTION

Destructive cyclones including Cyclone Althea (Trollope, 1972) and Cyclone Tracy (Walker, 1975) in Australia in the 1970s highlighted the poor performance of housing in comparison to engineered buildings (e.g., office buildings, commercial premises). Investigations of damage concluded that engineering design was required to improve the safety of house construction. House construction at

that time was largely based on traditional building methods that only evolve slowly in response to infrequent but severe events. Since then, engineering principles have been applied to develop Australian Standards used in house design and construction that provide rationally based guidance on resisting wind loads.

Light-framed timber construction is the most common form of residential construction in Australia and North America. This type of construction is characterized by the use of multiple small cross section timber members to create walls, roof, and floors. Light-framed construction developed in the early 1800s with the advent of industrial saw mills that were able to mass produce standard timber sections.

Due to the large numbers of repetitive structural members, a light-framed house is easy to construct but is an extremely complex structure to analyze. The interaction of structural elements result in load sharing, multiple load paths, partial composite action, and under severe wind loading—the non-linear behavior of connections results in load redistribution. **Figure 1** shows the multitude of structural elements that can compose a light-framed house, each of these is connected to others with various fasteners each with different structural behaviors.

Construction techniques for light-framed construction were largely developed by builders' and carpenters' traditions with codified structural engineering principles being implemented in only the last 30 years in Australia. This lack of engineering input along with the high complexity of the structure has meant that houses have been especially vulnerable to severe wind events compared to engineered structures.

Extensive research programs were required to support the rapid evolution of Codes and Standards and required structural

models of complete house behavior that had to be verified. The Cyclone Testing Station (CTS) undertook testing on full-scale houses to establish models of load paths and the structural behavior of houses under wind loads. The testing program was used to verify details proposed in a range of deemed-to-satisfy solutions for houses in high-wind areas.

While the initial tests replicated static and repeated applications of patch loads derived from wind-loading standards, the testing program has evolved to include replication of spatial and temporal variations in wind pressures on house surfaces and the combination of full-scale tests and computer models of behavior to model a number of different variations of normal construction practice.

EARLY FULL-SCALE STRUCTURAL TESTS ON WHOLE HOUSES AT CTS

Test Programs

By 1980, CTS had undertaken wind load tests on many components of houses in a laboratory setting. However, it was recognized that testing of structural components under simulated wind loads in the correct structural context required full-scale *in situ* testing. The most appropriate context could be delivered by testing a complete house.

A 40-year-old house that had survived Tropical Cyclone Althea in 1972 was used to test the concept of full-scale tests on houses in 1981. The house was located only 1,500 m from the anemometer that had recorded 52 m/s during the event (Trollope, 1972). The simulated wind loads were applied to the house on site and

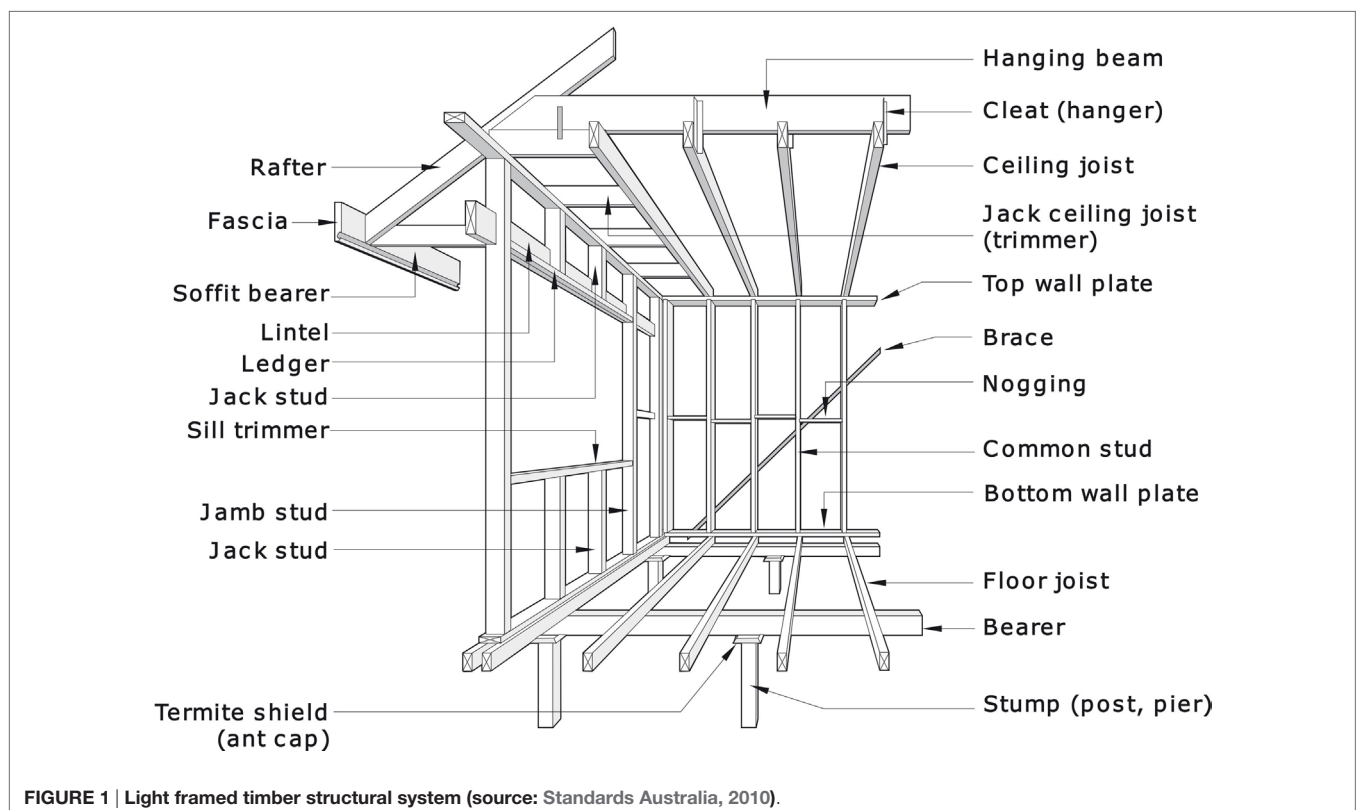


FIGURE 1 | Light framed timber structural system (source: Standards Australia, 2010).

intended to replicate the loads calculated from the anemometer data. The damage was compared with damage observed on similar houses in the area during TC Althea (Boughton and Reardon, 1982a,b). These tests demonstrated the applicability of full-scale house testing for assessing the interaction of the houses of many interconnected components.

The concept was further developed in 1982 and 1983 when full-scale tests were performed on a new house that had been built to comply with the planned deemed-to-satisfy provisions for suburban houses in tropical cyclone prone areas of Queensland. The house was a rectangular plan 12.8 m × 6.4 m with 10° roof pitch and gable ends. The house was subjected to wind loads calculated from the wind loading standard at the time, AS 1170.2 (Standards Australia, 1983) equivalent to a site wind speed of 42 m/s (Boughton and Reardon, 1983). **Figure 2** illustrates the application of:

- Lateral loads at the top of roof level using a hydraulic ram (a) that tensioned a cable passing through a pulley (b) to a load cell and load spreader (c). The reaction was taken through the stay at (d).
- Other lateral loads at floor level could be applied with hydraulic ram (e) that tensioned a cable passing through the floor system to the load cell and load spreader (f). The reaction was also taken by the stay (d).
- Uplift loads to the roof using a hydraulic ram (g) that moved a rocking beam (h) and applied uplift through a load cell and load spreaders attached to the roof battens (j). This loading system also created a reaction in the stay (d).

Where loads incorporating full internal pressure were applied to the underside of the roof, an equivalent downward load on the floor was created using drums of water to ensure that global loads on the house were representative. Cyclic load simulations were applied to the structure by regulating flow to the hydraulic rams based on the load cell signals. In the early tests, repeated loads at different percentages of the ultimate design wind loads were applied with thousands of uplift cycles and hundreds of lateral load cycles.

Wind forces do not reduce as the house deflects, so wind is very flexible compared with the structures it loads. Therefore, the loading system was designed to be very flexible compared with the house under test by incorporating flexible cables. The measured flexibility of the full-scale loading system was around three times that of the first house constructed for tests. (It was around 10 times the flexibility of later brick veneer houses.)

Displacement transducers that measured vertical and horizontal movement at a number of locations monitored the response of the house. The data were logged on computers. The limitations of early data logging equipment meant that it took 5 s to read all load cells and transducers. The combination of flexible loading systems and slow read times meant that it was difficult to obtain data on loads and deflections near to and immediately after failures. As the full-scale test house testing program developed, the equipment to control loads and monitor deformations became more sophisticated and could achieve more variability in loading regimes and faster response time for measurements.

The tests aimed to identify load paths through the structure under wind loads, identify any vulnerabilities in typical houses built to current standards and develop improved details, and confirm design methods for calculating wind resistance of houses. Each house was loaded with simulated wind loads evaluated from design wind speeds (Standards Australia, 1983) and appropriate for each house. (The houses were designed for a range of wind speeds.)

The following is a summary of complete houses tested in the program during the 1980s and 1990s using the same test equipment:

- The “Hyne house”—a high-set (elevated) house (single storey with floor level 2.4 m above ground), with rectangular floor plan 12.8 m × 6.4 m, a steel sheet roof on hardwood trusses with a 10° pitch and gable ends (Boughton and Reardon, 1983). The house included sawn hardwood timber wall and floor framing, timber floorboards, 6 mm thick fiber cement external cladding, and 10 mm plasterboard internal linings. The design wind speed at eaves level was 42 m/s.

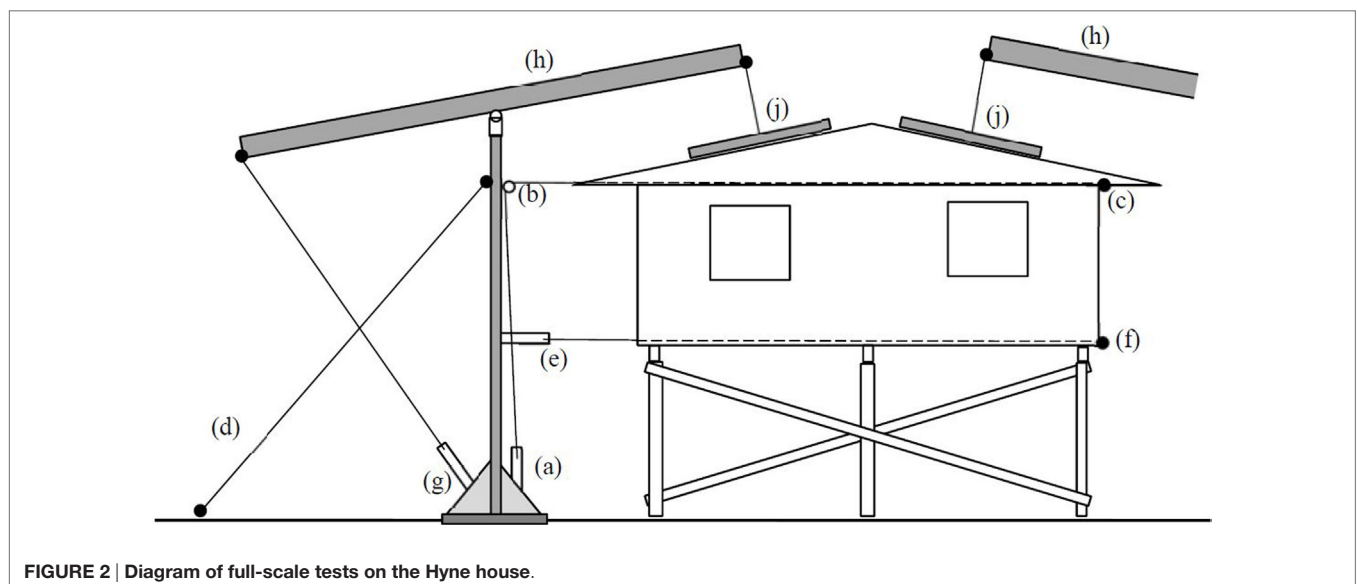


FIGURE 2 | Diagram of full-scale tests on the Hyne house.

- The “Logan house”—a single storey house with a concrete floor at ground level, a rectangular floor plan $14.2 \text{ m} \times 7.1 \text{ m}$, a steel sheet roof on graded metal purlins with a 2.5° pitch and gable ends (Boughton and Reardon, 1984a). The house included 1.01 m wide prefabricated steel-framed panels (1.15 mm steel stock), clad with 6 mm thick fiber cement externally and internally, and prefabricated ceiling panels with 6 mm fiber cement linings. All panels were bolted together on site. The design wind speed at eaves level was 63 m/s.
- The “Tongan house”—a house designed for a large scale reconstruction program following Tropical Cyclone Isaac in Tonga (Boughton and Reardon, 1984b) (**Figure 3**) The Tongan house was low-set (single storey with floor level less than 0.9 m above ground), with rectangular floor plan $7.2 \text{ m} \times 4.8 \text{ m}$, a steel sheet roof on softwood trusses with a 26° pitch and gable ends. The house included sawn softwood timber wall and floor framing, plywood floor, 8 mm thick plywood external cladding, and no internal linings. The design wind speed at eaves level was 62 m/s.
- The Brick veneer clad house for construction in tropical cyclone areas (Reardon, 1986)—a single storey slab on ground house of rectangular plan ($16.4 \text{ m} \times 7.2 \text{ m}$) with a 15° pitch gable roof clad with pressed metal tiles. The wall frames were constructed from hardwood with galvanized metal straps connecting alternate studs to top and bottom plates. The design wind speed at eaves height was 42 m/s.
- Brick veneer house for construction in non-tropical cyclone areas (Reardon and Mahendran, 1988) (**Figure 4**)—a house of similar outwards appearance to the cyclonic region house, e.g., slab on ground ($16.4 \text{ m} \times 7.2 \text{ m}$). However, the roof structure was pitch frame hardwood construction instead of manufactured trusses and roof clad with concrete tiles. The timber frame walls only had nominal tie down. The design wind speed at eaves height was 27 m/s.
- Light gage steel framed panelized building system for cyclone areas (Reardon, 1990) (**Figure 5**). The $14 \text{ m} \times 9 \text{ m}$ building had 300 mm deep cold formed steel I beams spanning between the long walls to support the roof. A high-tensile rod connected each roof beam at the wall top plate down to a ring beam



FIGURE 3 | Tongan house after low-cycle failure of truss-to-wall connection.

channel as part of the foundation. The design wind speed at eaves height was 50 m/s.

- Brick veneer split-level house for construction in non-tropical cyclone areas (Reardon and Henderson, 1996). The single storey section had a plan of $8 \text{ m} \times 9 \text{ m}$ connected to the two-storey plan of $10 \text{ m} \times 6 \text{ m}$. The test house replicated the new trend of large open plan living areas. The design wind speed at eaves height was 27 m/s.

Results and Outcomes from the CTS House Testing

Each test series provided tens of thousands of data, which were analyzed to establish load paths for wind forces through the structure of the house, identify vulnerable elements, and provide feedback to designers and Australian Codes and Standards about the resilience and vulnerabilities of housing.

Vulnerable Elements

Leicester and Reardon (2010) postulate that all houses contain one or more elements with significantly less strength than the desired design capacity, through for example, an error in construction or defect material. The full-scale tests confirmed that at least one element/connection in the houses failed at less than the design load. In fact, for each full-scale cyclonic region test building, a loss of strength from low cycle fatigue of a major connection along the load path occurred resulting in the house not being able to achieve its original target design load. After minor changes were made to the vulnerable elements, the modified houses were able to resist the design wind speeds with an appropriate factor of safety:

- The tests on the Hyne house indicated that the vulnerable elements were the batten-to-truss connections and connections of floor to concrete piles. After redesigning those details, the house was able to resist lateral loads that were 140% of the design load and uplift loads that were 200% of the design load.
- The tests on the Logan house showed that the capacity of the metal brackets used in the connections between the roof



FIGURE 4 | Loading trees attached to roof battens of single storey house (the Hyne high-set house in background showing the damage to exterior wall cladding from simulated wind driven debris to evaluate loss of racking resistance in wall lining).

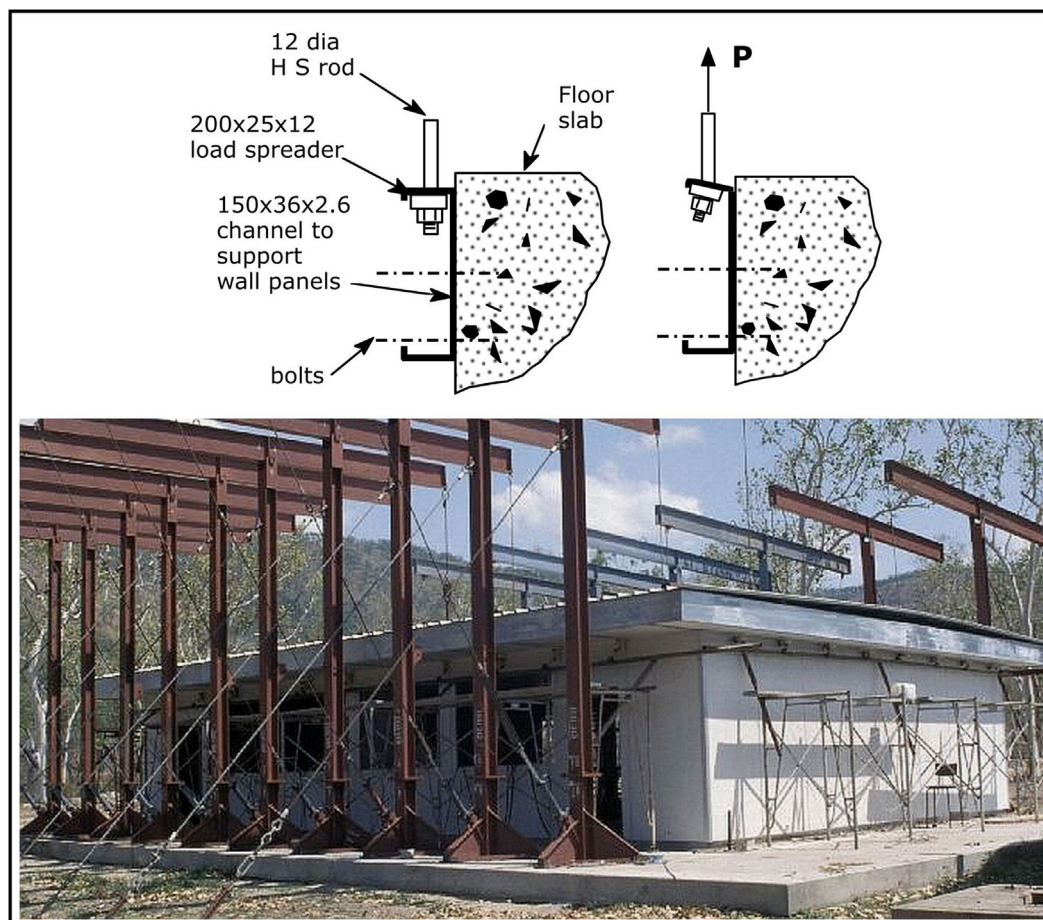


FIGURE 5 | View of light-gauge steel-frame house with details of anchorage failures (Reardon, 1996).

structure and wall were insufficient, and there was tearing around small washers under bolts between wall panels. After redesigning those details, the house was able to resist lateral loads that were 160% of the design load and uplift loads that were 130% of the design load.

- The tests on the Tongan house showed that some straps and truss nail plates were susceptible to fatigue damage. After redesigning those details, the house resisted loads that were 130% of the design lateral and uplift loads.
- The tests on the brick veneer cyclonic region house again highlighted the issue of loss of strength due to wind load cycles as the roof-to-wall tie down straps weakened and tore. A factor in the unexpected poor performance of the engineered straps was due to the installation requiring the builder to bend the strap from the top plate over the truss and down to the top plate again, which sometimes resulted in one of the straps being slightly looser than the other leading to one side of the strap connection receiving all the load. The testing resulted in changes being made to building standards and construction practice.
- The tests on the panelized engineered building revealed low-cycle fatigue failure of the main tie down system during the simulated wind load cycles. An eccentric tie down detail induced a prying effect on the ends of the high tensile tie down rods

resulting in the failure. A redesign of the connection to remove the eccentricity allowed the building to achieve its design load requirements.

The recommended changes to the vulnerable details were given to designers to implement in houses constructed for use in the community. The revised details were also incorporated into relevant Codes and Standards. For example, thousands of the Tongan house design were built during the 1980s and have since survived several tropical cyclones. The success of the Tongan house design through their long-term performance has resulted in a refinement of the design and the construction of more of these houses in 2014.

The tests also showed that, in general, bracing walls in full-scale houses were more vulnerable and less ductile than laboratory tests indicated. In laboratory testing, the reaction frame and the loading system are typically very stiff. First failure of a connection in a bracing wall during laboratory tests typically causes an immediate reduction in load and an effective redistribution to other fasteners. Subsequent increases in load show very ductile behavior of the wall with progressive yielding of the fasteners and an increase in strength of the wall following first fastener failure. However, tests on a house with a flexible loading system and a

flexible suspended timber floor system produced complete failure of the bracing walls when the first fastener failed. The energy stored in the floor and the flexible loading prevented release of load and redistribution to the whole panel following first fastener failure. Instead, the adjacent fasteners were rapidly overloaded. The full-scale test bracing capacity of the house was 60% of the capacity taken from the sum of individual bracing walls tested in laboratory conditions (Boughton, 1988).

Load Paths

Load paths for both lateral and uplift loads through the structure were identified by comparing results of each house loaded at a number of stages during construction. The increase in stiffness at each stage of construction gave an indication of the change in load path with the addition of each structural and non-structural element. (An example is plotted in **Figure 6** for the two-storey section of the brick veneer split level house.) The results of tests on all houses showed that some non-structural elements were effective in transferring wind loads through the structure. For example, on most houses, without the cornice, the lateral load transfer between the ceiling diaphragm and the top of bracing walls followed a circuitous path: ceiling to ceiling screws, to ceiling battens, to lower chords of trusses, to truss-to-wall connections, to the top of exterior walls, to frame-to-frame nailed connections, to internal bracing wall frames, and then through cladding fasteners to the bracing panels. After the installation of cornices, the load path was from the ceiling cladding through the cornice directly to the bracing panels; a very direct and stiff load path. Therefore, where glued cornices had been installed, almost no lateral load was transferred through the structural connections until the cornice cement had broken.

Many load paths included a number of parallel elements that had the capacity to share loads if one element failed. Therefore, weaker elements in load paths that incorporated redundancy did not pose a risk of significant structural damage. The vulnerable elements identified in Section “Vulnerable Elements” were not part

of a system that allowed alternate load paths or redundancies. This highlighted the need for further research into the structural redundancy of elements in houses and the progression of failure following first failure of a vulnerable element.

Models of Structural Load Transfer in Houses

The results from each series of tests on a house type were able to confirm or refine accepted models of load transfer between elements. For example:

- Tests on brick veneer houses indicated that uncracked brickwork carried all of the lateral wind loads without transferring any loads to the timber frame. However, when the brickwork cracked, the brick ties transferred the load from the brickwork to the timber frame until they buckled and allowed the bricks to touch the frame and transfer load by bearing.
- Tests on bracing walls indicated that in spite of their more brittle behavior indicated in the Section “Vulnerable Elements,” the high in-plane stiffness of roof and ceiling diaphragms enables load sharing between the bracing walls and delivers adequate total bracing capacity. This confirmed the load transfer model assumed in the design of bracing systems in Australian framed houses.

Limitations of Early Tests on Full-Scale Houses

In many of the full-scale tests, particular care was taken to ensure that correct construction practices were used. However, slight variation in design, workmanship, and materials has been observed in inspections of houses in the community and is one of the factors accounting for differences in the performance of similar houses in the same wind event. The cost of building full-scale test houses prevents using this method to test variations in construction practices; however, damage investigations show that this is still a major cause of house failures under wind loads.

The CTS-simulated wind loading across the building is an approximation of the pressure gradients derived from Standards or wind tunnel models. The patch loads and line loads are applied to the structure such that higher loads can be applied to edge regions compared to the field (middle) of the roof. The loads can also be cycled in a sinusoidal application. Although this simulated loading can be repeatedly applied to the test house following change of materials/components, it cannot replicate the spatial and temporal variations from aerodynamic loading, such as the full-scale testing discussed by Huang et al. (2009).

No new complete full-scale test houses have been built at the CTS since the late 1990s with the intervening two decades of research and development targeting the performance of components within the structural models identified in the full-scale house testing program. Recent research has extended the original concept of full-scale testing so that a range of component characteristics can be investigated in tests of full-scale sections of houses.

FULL-SCALE TESTS ON HOUSE ROOFS

Recently, several other full-scale house tests have been carried out to evaluate the structural response and load sharing of the

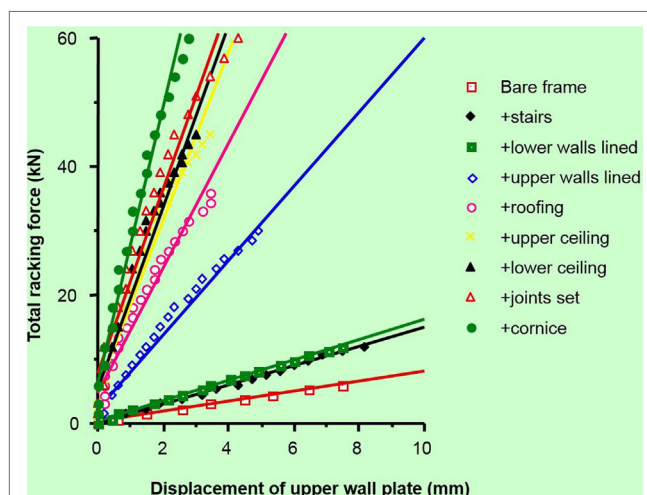


FIGURE 6 | Increase in horizontal displacement of top plate of upper storey with each additional construction stage (Reardon and Henderson, 1996).

North American and Canadian residential houses (Datin and Prevatt, 2007; Morrison, 2010; Canino et al., 2011; Doudak et al., 2012; Henderson et al., 2013). However, the usefulness of these experimental results to assess the structural response and load sharing of Australian residential house is limited, as their construction types are different. These variations in construction result in differences in their structural response and stiffness of roof-to-wall connections. Thus, it can be expected that the load sharing and reaction influence coefficients will be different in the Australian timber-framed structure compared to that of other countries' houses.

Based on the applied loads and displacements, the full-scale tests at the CTS (Boughton and Reardon, 1982a,b, 1983, 1984a,b; Reardon, 1986, 1990; Reardon and Mahendran, 1988; Reardon and Henderson, 1996) qualitatively showed the strength, stiffness, and load transfer of the house system subjected to wind load. These tests did not investigate the significance of reaction influence coefficients on the truss-hold down force. The reaction influence coefficient is used with wind pressure distribution to evaluate the truss hold-down forces of timber-framed houses (Ginger et al., 2000). The study presented in this section describes a full-scale test conducted to identify the load sharing and reaction force influence functions of timber-framed houses in Australia. A combination of; full-scale tests on sections of a house, numeric models, characterization of the variability of components, and detailed wind tunnel loading data has been used to investigate structural behavior of houses with a variety of construction practices, determine statistical distributions of strength and load/deflection relationships and load sharing mechanisms between parallel structural and non-structural elements (Satheeskumar et al., 2016a,b).

Data on houses under construction (see Investigation and Testing of Contemporary House Construction) have been incorporated into analytical models to represent variability in the strength of connections in a way that a single full-scale test cannot. The focus of these studies is the investigation of the effects

of defects in individual connections and the mechanics of progressive failure in the complex structural systems in timber-framed housing. The results of the test programs were used to calibrate the analytical models, which can be used for reliability studies.

This section discusses research projects that extend the previous CTS full-scale testing programs to evaluate the performance of full-scale roof structures under wind load using a combination of wind tunnel pressure records and full-scale testing of components and assemblies.

Investigation and Testing of Contemporary House Construction

As a collaborator in the Climate Adaptation Engineering for Extreme Events Cluster (CAEx) (Stewart et al., 2016), CTS undertook surveys of houses under construction in three Australian capital cities to document current design and construction practices. The surveys recorded data on structural members (size, grade, and span), connections (fasteners, spacing, and configuration), and identified inadequate design and installation of some elements. Incorrect site classifications for wind, errors in connections for tie-down of roof structural elements, over-driven nails on bracing elements, and incorrect window and door installation were observed. The plans of the inspected houses showed that their roof structure was more complex than the roofs of houses used in previous CTS tests on full-scale houses or in wind tunnel studies to derive peak wind pressures.

Cyclone Testing Station used these data from the surveys to develop a design of a representative house with specified dimensions, roof shapes and pitch, plan footprints, materials, and structural systems as shown in **Figure 7**. It included a non-rectangular floor plan with hips, valleys, and short ridges. Wind tunnel studies on this representative house were used to establish base-line peak pressure coefficients on all areas of the roof, as illustrated in **Figure 8**. Pressure taps were installed on the

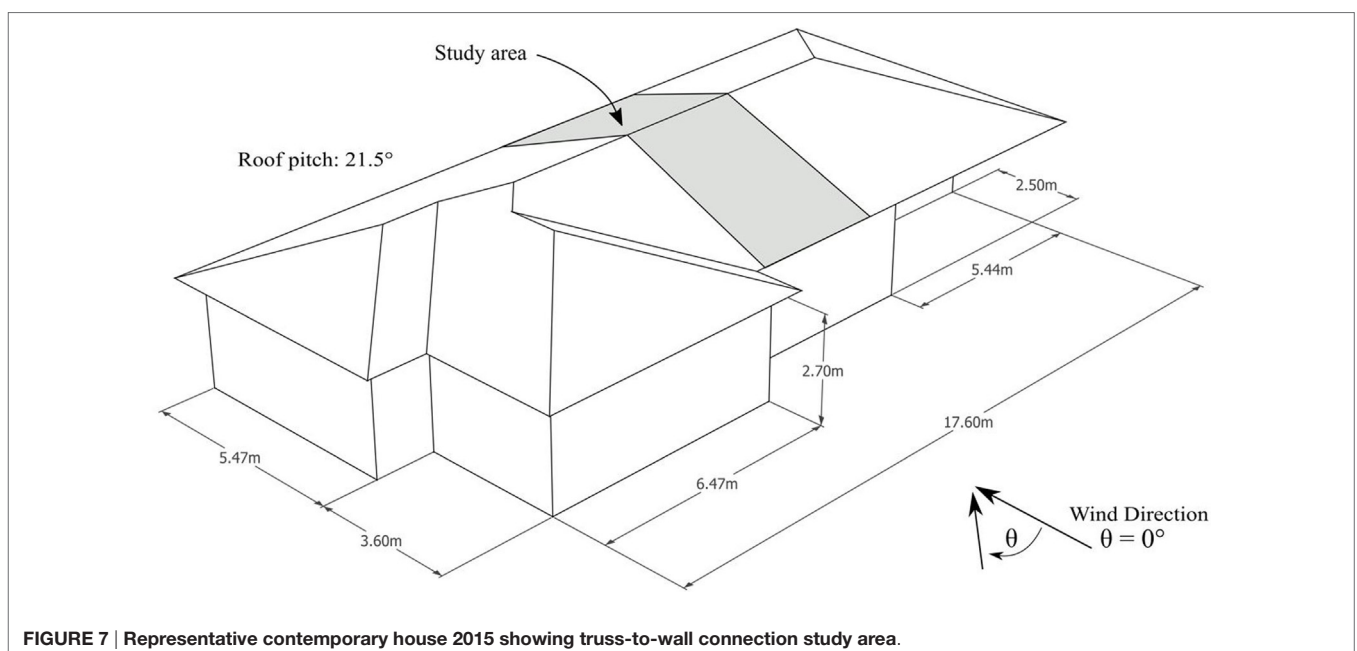


FIGURE 7 | Representative contemporary house 2015 showing truss-to-wall connection study area.

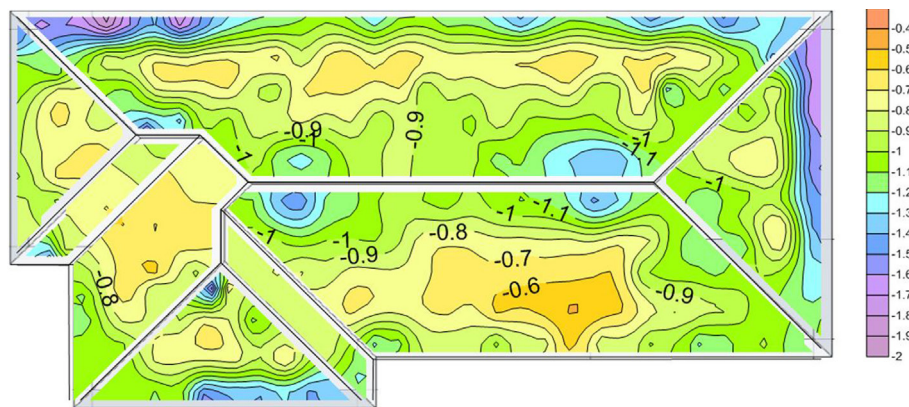


FIGURE 8 | External wind pressure coefficients on representative house.

models in a 12 mm × 18 mm grid-pattern (representative of the 600 mm × 900 mm truss-batten spacings in full-scale) to enable cladding loads, batten-truss loads, and the resulting wind load effects on the trusses to be determined.

Cyclone Testing Station has also conducted investigations of damage to houses following most major wind events in Australia since the mid 1980s. The data from these investigations have been used to highlight/identify deficiencies in design and construction practices that have contributed to changes in Codes and Standards and initiated research projects to improve building resilience. Many of the deficiencies in structural details that contributed to damage in houses during severe wind events were also observed in the CAEx surveys. These deficiencies have been incorporated into recent full-scale tests in order to establish their role in progressive failure and investigate whether redundancies in some elements provide alternative load paths around the deficiencies.

Behavior of Truss-to-Wall Connections

A 3.3 m-long section of house including five 6.6 m-long roof trusses, shown in **Figure 9**, was constructed for full-scale testing to evaluate the capacity of normal house components such as wall linings and cornices to carry loads (Satheeskumar et al., 2016a) around weak truss-to-wall connections. Vertical load transfer through the structural connections was measured at the top plate and the bottom plate. The full-scale test structure included five standard prefabricated nail plate trusses, metal battens, corrugated steel roof cladding, timber wall frames, plasterboard wall and ceiling lining, and cemented ceiling cornices.

Hand-nailed metal framing anchors that complied with recommended construction practices (“ideal”) were initially installed to connect the trusses to the wall frames. Some of the connections were altered (e.g., missing nails) for subsequent tests to reflect poor construction practices observed in some houses as discussed in the Section “Investigation and Testing of Contemporary House Construction.” The results showed that the load distribution of uplift forces was a function of the stiffness of the roof-to-wall connection. The lining elements (i.e., ceiling, ceiling cornice, and wall lining) contributed significantly to vertical load sharing.



FIGURE 9 | Full-scale tests on house cross-section.

A 3D finite element model (FEM) was also developed using ABAQUS (6.12-3) (ABAQUS, 2013) to further assess the load sharing and structural response of the timber-framed structure to different construction defects in roof-to-wall connections. The connections were represented in the FEM as either linear or non-linear spring elements. The connection forces in the FEM analysis were compared with measurements from full-scale structural testing using uniformly distributed loads. The results were similar, with a maximum variation of about 15% (Satheeskumar et al., 2016b). The validated FEM provided confidence to investigate the response of roof-to-wall connections to more realistic uplift forces that vary across a house roof.

The FEM was developed and analyzed for three different configurations: case 1 using “Ideal” connections; case 2 with a single nail missing in one of the truss tie-downs; case 3 with two nails missing from one truss-to-wall connection and one nail missing from an adjacent truss-to-wall connection. The force displacement relationships for these cases were obtained from the experimental tests and high resolution FEM of isolated connections (Satheeskumar et al., 2016c,d).

Table 1 presents the C_N (i.e., truss hold-down coefficient) at each connection when 1 kPa uniform suction pressure was applied on the roof. It shows that the loads in connections adjacent to the trusses that have defective tie-down are increased by

about 10% where there is only one defective tie-down (case 2). This figure is significantly less than the 50% redistribution from a statically determinate system. There is a higher load transfer if there are two adjacent defective connections. The research project demonstrated that the linings in normal house construction can carry load around defective truss-to-wall connections.

PROGRESSIVE FAILURE AND LOAD REDISTRIBUTION OF BATTEN-TO-TRUSS CONNECTIONS

Full-scale house testing conducted in the 1980s and 2015 examined the complex load paths, the effects of construction defects, and damage. However it is still largely unknown how loads are redistributed during a failure and how structural failure can propagate through the roof structure. Damage investigations have shown that the failure of a few batten-to-truss connections can trigger a progressive failure resulting in the loss of large sections of the roof structure.

The study presented in this section examines progressive failures of nailed timber batten-to-truss connections. Laboratory tests were conducted to determine the behavior of connections under wind loads. Wind tunnel studies were conducted to

determine the correlation of load time histories at neighboring batten-to-truss connections and its effect on the initiation of a progressive failure. Finally, non-linear structural analysis was undertaken to determine how loads are redistributed as connections fail under uplift loads.

Behavior of Batten-to-Truss Connections

Laboratory tests were conducted on new batten-to-truss connections and on connections taken from 50-year-old houses. The tests on 50-year-old connections provided data on the performance of nailed connections in service and enabled deterioration due to age to be quantified.

Static testing of batten-to-truss connections was conducted to determine the mean strength of the connections under slow load rates (2.5 mm/min as specified in Standards Australia, 2001). A representative load/deflection plot of a 50-year-old connection with a strength close to the mean strength is shown in **Figure 10**. The 50-year-old connections showed a much greater variability in strength than new connections.

Dynamic tests of single batten-to-truss connections were undertaken to characterize progressive failure or deterioration of connections under fluctuating wind loads. The connections were tested using a servo hydraulic universal testing machine with a synthetic test load trace based on the wind tunnel study discussed under Section “Investigation and Testing of Contemporary House Construction”. Appropriate time scaling was applied to determine the required full-scale frequency.

Dynamic testing applied repeated synthetic peak loads to full-scale specimens until failure. The loading rate and frequency of the time history signal was based on a gust wind speed of around 40 m/s for a nominal tributary area for the connections of 0.36 m².

The results of the dynamic tests still showed large variability in connection performance, with some connections able to survive only two or three peaks and some able to survive more than 100

TABLE 1 | C_N of truss-to-wall connections with uniform suction pressure 1 kPa applied to the roof with trusses affected by defective fasteners highlighted.

Detail	C_N				
	Truss A	Truss B	Truss C	Truss D	Truss E
Case 1 (ideal)	1.54	1.46	1.41	1.49	1.56
Case 2 (missing single nail)	1.57	1.60	1.07	1.64	1.59
Case 3 (missing single and two nails)	1.81	1.07	1.20	1.69	1.70

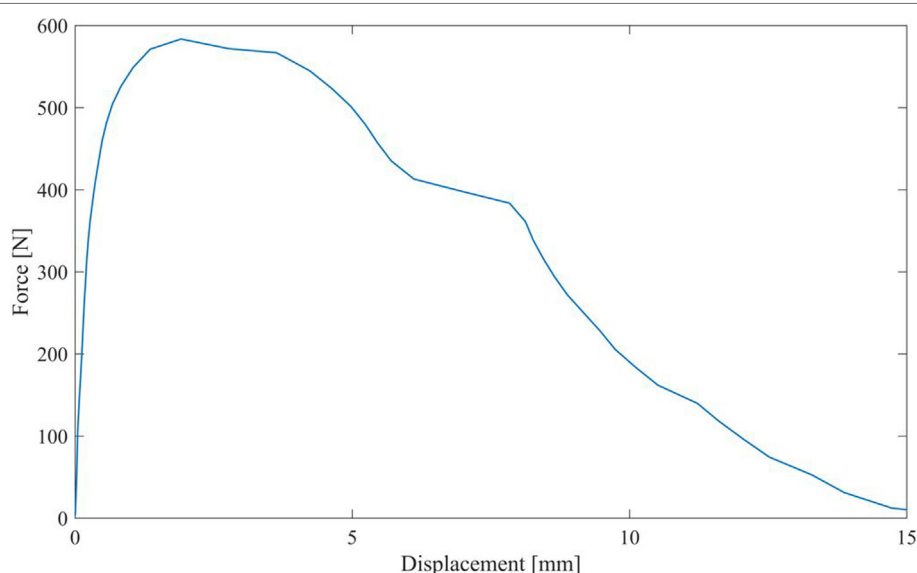


FIGURE 10 | Example of a force vs. displacement curve for static pull-out test of batten-to-truss nails.

peaks. All showed some ductility as they were able to sustain loads at deformations much higher than their elastic limit.

Figure 11 shows an example of 50-year-old connection behavior under dynamic loading. There was nail slip with each peak event. In most cases, there was an increase in performance similar to strain hardening behavior in steel; the magnitude of each slip decreased near the center of the plot. After the accumulated nail slip had reduced the depth of embedment to a critical level, the connection rapidly lost strength and failed as shown at the right hand side of the plot.

Preliminary testing also showed that for many of the 50-year-old connections, some nail slip occurred at peak loads below the mean connection strength. The accumulation of nail slip over a number of peak load cycles resulted in lower depth of embedment of the nail into the truss. This observation is compatible with older connections in service that have experienced nail slip in a number of previous wind events failing at loads lower than expected.

The dynamic tests showed that a connection's elastic stiffness, indicated by the gradient of the loading and unloading paths, does not change with accumulated damage through successive peak events, i.e., the elastic behavior of the connection is similar for each peak load event. This indicates that load redistribution to adjacent connections occurs due to total nail slip in a connection rather than to a decrease in elastic stiffness. Once a connection fails completely, load will be rapidly redistributed to adjacent connections.

The next phase of this study will involve the construction of a full-scale portion of a roof with full instrumentation of each batten-to-truss connection to evaluate the redistribution of load during progressive nail slip and complete connection failure of a single batten-to-truss connection.

Wind Tunnel Time-History of Loadings on Roof Elements

Previous CTS full-scale testing had focused on demonstrating that deemed-to-satisfy designs could withstand the design wind

loads and that models of structural behavior were valid, so loads calculated from contemporary wind loading standards were used. However, the Standard loading model is generalized. In order to use full-scale testing to evaluate progressive failure of elements within a house and demonstrate load sharing among elements close to the cladding, as noted in Section “Early Full-Scale Structural Tests on Whole Houses at CTS,” it is important to replicate the temporal and spatial variations in wind loads. Wind tunnel studies were used to create fluctuating load sequences that could be used to simulate wind forces on crucial elements of houses.

Boundary layer wind tunnel studies were conducted on 1/50 scale models to determine pressure distributions on the surface of houses for multiple wind directions (Parackal et al., 2016). Pressures were measured using hundreds of pressure taps on roof and wall surfaces. These pressures were integrated to calculate loads on connections supporting different areas of roof surfaces.

The tributary areas of batten-to-truss connections experienced the highest peak loads at roof corners and the apex of gables. The loads on a single connection were evaluated by summing the pressures over the tributary area of the surface for a single batten-to-truss connection. These loads were characterized by “peak events” of load more than 3.5 SDs from the mean lasting about 0.5–2.0 s for a mean wind speed of 100 km/h at full scale. The peak loads experienced varied with wind directions and were due to different aerodynamic mechanisms such as separation of flow or vortices entrained in the airflow.

In order to determine the factors that may promote failures to progress through a full-scale roof, correlation coefficients of load-time histories at connections were evaluated. The cross-correlation coefficient (r_{ij}) defined in Eq. 1 gives a measure of how well correlated the pressures on a specified connection (i) are with the pressures on an adjacent connection (j). A time lag term (τ)

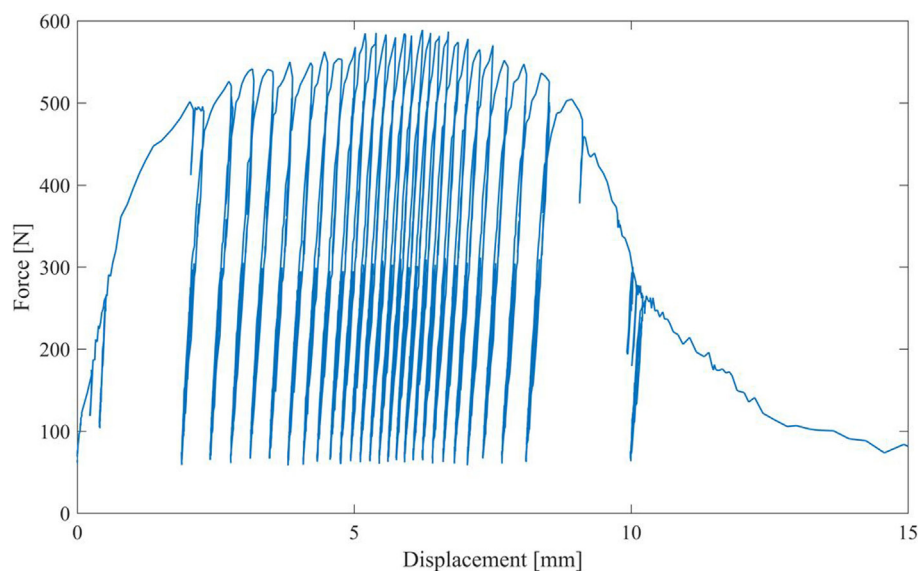


FIGURE 11 | Example of a force vs. displacement behavior of batten-to-truss nails connections under repeated wind uplift peak events.

is incorporated to allow for the time it takes for a gust vortex or eddy to move from one connection to another:

$$r_{ij} = \frac{1}{T \times \sigma_{p_i} \times \sigma_{p_j}} \int_0^T p'_i(t) \times p'_j(t + \tau) dt \quad (1)$$

where p_i and p_j are the fluctuating components of the pressure at locations i and j , σ_p is the SD of fluctuating load, and T is the time over which the signal is analyzed.

As shown in **Figure 12**, cross-correlations of time histories show that peak loads are correlated with pressures on adjacent connections. The negative lag times indicate that the pressure is well correlated with pressures on an upwind connection. For this wind direction, it was the connection on the same batten immediately upwind of the connection being evaluated. For other wind directions, the correlations indicated that the peak loads had been moving diagonally across the roof. It was also found that wind directions that caused the highest loads were not necessarily those that caused the highest correlations amongst adjacent connections.

The patterns of correlation can have implications on the initiation of progressive failures, especially if the correlation patterns align with the direction in which loads will be redistributed when a single connection fails or weakens. The direction the loads are redistributed between batten-to-rafter/truss connections is determined by the ratio of the bending stiffness of the battens to that of the cladding in the direction parallel to its corrugations as well as the batten and rafter/truss spacing. For example, the gable roof house studied may be most susceptible to progressive failures for wind direction 270° with the correlation patterns aligning along rafter lines and if the bending stiffness of the corrugated cladding is greater than the battens.

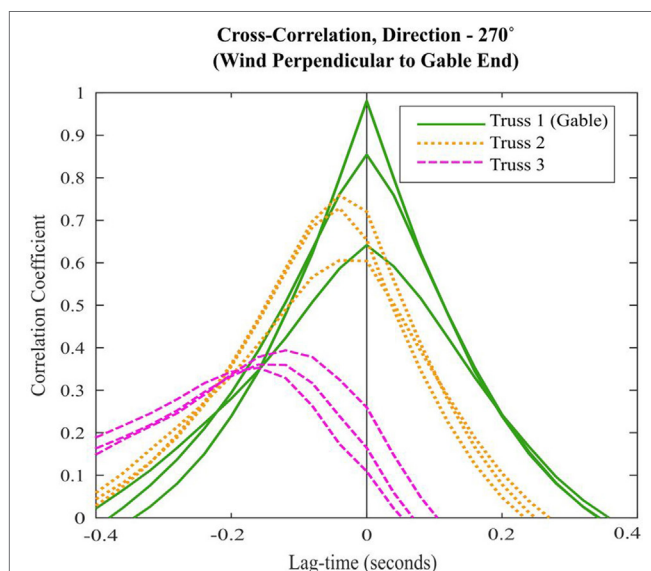


FIGURE 12 | Cross-correlations of time histories. Different lines within each color refer to different batten-to-truss connections on each truss. Truss 1 is over the gable, then, Truss 2 is one truss spacing from the gable, then Truss 3.

Non-Linear “Pull-Up” Analysis

To determine the direction loads are redistributed and to determine how progressive failure may propagate through the roof structure, a non-linear time history analysis using a finite element method structural analysis model was performed. An array of batten-to-truss connections representing the connections within a study area of a gable roof house was modeled as shown in **Figure 13**. Roof cladding is modeled as a thin shell with the thickness selected to give the same flexural rigidity (EI) as a 0.42 BMT “custom orb” cladding profile. A “stiffness modifier” of 0.1 is applied to EI of the sheeting in the direction parallel to the battens to represent the lower bending stiffness in the direction perpendicular to the cladding corrugations. Battens were modeled as frame elements that represent 45 mm \times 70 mm MGP10 battens. Batten-to-truss connections were modeled as multi-linear plastic link elements, with their force-displacement behavior determined from laboratory tests. These links are assigned a proportional limit 0.5 kN, plastic deformation for 10 mm at 0.5 kN, and complete failure at 15 mm extension. The roof structure below is not modeled.

A non-linear time history analysis was performed with a quasistatic ramp load (1 kN/min) applied at the location of connection T2-B7 (batten 7 fastened to truss 2 as shown in **Figure 13**). The ramp loads are continued as the first connection

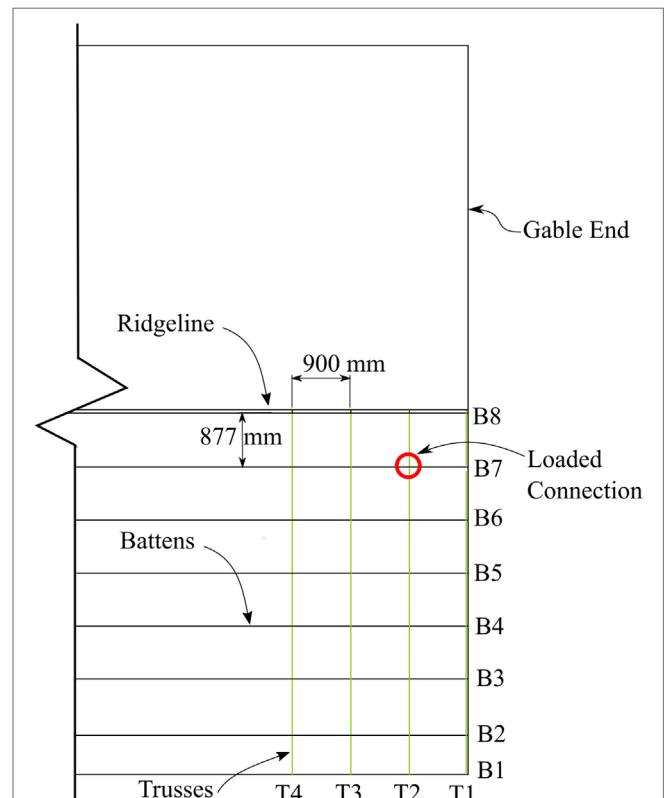
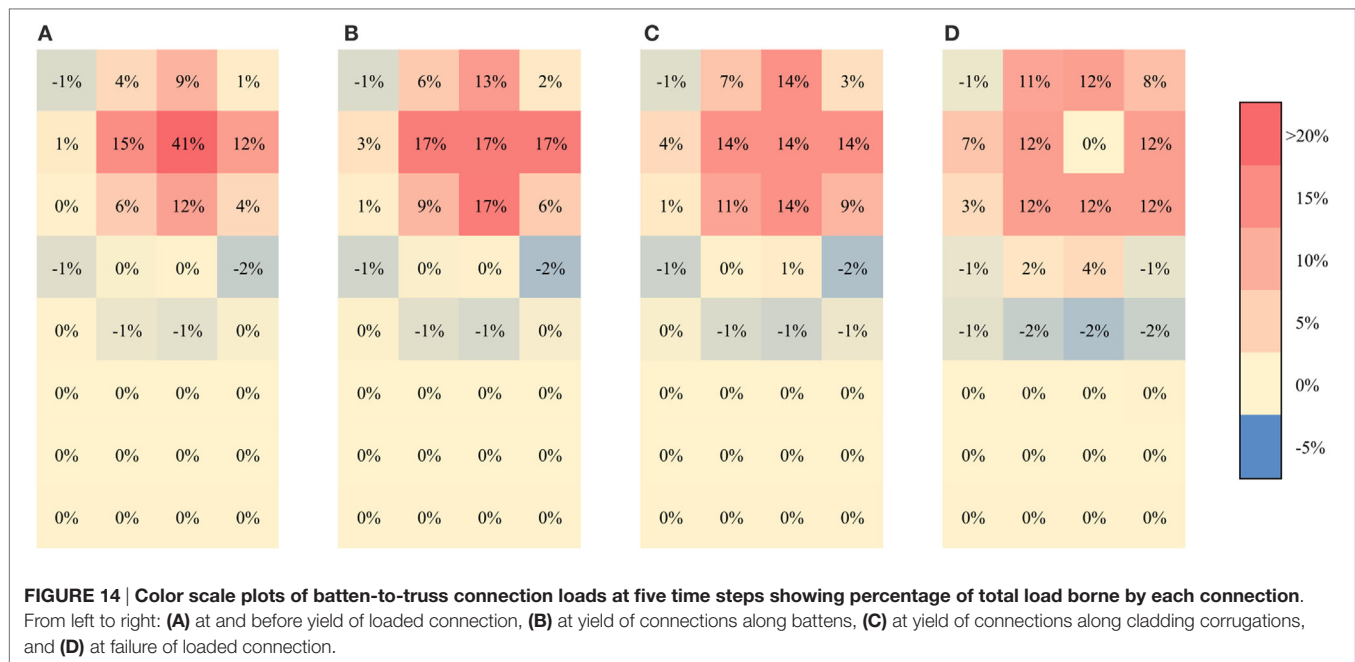


FIGURE 13 | Plan view of batten-to-rafter connections on the gable roof house modeled in the finite element model.



fails and a cascading failure takes place. Selected time steps of color scale plots showing the redistribution of load are shown in **Figure 14**.

As load is applied above T2-B7, the system behaves as a set of springs in parallel, with part of the load being resisted by the connection T2-B7 itself and the remaining resisted by the batten and the cladding in flexure as well as extension of the neighboring connections. Uplift loads are thus shared among neighboring connections even when T2-B7 is undamaged and in the elastic range.

Before connection, T2-B7 yields as shown in **Figure 14A**, a total of 27% of the load is shared among connections immediately to the left and right on the same batten (T3-B7 and T1-B7). Load is also resisted along the corrugations of the cladding, with a total of 21% shared with connections T2-B8 and T2-B6. Finally, 15% is shared among connections diagonally away from the loaded connection. One hundred three percent of the uplift load is resisted by connections in the 3×3 grid surrounding the loaded connection with connections outside of this grid having the sheeting pressing down on the batten (the remaining -3% of loads). These proportions of load sharing continue to the point where connection T2-B7 yields.

After connection T2-B7 yields, the proportion of load borne by this connection decreases and the amount of load sharing at all neighboring connections increases. When the connection to the left (T3-B7) yields, a total of 37% of load is taken by connections that are immediate neighbors on the same batten and 28% spans along corrugations. As the connection to the right (T1-B7) yields, the battens have reduced the proportion of load sharing and bear 34% of the load, as shown in **Figure 14B**. Loads are now redistributed along corrugations and connections T2-B8 and T2-B6 take 30% of the load. From this point on, the loads borne

by connections on the same batten reduce and load transferred along corrugations increases.

Once all connections adjacent to the loaded connection yield as shown in **Figure 14C**, load is shared equally among all the connections in the 3×3 grid including the loaded connection. However, when the loaded connection fails completely as shown in **Figure 14D**, loads are equally shared among battens and along corrugations. At this stage, loads are redistributed to diagonal connections.

The next connection to fail completely is T1-B7, to the right of the loaded connection. Loads are again redistributed to connections along the corrugations. At this stage, a cascading failure commences with loads being rapidly redistributed as connections fail in rapid succession resulting in the failure of all the connections in the study area.

The non-linear analysis has shown that load sharing and redistribution between batten-to-rafter connections is a complex process. Loads are shared among neighboring batten-to-truss connections depending on the ratio of stiffness of the battens and cladding as well as the batten and truss spacing. Additionally, the load path changes whenever a connection yields or fails completely. Connection failure and load redistribution occurs rapidly but in durations similar to pressure fluctuations experienced on the roof surface. Thus, the correlations of wind pressures may play a significant role in the initiation of a progressive failure. In future work, time history analysis with spatial and temporally varying loads can be used to determine the effects of the load correlations. This will lead to a study of the propagation of the failure cascade as well as how the structural system responds under fluctuating dynamic loads. Similar techniques can be applied to other connections in the vertical load path such as roof-to-wall connections discussed in Section “Full-Scale Tests on House Roofs.”

DISCUSSION OF BENEFITS AND LIMITATIONS

The original house testing research program at CTS was able to demonstrate the strengths and weaknesses of contemporary house design and enabled the validation of structural details and prescriptive standards (codes) for Australian housing. Typically, once any weak links in the load path were found and repaired, the test houses were stronger than design expectations. The test program led to a greater understanding of the transfer of load and distribution of forces through the various elements of the house structure—the program repeatedly highlighted the complex non-engineered load path of typical house construction. Also, through the application of repeated load cycles representing the duration of a tropical cyclone, issues of low-cycle fatigue on structural connections of light gage steel were highlighted.

In recent years, full-scale testing of US and Canadian houses subjected to wind loads has been conducted to evaluate structural and component response (Datin and Prevatt, 2007; Morrison, 2010; Canino et al., 2011; Henderson et al., 2013). However, there are only limited data available on the load distributions in inter-component connections, and progressive damage due to connection failure to wind loading.

However, full-scale test programs are expensive and time consuming. In early full-scale tests, the costs were justified by the value of these data and outcomes from each test. The current full-scale test program incorporates detailed FEA modeling during the experimental design to ensure that the load and displacement data are recorded for the locations required to best assess the FEA models. Using a validated model, changes in material properties and construction defects can be analyzed with confidence.

Full-scale studies on houses and parts of houses have identified a number of elements that provide structural redundancies. For example, grid systems in roof structures can bridge over weaknesses in specific elements. Wall systems also incorporate multiple parallel elements that can also share load. In addition, there are many non-structural elements such as plasterboard wall linings and ceiling cornices that can also transmit loads around structural systems if the primary structural system fails. However, that does not mean that there is enhanced resilience for all critical elements in the tie-down chain.

The most recent full-scale tests indicate that battens and roof cladding provide some bridging between batten-to-rafter/truss connections. Battens have the potential to carry the load from a failed batten-to-truss connection to only the adjacent connections along the batten. This study also indicates that the roofing provided a stiffer load transfer mechanism that only transfers load in a direction perpendicular to the ridge of the roof. However, in completed buildings, a failure of an edge batten-to-truss connection at the eaves could transfer load *via* bending in the battens to the fasteners in the same batten or *via* cantilever bending of the roof sheeting to the batten connector on the next batten up the roof. The load transfer from the failed connector significantly

increases the load on the adjacent fasteners and can lead to progression of the failure. Where first failure is near a corner of a roof panel, there can be a rapid spread of failure through the roof in both directions.

Connections deeper within the tie-down load path have greater redundancy and resilience than connections immediately under the roof cladding. Recent tests indicate that at lower levels in the house, many more elements have the potential to provide bridging systems that can transfer load to other elements if a connection fails. Roof sheeting, battens, ceiling elements, ceiling cladding, and other roof structural elements can transfer load laterally in wall systems over a significant distance if tie-down elements in walls fail. In addition, non-structural elements such as plasterboard wall linings and ceiling cornices can also contribute to load transfer and make roof-to-wall connections and wall systems less vulnerable to progressive failure.

However, in examining the load path progression from cladding through rafter to wall, the gust pressure correlation over the time domain follows the load sharing path for a number of wind directions. These correlation results indicate that in an overload situation, the peak gust pressures are applied to connections that have already attracted extra load as a result of load sharing from a failed fastener. This effect can also contribute to rapid progression of failure of batten-to-truss connections. Therefore, the limited load sharing at batten-to-truss connections coupled with the pressure correlation does not lead to an improvement in resilience of the structure, so it is important that each and every connection has the capacity to resist its design loads.

As further research on progressive failure in roofs continues, the varying resilience of connections within houses can be quantified.

AUTHOR CONTRIBUTIONS

DH, GB, KP, and NS: all revised the work critically, gave final approval for publication, agreed to be accountable for all aspects of the work, and have ensured the accuracy, integrity of the work. In addition, they have all contributed to the conception or design of the work and drafted the following sections: DH—Sections “Full-Scale Tests on House Roofs” and “Discussion of Benefits and Limitations,” GB—Sections “Introduction” and “Early Full-Scale Structural Tests on Whole Houses at CTS,” KP—Sections “Full-Scale Tests on House Roofs” and “Progressive Failure and Load Redistribution of Batten-to-Truss Connections,” and NS—Section “Full-Scale Tests on House Roofs.”

ACKNOWLEDGMENTS

This work was supported by Greg Reardon and Debbie Falck.

FUNDING

The authors and CTS would like to acknowledge the long-standing support of the Cyclone Testing Station's Supporters <https://cyclonetestingstation.com.au/benefactors-links>.

REFERENCES

- ABAQUS. (2013). *FEA Computer Software, Version 6.12-3*. Providence, RI: Dassault Systemes Simulia Corp.
- Boughton, G. N. (1988). *An Investigation of the Response of Full-Scale Timber-Framed Houses to Simulated Cyclonic Wind Loads*. Ph.D. thesis, James Cook University, Townsville.
- Boughton, G. N., and Reardon, G. F. (1982a). *Simulated Wind Tests on a House Part 1 – Description Technical Report No. 12*. Townsville: Cyclone Testing Station, James Cook University.
- Boughton, G. N., and Reardon, G. F. (1982b). *Simulated Wind Tests on a House Part 2 – Results Technical Report No. 14*. Townsville: Cyclone Testing Station, James Cook University.
- Boughton, G. N., and Reardon, G. F. (1983). *Testing a High-Set House Designed for 42 m/s Winds Technical Report No. 19*. Townsville: Cyclone Testing Station, James Cook University.
- Boughton, G. N., and Reardon, G. F. (1984a). *Testing a Logan Unit House Designed for 63 m/s Winds Technical Report No. 22*. Townsville: Cyclone Testing Station, James Cook University.
- Boughton, G. N., and Reardon, G. F. (1984b). *Simulated Wind Load Tests on the Tongan Hurricane House Technical Report No. 23*. Townsville: Cyclone Testing Station, James Cook University.
- Canino, I., Chowdhury, A., Mirmiran, A., and Suksawang, N. (2011). Triaxial load testing of metal and FRP roof-to-wall connectors. *J. Archit. Eng.* 17, 112–120. doi:10.1061/(ASCE)AE.1943-5568.0000039
- Datin, P. L., and Prevatt, D. O. (2007). “Wind uplift reaction at roof to wall connections of wood framed gable roof assembly,” in *12th International Conference on Wind Engineering* (Cairns, Australia).
- Doudak, G., McClure, G., and Smith, I. (2012). Experimental evaluation of load paths in light-frame wood structure. *J. Struct. Eng.* 138, 258–265. doi:10.1061/(ASCE)ST.1943-541X.0000439
- Ginger, J. D., Reardon, G. F., and Whitbread, B. J. (2000). Wind load effects and equivalent pressures on low-rise house roofs. *Eng. Struct.* 22, 638–646. doi:10.1016/S0141-0296(99)00015-2
- Henderson, D. J., Morrison, M. J., and Kopp, G. A. (2013). Response of toe-nailed, roof-to-wall connections to extreme wind loads in a full-scale, timber-framed, hip roof. *Eng. Struct.* 56, 1474–1483. doi:10.1016/j.engstruct.2013.07.001
- Huang, P., Chowdhury, A. G., Bitsuamlak, G., and Liu, R. (2009). Development of devices and methods for simulation of hurricane winds in a full-scale testing facility. *Wind Struct.* 12, 151–177. doi:10.12989/was.2009.12.2.151
- Leicester, R. H., and Reardon, G. F. (2010). Impact statistics of Tracy and an opportunity missed. *Aust. Meteorol. Oceanograph. J.* 60, 207–212. doi:10.22499/2.6003.009
- Morrison, M. J. (2010). *Response of a Two-Story Residential House under Realistic Fluctuating Wind Loads*. Ph.D. thesis, Department of Engineering, The University of Western Ontario, London, ON, Canada.
- Parackal, K., Ginger, J. D., and Henderson, D. J. (2016). “Correlation of peak wind loads at batten truss connections,” in *18th Australasian Wind Engineering Society Workshop* (McLaren Vale, South Australia).
- Reardon, G. F. (1986). *Simulated Cyclone Wind Loading of a Brick Veneer House Technical Report No. 28*. Townsville: Cyclone Testing Station, James Cook University.
- Reardon, G. F. (1990). *Simulated Cyclone Wind Loading of a Nu-Steel House Technical Report No. 36*. Townsville: Cyclone Testing Station, James Cook University.
- Reardon, G. F. (1996). “Simulated wind load testing of full size houses,” in *Structural Assessment – The Role of Large and Full Scale Testing* (London: Institution of Structural Engineers). City University International Seminar, City University.
- Reardon, G. F., and Henderson, D. J. (1996). “Simulated wind loading of a two storey test house,” in *Int. Wood Engineering Conference*, Vol. 4 (New Orleans, USA), 313–319.
- Reardon, G. F., and Mahendran, M. (1988). *Simulated Cyclone Wind Loading of a Melbourne Style Brick Veneer House Technical Report No. 34*. Townsville: Cyclone Testing Station, James Cook University.
- Satheeskumar, N., Henderson, D. J., Ginger, J. D., Humphreys, M. T., and Wang, C. H. (2016a). Load sharing and structural response of roof-wall system in a timber-framed house. *Eng. Struct.* 122, 310–322. doi:10.1016/j.engstruct.2016.05.009
- Satheeskumar, N., Henderson, D. J., Ginger, J. D., and Wang, C. H. (2016b). Three-dimensional finite element modelling and validation of timber-framed house to wind loading. *J. Struct. Eng. (ASCE)* doi:10.1061/(ASCE)ST.1943-541X.0001850
- Satheeskumar, N., Henderson, D. J., Ginger, J. D., and Wang, C. H. (2016c). Wind uplift strength capacity variation in roof-to-wall connections of timber-framed houses. *J. Archit. Eng.* 22, 04016003. doi:10.1061/(ASCE)AE.1943-5568.0000204
- Satheeskumar, N., Henderson, D. J., Ginger, J. D., and Wang, C. H. (2016d). Finite modelling of the structural response of roof to wall framing connections in timber-framed houses. *Eng. Struct.* 134, 25–36. doi:10.1016/j.engstruct.2016.12.034
- Standards Australia. (1983). *AS 1170.2 SAA Loading Code Part 2: Wind Loads*. Sydney: Standards Australia.
- Standards Australia. (2001). *AS 1649 Timber – Methods of Test for Mechanical Fasteners and Connectors – Basic Working Loads and Characteristic Strengths*. Sydney: Standards Australia.
- Standards Australia. (2010). *AS 1684.3 Residential Timber-Framed Construction – Part 3: Cyclonic Areas*. Sydney: Standards Australia.
- Stewart, M. G., Wang, X., Bradford, M., Ginger, J., Hao, H., Sanjayan, J., et al. (2016). “Final report – climate adaptation engineering for extreme events cluster,” in *CAEx Report 2016* (Canberra: CSIRO).
- Trollope, D. H. (1972). *Cyclone “Althea” – Part 1 – Buildings*. Townsville: James Cook University.
- Walker, G. R. (1975). *Report on Cyclone Tracy*. Canberra: Australian Department of Housing and Construction.

Conflict of Interest Statement: The authors declare that the research was conducted in the absence of any commercial or financial relationships that could be construed as a potential conflict of interest.

Copyright © 2017 Boughton, Parackal, Satheeskumar and Henderson. This is an open-access article distributed under the terms of the Creative Commons Attribution License (CC BY). The use, distribution or reproduction in other forums is permitted, provided the original author(s) or licensor are credited and that the original publication in this journal is cited, in accordance with accepted academic practice. No use, distribution or reproduction is permitted which does not comply with these terms.



A Cyber-Based Data-Enabled Virtual Organization for Wind Load Effects on Civil Infrastructures: VORTEX-Winds

Ahsan Kareem* and Dae Kun Kwon

NatHaz Modeling Laboratory, Department of Civil & Environmental Engineering and Earth Sciences,
University of Notre Dame, Notre Dame, IN, United States

OPEN ACCESS

Edited by:

Gregory Alan Kopp,
University of Western Ontario,
Canada

Reviewed by:

Franklin Lombardo,
University of Illinois at Urbana-
Champaign, United States
Chris Letchford,
Rensselaer Polytechnic Institute,
United States

*Correspondence:

Ahsan Kareem
kareem@nd.edu

Specialty section:

This article was submitted to Wind
Engineering and Science,
a section of the journal
Frontiers in Built Environment

Received: 09 January 2017

Accepted: 21 July 2017

Published: 21 August 2017

Citation:

Kareem A and Kwon DK (2017)
A Cyber-Based Data-Enabled
Virtual Organization for Wind Load
Effects on Civil Infrastructures:
VORTEX-Winds.
Front. Built Environ. 3:48.
doi: 10.3389/fbuil.2017.00048

Despite many advances in the area of wind effects on structures in recent decades, research has been traditionally conducted within limited resources scattered geographically. With the trend toward increasingly complex designs of civil infrastructure combined with the escalating potential for losses by extreme wind events, a new culture of research needs to be established based on innovative and collaborative solutions for better management of the impact of extreme wind events. To address this change, this paper presents a new paradigm of a multiscale cyber-based laboratory framework for the analysis/design, modeling, and simulation of wind load effects based on an ongoing collaborative cyberinfrastructure-based platform, Virtual Organization for Reducing the Toll of EXtreme Winds (VORTEX-Winds, <https://vortex-winds.org>), and discusses its current status since its inception in 2007 and ongoing developments. This collaborative framework as it evolves would enable a paradigm shift by offering advanced cyber-enabled modules (e-modules) for accelerating advances in research and education to achieve improved understanding and better modeling of wind effects on structures. Accordingly, it will enhance wind community's analysis and design capabilities to address next-generation challenges posed by wind. Through empowering those without computational or experimental resources, the e-modules will encompass a large set of subject areas and topics categorized as Database-enabled design, Full-scale/Field site data repository, Statistical/Stochastic toolboxes, Tele-experimentation, Uncertainty modeling, Damage assessment, and Computational platforms. This prototype will allow access to the individual e-module, while it is envisaged that next level of development in VORTEX-Winds will have the capability for an automated and integrated analysis/design through a nexus of e-modules. A highlight of the e-modules currently completed or in development is presented not only to show the efficacy of the framework to enhance and supplement the limitation of traditional off-line approaches but also to describe architecture and features of e-modules to promote additional cyber-enabled data-driven developments in the field.

Keywords: virtual organization, cyberinfrastructure, extreme winds, wind load effects, modeling, simulation, analysis, design

INTRODUCTION

Wind-related catastrophes by extreme winds such as hurricanes, tornadoes, thunderstorms/down-bursts, etc. inflict enormous devastation on the built environment and result in a staggering number of fatalities. A recent report by Munich Re Group (2012) showed that North America has been most affected by weather-related extreme events in the world in recent decades. To better understand and

manage the impact of such extreme wind events, a new culture of research needs to be developed based on innovative solutions. In this regard, a virtual organization (VO) or cyberinfrastructure (CI) has been recognized as a possible means in many disciplines to offer real-time shared access to geographically dispersed resources, which would enable the pooling of resources reliant on Internet and information technology (IT) (Kijewski et al., 2003; Frame et al., 2009). A conceptual example framework for integrated design for wind effects is envisioned in **Figure 1A** in which computational, experimental, and other features are managed and coordinated by a cyber studio using a cloud platform.

Other fields are fast recognizing the potential impact of such a technology. An example is NERC environmental eScience consortia comprising a variety of VOs in the fields of environmental sciences to share resources and perform collaborator (Gurney et al., 2009). Similarly, the structural design field is currently at the dawn of adopting a new IT known as Building Information Modeling, which promises to revolutionize the design and the construction of buildings. Building Information Models are 3-D, smart, parametric e-models of buildings that are shared by a team of designers and builders to facilitate the exchange and interoperability of information in a digital format. However, such a conventional concept of VO or CI that simply shares valuable resources for collaboration has now evolved into the new stage with the rapid IT developments. For example, nanoHUB for nanotechnology offers not only community-contributed resources but also online computational tools based on grid computing (Goasguen et al., 2008). In structural engineering field, the Network for Earthquake Engineering Simulation (NEES) (Van Den Eende et al., 2007) offered a feature of networked facilities for enhancing seismic hazard research through hybrid tests. These facilities have made high-end resources accessible to groups otherwise limited by their personal research tools allowing them to expand the scope of their research to address complex problems. NEES also offered computational tools by adopting the framework of nanoHUB, named NEEShub (Rodgers, 2011). Although those advanced CI frameworks despite their promise were either to computational or experimental/hybrid methods.

Similar to other disciplines that usually include broad research subjects, the topic of wind effects on structures is of an interdisciplinary nature that requires a knowledge base from a large number of subject areas. It includes meteorology, structural engineering, engineering mechanics, probabilistic/statistical methods, fluid dynamics, turbulence, structural dynamics, experimental methods, risk, reliability, etc. (e.g., Kareem, 2005, 2008). For better quantifying the load effects, a new paradigm shift is required to provide efficient and reliable tools or procedures for both research and practice. Certainly, it is a daunting task to develop such innovative solutions by a group or two, thus community-level efforts are necessary. With the recognition of this demand, for example, the National Science Foundation (NSF) has recently launched a new initiative, Natural Hazards Engineering Research Infrastructure (NHERI) [National Science Foundation (NSF), 2014], replacing NEES, which is a distributed, multiuser, national platform to provide the natural hazards engineering community (e.g., earthquake and wind engineering) with access to research infrastructure. A CI underpins and integrates NHERI as a VO

that offers researchers a platform for research collaboration and knowledge sharing (DesignSafe-CI¹). Central to NHERI is the experimental testing, computational modeling and simulation, research data and their integration with theory for generating knowledge, and innovation needed to mitigate the impact of future natural hazards such as earthquakes, windstorms, etc. [National Science Foundation (NSF), 2014].

In anticipation of a CI based data-enabled engineering as a central component of a computational/experimental infrastructure, this study describes the evolution of a cyber-enabled framework for analysis/design, modeling, and simulation of wind load effects, Virtual Organization for Reducing the Toll of EXtreme Winds (VORTEX-Winds) at <https://vortex-winds.org>, and discusses its current status since its inception in 2007 and ongoing developments that predate the current CI-based initiatives. It aimed not only to facilitate an effective, transformative, and conveniently accessible methodology for the acceleration of advances in research and education in the broad area of wind effects but also offered initial developments in an end-to-end automated and integrated wind design approach for practical application in the end. This framework would enhance analysis and design capabilities to address the challenges of innovative structural systems needed to realize, in a cost effective manner, buildings with ever increasing heights, bridges that span oceans, and offshore platforms tapping hydrocarbons in deeper waters exposed to weather extremes like hurricanes. This challenge is envisaged to be accomplished by cyber-enabled e-modules classified into *Database-enabled design (DED)*, *Full-scale/Field site data repository*, *Statistical/Stochastic toolboxes*, *Tele-experimentation*, *Uncertainty modeling*, *Damage assessment*, and *Computational platforms*. The prototype framework would allow access to the modules individually, while the fully functional VORTEX-Winds may also have the capability for automated, integrated analysis and design by interactively stitching multiple modules. Throughout a highlight of ongoing e-module projects encompassing broad wind research areas, the efficacy of the framework to enhance and supplement traditional off-line approaches is demonstrated. In addition, architectures and implementations of e-modules are described to serve as a reference or direction for prompting additional cyber-enabled developments by the community.

OVERVIEW OF VORTEX-WINDS

The basic vision of VORTEX-Winds is the development of a comprehensive gateway for research and education to achieve improved understanding and modeling of wind effects on structures to counter the escalating loss of property and associated indirect losses and the increase in the sensitivity of emerging structural systems to winds. In response to this vision, the VORTEX-Winds was established in 2007 with the following goals:

- (i) to establish and sustain a community contributing to and employing the resources integrated by CI technologies to facilitate the mitigation of escalating damage, loss of life, and disruption of local economies posed by wind;

¹<https://www.designsafe-ci.org>.

- (ii) to enhance analysis and design capabilities to address the challenges of innovative structural systems needed to realize, in a cost effective manner, buildings with ever increasing heights, bridges that span oceans, and offshore platforms in deeper waters exposed to weather extremes like hurricanes; and
- (iii) to facilitate education and training of the future workforce in the field so that the growing competition in the global market is met through a cadre of well-trained professionals and educators.

VORTEX-Winds envisions offering all aspects of CI capabilities to research and engineering community in the area of wind effects on structures, including (1) communication tools to support collaboration, (2) high-performance computational infrastructure, (3) data storage, data mining, visualizations, and data warehousing, and (4) access to remote sensors and tele-experimentation. The structure of VORTEX-Winds consists of two main branches: the knowledge base and the cyber-enabled e-modules as shown in **Figure 1B** (Kareem et al., 2009). The knowledge base is similar to the functionality of a conventional VO to aggregate and centralize the shared knowledge of the collaboratory. Services in this

area include the virtual encyclopedia, *Wind-Wiki*, encompassing basic terminology and concepts pertaining to wind-structure interaction, *Damage database* that is curated archives of postdisaster reconnaissance (e.g., Kareem, 1985, 1986), *Help desk*, where users can submit a question to the collaboratory and where past responses are archived as *FAQ*, *Bulletin boards* hosting open discussions, *Email list servers* for rapidly circulating announcements and other information, and *Curriculum tools* to provide educators a means to formally integrate VO services into their teaching.

A key component of VORTEX-Winds is the cyber-enabled e-modules to not only offer an automated and integrated design approach under CI but also facilitate research activities by researchers and students, which are developed by authors as well as harvested from the independent work of a number of universities (largely supported by federal funding) and government agencies such as NIST, etc. (Kareem et al., 2009). For wind design, a traditional off-line procedure for civil infrastructures as shown in **Figure 2A** relies on a broad-band knowledge and extensive procedures involving a variety of subjects. The integrated design approach proposed in this study mimics the traditional procedure schematically depicted in **Figure 2B** for providing more efficient and accurate assessment of wind effects on structures and design

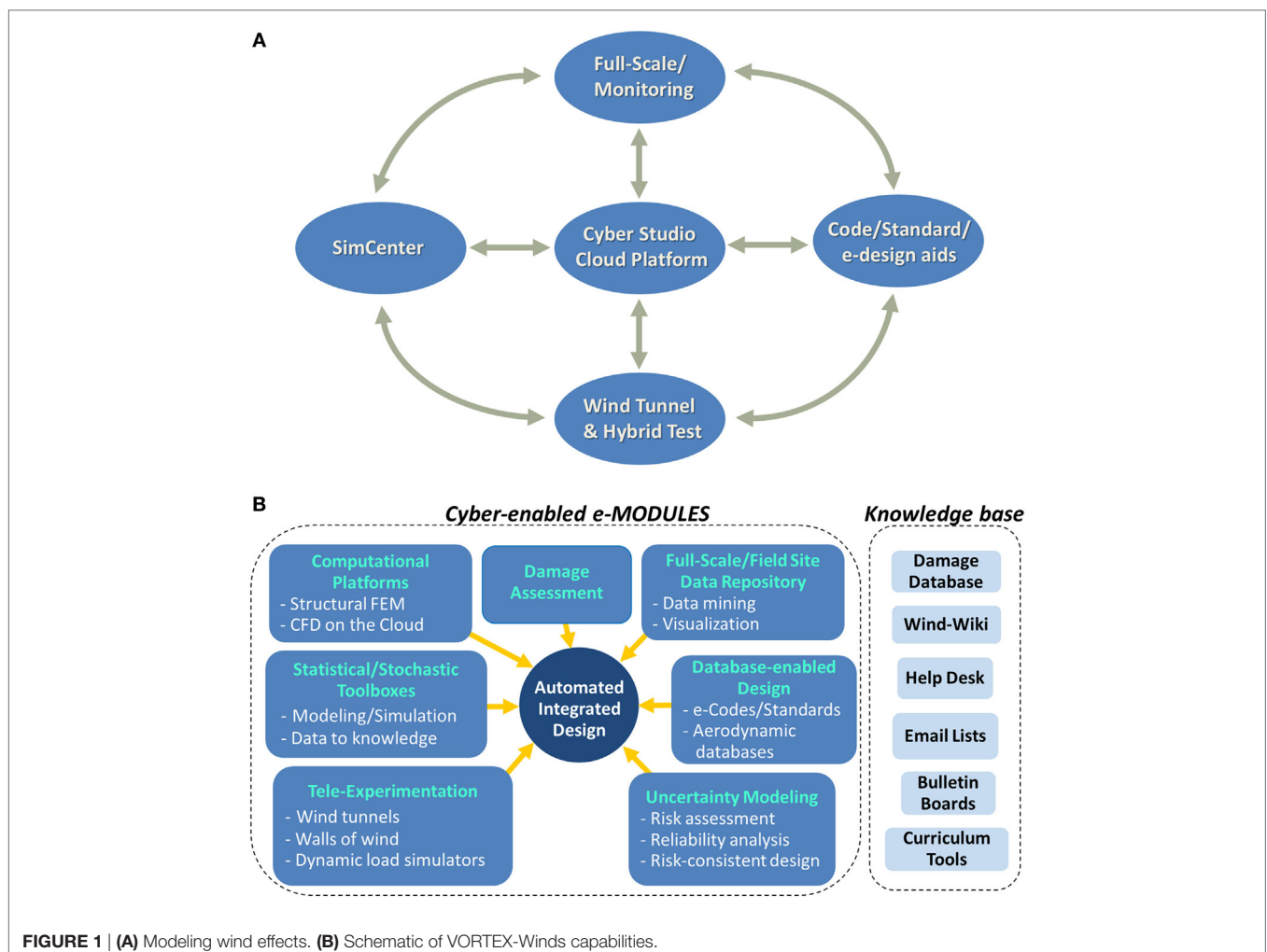


FIGURE 1 | (A) Modeling wind effects. (B) Schematic of VORTEX-Winds capabilities.

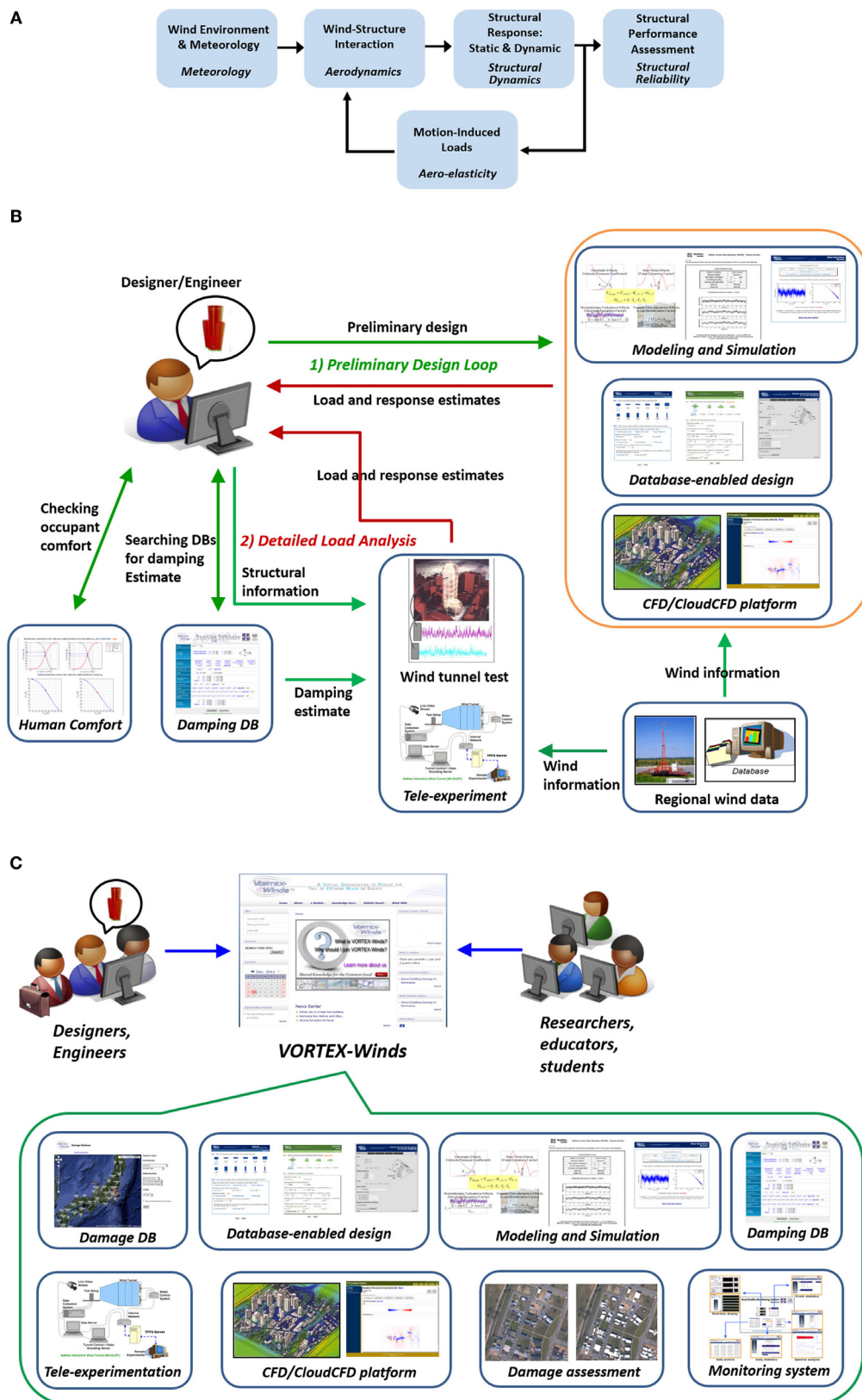


FIGURE 2 | (A) Traditional off-line design. **(B)** Integrated analysis and design concept in VORTEX-Winds. **(C)** An overview of ongoing cyber-enabled modules.

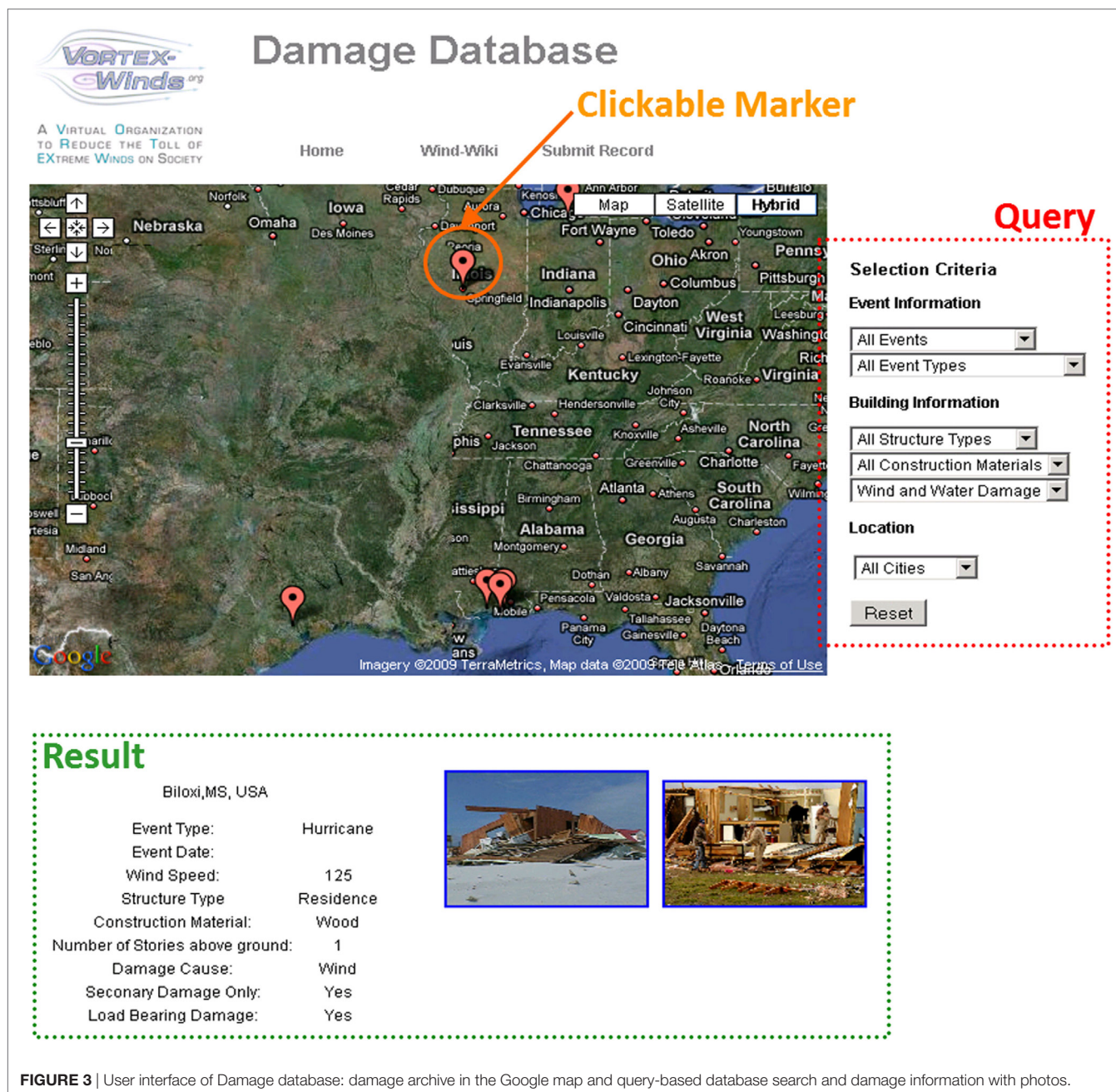


FIGURE 3 | User interface of Damage database: damage archive in the Google map and query-based database search and damage information with photos.

process. In view of the interdisciplinary nature of wind effects on structures requires knowledge from a large number of subject areas, the e-modules are classified into seven categories: *Database-enabled design*, *Full-scale/Field site data repository*, *Statistical/Stochastic toolboxes*, *Tele-experimentation*, *Uncertainty modeling*, *Damage assessment*, and *Computational platforms* (Figure 1B). Examples of the modules offered within each category are shown in Figures 3 and 4. The modules are currently interrogated independently but the final goal is that modules can be automatically queried and input into an integrated analysis and design approach by stitching together multiple modules. A more advanced framework will be the inclusion of a knowledge-based expert system

in the loop of the integrated design concept (e.g., Kareem and Allen, 1990). Consequently, it is envisaged that VORTEX-Winds will provide access to communication, data, computational, and remote sensing and tele-experimentation services to generate a comprehensive, interactive design aid. Users will be able to execute either individual services or composite services integrated from multiple atomic services for the purpose of research activity or wind design process. This will require format conversion of data and those conversions will be provided as stand-alone services or directly integrated into the prepackaged web-service workflows. It should be noted that the interactive design aid will take the notion of hybrid simulation a step further by utilizing databases,

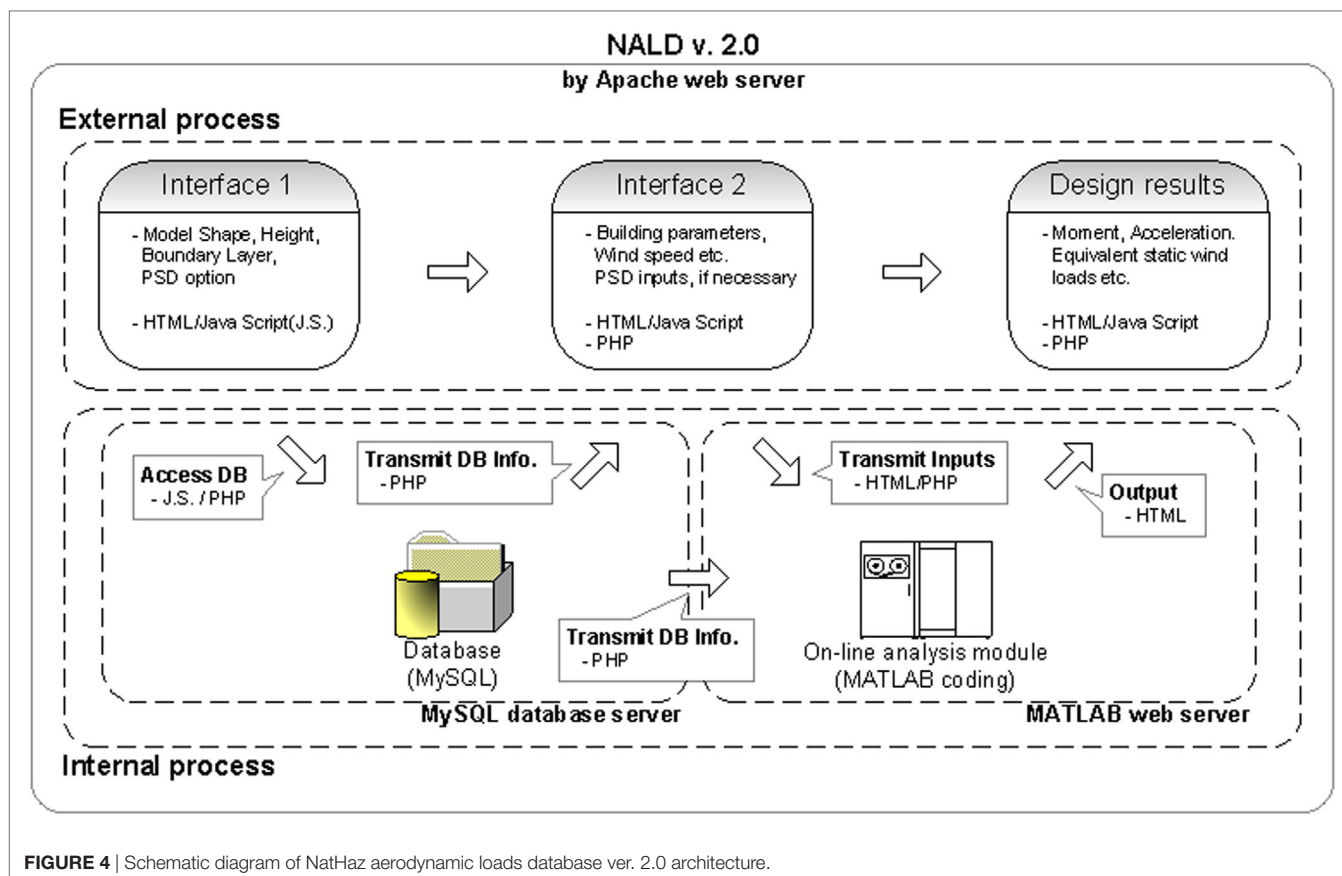


FIGURE 4 | Schematic diagram of NatHaz aerodynamic loads database ver. 2.0 architecture.

experiments, full-scale measurements, and analytical models through repeated queries and multistage analyses.

From an educational perspective, VORTEX-Winds' introduction of a knowledge-based framework and cyber-enabled e-modules can indirectly serve as educational tools to countless professional end users as well as K-12 and postsecondary education. This is particularly important considering the general shortage of engineers formally educated in wind effects in this country and requires intervention with K-12 students as early as possible as part of a STEM education. At the postsecondary level, for example, these services can be integrated into an introductory structural engineering course at the freshman level and a vital resource for the wind engineering and structural system courses for graduate students emphasizing the cross-disciplinary nature of modern design subject to winds. Similar efforts using web-based technology have been reported by researchers (e.g., Wang and Adeli, 2012a,b). In addition, educators such as K-12 teachers and college/university professors can use these services to develop curriculum tools. Then, these will be archived in the knowledge base for access by other educators nationwide so that VORTEX-Winds will provide an effective pedagogical tool to learn a highly technical subject, which has its roots in a host of interdisciplinary fields, through the use of cyberspace and visualization capabilities.

These services are hosted on the front end by a single gateway server with computation and analysis conducted on back-end

parallel servers. The primary technical hurdle is in achieving e-module developments and their integration, which will require significant effort and coordination, particularly with respect to the integrated design feature. At this stage, VORTEX-Winds has been focusing on the achievement of individual e-modules. An overview of ongoing cyber-enabled modules is shown in **Figure 2C** and their current and ongoing statuses are listed in **Table 1**. More detailed information about the highlights of CI modules for analysis/design, modeling, and simulation modules of wind load effects on structures in the VORTEX-Winds is presented in the following sections. It is anticipated that the architecture and implementation of e-modules demonstrated in the following will serve as a reference or direction for prompting additional cyber-enabled developments by the community.

CYBER-ENABLED ANALYSIS/DESIGN, MODELING, AND SIMULATION MODULES

Damage Database

The Damage database is a digital repository of postdisaster investigation documenting damage to structures during extreme wind events such as hurricane/typhoon/cyclone, tornado, thunderstorm/downburst, extratropical winds, etc. The information provided by this database may be beneficial to a variety of studies, e.g., evaluation of extreme wind effects on structures

TABLE 1 | Current and ongoing statuses of e-modules in the VORTEX-Winds.

e-Module category	e-Modules in service	In preparation/beta testing
Database-enabled design	NALD, DEDM-HR, DEDM-HR-INT, DEDM-HRP, DEDM-LR, PBDED-OC ^a	–
Data repository	Damping database, Damage database	Full-scale data sets
Statistical/Stochastic toolbox	NOWS, NGFF, VOWS	Non-Gaussian/non-stationary simulation modules
Computational platform	–	Cloud-CFD/VWT
Tele-experimentation	–	NH-GUST
Uncertainty modeling	PBDED-OCa	–
Damage assessment	–	Damage assessment using aerial/satellite imagery

^aPBDED-OC involves an uncertainty analysis through a Monte Carlo simulation. CFD, Computational Fluid Dynamics; DEDM-HR, Database-enabled design module for high-rise; DEDM-HRP, Database-enabled design module for high-rise building with pressure data; DEDM-LR, DED module for low-rise buildings; NALD, NatHaz aerodynamic loads database; NGFF, NatHaz gust-front factor; NH-GUST, NatHaz interactive wind tunnel; NOWS, NatHaz online wind simulator; PBDED-OC, performance-based design of high-rise buildings for occupant comfort; VOWS, VORTEX-Winds online wind simulator; VWT, Virtual Wind Tunnel.

in full-scale, learning lessons from extreme events to improve structural design, postdisaster assessment in a regional area, correlation between wind speed and structural performance in damage aspect, etc. (e.g., Kareem, 1985, 1986). The database was established based on a web-based database-query method and powered by Google Map/Earth API (Google, 2015), which allows users to geographically view submissions of fellow VORTEX-Winds members, sorting by location, event classification, and damage attributes automatically (**Figure 3**). Users can search damage archives either by pointing at a spot in the Google map or by using query-criteria in the right side of the map. Each damage report is comprised of wind event on damage, maximum wind speed, damage location in either addresses or GPS coordinates, structural properties, damage photos, etc. which registered members can upload their own damage reports to the database through a web interface.

It is worth noting that this Damage database is one of the first e-module developed for the VORTEX-Winds in 2009, thus rather old technology in view of current rapid developments in web-based technologies. For this reason, we are in the process of eventually retiring this module and transfer the existing data to newly developed “Data Intake and Discovery” module in CyberEye (Kijewski-Correa et al., 2014) in which authors are also involved. It is envisioned that this new module will be further enriched with the contribution of members over time.

DED Frameworks

Most international wind codes and standards traditionally have relied on reductive formats and simplifications, which often lead to tables and plots that describe wind loads on structures, especially, focusing primarily on the alongwind response owing to the introduction of the well-known quasi-steady/strip theories and gust loading factor approach introduced by Davenport (1967) and later further refined over the years by

several researchers (e.g., Solari, 1993a,b; Solari and Kareem, 1998; Zhou and Kareem, 2001; Kareem and Zhou, 2003). However, failure of the basic assumptions in these theories and the gust loading factor approach in the acrosswind and torsional directions has precluded a formulation based on first principles. Some codes and standards do provide limited guidelines on these aerodynamic loads, however, they are restricted to empirical expressions based on measured response of limited number of building models tested in wind tunnels. Although these expressions are still valuable for assessing preliminary estimates of response, their accuracy may not be consistent for different shapes as often small changes in the shape result in major changes in the aerodynamic effects. In addition, the level of accuracy inherent in codification information in this format and the uncertainty associated with interpolation or extrapolation of information may compromise the overall accuracy in code-specified load effects.

To overcome the aforementioned limitation, a DED procedure has been gradually gaining acceptance. The basic concept of DED is to directly use wind tunnel-derived data to better estimate the response instead of relying on code/standard-based procedure. A DED generally offers convenient meshing of a database with analysis software for either low to mid-rise and high-rise buildings. The NatHaz aerodynamic loads database (NALD) ver. 1.0 introduced in 2000 has served an important first step in establishing a DED through online experimental archive of high frequency base balance (HFBB) data for use in the preliminary design of high-rise buildings subjected to wind loads. As a result, NALD ver. 1.0 was introduced in the Commentary of ASCE 7-05 (C6.5.8) [American Society of Civil Engineers (ASCE), 2005] and the latest ASCE 7-10 (C26.9) [American Society of Civil Engineers (ASCE), 2010] as an alternative means of assessing the dynamic wind load effects on high-rise buildings. This includes the web-enabled wind tunnel data dissemination to evaluate the response of tall buildings (Zhou et al., 2003). However, it required manual dynamic analyses based on random vibration theory for the preliminary design.

To overcome the last step in NALD v. 1.0 (Zhou et al., 2003) involving off-line calculations, a more advanced DED framework for estimating the wind-induced response of tall buildings has been proposed with the help of recent developments in IT (Kwon et al., 2008). This new paradigm offers an attractive solution with a concept of a cyber-based online on-the-fly analysis/design *via* user-friendly web interfaces. It is particularly useful for those who may not be very familiar with the details of the random vibration-based dynamic analysis procedure generally used in conjunction with wind tunnel-driven data. Accordingly, NALD evolved into version 2.0 in 2004 using this advanced framework. NALD ver. 2.0 (Kwon et al., 2005, 2008) has integrated the latest advances in data management and mining for interactive queries of aerodynamic load data and an integrated web-based analysis framework for determining the resulting maximum displacements, base moments, and equivalent static wind loads (ESWL) for survivability and peak/root mean square (RMS) accelerations for serviceability (habitability). The key feature of NALD ver. 2.0 is the flexibility that its analysis module offers: users may select not only the data from the online NALD but also may input desired

power spectral density (PSD) expressions or wind tunnel-derived PSD data set obtained from HFBB experiment for the evaluation of wind load effects on high-rise buildings. Thus, it also serves as a stand-alone analysis engine. The NALD ver. 2.0 provides a platform that can be readily expanded and supplemented to yield a comprehensive, simplified, and efficient avenue for e-analysis/design of high-rise buildings. The architecture of NALD ver. 2.0 and the role of various web-based tools such as HTML/JavaScript and PHP are summarized in **Figure 4**. It is basically operated by Apache web server with two main processes, i.e., external (foreground) process and internal (background) process. The external process includes user-friendly web interfaces for the selection of a desired analysis case (interface 1 as shown in **Figure 5A**), additional interfaces for design inputs such as structural parameters of building (interface 2), and display of analysis results for the user-specified building. On the other hand, the internal processes are server-side operations involving MySQL for database operations and MATLAB (Mathworks, 2015) for the computation, which are implicitly utilized in NALD ver. 2.0. The MySQL database server handles data transmissions between interfaces and if necessary transmits information stored in the database. Preprogrammed MATLAB and PHP codes function as a numerical analysis engine for on-the-fly calculations as well as serving as the nexus between interface 2 and the design results. The cyber-based online analysis module performs the requisite calculations and then generates meaningful figures such as the non-dimensional PSD and ESWL, as well as downloadable output file. This architecture became a prototype cyber-based framework, which prompted further development of DED modules such as DEDM-HR, Database-enabled design module for high-rise building with pressure data (DEDM-HRP), DED module for low-rise buildings (DEDM-LR), and performance-based design of high-rise buildings for occupant comfort (PBDED-OC), which will be discussed in the following.

Database-Enabled Design Module for High-Rise

Although DED is a promising design procedure for better and more reliable wind-induced responses than conventional codes and standards, it requires a database of wind tunnel data, which are often limited in building shapes and configurations. As more data sets become available, the designers/researchers will have more flexibility. To alleviate this limitation, a DEDM-HR introduced a new concept of DED, which seamlessly pools multiple HFBB measurement databases from geographically dispersed locations and merges them efficiently to expand the number of available building configurations for the preliminary design (Kwon and Kareem, 2013a). This feature not only offers a new direction for the research and professional community that can be utilized to efficiently pool multiple databases, expand capability of individual database and ensures the reliability of design estimates to pool databases in the future. In addition, the DEDM-HR embeds a novel feature that allows the employment of wind characteristics defined differently between codes/standards to supplement the specifications of a specific code or standard, which in many cases lacks guidance on the acrosswind and torsional response estimates (**Figure 5B**). Currently, the DEDM-HR is associated with two databases: one is the NatHaz database from

the NatHaz Modeling Laboratory, University of Notre Dame, USA, which is also the one used in the NALD (Zhou et al., 2003; Kwon et al., 2005, 2008), and the other is the Tamkang University database from the Wind Engineering Research Center, Tamkang University, Taiwan (Cheng and Wang, 2004).

Database-Enabled Design Module for High-Rise Building with Pressure Data

The aforementioned DED modules such as NALD and DEDM-HR have utilized HFBB database(s) resulting from the HFBB technique, which is a relatively simple and popular experiment to measure base forces/moments. Nonetheless, it involves some inherent drawbacks such as mode shape corrections and the assumption of wind pressure distribution over the building surface. On the other hand, the synchronous pressure measurement (SPM) technique in wind tunnel test is to synchronously measure the pressure fields using a test model with quite a number of pressure taps distributed at a model surface, which has the advantage to directly assess local and global aerodynamic loads acting on the structure without specific assumptions. Thus, the technique offers the direct estimation of the generalized forces including any coupled effects, non-linear and higher mode shapes (e.g., Kwon et al., 2005, 2008; Cluni et al., 2011). A drawback concerning the SMP technique is that a large number of pressure taps are required to accurately estimate wind loads, which may cause an issue of manufacturing test models, especially for complex geometries to locate pressure taps. In addition, the amount of data is generally much larger than HFBB experiments. Furthermore, the treatment and management of SMP datasets with the knowledge of complex background theories and procedures are often difficult. For an effective treatment of a large SPM data set within the concept of cyber-based DED framework, a DEDM-HRP has been developed (Kwon et al., 2014). It addresses the management of synchronously measured pressures and their reduction to global loads, which is often a daunting task due to the large amount of data information involving highly sampled time histories by its experimental nature. DEDM-HRP currently hosts a publicly available Tokyo Polytechnic University (TPU) aerodynamic database for a variety of building configurations for side and aspect ratios and various wind directions for each test model to account for directional effects of winds (Tamura, 2013). However, the e-module can be easily expanded to host multiple SPM databases similar to DEDM-HR. This framework is based on a time domain treatment of the random vibration (e.g., Simiu et al., 2008) and uses a minimal set of easily obtainable parameters as input such as wind speed, natural frequencies, and mode shapes of a target building etc., which the user can interact with user-friendly web interfaces (**Figure 5C**). For efficient calculation to minimize online computational time, this module employed a dynamic analysis based on floor level loads, precalculated and stored within the module. Estimated outputs are maximum base shears and moments, maximum top displacement/acceleration responses for alongwind, acrosswind, and torsional directions, and various oncoming wind directions. In addition, DEDM-HRP also offers the assessment of ESWL based on the formulation in Chen and Kareem (2005) for preliminary design purposes.

A

Welcome to the Vortex
**AERODYNAMIC LOADS
DATABASE**

User Interface for Design Inputs (1 of 2 page)

Step 1 : Select Shape of Interest

01 D=2" B=6" 02 D=3" B=6" 03 D=4" B=6"
04 D=4" B=4" 05 D=6" B=4" 06 D=6" B=3"
07 D=6" B=2" 08 D=4" B=4" 09 D=6" B=6"

Step 2 : Select Height of Interest

15' 20' 25'

Step 3 : Select Exposure Category of Interest

Urban Exposure A Open Exposure C

Step 4 : Options of Non-dimensional power spectral density(PSD)

- Use PSD data tested by NatHaz (Default)
- Use User's PSD Expression ($C_{MN}(\theta) = f \cdot S_{MN}(\theta) / \sigma_{MN}^2$)
- Use User's PSD Data, X,Y pairs

Next Reset

B

Vortex-Wind A VISUAL REPRESENTATION TO BRIDGE THE GAP OF EXISTING WIND ON SOCIETY

DEDM-HR : Design Inputs (1/2)

Collaborators

Step 1 : Select cross-sectional shape of interest: values are side ratios (D/B)

0.20 0.25 0.33 0.50 0.67
1.00 1.50 2.00 3.00 4.00 5.00

Step 2 : Units, exposure category (ASCE 7), building dimensions and 3-sec gust wind speed

Input units (default : Metric). Checkbox for English unit output (default : Metric)

☒ Metric(SI) unit [kg, m, m/s] ☐ English unit [lb, ft, mph] ☐ Output : English unit

Building width (B), depth (D) and height (H)

B [m, ft] : 33 D [m, ft] : 33 H [m, ft] : 200

Exposure Category [Help](#)

☒ A (Large city center) ☐ B (Urban/Suburban) ☐ C (Open terrain)

A Code/Standard to use (additional input boxes will be displayed)

Eurocode (2010)

Basic/Reference wind speed (10-min mean) for survivability (U_{sur}) and serviceability (U_{ser}) designs from country specific data, e.g., wind map

U_{sur} [m/s, mph] : 28.1 U_{ser} [m/s, mph] : 24

Eurocode (2010)
Plz select a Code/Standard ...
ASCE 7-10 (2010)
AIJ (2004)
Eurocode (2010)
NBCC (2010)

Next Reset

FIGURE 5 | Continued

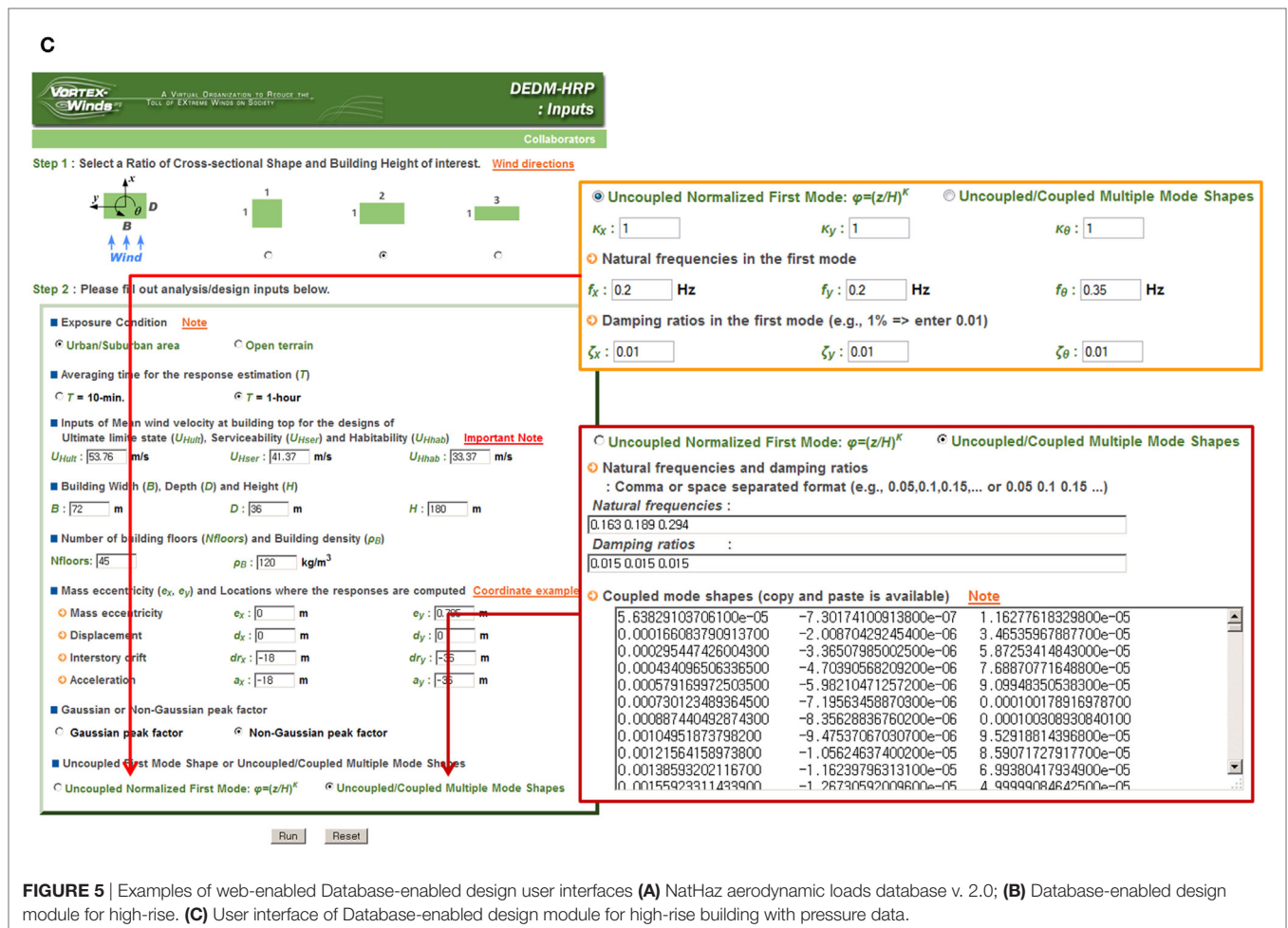


FIGURE 5 | Examples of web-enabled Database-enabled design user interfaces (A) Nat-Haz aerodynamic loads database v. 2.0; (B) Database-enabled design module for high-rise. (C) User interface of Database-enabled design module for high-rise building with pressure data.

DED Module for Low-Rise Buildings

This new DED concept has been expanded to address a need for a preliminary design of low-rise buildings, namely, a DEDM-LR, which provides calculation of wind loads for main frames in low-rise buildings that make direct use of pressure time histories measured at a large number of pressure taps over building models in wind tunnel tests (Kwon et al., 2016). Presently, DEDM-LR works for a database constructed at TPU, Japan (Tamura, 2013), which includes various building configurations, but it will be expanded with more available databases. The main analysis/design engine inside DEDM-LR searches for extreme load effects based on pressure data at multiple locations and wind directions given the influence line coefficient for the load effect. The fundamental theory employed in DEDM-LR have mainly been adopted from a procedure developed at NIST (Main and Fritz, 2006), which utilizes synchronous pressure data sets measured in various wind directions of a test model to evaluate responses in a low-rise building such as base moments at knee, ridge etc. using influence line coefficient-based approaches, computed using a structural analysis program such as SAP2000, etc. The DEDM-LR is basically operated under an Apache web server with two main processes, i.e., foreground and background processes as shown in **Figure 6**, which is similar to the architecture used in

other DED modules. Foreground process functions interactive web interfaces for user inputs and analyzed/designed results and background process performs database-query and computational analysis/design.

Performance-Based Design of High-Rise Buildings for Occupant Comfort

Recently, the concept of web-enabled DED has also been applied to a newly developed probabilistic framework for the PBDED-OC (Bernardini et al., 2015). The performance is expressed in terms of the probability that the fraction of people on a target floor that perceive the motion exceeds a chosen value, given a mean recurrence interval for the wind event. In addition to the random perception threshold characterizing each individual occupant, other uncertainties affecting the structural response have been included concerning the wind speed, the modal characteristics of the structure, and the use of wind tunnel tests (in particular, HFBB tests), taking advantage of probabilistic models that can be found in the literature. Fully in accordance with the principles of performance-based design, the proposed framework provides the designer with a flexible tool for the description of the structural performance, where the acceptable probability of exceedance can be chosen by a team of decision-makers (designers,

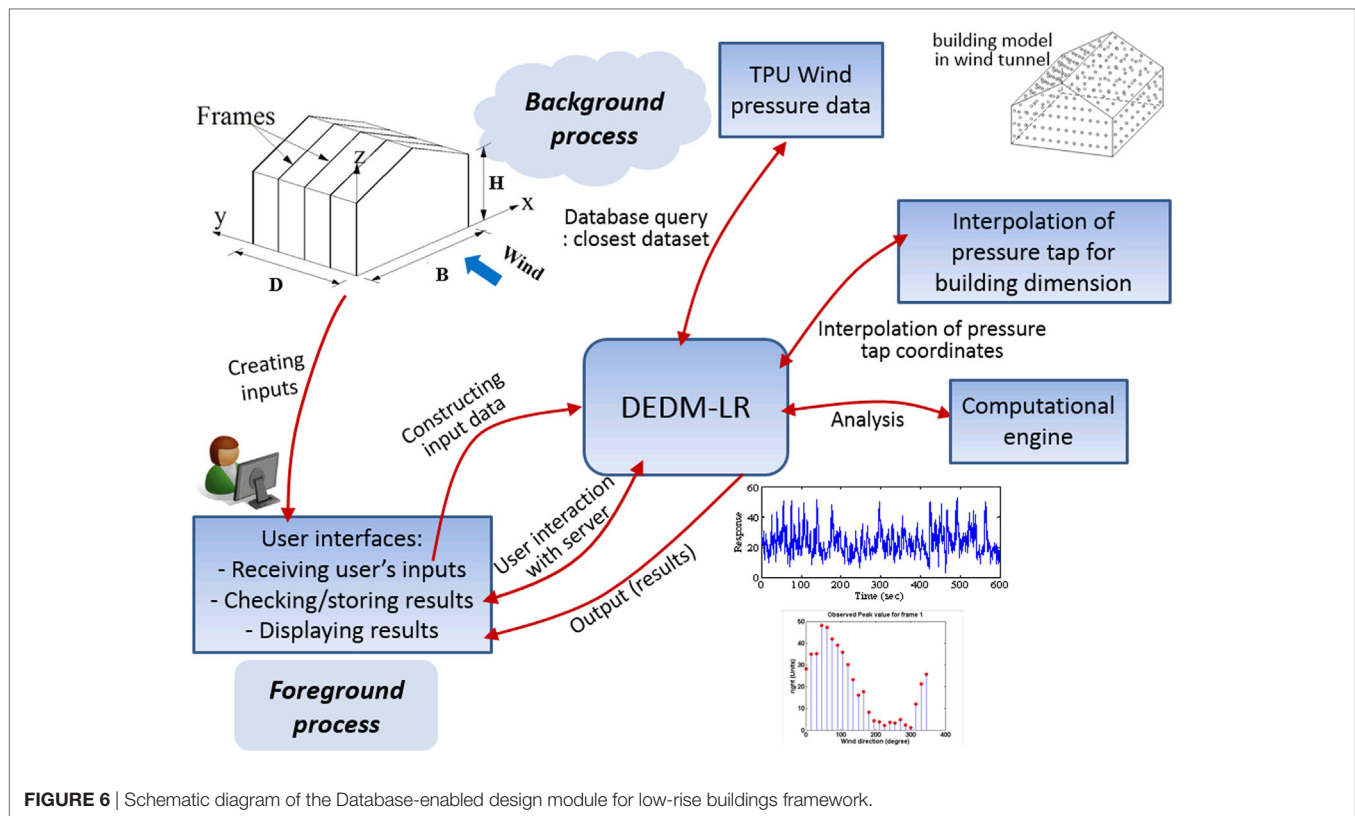


FIGURE 6 | Schematic diagram of the Database-enabled design module for low-rise buildings framework.

building owner, tenants, etc.) depending on the peculiarities of the structure, and is seen as an alternative to the use of prescriptive approaches, which are instead based on a simple comparison between demand and capacity and do not provide any information on the reliability of the structure. The input fields concern the building geometry, the 3-s gust wind speed, the type of exposure according to the ASCE Standards, and the averaging time for the response estimation (in particular a 10 min or a 1 h averaging time) can be selected, as these are the typical values adopted in most international codes and standards, the mean value of the building bulk density, the mean values of the natural frequencies and of the modal damping ratios for the first three modes (two sway modes and one torsional mode). Concerning the performance assessment, the user can choose the fraction of people perceiving the motion which is considered acceptable and the target floor. Another section of the input interface shows default values of the coefficients of variation (CoV) of the uncertain parameters considered in the analysis with a provision to change. It also offers the choice of carrying out the analyses with specific user-supplied HFBB data. In this case, the user needs to input their own PSD data. The default value for the number of samples utilized in the embedded Monte Carlo simulation for uncertainty analysis is currently set at 10,000. The results obtained from the analyses (**Figure 7**) are the probability of exceedance in the x and y directions, plots for performance assessment in the x and y directions for the user-defined acceptable% of people perceiving the motion ($X_p\%$), and global performance curves for various $X_p\%$, providing rapid estimate of the building's performance

on occupant comfort, which can be conveniently used in the preliminary design phase.

Modeling and Simulation

Modeling of Gust-Front Winds: NatHaz Gust-Front Factor (NGFF)

In comparison with atmospheric boundary layer winds, which are customarily treated as stationary, winds associated with gust-fronts originating from a thunderstorm/downburst exhibit rapid changes during a short time period which may also be accompanied by changes in wind direction. This introduces non-stationarity both in the mean and the SD of wind fluctuations. In order to realistically capture characteristics of gust-front winds and their attendant load effects, a new analysis framework, gust-front factor, was proposed (Kwon and Kareem, 2009). This is akin to the gust loading factor format used in codes and standards worldwide for the treatment of conventional boundary layer winds. The gust-front factor expresses a generalized description of the genesis of the overall wind load effects on structures under both gust-front and boundary layer winds and it reduces to the gust loading factor for the case of conventional boundary layer winds. This approach encapsulates both the kinematic and dynamic features of gust-front induced wind effects on structures which distinguish themselves from those experienced in conventional boundary layer flows, i.e., variation in the kinematics of the velocity profile and its effects on the associated aerodynamics; dynamic effects induced by the sudden rise in wind speed;



User selected **Side Ratio (D/B) = 1.00** in wind tunnel model for full-scale building dimensions of **B = 40 m**, **D = 40 m** and **H = 200 m** under **Exposure A** with **Aspect Ratio (AR = H/√BD) = 5.00**.

The best available dataset was found in the **NALD_DB** with **AR = 5.00**.

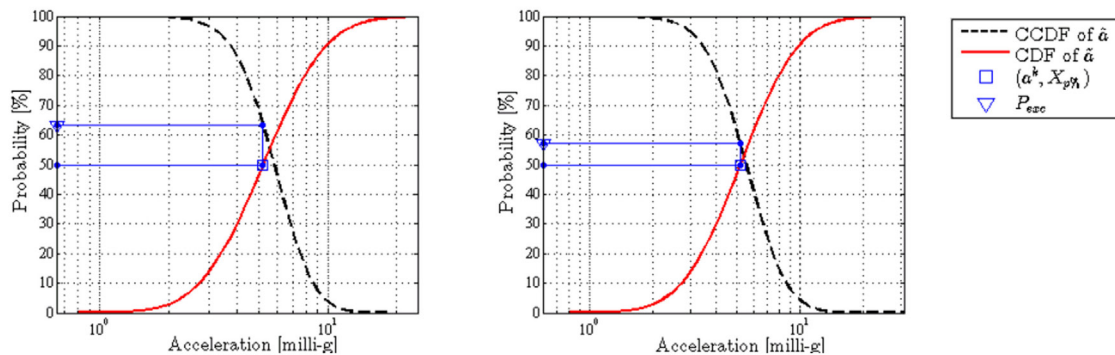
■ Input parameters by user [On-line Unit Converter](#)

B	40 m	D	40 m	H	200 m
ρ_B	180 kg/m³	ΔH	4 m	γ	18 m
β_x	2	β_y	2	β_θ	0.8
f_x	0.2 Hz	f_y	0.2 Hz	f_θ	0.3 Hz
ζ_x	1.5 %	ζ_y	1.5 %	ζ_θ	1.5 %
V	24.5 m/s (10-year)	T	3600 sec	NALD_DB with AR = 5.00	
Acceptable % of people perceiving ($X_{p\%}$) was set to 50% at 50th Floor					

⦿ Performance for the **x** direction: **$P_{exc,x} = 63\%$**

⦿ Performance for the **y** direction: **$P_{exc,y} = 57\%$**

■ Performance assessment in the **x** (left) and **y** (right) directions for the User-defined **$X_{p\%}$ (50% at 50th Floor)** [Note](#)



■ Global performance curves in the **x** (left) and **y** (right) directions for various **$X_{p\%}$**

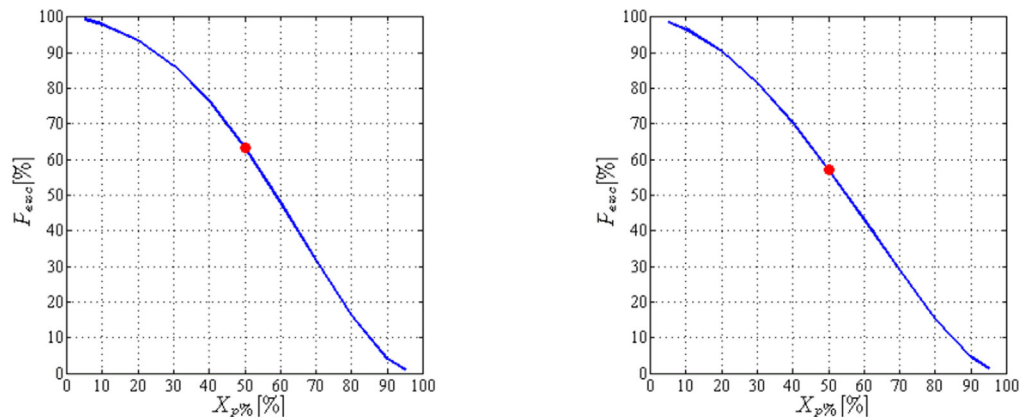
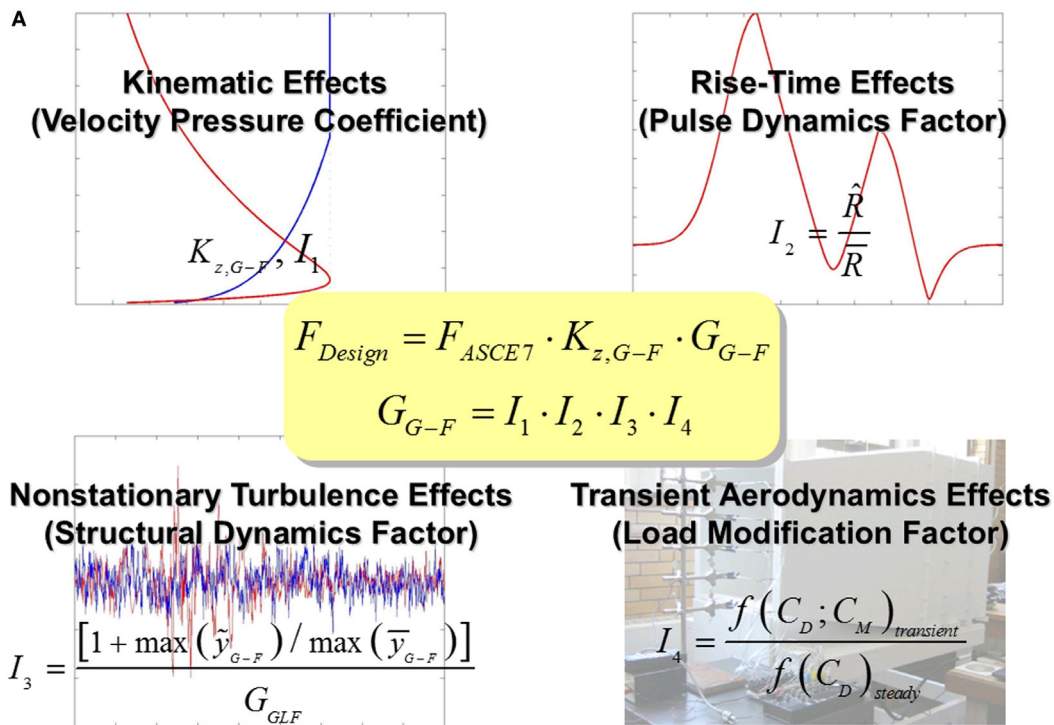


FIGURE 7 | Result interface of performance-based design of high-rise buildings for occupant comfort.



B

NatHaz GFF

User Interface of Gust-front factor approach

■ Please select the unit of input values (default : Metric) [On-line Unit Converter]
 If user would like to see English unit output, please select checkbox (default : Metric)

☒ Metric(SI) unit [kg, m, m/s]
 ☐ English unit [lb, ft, mph]
 ☐ Output : English unit

■ Building width B , depth D and height H

B [m, ft]
 D [m, ft]
 H [m, ft]

■ 1st frequency for alongwind f_x , Mode shape exponent β , Floor-to-floor height of building ΔH

f_x [Hz]
 β
 ΔH [m, ft]

■ Bulk Density ρ_B , Damping ratio of building ζ (e.g., enter 0.01 for 1% damping)

ρ_B [kg/m³, lb/ft³]
 ζ

■ Pulse duration t_d , 3-second basic wind speed in ASCE 7 V_{3-s} , storm-moving speed V_{s-m}

t_d [sec]
 V_{3-s} [m/s, mph]
 V_{s-m} [m/s, mph]

■ Exposure Category (A,B,C,D based on ASCE 7) & Select checkbox if building is located in Alaska

☐ A
 ☐ B
 ☒ C
 ☐ D
 ☐ Alaska

■ Category selection for Importance factor I (I, II, III, IV in Table 1-1 of ASCE 7) : Default is II ($I = 1.0$)

☐ I
 ☒ II (Default)
 ☐ III
 ☐ IV

■ Criteria for profile comparison in gust-front and boundary-layer winds; $V_{G-F}(z)$ (Vicroy 1991)
 Third option is user-defined inputs of V_{max} [m/s, mph] and z_{max} [m, ft], e.g., 67.67 or 67 67

☐ $V_{G-F}(10) = V_{B-L,3-s}(10)$
 ☒ $V_{max,G-F} = V_{B-L,3-s}(z_G)$
 ☐ V_{max}, z_{max}

○ Design/analysis options

☒ Gust-front factor approach in gust-front wind (Default)
 ☐ ASCE 7 design procedure in boundary-layer wind

FIGURE 8 | Continued

C


NatHaz
GFF

Results : Gust-Front Factor Approach

Input parameters by user

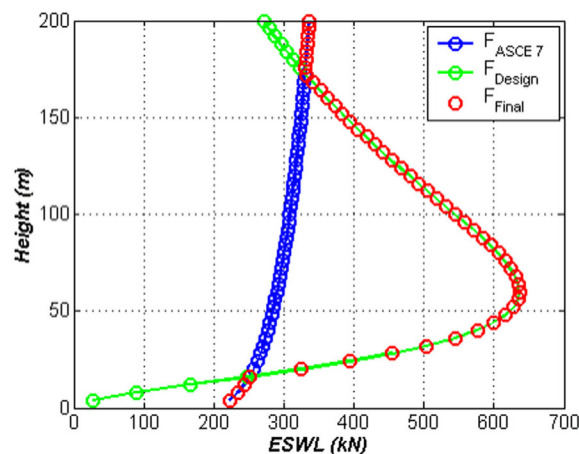
B	40 m	D	40 m	H	200 m
f_x	0.2 Hz	β	1	ΔH	4 m
ρ_B	180 kg/m ³	ρ_a	1.225 kg/m ³	ζ	0.01
t_d	200 sec	V_{3-s}	40 m/s	V_{s-m}	12 m/s
Exposure C		$V_{max,G-F} = V_{B-L,3-s}(z_G)$			
Input unit : Metric (SI)		Output unit : Metric (SI)		[On-line Unit Converter]	

Gust-front factor : $G_{G-F} = I_1 \cdot I_2 \cdot I_3 \cdot I_4$, total dynamic effects = $I_2 \cdot I_3 \cdot I_4$ ($I_4 = 1.0$)

I_1	I_2	I_3	I_4	$I_2 \cdot I_3 \cdot I_4$	G_{G-F}
1.348	1.000	0.853	1.000	0.853	1.150

* $G_{GLF} = 1.820$: Gust loading factor in the ASCE 7

Equivalent static wind loads (ESWL) : $F_{ASCE\ 7}$, F_{Design} and F_{Final}



(F_{Final} is taken as larger design load (ESWL) between $F_{ASCE\ 7}$ and F_{Design} at each interstory height.)

Download data file (design wind loads): [GFF_out_all_m100219.dat](#)

(Col. 1: Height [m]; Col. 2: $F_{ASCE\ 7}$ [kN]; Col. 3: F_{Design} [kN]; Col. 4: F_{Final} [kN])

FIGURE 8 | Gust-front factor framework: (A) Schematic diagram. (B) Web-based user interface. (C) Result interface.

non-stationarity of turbulence in gust-front winds; and transient aerodynamics (Figure 8A).

To facilitate expeditious utilization of this framework in design practice and inclusion in codes and standards, the analysis framework and its workflow were introduced within a web-based portal. This eliminates the need for an in-depth understanding of the background within the framework and the need for

associated computational effort. The portal has a user-friendly interface, permitting convenient analysis of several design scenarios with a host of potential loading conditions including the current ASCE 7 procedure in boundary layer winds for immediate comparison. Note that the user can utilize not only the two predefined profile criteria (see Kwon and Kareem, 2009) but also arbitrary V_{max} and z_{max} values to determine the gust-front factor

on-the-fly and corresponding design loads (ESWL). This offers a modeling capability of gust-front wind load effects on buildings. Based on the inputs, the following quantities are then shown in the output interface (Figures 8B,C): user inputs; gust-front factor and its subfactors (I_1 to I_4); a comparison between ASCE 7-based and gust-front-based ESWLs. More detailed information on the theoretical background can be found in the studies of Kwon and Kareem (2009, 2013b).

Wind Simulation: NatHaz On-Line Wind Simulator (NOWS) and VORTEX-Winds On-Line Wind Simulator (VOWS)

The NOWS introduced in 2005 was designed to provide users with on-line on-the-fly simulation of stationary Gaussian multivariate wind fields for the longitudinal direction. Simple and intuitive user-friendly interfaces (Figures 9A,B) easily allow user to input any terms and check simulation results such as simulated

A

NatHaz NOWS

NatHaz On-line Wind Simulator (NOWS) : Input Interface

User Inputs : Please select options and fill out input values. [On-line Unit Converter](#)

■ Please select the unit of input values (default : Metric)
If user would like to see English unit output, please select checkbox (default : Metric)

☒ Metric(SI) unit [m, m/s] ☐ English unit [ft, mph] ☐ Output : English unit

■ Vertical (z), Horizontal (x) or 2-dimensional (x,z) locations for wind speed simulation
(Acceptable formats : Delimited by comma(,) or MATLAB-compatible, e.g., 4,8,12 or 4:4:12)

☒ z [m, ft] :

☐ x [m, ft] :

☐ x [m, ft] :

☐ z [m, ft] :

■ Total number of frequency (N), cut-off frequency (f_c).
Note that $\Delta t = 1/(2f_c)$; $T = 2 \cdot N \cdot \Delta t$ [in Ergodic SRM, $T = 2 \cdot N \cdot \Delta t$ (total number of locations)]

N (max = 18000) : f_c [Hz] (max = 5) :

■ Exposure category (A,B,C,D based on ASCE 7-98) and 3-sec gust wind speed ($U_{3-s,10}$)

☐ A ☐ B ☒ C ☐ D $U_{3-s,10}$ [m/s, mph]

■ Wind simulation schemes

☒ Discrete frequency function with Cholesky decomposition and FFT (max 200 locations)

☐ Schur decomposition by AR model and polynomial approximation (max 100 locations)

☐ Ergodic spectral representation with Cholesky decomposition and FFT (max 50 locations)

☐ Conventional spectral representation method (max 200 locations)

FIGURE 9 | Continued

B


**NatHaz
NOWS**

NatHaz On-line Wind Simulator (NOWS) : Result interface

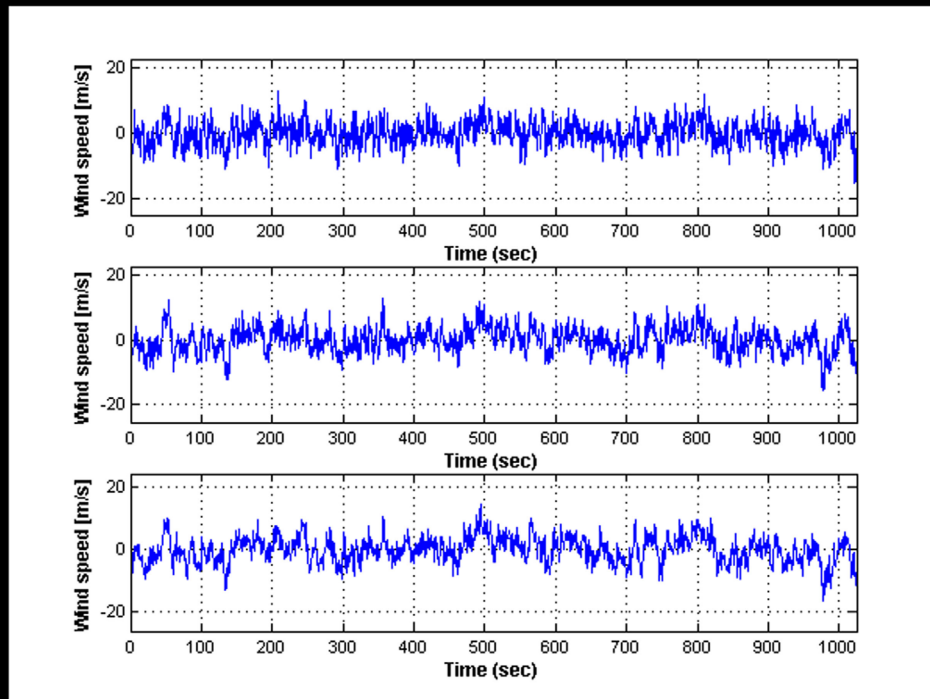
Message:

Discrete frequency function approach with Cholesky decomposition and FFT was used for wind simulation.

Input parameters by user

Number of Locations	Vertical 5 points	
Exposure category	Exposure C	
Total number of frequency	N	1024
Cut-off frequency [Hz]	f_c	1
3-sec gust wind speed [m/s]	$U_{3-s,10}$	40
Input unit	Metric(SI)	
Output unit	Metric(SI)	


Fluctuating wind speed at Location 1, 3 and 5



Download data file including all wind force components : w_out_all_m100087.mat
 (MATLAB variables: t_scale = time steps [sec]; mean_speed = mean wind speed(s) [m/s];
 Y_speed = fluctuating wind speed(s) [m/s])

FIGURE 9 | Continued

C



A VIRTUAL ORGANIZATION TO REDUCE THE
TOLL OF EXTREME WINDS ON SOCIETY

Wind Simulation User Interface

Researchers | Document

Please select options and fill out input values in SI units: [m] & [m/s] [On-line Unit Converter]

■ Available input options (place mouse cursor on parameter to see its description)

☒ u^* : z_0 :

☐ U_{ref} : z_0 :

☐ V_b : z_0 : Eurocode

☐ U : Sig : L :

z coordinates are necessary

z coordinates are necessary

z coordinates are necessary

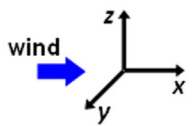
■ Total # of locations and their 3-D coordinates (x,y,z) of the locations for wind simulation
[acceptable coordinate : delimited by comma(,) or MATLAB-compatible, e.g., 4,8,12 or 4:4:12]

Total number of locations :

x :

y :

z :



■ Total number of points in time (Nt), Time step (Δt)
[Note that it is recommended to use Nt as power of 2 (2^x) in order to benefit simulation speed]

Nt (max.=360000) : Δt [sec] :

■ Wind turbulence component (u, v or w)

Wind turbulence component : ☒ u ☐ v ☐ w

FIGURE 9 | Continued

wind histories and comparison of target (analytical model) and simulated PSDs. This web framework features supporting both Metric (SI) and English units as input/output with on-line unit converter, location inputs for vertical, horizontal, or arbitrary 2-D coordinates, ASCE 7-based mean wind calculation in terms of terrain roughness to minimize user's input, offering users the ability to download simulation results as a file for further off-line analysis such as structural dynamic analysis under wind loads. In particular, one unique feature of this module is a flexibility to choose one of four popular wind simulation schemes such as Discrete frequency function with FFT (Wittig and Sinha, 1975), Schur decomposition approach with autoregressive (Di Paola, 1998; Di Paola and Gullo, 2001), Ergodic spectral representation method (Deodatis, 1996; Ding et al., 2006), and Conventional

spectral representation method (e.g., Shinozuka and Deodatis, 1991). A modified Kaimal spectrum was employed for the PSD of longitudinal wind velocity fluctuations (Kaimal et al., 1972), and Davenport coherence function (Davenport, 1967) was utilized to describe spatial correlation in the frequency domain.

Similarly, VOWS also offers wind simulations, but it features a wind simulation of three atmospheric turbulence components such as the longitudinal (u), lateral (v), or vertical (w) component, which the fluctuating component of the wind velocity is modeled as a Gaussian stationary random process with zero-mean. The three components of turbulence are considered as statistically independent and are simulated independently of each other. The wind profile in this module was described by a logarithmic law, and this module employs one of the four different input options:

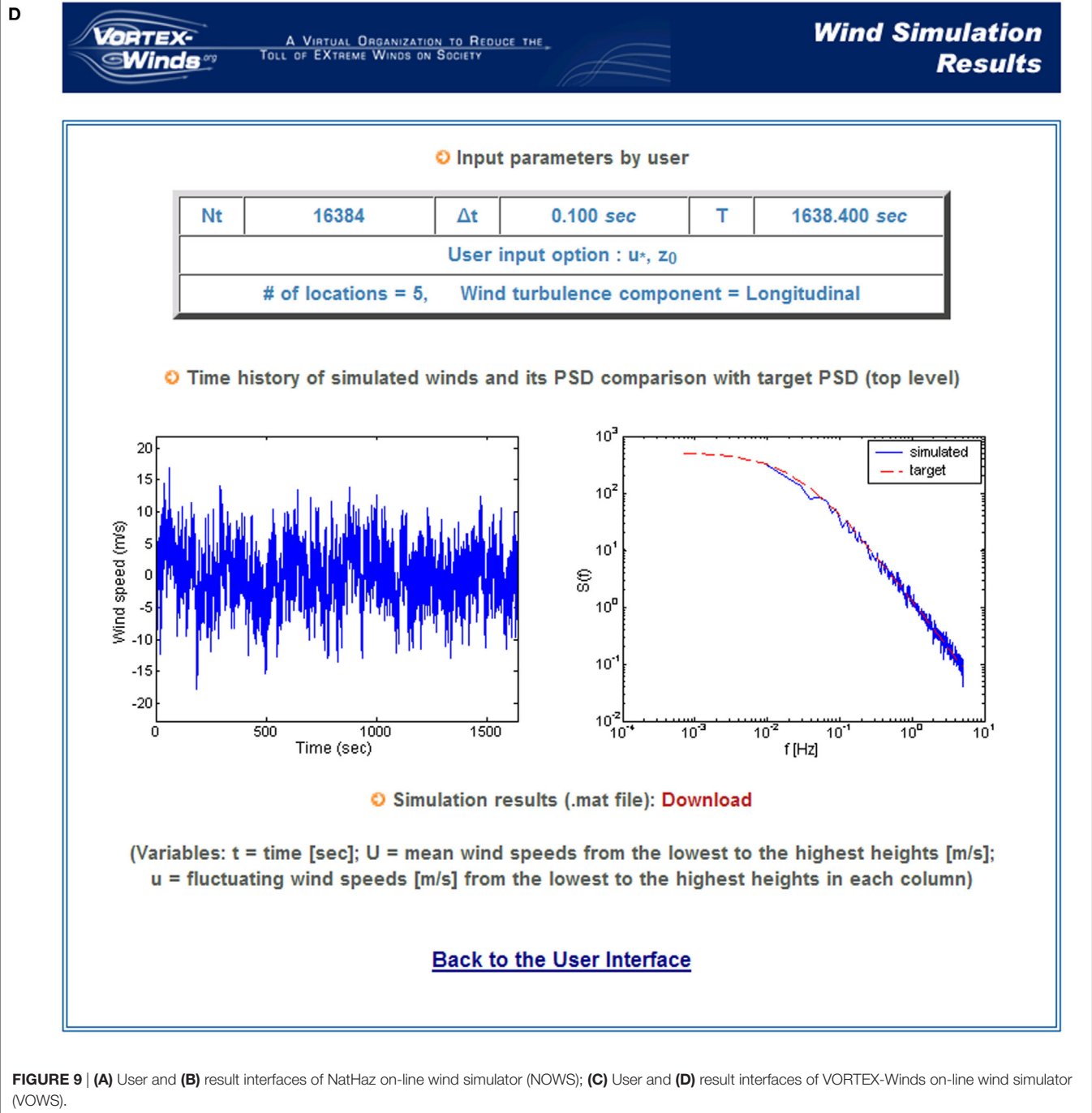


FIGURE 9 | (A) User and **(B)** result interfaces of NatHaz on-line wind simulator (NOWS); **(C)** User and **(D)** result interfaces of VORTEX-Winds on-line wind simulator (VOWS).

friction velocity and roughness length, reference velocity at 10 m and roughness length, Eurocode (CEN, 2010)-based inputs, and mean wind velocity and SD/integral length scale of wind components. In addition, users can select one of three wind turbulence components (u , v , or w) to be simulated (Solari and Piccardo, 2001; Carassale and Solari, 2006). The PSD function of the turbulence component (u , v , w) proposed by Solari and Piccardo (2001) and coherence function of the turbulence component by Vickery (1970) were employed in this module. The simulation of the

turbulence field is carried out by the spectral representation algorithm described in Carassale and Solari (2006). Similar to NOWS, VOWS also offers the ability to download simulation results as a file in the result interface, in addition to a comparison between target and simulated PSD for verification (**Figures 9C,D**).

Damping Database

Despite the advances that have been made in structural engineering in the last century, one critical parameter, damping continues

to remain a source of complexity which is due in part to the diversity of sources contributing to the overall energy dissipation. The viscous damping levels on the order of 1% critical damping for steel structures and 2% for concrete are commonly assumed as some codes recommend these values. However, measurements of light and flexible structures suggest that assumed levels of damping were often not realized in the constructed building (Kijewski-Correa et al., 2006; Spence and Kareem, 2014). For this class of tall buildings, the diminishing level of damping may cause issues related to habitability as damping plays a pivotal role in the building

response estimates. This is a concern often experienced by design professionals. Since the inherent damping in these structures cannot be engineered, reliance is placed on augmenting damping through auxiliary damping devices. Introduction of these devices leads to measurable and controllable levels of damping in buildings (Kareem et al., 1999). The Damping database is an initiative to provide users with on-line damping information for various full-scale building structures in terms of a query-based database module. The query parameters include not only building information such as cross-sectional shapes, widths, depths, and heights

VORTEX-Winds **Damping Database** **NHAZ** **GCOE Program TPU**

Country: Japan

X-Section: B-D Value
 B (Short dimension): from: 0.0 m to: No Limit m
 D (Short dimension): from: 0.0 m to: No Limit m

X-Section: Shape Type
 Rectangular ☒ Square ☐ Circular ☐ Diamond ☐ Hexagonal ☐ Fan-Shaped ☐
 Multilateral ☐ Elliptical ☐ Convex ☐ Triangular ☐ Double-Barreled ☐ Irregularity ☐
 Semi. Ring ☐ Arc ☐ Y-Shape ☐ Z-Shape ☐ V-Shape ☐ S-Shape ☐
 L-Shape ☐ T-Shape ☐ <-Shape ☐ Select All ☐ **HELP**

Foundation Type
 Spread ☒ Pile ☒ Select All ☒

Height
 from: 0.0 m to: No Limit m

Natural Frequency (1st mode)
 f_y : from: 0.00 to: No Limit
 f_x : from: 0.00 to: No Limit
 Torsion: from: 0.00 to: No Limit

Structural Type
 SF ☒ RC ☐ SRC ☐ Select All ☐ **HELP**

Usage
 Office ☒ Hotel ☒ House ☒ Hospital ☒ School ☒ Store ☒ Lab ☒ Select All ☒ **HELP**

Test Excitation
 FrM ☒ FoM ☒ FrV ☒ FoV ☒ MP ☒ PR ☒ SW ☒ Mic ☒ Wind ☒ EQ ☒ Fr ☒ Select All ☒ **HELP**

Damping Estimation Method
 LDF ☒ RDT ☒ HPB ☒ SHP ☒ SID ☒ CFT ☒ CFP ☒ ACD ☒ PGM ☒ Select All ☒ **HELP**

Damping (1st mode)
 y: from: 0.00 % to: No Limit %
 x: from: 0.00 % to: No Limit %
 Torsion: from: 0.00 % to: No Limit %

Query Database **Reset to Default**

Copyright © 2010 NatHaz Lab & VORTEX-Winds Group

FIGURE 10 | Continued

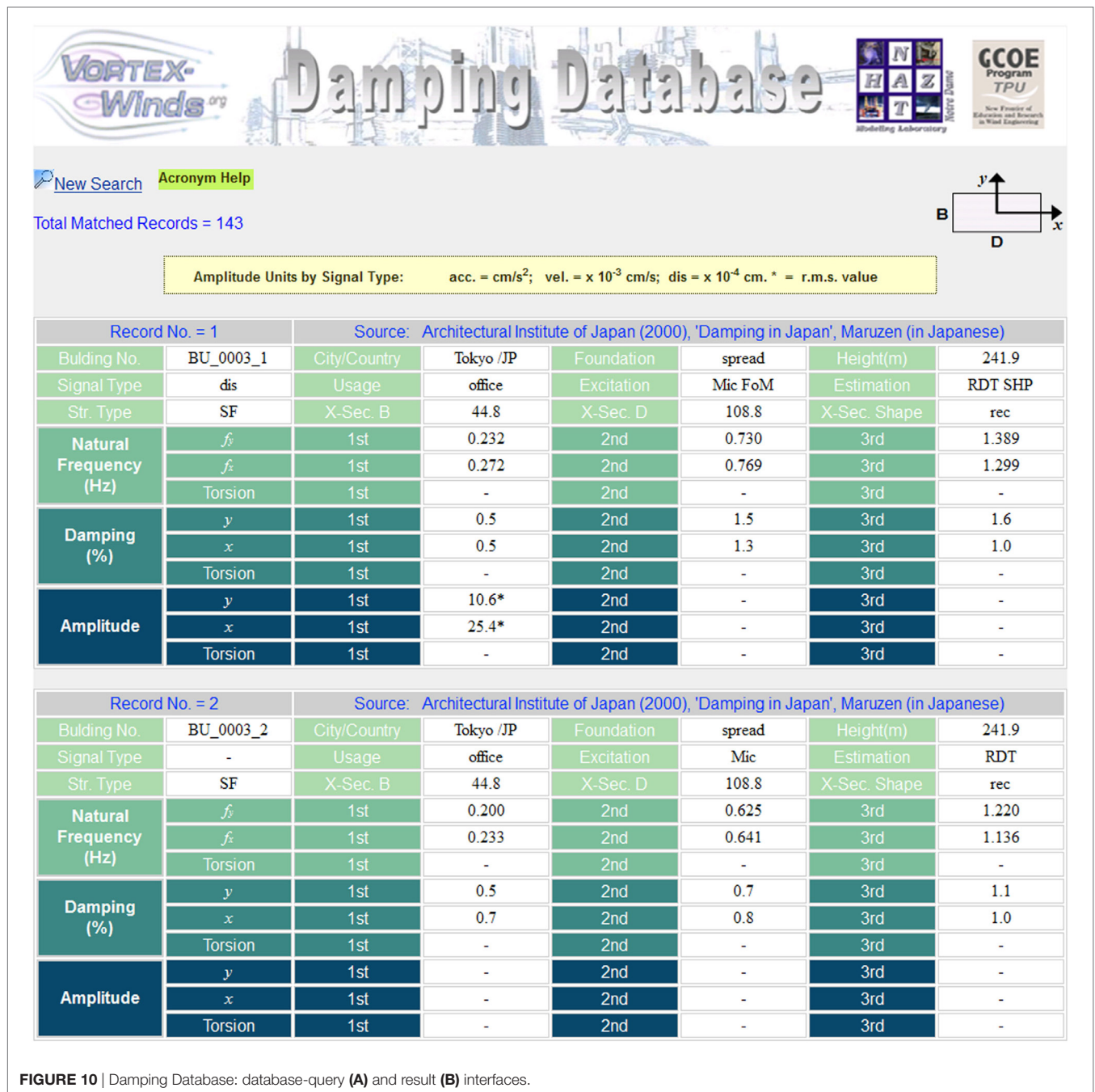


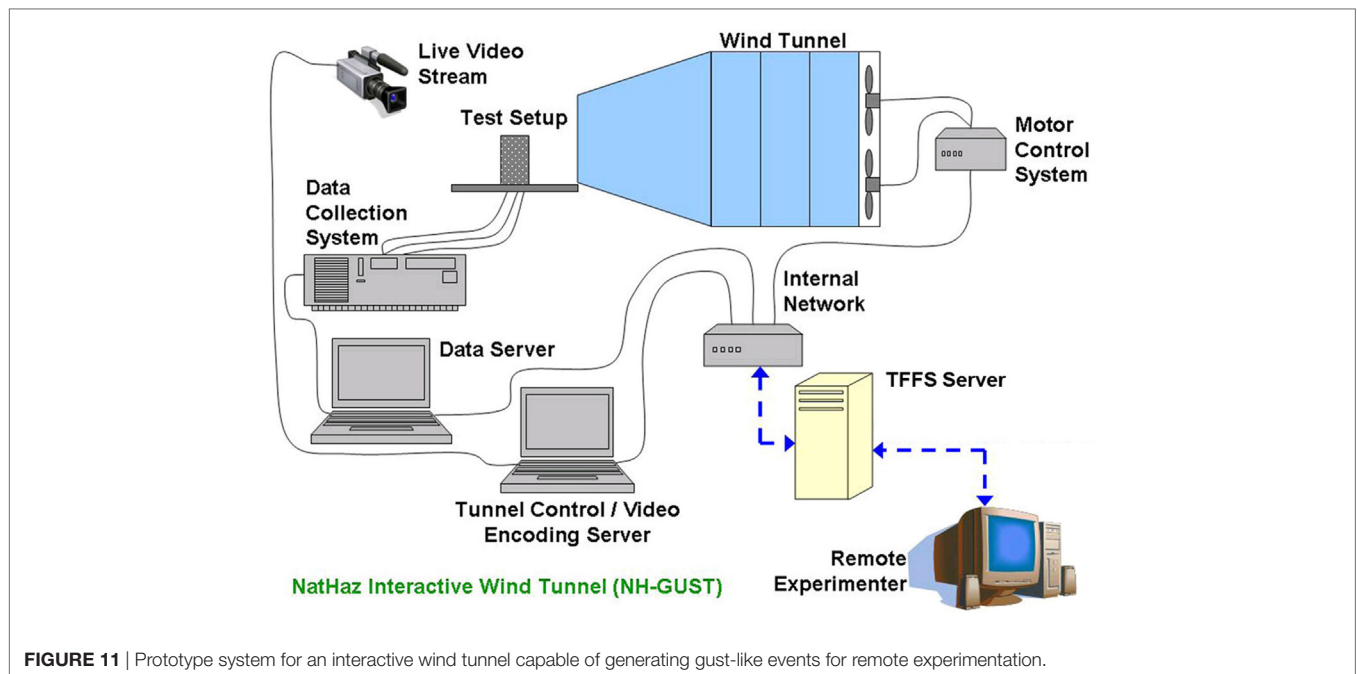
FIGURE 10 | Damping Database: database-query (A) and result (B) interfaces.

but also test excitations, damping estimation methods, ranges of damping ratios, etc. (Figure 10). This database is currently established with the Japanese damping data sets [Architectural Institute of Japan (AIJ), 2000; Satake et al., 2003], but it is anticipated that the contents will be expanded with other damping datasets in the future (e.g., Kijewski-Correa et al., 2006, 2013).

Tele-Experimentation: NatHaz Interactive Wind Tunnel (NH-GUST)

Given the interconnectedness of research and the lack of available experimental hardware at every research location, developing a

system that can bring the greatest amount of technology to as many people as possible is certainly warranted. To that end, a prototype system for an interactive wind tunnel, NH-GUST, has been developed as a proof-of-the-concept (Butler, 2010). This system, conceptualized in Figure 11, consists of various components arranged within a local network. The end user operates the wind tunnel remotely through a dedicated web interface that connects to the networked components, though test models need to be physically set up by on-site personnel before allowing remote users to perform the experiments. An interactive web user interface was introduced to be controlled using embedded



LabVIEW software (National Instruments, 2015) to provide a cross-platform simulation framework. The software is designed to set the limits to protect wind tunnel system from unexpected or undesirable operations. In addition, it is preferable to have an on-site personnel to communicate with remote users and check out overall experiments. Similar to that of the NEES (Van Den Eende et al., 2007), this framework for severe wind experiments may offer a method for improving both the range and quantity of experimental data and for enhancing the wind engineering field as a whole. Instead of only a few schools sharing a limited number of wind tunnel facilities, a customizable (although limited) wind tunnel framework may be developed for anyone to input a wind field scenario to see how it will impact a physical model, either through SPM or through a HFBB technique. Modification of existing wind tunnels and the development of research portals can have the effect of quickly building the body of knowledge for the effect of severe storm events, matching the body of knowledge that has been produced over several decades regarding the effects of boundary layer flows on structures. The current NHERI wind tunnel facilities have similar features, which would permit sharing of advanced wind tunnel facilities with programs that do not have experimental capabilities.

Cloud-Computational Fluid Dynamics (CFD): A Virtual Wind Tunnel (VWT)

The complexity of multiscale turbulence–structure interactions has thus far precluded a functional relationship between wind speed and its load effects on structures immersed in atmospheric boundary layer. Recent advances in numerical schemes and escalating growth in computational resources have aided efforts in developing computational simulation of flow around structures using CFD. In order to capture multiple-scale interactions and to resolve small-scale fluctuations, one faces major challenges that

include both computation speed as well as memory to manipulate millions of pieces of information at grid points or control volume nodes. These challenges have limited the success of CFD in simulating real world scenarios. Commercial software has provided access to CFD and is increasingly used in the industry which often lacks verification and validation of the codes. Users without the necessary background in fluid mechanics and numerical techniques embark on using these codes resulting in a product that may have inaccuracies and uncertainties. Users of these codes have been alerted in several earlier publications regarding the possible pitfalls (e.g., Castro and Graham, 1999). In this context, CFD is quite different from the use of numerical methods in structural mechanics. Proper training in fluid mechanics, numerical methods, and access to user friendly portals with embedded CFD codes would help to enhance the user community, which will lead to additional advances [National Science Foundation (NSF), 2014; NHERI SimCenter²].

Despite major challenges even for the experts, some groups around the world have made significant progress, especially in Japan where Architectural Institute of Japan [Architectural Institute of Japan (AIJ), 2004] now permits use of CFD in determining wind effects on structure with a caveat that it will be carried out under the direction of an expert and subjected to verification by a committee designated by the Building Law of Japan.

These challenges impose a steep learning curve and have kept this venue of quantifying wind loads on structures closed for the majority of wind engineering researchers and practitioners. To address these challenges, “Virtual Wind Tunnel (VWT)” has been developed to help people not fully versed in the nuances of CFD be able to simulate wind–structure interactions and benefit

²<https://www.designsafe-ci.org/facilities/simcenter/>.

from the emerging power of simulation driven technologies. This effort combined with useful tutorials was intended to allay the very concerns raised in for example Castro and Graham (1999). Despite initial serious criticism by some with background in computational wind engineering, we are pleased to report that we have measureable success in the initial development and have noticed a step forward in potentially removing the commonly perceived fear out of CFD that has haunted many earlier users

(Sempolinski et al., 2015). It has been demonstrated that the concept, though initially opposed by some experts, is feasible as a group of student engineers, low-skill volunteers from Amazon Mechanical Turks, graduate students, and postdoctoral graduates were able to simulate flow around a cross-section of the Empire State Building with very reliable results as the users went through helpful tutorials, explored various grid options, turbulence models, and undertook convergence studies (Staffelbach et al., 2015).



FIGURE 12 | Continued

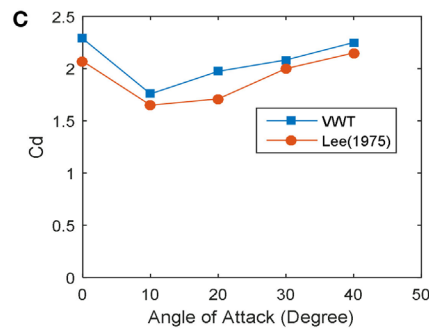


FIGURE 12 | (A) Virtual Wind Tunnel login screen. (B) An example of a completed task. (C) Drag coefficient of a square cylinder at various angles of attack.

VWT is a user-friendly web-enabled CFD collaborative platform that does not require expertise of CFD simulation and extensive computer resources. In place of this, it offers ample tutorial help and FAQs for CFD simulation. It employs Gmsh³ as the unstructured mesh generator and OpenFOAM (2015) as the CFD simulator and allows users to import various designs and run two dimensional wind simulations. The simulations are automatically sent to powerful cloud and/or grid-based computing backend. **Figure 12A** shows the login screen of the VWT portal.

To help create a new geometry easier, users can use SketchUp.⁴ In SketchUp, users can either draw the design by themselves or download from its 3D warehouse where there are millions of models such as autos, aircrafts, buildings, including famous tall buildings like Burj Khalifa, World Trade Center, etc. Users can also create geometry from templates on the platform. With such templates, users can create new designs by specifying geometric dimensions such as height, width, etc., and control points, and the points can be segment end points or spine control points. The feature of Template makes creating the geometry easier when users want to change the location of some control points, and it can be particularly useful for exploring shape optimization.

Once the geometry is created, mesh control should be set. Mesh generation is the most complex part of CFD simulations and it requires necessary experience, thus it becomes a key problem for non-experienced CFD users. VWT makes the mesh generation task easier. It only requires simple mesh control parameters input such as the distances to four sides of the fluid domain, boundary conditions, and grid sizes. Subdomains can be created to refine the mesh in specified regions. By following the solution control setting, inflow velocity, simulation time step and duration, kinematic viscosity, turbulence model, etc. can be managed. Default values are automatically imported in on the setting page, which makes it easier for new comers in CFD use to start a simulation, it is especially helpful for the most difficult but important part of mesh generation. The system gives suggestions to modify the settings when errors occur during the simulation. In terms of turbulence models, there are laminar flow model, S-A

one equation model, k-epsilon model, Smagorinsky turbulence model (large eddy simulation, LES), and Dynamic One Equation model (LES) to choose from at this stage.

New cases can be duplicated from existing ones, which makes it convenient to set similar cases, this feature is very useful for parameter comparison which is widely used in CFD. The user receives an email once the simulation is completed, and results of plots and data of pressures, velocities, force coefficients, and mean Reynolds stress are outputted automatically for further viewing and analysis. Users can also download the simulation which are OpenFOAM case files, as well as force coefficient data for further postprocessing. Users are also able to access the VWT portal through a console-based interface, which is useful when using tools like MATLAB (Mathworks, 2015). This makes it more convenient to run a large amount of simulations that share similar parameters, as well as to analyze the output data.

Virtual Wind Tunnel implements some of the ideas of collaborative software design in computational wind engineering, letting users edit structural geometries, compile geometries into usable models for simulation, perform wind simulations, evaluate results, and then share and discuss their work with other users. This feature is an attractive feature that promotes a culture of collaboration toward complex problems and empowers those who are beginning in the field. This has the promise of building a virtual community of users, especially in the era of ubiquitous internet, to reach a new level of potential.

These features make VWT helpful for different users, varying from CFD experts to initially untrained potential users with the aid of sufficiently comprehensive tutorials. Professional CFD users can employ VWT to get a quick and easy prediction and validation. Structural engineers without CFD background can run wind simulations to get a better understanding of aerodynamics of a building or a bridge cross-section by utilizing a tutorial detailing how to reject flawed simulations, along with some suggested parameter settings on VWT. Untrained workers can also run simulations by taking advantage of a bank of preliminary analyses of complex data they can import from the platform. Investigations to examine the feasibility of using crowdsourcing for various complexities of technical tasks using VWT have been carried out, and it shows that crowd workers with no background in engineering could follow tutorials and come up with acceptable

³<http://gmsh.info>.

⁴<http://www.sketchup.com>.

TABLE 2 | Drag coefficient of various shapes.

Test model	VWT		Wind tunnel data	
	Cells	CFD scheme	C_d	C_d
Circular cylinder ($Re = 10^5$)	27,468	S-A one equation model	1.30	1.2 ($Re = 10^5$) (Wieselsberger, 1921)
Square cylinder ($Re = 10^5$)	83,582	LES	2.29	2.19 ($Re = \text{unknown}$) (Bearman and Trueman, 1972)
Rectangular cylinder ($B/D = 2$, $Re = 10^5$)	94,732	LES	1.63	1.60 ($Re = 1.05 \times 10^5$) (Mizota et al., 1988)
Flat plate perpendicular to flow ($Re = 1.33 \times 10^6$)	174,212	S-A one equation model	2.03	2.13 ($Re = \text{unknown}$) (Fage and Johansen, 1927)

CFD, Computational Fluid Dynamics; LES, large eddy simulation; VWT, Virtual Wind Tunnel.

solutions (Staffelbach et al., 2015). To complete a task on VWT, a user should create the design, generate the mesh, and run the simulation. The long-running simulations are automatically sent to powerful backend computing platforms. **Figure 12B** shows a completed task sequence.

An example case to demonstrate verification and validation involving flow around various shaped prism cylinders is presented. **Figure 12C** shows a comparison of the drag coefficient (C_d) of a 2D square cylinder at various angles of attack (α). For the simulation, LES scheme was employed with the Reynolds number (Re) of 10^5 , while the experiment results were performed with $Re = 1.76 \times 10^5$. Mesh convergence study was first carried out at $\alpha = 0^\circ$ with the number of cells that was chosen to be 83,582, 144,400, and 189,694, respectively, with corresponding C_d values of 2.26, 2.09, and 2.10, respectively. The difference in the C_d with respect to the number of cells was within acceptable range of $\pm 10\%$ compared to the experimental result, thus the lowest number of cells, 83,582, was chosen for this example because the larger number of cells is used, the more computational resources are demanded.

Table 2 shows the drag coefficient of various shapes performed in this study. Results obtained through the VWT simulations after mesh convergence tests were compared to the available wind tunnel data. A good agreement was observed as shown both in **Figure 12C** and **Table 2**. More examples can be found in Staffelbach et al. (2015).

The VWT has been expanded to include 3-D simulations and being transported through NHERI SimCenter to the NHERI DesignSafe CI for convenient distribution and computational resources needed for advanced simulations. After extensive verification and validation exercises it will be released to the NHERI community of users.

Damage Assessment from Aerial/Satellite Imagery

This module is focused on automating damage assessment schemes based on before-and-after storm satellite/aerial imagery to provide an accurate individual building assessment of damage (Thomas et al., 2011). The framework for damage estimation consists of three steps. First, objects of interests such as buildings are

detected automatically from prestorm images. Next, correction of photometric and geometric differences between before and after image-pairs is done (**Figure 13A**). Third, change detection is performed, and the damage is classified based on quantitative measures of change (**Figure 13B**).

Note that Speeded Up Robust Feature, which is robust and fast, was employed (Bay et al., 2006) to extract features from the two images of before and after events. An approximate k-Nearest Neighbor algorithm (Muja and Lowe, 2009) is used for feature matching. A speed-up of 10 \times was achieved without compromising robustness through randomized Kd-trees and a constrained RANSAC algorithm (Thomas et al., 2012b).

Automatic color balancing approaches for different applications have been studied by different research communities in the past decade. For multitemporal images to identify damage, an ideal color correction approach should be effective at transferring the color palette of the source image to the target image for the unchanged areas while being able to transfer the global color characteristics for the changed area without creating visual artifacts. Toward this goal, a new local color balancing approach that uses adaptive windowing was proposed, which was evaluated against other state-of-the-art approaches using a database consisting of aerial image pairs (Thomas et al., 2012a). The test image pairs were taken at different times, under different lighting conditions, and with different scene geometries and camera positions (**Figure 13A**).

A segmentation-based scheme that uses a maximum likelihood classifier along with k-means clustering was adopted for building detection. Measure of Estimated and Predicted Shadows features along with shape-based features to combine segments together were utilized. In addition, a fusion of color- and edge-based features to classify rooftops into damage states was proposed. The evaluation was performed on a database of posthurricane rooftop images that is larger than the ones used in previous studies. The classifier was found to perform with 80% accuracy for a 3-scale damage metric and 72% accuracy for a finer grained 4-scale damage metric (Thomas et al., 2011). To further validate results of building segmentation and damage classification, preparation of ground truth data sets is in progress.

The first row in **Figure 13C** shows a collapsed building and the corresponding false color images for edge density, V histogram (edge-based features) and H means (color-based feature). Note that the edge density values are significantly higher in this case. The second row corresponds to a partially damaged building with a cavity in the rooftop. V histogram indicates a significant change in the cavity area and H means shows a minor damage on the roof (Thomas et al., 2011). This automated damage assessment scheme based on satellite imagery is being transported to a web-based portal for inclusion in VORTEX-Winds.

Monitoring System: Data Management Based on Cyber-Based Framework

Possibly the greatest challenge in long-term monitoring projects is the transfer, processing, dissemination, and management of collected data, in particular for geographically dispersed collaborators. The fusion of engineering and information technologies provides today's engineer with the potential for analysis and

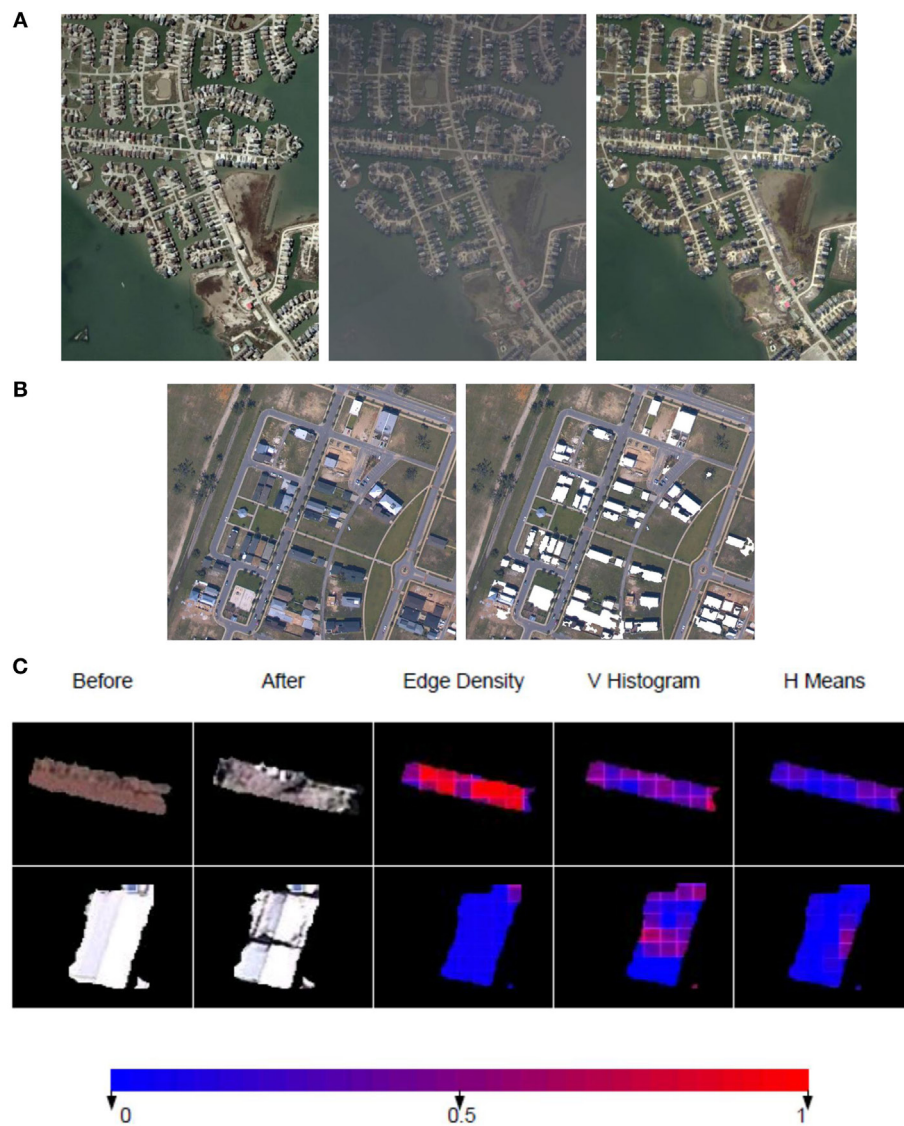


FIGURE 13 | (A) Source images (left), Target images (middle) that have been corrected geometrically. New target image transformed using the proposed local color transfer technique (right). **(B)** Example of a satellite image (left) and extracted buildings in white (right). **(C)** Damage assessment: extracted features for a collapsed building (top) and a partially damaged building (bottom).

research programs that defy geographic boundaries and create new venues for remote sensing and data analysis and archiving. The following two monitoring programs demonstrate the use of cyber-based technologies to enhance the accessibility, organization, interpretation, and dissemination of long-term data sets. The first example is an ongoing full-scale monitoring program involving several tall buildings in the city of Chicago, which was established in 2001 (Kijewski-Correa et al., 2006). As the management of years of full-scale data from this project poses a daunting task, information/Internet technologies provide an attractive solution, through local communication hubs and secured web interfaces to catalog, convert, download, and display the measured time histories. In the Chicago program, the dataloggers that store data at its backup storage module are remotely interrogated

by Internet. This information is then uploaded to an Apache web server, called Windycity,⁵ for access by the geographically dispersed project team. A variety of IT tools such as HTML/Java Script, PHP (2015), etc. were utilized to create interactive displays allowing users to select any record available for a given building. An alternative mode of data access was provided *via* structured query language, enabling a database query using a database management system, e.g., MySQL (2015), to identify records with a desired level of wind velocity or response resulting in an automatically updated listing of the available files satisfying these criteria (Figure 14A). Upon selecting a record, a data set is postprocessed

⁵<http://windycity.ce.nd.edu>.

A

Chicago Full-Scale Monitoring Project

Home | Project | Instrumentation | Collaborators | Data | Contact

Data

Data Selection

- Accelerometer
 - by Filename
 - by Database
- GPS

Accelerometer Database

Database Search Inputs

Building Name

☒ Building1 ☒ Building2 ☒ Building3

Year

☒ 2002 ☒ 2003 ☐ 2004

Search Values

20 ≤ Wind Speed [m/s] ≤ 25

10 ≤ Wind Direction [deg] ≤ 45

0.50 ≤ Peak [mG] ≤ 5.50

0.15 ≤ RMS [mG] ≤ 2.5

Search

* Conversion between Calendar day and Julian day

Month (1~12) Date (1~31) Year (e.g. 2002) submit Julian day

2 22 2003 submit 53

Year (e.g. 2002) Julian day (1~366) submit Calendar day

2003 53 submit Feb. 22, 2003

Search Results

Building 1	Building 2	Building 3
hm20030532026.rec	pm20030532134.rec	
hm20030532226.rec		
hm20030532326.rec		
hm20030540112.rec		

Analysis

Copyright (c) 2002 NatHaz Laboratory. All rights reserved.

B

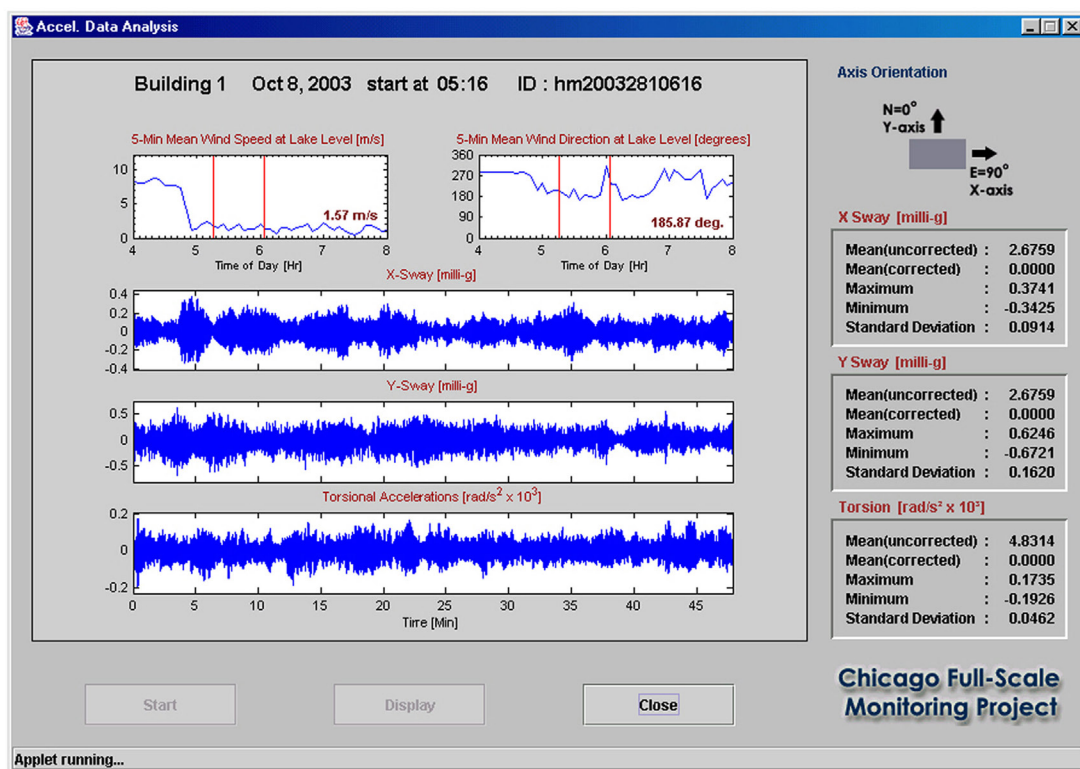
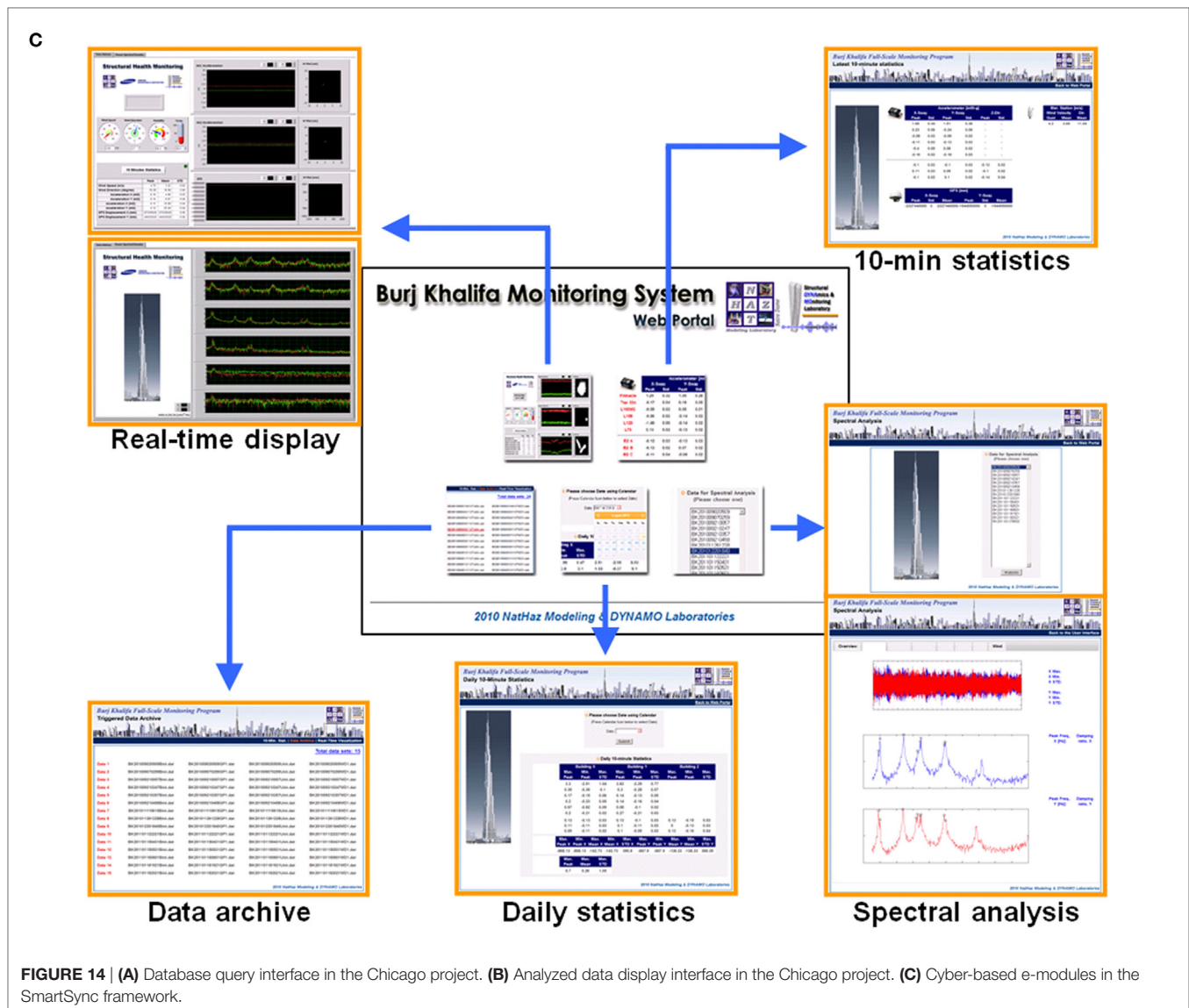


FIGURE 14 | Continued



on-the-fly *via* preprogrammed MATLAB codes on the server side with JAVA (2015) technology providing the interfacing capabilities. Through this process, any spikes and drifts are removed to preserve data quality, voltages are converted to engineering units and responses at the corners of the building are decoupled to extract the sway and torsional accelerations in a computationally efficient manner (**Figure 14B**). Detailed information is given in the studies of Kijewski et al. (2003) and Kijewski-Correa et al. (2006).

SmartSync System: Internet of Things (IoT)

Conventional monitoring program such as the Chicago Monitoring Program is often limited to being a manual or semi-automated system requiring several manual interventions by project teams due to the incapability of hardware/software configuration to autonomously comply with the central command. To overcome this limitation, a unique prototype system for full-scale measurement and long-term structural

health monitoring (SHM), SmartSync, which utilizes the building's existing Internet backbone as a system of "virtual" instrumentation cables to permit modular and largely "plug-and-play" deployments including advanced and automated software packages to establish a fully automated system has been introduced. Within this framework, data streams from distributed sensors are pushed through network interfaces in real-time and seamlessly synchronized and aggregated by a centralized server, which performs basic data acquisition, event triggering and database management, while also providing an interface for data visualization and analysis that can be securely accessed. The system enables a scalable approach to monitoring tall and complex structures that can readily interface variety of heterogeneous sensors and data formats (analog and digital) and can even accommodate variable sampling rates. With the help of rapid development in hardware systems that nowadays offers Ethernet-enabled hardware, e.g., dataloggers, all process can be automated without the need of human intervention. To

insure reliability of the system, TCP/IP (Transmission Control Protocol/Internet Protocol) was invoked as a stable stream delivery service that guarantees transmission of data sent from one host to another without duplication or loss, ideally suited

for data from variable sensors coordinated over local area network (LAN). Though, the realization of a network-based architecture significantly depends on the software development operating on the system's centralized server housed within the

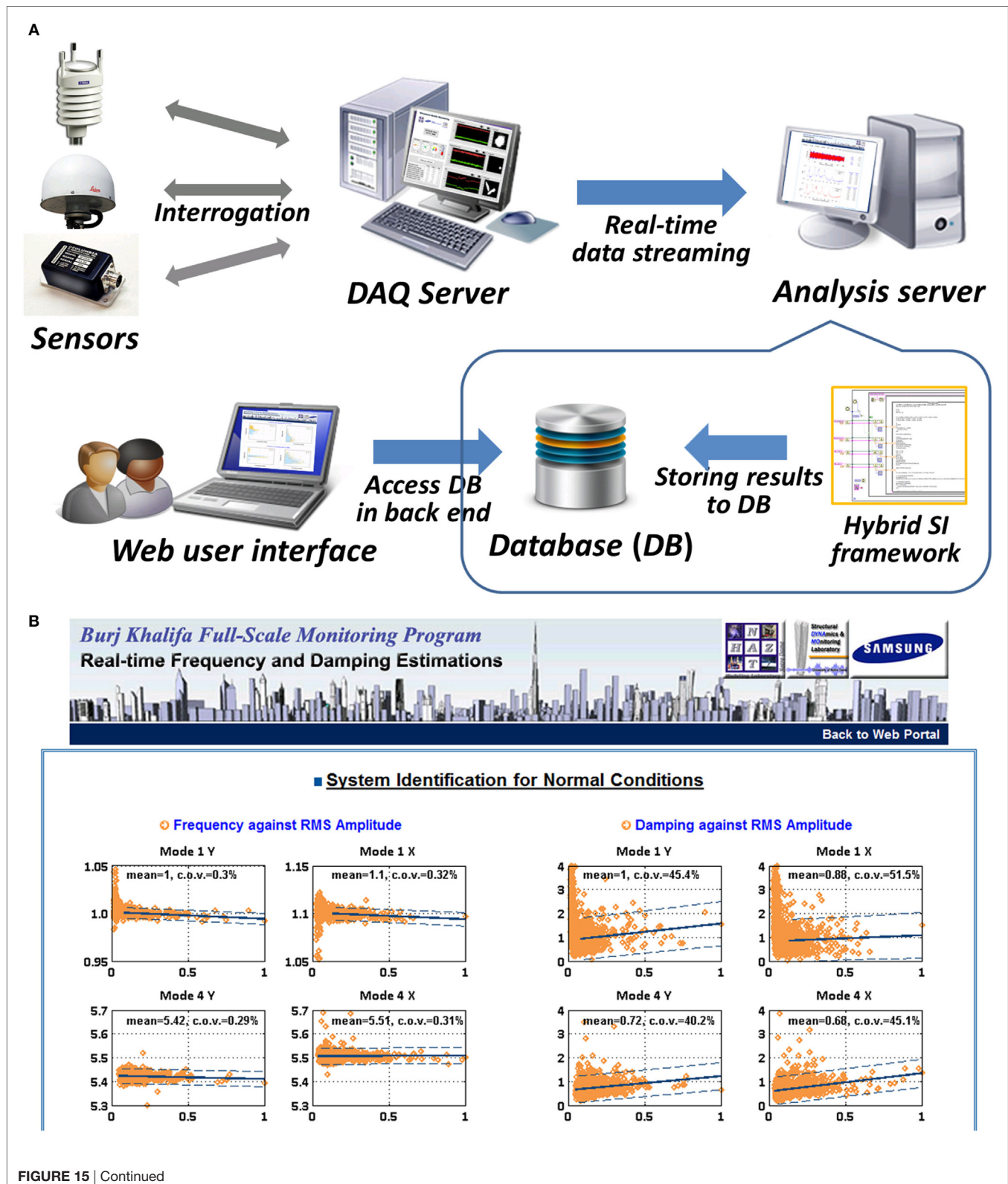


FIGURE 15 | Continued

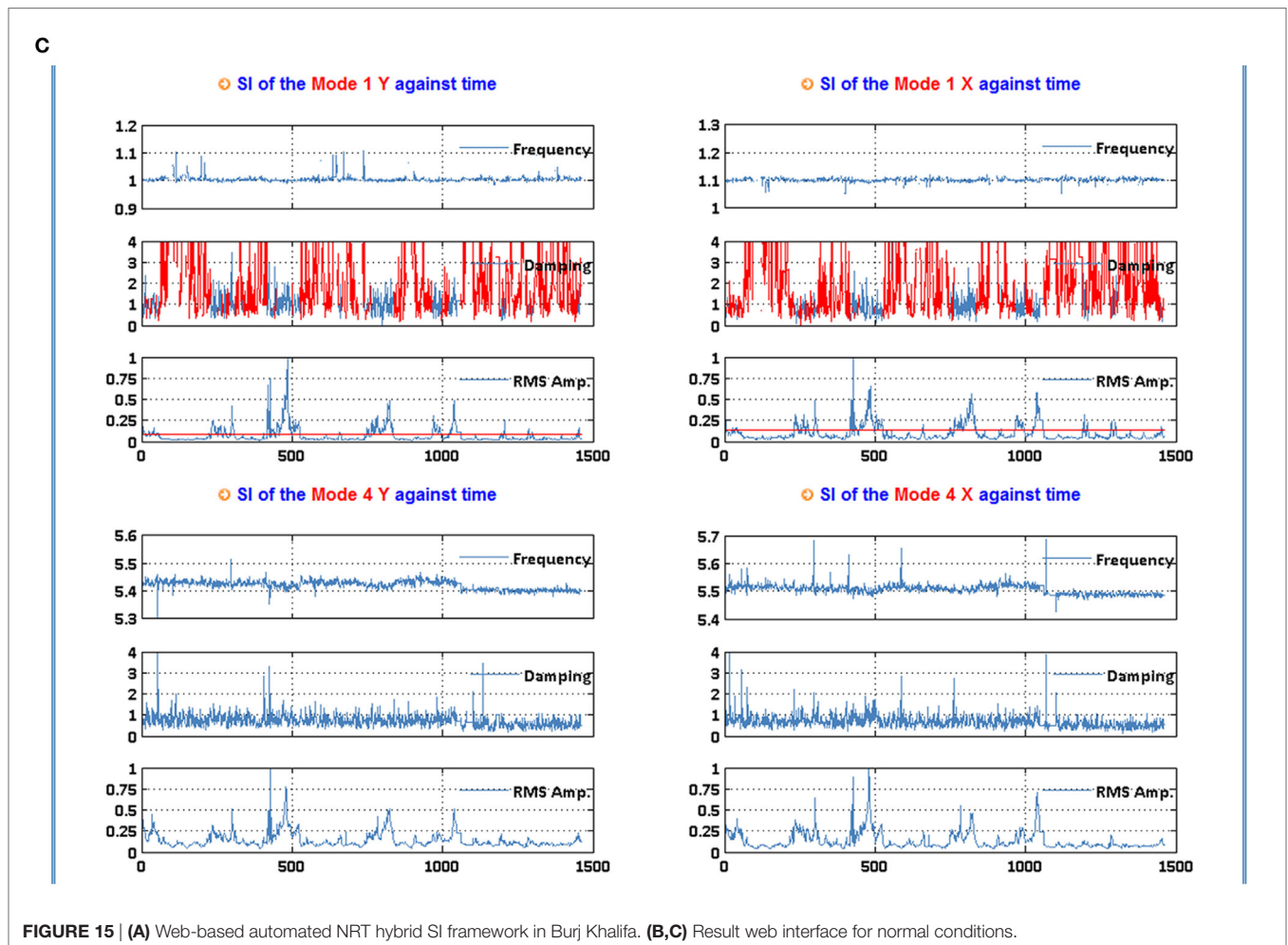


FIGURE 15 | (A) Web-based automated NRT hybrid SI framework in Burj Khalifa. **(B,C)** Result web interface for normal conditions.

building being monitored. To facilitate this, all data acquisition operations in SmartSync, including synchronization, are programmed in LabVIEW at the central server, while higher level processing and analyses are facilitated by cyber-based on-line modules on an additional analysis server with results pushed to web user interfaces that are streamlined in terms of cyber-based schemes described earlier. Note that the SmartSync framework has deployed to the world's tallest building, Burj Khalifa, for a proof-of-concept in triggering under dual excitations (wind and earthquake) and has successfully been performing since 2008. For reference, cyber-based modules developed in this project are shown in **Figure 14C** including real-time display in both time and frequency domains, the latest 10-min statistics, archived daily statistics, triggered data depository, on-demand spectral analysis (Kwon et al., 2010, 2011; Kijewski-Correa et al., 2013). Note that these modules are not currently associated with VORTEX-Winds and operated independently due to agreements of confidentiality with building owners for monitoring datasets.

Near Real-time Monitoring

The concept of cyber-based SHM has also applied to a newly developed near real-time (NRT) hybrid framework (Guo et al., 2016).

Particularly, a hybrid framework was introduced to enhance the damping estimation in terms of the combination of two system identification (SI) schemes such as WT-TSVD-Laplace wavelet filtering for non-stationary data, e.g., earthquake response and SSI-COV for stationary data such as wind response (e.g., Van Overschee and De Moor, 1996; Peeters and De Roeck, 1999). It is worth noting that an innovative web-based framework was designed and applied to the SHM of Burj Khalifa. This streamlines the overall procedure as an “Internet of Things” (IoT) concept in SHM. **Figure 15A** depicts a web-enabled NRT hybrid SI framework being employed in Burj Khalifa. Details can be found in Guo et al. (2016).

Through the back-end process, the hybrid SI framework embedded in the analysis server is continuously performed whenever a data segment is ready. After the analysis, the estimated results are automatically stored in the database management system, MySQL in this study, to gain more flexibility for additional data analysis with accumulated valuable SI datasets in the future. For a convenient data visualization, several web interfaces in the front-end process are established, where the interfaces implicitly interrogate with the database and then display the results on the interface on-demand, on-the-fly. In the case of transient events such as earthquake events, users can see a table containing event

time, frequency and damping information for each mode. A table format is a better choice than a plot in this case due to the fact that such events are relatively rare, thus a collection of all extreme events would provide useful information for a user to grasp all past events. For the cases of normal conditions such as under extra-tropical winds and/or ambient excitations, two kinds of plots are illustrated in the result interface (**Figures 15B,C**). One is a plot to show the trend of accumulated frequency and damping information against RMS amplitude in each mode, which is valuable to examine the trend of amplitude dependence (**Figure 15B**). Updated statistics of estimates, i.e., mean and CoV, are also included inside each plot. The other is a display of time history of frequency, damping and RMS amplitude, which is very useful to check the variation of dynamic properties of the structure such as natural frequencies and damping over time (**Figure 15C**). In this manner, users can see both the latest and accumulated SI results whenever accessing to the web interface. It is anticipated that the proposed framework in the context of the *IoT* has the potential of being well-suited for the SHM system to meet the demand of quick near real-time structural performance assessment involving minimal human intervention and ultimately offering a decision-support system for the building operation regarding structural operation as currently employed by the owners. More detailed information can be found in the study of Guo et al. (2016).

CONCLUDING REMARKS

The enormous reported losses from wind-related events and the increased sensitivity of civil infrastructures such as freeform super tall buildings, long-span bridges, and deep water offshore platforms etc. to wind call for a new paradigm for their analysis, modeling, and performance assessment. A cyber-enabled framework based on a VO, VORTEX-Winds,⁶ presented in this paper offers these such analysis/design tools. VORTEX-Winds is viewed by some as a microcosm of the CI and SimCenter of the new NSF NHERI initiative. Through the development of e-modules stitched and networked with a flexible architecture and interfaces to support research and education objectives in real-time, these cyber-enabled analysis, modeling, and simulation tools in the VORTEX-Winds promise to enhance the capability of individuals beyond their current resources through a synergistic, integrative approach to understanding and modeling the complexity of wind-structure interactions. This framework can help the wind community minimize windstorm damage and meet the challenges posed by burgeoning emergence of wind-sensitive structures. Consequently, the result will be a community as a whole better positioned to address the next frontiers in the field. Currently, most of the modules are available to the general public *via* registration at <https://vortex-winds.org> and one of

DED modules (VORTEX-Winds: DEDM-HR) has been ported to the NHERI DesignSafe Discovery portal at <https://www.designsafe-ci.org>. Some of the modules are still being beta tested and others are restricted and require additional registration and login for additional firewall equipment of cloud platform and external servers.

It is envisaged that this cyber-enabled framework would facilitate an effective, transformative, and conveniently accessible framework for the acceleration of advances in research and design practice, as well as teaching and learning, in the broad wind effects area and would have a revolutionary impact on this field due to its unprecedented potential of dissemination of knowledge and tools through easily accessible NHERI or NatHaz CI. In addition, the architecture and implementation of e-modules demonstrated in this study will serve as a reference or direction for prompting additional cyber-enabled developments by the community.

AUTHOR CONTRIBUTIONS

AK has overseen the management of the project to build the cyber-enabled framework, VORTEX-Winds, taken lead in assessment of overall development and prepared and revised this paper with DK. DK has coordinated overall project among collaborators, developed, and validated a variety of e-modules with collaborators, and written this paper with AK.

ACKNOWLEDGMENTS

The authors are greatly appreciated for the financial support by the National Science Foundation *via* grant CBET-0742191 and the matching support provided by the University of Notre Dame in the initial phase of the project. Support by the Global Center of Excellence (GCOE): New Frontiers of Education and Research in Wind Engineering at TPU, Ministry of Education, Culture, Sports, Science and Technology (MEXT), Japan, under the direction of Prof. Y. Tamura has been critical in sustaining the long-term goals of this cyber-based vision and it is gratefully acknowledged. The support for this paper was also in part provide by the National Science Foundation Grants # CMMI-1301008; CMMI-1520817; CMMI-1612843. The authors are grateful to their colleagues who kindly agreed to serve as members of the collaboratory and have contributed many fundamental developments at various stages of the project. The authors are indebted to Drs. Y. Tamura (Tokyo Polytechnic University, Japan), T. Kijewski-Correa, G. Madey, N. Regola, R. Lichtenwalter, J. Thomas, P. Sempolinski, D. Thain (University of Notre Dame, USA), C.-M. Cheng, and J. Wang (Tamkang University, Taiwan) for their many invaluable contributions, without their support this dream would not have been materialized. The authors also acknowledge students from the University of Notre Dame and Beijing Jiaotong University for their participation in the crowd-sourcing experiment.

⁶<https://vortex-winds.org>.

REFERENCES

- American Society of Civil Engineers (ASCE). (2005). *Minimum Design Loads for Buildings and Other Structures*. ASCE 7-05. Reston, VA: ASCE.
- American Society of Civil Engineers (ASCE). (2010). *Minimum Design Loads for Buildings and Other Structures*. ASCE 7-10. Reston, VA: ASCE.
- Architectural Institute of Japan (AIJ). (2000). *Damping in Japan*. Japan: Maruzen.
- Architectural Institute of Japan (AIJ). (2004). *RLB Recommendations for Loads on Buildings*. Tokyo, Japan: Structural Standards Committee, Architectural Institute of Japan.
- Bay, H., Tuytelaars, T., and Gool, L. V. (2006). "Surf: speeded up robust features," in *European Conference on Computer Vision*, Graz, Austria. p. 404–417.
- Bearman, P. W., and Trueman, D. M. (1972). An investigation of the flow around rectangular cylinders. *Aeronaut. Qtrly.* 23, 229–237.
- Bernardini, E., Spence, S. M. J., Kwon, D. K., and Kareem, A. (2015). Performance-based design of high-rise buildings for occupant comfort. *J. Struct. Eng.* 141, 04014244. doi:10.1061/(ASCE)ST.1943-541X.0001223
- Butler, K. (2010). *The Impact of Extreme Wind Events on Structures*. Ph.D. Dissertation. Notre Dame, IN, USA: University of Notre Dame.
- Carassale, L., and Solari, G. (2006). Monte Carlo simulation of wind velocity fields on complex structures. *J. Wind Eng. Ind. Aerodyn.* 94, 323–339. doi:10.1016/j.jweia.2006.01.004
- Castro, I. P., and Graham, J. M. R. (1999). Numerical wind engineering: the way ahead. *Proc. Inst. Civ. Eng. Struct. Build.* 134, 275–277. doi:10.1680/istbu.1999.31569
- CEN. (2010). *Eurocode 1: Actions on Structures – Part 1-4: General Actions – Wind Actions*. EN 1991-1-4:2005/AC:2010 (E). Europe: European Standard (Eurocode), European Committee for Standardization (CEN).
- Chen, X., and Kareem, A. (2005). Dynamic wind effects on buildings with 3-D coupled modes: application of HFFB measurements. *J. Eng. Mech.* 131, 1115–1125. doi:10.1061/(ASCE)0733-9399(2005)131:11(1115)
- Cheng, C.-M., and Wang, J. (2004). "Wind tunnel database for an intermediate wind resistance design of tall buildings," in *Proc. 1st Int. Sym. on Wind Effects on Buildings and Urban Env.*, Tokyo Polytechnic University (Tokyo, Japan).
- Cluni, F., Gusella, V., Spence, S. M. J., and Bartoli, G. (2011). Wind action on regular and irregular tall buildings: higher order moment statistical analysis by HFFB and SMPSS measurements. *J. Wind Eng. Ind. Aerodyn.* 99, 682–690. doi:10.1016/j.jweia.2011.01.020
- Davenport, A. G. (1967). Gust loading factors. *J. Struct. Div.* 93, 11–34.
- Deodatis, G. (1996). Simulation of ergodic multivariate stochastic processes. *J. Eng. Mech.* 122, 778–787. doi:10.1061/(ASCE)0733-9399(1996)122:8(778)
- Di Paola, M. (1998). Digital simulation of wind field velocity. *J. Wind Eng. Ind. Aerodyn.* 74–76, 91–109. doi:10.1016/S0167-6105(98)00008-7
- Di Paola, M., and Gullo, I. (2001). Digital generation of multivariate wind field processes. *Probab. Eng. Mech.* 16, 1–10. doi:10.1016/S0266-8920(99)00032-6
- Ding, Q., Zhu, L., and Xiang, H. (2006). Simulation of stationary Gaussian stochastic wind velocity field. *Wind Struct.* 9, 231–243. doi:10.12989/was.2006.9.3.231
- Fage, A., and Johansen, F. C. (1927). On the flow of air behind an inclined flat plate of infinite span. *Proc. R. Soc. A* 116, 170–197. doi:10.1098/rspa.1927.0130
- Frame, I., Austen, K. F., Calleja, M., Dove, M. T., White, T. O. H., and Wilson, D. J. (2009). New tools to support collaboration and virtual organizations. *Phil. Trans. R. Soc. A* 367, 1051–1056. doi:10.1098/rsta.2008.0193
- Goasguen, S., Madhavan, K., Wolinsky, D., Figueiredo, R., Frey, J., Roy, A., et al. (2008). Middleware integration and deployment strategies for cyberinfrastructures. *Adv. Grid Pervasive Comput.* 5036, 187–198. doi:10.1007/978-3-540-68083-3_20
- Google. (2015). *Google Maps API*. Google Inc. Available at: <https://developers.google.com/maps/>
- Guo, Y., Kwon, D. K., and Kareem, A. (2016). Near-real-time hybrid system identification framework for civil structures with application to Burj Khalifa. *J. Struct. Eng.* 142, 04015132. doi:10.1061/(ASCE)ST.1943-541X.0001402
- Gurney, R. J., Badcock, N. S., Garnett, E. A., and Godfray, H. C. J. (2009). The environmental eScience revolution. *Phil. Trans. R. Soc. A* 367, 803–813. doi:10.1098/rsta.2008.0253
- JAVA. (2015). *JAVA Software*. Oracle Corporation. Available at: <http://www.java.com/>
- Kaimal, J. C., Wyngaard, J. C., Izumi, Y., and Cote, O. R. (1972). Spectral characteristics of surface-layer turbulence. *J. R. Meteorol. Soc.* 98, 563–589. doi:10.1002/qj.49709841707
- Kareem, A. (1985). Structural performance and wind speed-damage correlation in hurricane Alicia. *J. Struct. Eng.* 111, 2596–2610. doi:10.1061/(ASCE)0733-9445(1985)111:12(2596)
- Kareem, A. (1986). Performance of cladding in hurricane Alicia. *J. Struct. Eng.* 112, 2679–2693. doi:10.1061/(ASCE)0733-9445(1986)112:12(2679)
- Kareem, A. (2005). "Bluff body aerodynamics and aeroelasticity: a wind effects perspective," in *Proc. the Fourth European and Africa Conference on Wind Engineering* (Prague, Czech Republic).
- Kareem, A. (2008). Numerical simulation of wind effects: a probabilistic perspective. *J. Wind Eng. Ind. Aerodyn.* 96, 1472–1497. doi:10.1016/j.jweia.2008.02.048
- Kareem, A., and Allen, R. (1990). Development of knowledge-based systems in wind engineering. *J. Wind Eng. Ind. Aerodyn.* 36, 1245–1257. doi:10.1016/0167-6105(90)90121-R
- Kareem, A., Kijewski, T., and Tamura, Y. (1999). Mitigation of motions of tall buildings with specific examples of recent applications. *Wind Struct.* 2, 132–184. doi:10.12989/was.1999.2.3.201
- Kareem, A., Kijewski-Correa, T., Tamura, Y., and Madey, G. (2009). "Next frontiers of innovation, discovery and learning in wind engineering: a cyberinfrastructure perspective," in *Proceedings of 4th International Symposium on Wind Effects on Buildings and Urban Environment* (Tokyo, Japan).
- Kareem, A., and Zhou, Y. (2003). Gust loading factor – past, present and future. *J. Wind Eng. Ind. Aerodyn.* 91, 1301–1328. doi:10.1016/j.jweia.2003.09.003
- Kijewski, T., Kwon, D. K., and Kareem, A. (2003). "E-technologies for wind effects on structures," in *Proc. 11th Int. Conf. on Wind Engineering (CD-ROM)* (Lubbock, TX: Texas Tech Univ.).
- Kijewski-Correa, T., Kilpatrick, J., Kareem, A., Kwon, D. K., Bashor, R., Kochly, M., et al. (2006). Validating the wind-induced response of tall buildings: a synopsis of the Chicago full-scale monitoring program. *J. Struct. Eng.* 132, 1509–1523. doi:10.1061/(ASCE)0733-9445(2006)132:10(1509)
- Kijewski-Correa, T., Kwon, D. K., Kareem, A., Bentz, A., Guo, Y., Bobby, S., et al. (2013). SmartSync: an integrated real-time structural health monitoring and structural identification system for tall buildings. *J. Struct. Eng.* 139, 1675–1687. doi:10.1061/(ASCE)ST.1943-541X.0000560
- Kijewski-Correa, T., Smith, N., Taflanidis, K. A., Liu, C., Krusche, M., and Vardeman, C. II (2014). CYBER-EYE: development of integrated cyber-infrastructure to support rapid hurricane risk-assessment. *J. Wind Eng. Ind. Aerodyn.* 133, 211–224. doi:10.1016/j.jweia.2014.06.003
- Kwon, D., Kijewski-Correa, T., and Kareem, A. (2005). "e-Analysis of tall buildings subjected to wind loads," in *Proc. 10th Americas Conference on Wind Engineering* (Baton Rouge, LA: AAWE).
- Kwon, D. K., and Kareem, A. (2009). Gust-front factor: new framework for wind load effects on structures. *J. Struct. Eng.* 135, 717–732. doi:10.1061/(ASCE)0733-9445(2009)135:6(717)
- Kwon, D. K., and Kareem, A. (2013a). A multiple database-enabled design module with embedded features of international codes and standards. *Int. J. High Rise Build.* 2, 257–269.
- Kwon, D. K., and Kareem, A. (2013b). Generalized gust-front factor: a computational framework for wind load effects. *Eng. Struct.* 48, 635–644. doi:10.1016/j.engstruct.2012.12.024
- Kwon, D. K., Kareem, A., Kumar, D., and Tamura, Y. (2016). A prototype on-line database-enabled design framework for wind analysis/design of low-rise buildings. *Front. Struct. Civil Eng.* 10, 121–130. doi:10.1007/s11709-015-0329-3
- Kwon, D. K., Kijewski-Correa, T., and Kareem, A. (2008). e-Analysis of high-rise buildings subjected to wind loads. *J. Struct. Eng.* 134, 1139–1153. doi:10.1061/(ASCE)0733-9445(2008)134:7(1139)
- Kwon, D. K., Kijewski-Correa, T., and Kareem, A. (2010). "SmartSync: an integrated real-time monitoring and SI system for tall buildings," in *2010 ASCE Structures Congress* (Orlando, Florida: ASCE).
- Kwon, D. K., Kijewski-Correa, T., and Kareem, A. (2011). "Event-driven SmartSync system for structural health monitoring of tall buildings," in *Proceedings of 13th International Conference on Wind Engineering (ICWE 13)* (Amsterdam, Netherlands).
- Kwon, D. K., Spence, S. M. J., and Kareem, A. (2014). A cyberbased data-enabled design framework for high-rise buildings driven by synchronously measured surface pressures. *Adv. Eng. Softw.* 77, 13–27. doi:10.1016/j.advengsoft.2014.07.001
- Main, J. A., and Fritz, W. P. (2006). *Database-Assisted Design for Wind: Concepts, Software, and Examples for Rigid and Flexible Buildings*. Gaithersburg, MD, USA: NIST Building Science Series 180, NIST.

- Mathworks. (2015). *MATLAB*. The Mathworks, Inc. Available at: <http://www.mathworks.com/>
- Mizota, T., Yamada, H., Kubo, Y., Okajima, A., Knisely, C. W., and Shirato, H. (1988). Aerodynamic characteristics of fundamental structures. Part 1, Section 2. (in Japanese). *J. Wind Eng.* 1988, 50–52. doi:10.5359/jawe.1988.36_50
- Muja, M., and Lowe, D. G. (2009). “Fast approximate nearest neighbors with automatic algorithm configuration,” in *International Conference on Computer Vision Theory and Applications (VISAPP 2009)*, Lisboa, Portugal, 331–340.
- Munich Re Group. (2012). *Severe Weather in North America*. Munich, Germany: Munich Re Group. Press Release.
- MySQL. (2015). *MySQL: The World's Most Popular Open Source Database*. Oracle Corporation. Available at: <http://www.mysql.com/>
- National Instruments. (2015). *LabVIEW – System Design Software*. National Instruments Corporation. Available at: <http://www.ni.com/>
- National Science Foundation (NSF). (2014). *Natural Hazards Engineering Research Infrastructure (NHERI)*. Division of Civil, Mechanical and Manufacturing Innovation, NSF. Available at: http://www.nsf.gov/funding/pgm_summ.jsp?pins_id=503259
- OpenFOAM. (2015). *Open Source CFD Software Package*. OpenCFD Ltd (ESI Group). Available at: <http://www.openfoam.com/>
- Peeters, B., and De Roeck, G. (1999). Reference-based stochastic subspace identification for output-only modal analysis. *Mech. Syst. Signal Process.* 13, 855–878. doi:10.1006/mssp.1999.1249
- PHP. (2015). *PHP: Hypertext Preprocessor*. The PHP Group. Available at: <http://www.php.net/>
- Rodgers, G. (2011). “NEES cyberinfrastructure and cloud simulation features of the NEEShub,” in *Advances in Real-Time Hybrid Simulation Workshop* (Bethlehem, PA: NEES@Lehigh).
- Satake, N., Suda, K., Arakawa, T., Sasaki, A., and Tamura, Y. (2003). Damping evaluation using full-scale data of buildings in Japan. *J. Struct. Eng.* 129, 470–477. doi:10.1061/(ASCE)0733-9445(2003)129:4(470)
- Sempolinski, P., Wei, D., Kareem, A., and Thain, D. (2015). Adapting collaborative software development techniques to structural engineering. *IEEE Comput. Sci. Eng.* 17, 27–34. doi:10.1109/MCSE.2015.88
- Shinozuka, M., and Deodatis, G. (1991). Simulation of stochastic processes by spectral representation. *Appl. Mech. Rev.* 44, 191–204. doi:10.1115/1.3119501
- Simiu, E., Gabbai, R. D., and Fritz, W. P. (2008). Wind-induced tall building response: a time domain approach. *Wind Struct.* 11, 427–440. doi:10.12989/was.2008.11.6.427
- Solari, G. (1993a). Gust buffeting. I: Peak wind velocity and equivalent pressure. *J. Struct. Eng.* 119, 365–382. doi:10.1061/(ASCE)0733-9445(1993)119:2(365)
- Solari, G. (1993b). Gust buffeting. II: Dynamic along-wind response. *J. Struct. Eng.* 119, 383–397. doi:10.1061/(ASCE)0733-9445(1993)119:2(383)
- Solari, G., and Kareem, A. (1998). On the formulation of ASCE 7-95 gust effect factor. *J. Wind. Eng. Ind. Aerodyn.* 7, 673–684. doi:10.1016/S0167-6105(98)00182-2
- Solari, G., and Piccardo, G. (2001). Probabilistic 3-D turbulence modeling for gust buffeting of structures. *Probab. Eng. Mech.* 19, 73–86. doi:10.1016/S0266-8920(00)00010-2
- Spence, S. M. J., and Kareem, A. (2014). Tall buildings and damping: a concept-based data-driven model. *J. Struct. Eng.* 140, 04014005. doi:10.1061/(ASCE)ST.1943-541X.0000890
- Staffelbach, M., Sempolinski, P., Kijewski-Correa, T., Thain, D., Wei, D., Kareem, A., et al. (2015). Lessons learned from crowdsourcing complex engineering task. *PLoS ONE*, 10:e0134978. doi:10.1371/journal.pone.0134978
- Tamura, Y. (2013). “TPU global COE program – new frontier of education and research in wind engineering,” in *The 6th International Symposium on Wind Effects on Buildings and Urban Environment (ISWE6) – Current-State-of-the-Art in Wind Engineering and Outlook for the Future* (Tokyo, Japan).
- Thomas, J., Bowyer, K. W., and Kareem, A. (2011). “Towards a robust automated hurricane damage assessment from high resolution images,” in *13th International Conference on Wind Engineering (ICWE 13)* (Amsterdam, Netherlands).
- Thomas, J., Bowyer, K. W., and Kareem, A. (2012a). “Color balancing for change detection in multitemporal images,” in *IEEE Workshop on Applications of Computer Vision* (Colorado Springs, CO).
- Thomas, J., Kareem, A., and Bowyer, K. W. (2012b). “Fast, robust feature-based matching for automatic image registration in disaster response applications,” in *IEEE International Geoscience and Remote Sensing Symposium (IGARSS)* (Munich, Germany).
- Van Den Einde, L., Kinderman, T. L., Masuda, M., and Elgamal, A. (2007). “NEES IT tools to advance earthquake engineering research,” in *Proceedings of Structures Congress 2007* (Long Beach: CD-ROM).
- Van Overschee, P., and De Moor, B. (1996). *Subspace Identification for Linear Systems*. Dordrecht, Netherlands: Kluwer Academic Publishers.
- Vickery, B. J. (1970). “On the reliability of gust loading factors,” in *Proceedings of the Technical Meet Concerning Wind Loads on Buildings and Structures* (Washington: National Bureau of Standards), 93–104.
- Wang, N., and Adeli, H. (2012a). Web-based tutor for interactive design of single-span and continuous steel beams. *Comput. Appl. Eng. Educ.* 20, 383–389. doi:10.1002/cae.20474
- Wang, N., and Adeli, H. (2012b). Web-based tutor for interactive design of connections in steel buildings. *Comput. Appl. Eng. Educ.* 20, 568–577. doi:10.1002/cae.20474
- Wieselsberger, C. (1921). Neuere Feststellungen über die Gesetze des Flüssigkeits- und Luftwiderstands. *Physics* 2, 321–328.
- Wittig, L. E., and Sinha, A. K. (1975). Simulation of multicorrelated random processes using the FFT algorithm. *J. Acoust. Soc. Am.* 58, 630–633. doi:10.1121/1.380702
- Zhou, Y., and Kareem, A. (2001). Gust loading factor: new model. *J. Struct. Eng.* 127, 168–175. doi:10.1061/(ASCE)0733-9445(2001)127:2(168)
- Zhou, Y., Kijewski, T., and Kareem, A. (2003). Aerodynamic loads on tall buildings: an interactive database. *J. Struct. Eng.* 129, 394–404. doi:10.1061/(ASCE)0733-9445(2003)129:3(394)

Conflict of Interest Statement: The authors declare that the research was conducted in the absence of any commercial or financial relationships that could be construed as a potential conflict of interest.

Copyright © 2017 Kareem and Kwon. This is an open-access article distributed under the terms of the Creative Commons Attribution License (CC BY). The use, distribution or reproduction in other forums is permitted, provided the original author(s) or licensor are credited and that the original publication in this journal is cited, in accordance with accepted academic practice. No use, distribution or reproduction is permitted which does not comply with these terms.

Advantages of publishing in Frontiers



OPEN ACCESS

Articles are free to read
for greatest visibility
and readership



FAST PUBLICATION

Around 90 days
from submission
to decision



HIGH QUALITY PEER-REVIEW

Rigorous, collaborative,
and constructive
peer-review



TRANSPARENT PEER-REVIEW

Editors and reviewers
acknowledged by name
on published articles

Frontiers

Avenue du Tribunal-Fédéral 34
1005 Lausanne | Switzerland

Visit us: www.frontiersin.org

Contact us: info@frontiersin.org | +41 21 510 17 00



REPRODUCIBILITY OF RESEARCH

Support open data
and methods to enhance
research reproducibility



DIGITAL PUBLISHING

Articles designed
for optimal readership
across devices



FOLLOW US

@frontiersin



IMPACT METRICS

Advanced article metrics
track visibility across
digital media



EXTENSIVE PROMOTION

Marketing
and promotion
of impactful research



LOOP RESEARCH NETWORK

Our network
increases your
article's readership